THÈSE

Pour obtenir le grade de

DOCTEUR DE L'UNIVERSITÉ GRENOBLE ALPES

École doctorale : EEATS - Electronique, Electrotechnique, Automatique, Traitement du Signal
Spécialité : Automatique - Productique
Unité de recherche : Laboratoire de conception et d'intégration des systèmes

Commande avancée pour un four électrique triphasé produisant du silico manganèse

Advanced control for a three-phase electric arc furnace producing silico-manganese

Présentée par :

Minh Tuan DINH

Direction de thèse :

Ionela PRODAN MAITRE DE CONFERENCES, GRENOBLE INP - UGA	Directrice de thèse
Eduardo MENDES PROFESSEUR DES UNIVERSITES, GRENOBLE INP - UGA	Co-directeur de thèse
Olivier LESAGE Ingénieur, Eramet Ideas	Co-encadrant de thèse

Rapporteurs :

Gabriele PANNOCCHIA
FULL PROFESSOR, University of Pisa
Vicenç PUIG
FULL PROFESSOR, Polytechnic University of Catalonia

Thèse soutenue publiquement le **13 février 2026**, devant le jury composé de :

John Jairo MARTINEZ MOLINA, PROFESSEUR DES UNIVERSITES, Grenoble INP - UGA	Président
Gabriele PANNOCCHIA, FULL PROFESSOR, University of Pisa	Rapporteur
Vicenç PUIG, FULL PROFESSOR, Polytechnic University of Catalonia	Rapporteur
Alexandra GRANCHAROVA, FULL PROFESSOR, University of Chemical Technology and Metallurgy	Examinatrice

Invités :

Dina IROFTI
INGENIEURE DOCTEURE, EDF R&D
Alexandre CHEANU
INGENIEUR DOCTEUR, Eramet Ideas

UNIVERSITÉ GRENOBLE ALPES (UGA)

Électronique, Électrotechnique, Automatique, Traitement du Signal (ED EEATS)

Laboratoire de Conception et d'Intégration des Systèmes (LCIS)

Coordination, Coopération & Commande des Systèmes Complexes (Co4Sys)

Abstract

Doctorate degree

Specialty: Automation - Production

Advanced Control for a Three-Phase Electric Arc Furnace Producing Silico-Manganese

by **Minh Tuan DINH**

Electric arc furnace (EAF) is widely used in the steel industry for melting and refining steel or alloy products, particularly manganese (Mn) ferroalloys, essential and irreplaceable ingredients in carbon steel production. In recent years, EAF technologies have shown steady growth in production capacity and global market share, driven by increasing demand for highly energy-efficient methods and the need for more environmentally friendly production. This has become especially important in the context of France's ambition to achieve the 2050 Carbon Neutrality Plan.

Mn ferroalloys are made by melting and reducing manganese ores, coke and fluxes in an EAF. This furnace relies on the Joule effect from a three-phase alternating current, transmitted through three electrodes, to provide the thermal energy for melting and reduction reactions. Electrical regulation, which directly controls energy use, is critical to furnace operation because it operates and reacts on short timescales, unlike most other process levers and indicators, such as input/output materials or temperatures.

However, effective automatic control of the EAF electrical system remains challenging due to its complex, poorly understood dynamics and the lack of well-established control strategies. The main difficulty is that the reaction zone of the furnace bath cannot be directly observed. In addition, strong interactions among the three phases can lead to instability if not adequately addressed. The system is also subject to various hard operational constraints (discrete tap operations, limited electrode current, and the like) that conventional current control methods handle poorly. Furthermore, while recent studies tend to focus on energy optimization or economic control, issues specific to the EAF electrical system, considered as the backbone of furnace operation, are often overlooked.

As a result, the goal of this thesis is to develop an advanced, scalable, and flexible control framework for a three-phase EAF producing Silico-Manganese capable of handling the complex interconnections in the system. Importantly, this framework explicitly incorporates operational constraints while ensuring optimal performance of the EAF electrical system, thereby improving the EAF's stability and productivity.

To this end, electrical principles such as Kirchhoff's laws and Ohm's law are used to model the system's electrical behavior accurately. Moreover, well-established concepts such as Model Predictive Control (MPC) and Mixed-Integer Programming (MIP) are adapted and integrated into the optimization-based control design, ensuring effective and flexible strategic regulation of furnace operation. In addition, the design of a computationally efficient solving algorithm using heuristic approaches is considered to address the computational demands of the MIP problem in real-time implementation.

The thesis first focuses on understanding the complex behavior of the three-phase EAF electrical system through the development of comprehensive mathematical models. Then, different optimal control problems are formulated to achieve the desired objectives. MIP problems are efficiently solved by the proposed approximate algorithms and compared with state-of-the-art MIP solvers. The control frameworks are then validated through numerical simulations on the real-time Software-in-the-Loop (SIL) simulator.

Keywords: Electric Arc Furnace, Submerged Arc Furnace, Electrical System, Model Predictive Control, Mixed-Integer Programming, Heuristic Algorithm, Software-in-the-Loop Simulation.

UNIVERSITÉ GRENOBLE ALPES (UGA)

Électronique, Électrotechnique, Automatique, Traitement du Signal (ED EEATS)

Laboratoire de Conception et d'Intégration des Systèmes (LCIS)

Coordination, Coopération & Commande des Systèmes Complexes (Co4Sys)

Résumé

Diplôme de doctorat

Spécialité : Automatique - Productique

Commande Avancée pour un Four à Arc Électrique Triphasé Produisant du Silico-Manganèse

par **Minh Tuan DINH**

Le four à arc électrique (EAF) est largement utilisé dans l'industrie sidérurgique pour la fusion et le raffinage des aciers et alliages, tels que les ferroalliages de manganèse (Mn), ingrédients essentiels et irremplaçables dans la production d'acier au carbone. Ces dernières années, les technologies EAF ont montré une croissance régulière en termes de capacité de production et de part de marché mondial, poussées par la demande croissante de méthodes à haute efficacité énergétique et par le besoin de productions plus respectueuses de l'environnement. Les objectifs fixés par le Plan de Neutralité Carbone 2050 de la France, accélèrent le développement des fours électriques.

Les ferroalliages de Mn sont fabriqués en fondant et en réduisant des minerais de manganèse, mélangés avec du coke dans un EAF. Son procédé repose sur l'effet Joule d'un courant électrique alternatif triphasé transmis par trois électrodes pour fournir l'énergie thermique nécessaire aux réactions de fusion et de réduction. La régulation électrique, qui contrôle directement l'énergie utilisée, est essentielle au fonctionnement du four, car elle opère et réagit sur des échelles de temps courtes, contrairement aux autres leviers et indicateurs de processus tels que la chimie des échantillons et les températures mesurées.

Cependant, le contrôle automatique du système électrique de l'EAF est difficile en raison de dynamiques complexes et mal comprises, à tel point que des experts procédé et métallurgie sont nécessaires pour décider comment conduire ces fours au quotidien. La raison vient du fait qu'il est impossible d'observer ce qui se passe dans la zone de réaction du bain du four. De plus, il existe une présence inhérente d'effets de couplage entre les trois phases qui, s'ils ne sont pas pris en compte, peuvent conduire à un contrôle instable. En outre, le système est soumis à diverses contraintes opérationnelles strictes (par exemple, ajustement des tensions transformateurs étagées par plot, limitations en courant des composants, etc.) qui ne sont pas efficacement traitées par les méthodes de contrôle conventionnelles. En outre, les recherches récentes tendent à se concentrer sur l'optimisation énergétique et économique, tandis que problèmes associés au système électrique de l'EAF, considéré comme la colonne vertébrale du fonctionnement du four, sont peu étudiés.

Par conséquence, l'objectif de cette thèse est de développer contrôle avancé, évolutif et flexible pour un EAF triphasé tel qu'utilisé pour produire du SiMn, capable de gérer l'interconnexion complexe du système. Il est important que ce cadre intègre explicitement les contraintes opérationnelles tout en assurant efficacement des performances optimales au système électrique de l'EAF, améliorant ainsi sa stabilité et sa productivité.

À cette fin, des principes électriques tels que les lois de Kirchhoff ou la loi d'Ohm sont utilisés pour modéliser le comportement électrique du système. De plus, des concepts bien établis comme la commande prédictive (MPC) et la programmation mixte en nombres entiers (MIP) sont adaptés et intégrés dans la conception de cette nouvelle méthode de contrôle. L'identification d'une solution optimale offre une régulation efficace et flexible du fonctionnement du four. Pour cela, un algorithme de résolution efficace et rapide utilisant des approches heuristiques est envisagé pour répondre aux exigences de calcul du problème MIP dans une mise oeuvre en temps réel.

Mots-clés : Four à arc électrique, four à arc submergé, système électrique, commande prédictive, programmation en nombres entiers mixtes, algorithme heuristique, simulation par logiciel en boucle.

Contents

Abstract i

Resumé iv

List of Figures ix

List of Tables xiii

List of Algorithms xv

Notation xv

1 Introduction 1
- 1.1 Sustainable electric arc furnaces . . . 1
  - 1.1.1 Growth in recent years . . . 3
  - 1.1.2 Years in EAF automation and control . . . 6
  - 1.1.3 Motivation for the thesis . . . 13
- 1.2 Thesis orientation . . . 15
  - 1.2.1 Study scope . . . 15
  - 1.2.2 Approaches . . . 16
- 1.3 Contributions of the thesis . . . 18
- 1.4 Organization of the manuscript . . . 21

2 High-intensity submerged-arc furnace 23
- 2.1 Electric arc furnace (EAF) . . . 24
  - 2.1.1 History of development . . . 24
  - 2.1.2 Classification of EAF . . . 26
  - 2.1.3 Control of EAF . . . 31
- 2.2 Silico-manganese (SiMn) submerged-arc furnace (SAF) . . . 35
  - 2.2.1 SiMn furnace design . . . 36

2.2.2 SiMn furnace operation . . . 40
2.3 SAF electrical control system . . . 43
2.3.1 Measurement system . . . 44
2.3.2 Control architecture . . . 46
2.4 Concluding remarks . . . 52

3 SiMn modeling in view of electrical control 54
3.1 Electrical circuit . . . 55
3.2 Modeling subsystem . . . 57
3.2.1 Three-phase transformer . . . 57
3.2.2 Electrode-process model . . . 59
3.3 Mathematical model formulation . . . 61
3.3.1 Dynamic relationships with actuators . . . 63
3.3.2 Steady state electrical models . . . 69
3.3.3 Output linearized model . . . 76
3.4 Open-loop system analysis based on models . . . 77
3.5 Concluding remarks . . . 81

4 SiMn control design and optimization tools 84
4.1 Operational requirements . . . 85
4.1.1 Control objective . . . 85
4.1.2 Tolerance ranges . . . 88
4.1.3 Hunting problem . . . 88
4.1.4 Operational constraints . . . 91
4.2 Validation frameworks . . . 94
4.2.1 Performance metrics . . . 94
4.2.2 Software-in-the-loop (SIL) environment . . . 96
4.3 Optimization-based control tools . . . 101
4.3.1 Model predictive control (MPC) . . . 102
4.3.2 Mixed-integer MPC . . . 112
4.3.3 Modeling languages and solvers . . . 117
4.4 Concluding remarks . . . 129

5 Independent power and current control 131
5.1 Electrode current control . . . 132
5.1.1 Multi-phase current control architecture . . . 132
5.1.2 Magnitude control formulation . . . 133
5.1.3 Long-term simulation analysis . . . 134
5.2 Integer-based power control . . . 141
5.2.1 Multi-phase power architecture . . . 142
5.2.2 Integer programming formulation . . . 143

5.2.3 Model-informed optimal rounding . . . 145
5.2.4 Long-term simulation analysis . . . 146
5.3 Concluding remarks . . . 159

6 Coordinated power and current control **161**
6.1 Mixed-integer power and current predictive control . . . 162
6.1.1 Coordinated power and current architecture . . . 162
6.1.2 Mixed-integer programming formulation . . . 163
6.1.3 Bilevel strategy . . . 166
6.2 SIL simulation results . . . 172
6.2.1 Scenario setup . . . 172
6.2.2 Performance analysis . . . 175
6.2.3 Discussion . . . 185
6.3 Concluding remarks . . . 186

7 Conclusions and future developments **188**
7.1 Conclusions . . . 188
7.1.1 Comprehensive electrical modeling and analysis . . . 189
7.1.2 Advanced control design and real-time optimization . . . 189
7.1.3 SIL validation in a more realistic environment . . . 190
7.2 Future developments . . . 191
7.2.1 Model enhancement . . . 191
7.2.2 Alternative control strategies . . . 192
7.2.3 Multi-level control frameworks . . . 196
7.2.4 Open-loop implementation . . . 197

Appendices **200**

A Appendix **200**
A.1 Electrical steady-state model analysis in Section 3.3 . . . 200
A.2 Classical mixed-integer linear programming algorithms . . . 201
A.2.1 Branch-and-bound algorithm . . . 202
A.2.2 Cutting plane method . . . 202

Bibliography **204**

List of Figures

1.1 Different design of EAF, including AC-EAF with three electrodes (top) and DC-EAF with one or two electrodes (bottom). 2
1.2 The comparison of the production capacity and share in steelmaking between basic oxygen furnace (BOF) and electric arc furnace (EAF) across the countries and regions in based on data in 2023 and prediction in 2030 [BigMint, 2024]. 3
1.3 Global average value for CO_2 emissions and energy intensity including blast furnace-basic oxygen furnace (BF-BOF), direct reduced iron (DRI)-based and scrap-based electric arc furnace (EAF) steel production routes [Enrico et al., 2019]. 4

2.1 Evolution of the electric arc furnace technology including key milestones and advancements with performance indicators on energy consumption, electrode consumption and tap-to-tap time from 1960s to 2020s. [Karbowniczek, 2021]. 25
2.2 Classification of Electric Arc Furnaces (EAF). 26
2.3 Schematic of different DC EAF configurations. 27
2.4 SAF schematic cross-section, showing difference between high-intensity SAF (left) and normal SAF (right). Reproduced with permission from Eramet Ideas. 30
2.5 Classification of control strategies for an EAF. 33
2.6 Schematic of a SiMn submerged-arc furnace. 36
2.7 SiMn SAF electrodes at COMILOG Dunkerque, France. 38
2.8 Søderberg electrode with hydraulic actuator systems. 39
2.9 Charging and stoking operations in SiMn SAF. 41
2.10 Casting operation in SiMn SAF. 43
2.11 Electrical measurement system of a SiMn SAF. 44
2.12 Control architectures of an EAF based on cooperation of submodules. . . 46
2.13 Overall EAF control architectures. 48
2.14 Conventional control with decentralized and decoupled architecture. . . . 49
2.15 Model predictive control (MPC) with coordinated architecture. 51

3.1 Electrical equivalent circuits for a SiMn electric arc furnace (EAF) system illustrating the two different transformer configurations in the primary side. 56
3.2 Schematic representation of a delta-delta three-phase transformer model, illustrating the primary and secondary windings connected in a Δ-Δ configuration. 58
3.3 Schematic winding arrangements of OLTC in the furnace transformer. . . 59
3.4 Schematic representation of a delta-wye electrode-process model, illustrating lumped impedance of electrodes and process burden in the molten bath. 60
3.5 Visualization of the transformer ratio parameters (m_a, m_b, m_c) as functions of the respective tap changer positions (τ_a, τ_b, τ_c) for all three phases using B-spline interpolation. 64
3.6 Visualization of the transformer internal impedance (Z_a^t, Z_b^t, Z_c^t) as functions of the respective tap changer positions (τ_a, τ_b, τ_c) for all three phases using least absolute deviation regression. 66
3.7 Visualization of the electrode-process impedance estimation in phase one using backward difference finite with 17 sample data and sampling is 1s. . 68
3.8 Dynamic response of transformer power (left) and electrode current (right) to control signal variations. The 4D plots demonstrate the effect of control action, i.e., transformer tap variation and electrode displacement on secondary active power of the transformer and the current magnitude in the electrode. 80

4.1 Logistic function (4.5) behavior based on $\|\mathbf{E}(k)\|_\infty$. 90
4.2 SIL simulation environment 97
4.3 SiMn furnace control system interface 100
4.4 SIL SiMn furnace interface with a focus on metallurgical system. 102
4.5 The receding horizon principle of MPC. 106
4.6 Classification of solution techniques for MINLP. 116
4.7 Architectural overview of the CasADi framework, illustrating its role as an interface between high-level modeling languages and high-performance numerical optimization solvers. A representative set of the supported solvers is also illustrated. 122
4.8 An example of CasADi expression graph representing the mathematical expression $f(x_1, x_2) = a(\sin x_1 + x_1 x_2)$, where x_1, x_2 are inputs, a is constant. 123

5.1 Proposed centralized MPC architectures to control electrode currents in all three phases by adjusting electrode heights. 132
5.2 Controlled output and input performance comparison between GS (blue), NMPC (orange) and LMPC (green) approaches under balanced setpoints (Scenario 1). 136
5.3 Electrical outputs under operational constraints (Scenario 1). 137

5.4 Current magnitude control performance comparison between GS (blue), NMPC (orange) and LMPC (green) approaches under unbalanced setpoints (Scenario 2). 139
5.5 Electrode-process impedance behaviors (Scenario 2). 140
5.6 Comparison of computation time per time step. 140
5.7 Proposed centralized MI-MPC architecture to control the transformer active powers in all three phases by adjusting tap positions. 142
5.8 Controlled active power across three phases and corresponding control actions as tap changer positions under normal and equal setpoints (Scenario 1). 151
5.9 Controlled active power across three phases and corresponding control actions as tap changer positions under high and equal setpoints (Scenario 2). 153
5.10 Electrical currents under operational constraints (Scenario 2). 154
5.11 Controlled active power across three phases and corresponding control actions as tap changer positions under unequal setpoints (Scenario 3). . . 156

6.1 Proposed centralized MI-MPC architectures to coordinately control both the active powers and current magnitudes in all three phases by adjusting tap positions and electrode heights. 162
6.2 Flowchart of the proposed BILEVEL optimization strategy for real-time solution of the MINLP problem. The approach consists of an inner QP-relaxation problem and is followed by multiple outer QP problems to select the (sub)-optimal control input for the initial MINLP problem (6.1). . . . 167
6.3 Performance comparison in phase 1: transformer power (top), electrode current (middle), and transformer current (bottom) under conventional GS control (blue) and the proposed BILEVEL approach (red) over 24 hours (Scenario 1). 176
6.4 Performance of the BILEVEL approach under time-varying, unbalanced setpoints (Scenario 2). The controller effectively tracks references while respecting all operational constraints, including tap balancing. 179
6.5 Tracking performance metrics for the four optimization-based approaches, averaged over three phases. 182
6.6 Performance comparison across four different optimization-based control strategies in phase 1: critical electrical output behaviors and corresponding control actions over 28 hours with time-varying unbalanced references (Scenario 2). 183
6.7 Total tap switching operations for each approach. The BILEVEL strategy finds a good compromise between performance and actuator usage. 184
6.8 Distribution of computation time per control step. The BILEVEL approach is significantly faster than MINLP and MIQP, making it suitable for real-time implementation. 184

7.1 Phase-magnitude predictive control scheme. 193

7.2 Performances of current magnitude and phase shift regulation under NMPC-based controller over a 24-hour simulation. 195

List of Tables

2.1 Comparison of AC EAF types based on heating method. 28
2.2 DC EAF applications demonstrated by Mintek [Jones and Curr, 2006]. . . 29
2.3 AC EAF for manganese alloy production by Eramet [Folmo et al., 2010]. . 29
2.4 Comparison of current and resistance control strategies. 35

3.1 Electrical output variables of interest in the SiMn SAF system. 62
3.2 Electrical parameter vectors in the SiMn SAF system. 62
3.3 Control actuator variables of the SiMn SAF system. 63
3.4 SiMn electrical variables at specific operating point for open-loop analysis. 78

4.1 Definitions of the performance metrics used for evaluation. 94
4.2 Comparison of Classical PID and Modern MPC Control. 111
4.3 Classification of main types of MIP problems. 115
4.4 Modeling tools comparison for optimization and control used in this thesis. 120
4.5 Overview of solvers can be used via CasADi QP interface (`qpsol`/`conic`). 125
4.6 Overview of some solvers can be used via CasADi NLP interface (`nlpsol`). 127

5.1 Details of implemented scenarios for electrode current control. 135
5.2 A brief explanation of the control approaches for electrode current regulation. 135
5.3 Numerical values of control parameters for electrode current control. . . . 136
5.4 Statistical results across three phases over 24 hours (Scenario 1 & 2). . . . 141
5.5 Details of implemented scenarios for transformer active power regulation. 148
5.6 A summary of optimization-based approaches for power control. 150
5.7 Numerical values of control parameters for Ps control. 150
5.8 Statistical results of power control over 24 hours (Scenario 1). 152
5.9 Statistical results of power control over 24 hours (Scenario 2). 155
5.10 Constraint violation rate among approaches (Scenario 2). 155
5.11 Statistical results of power control over 24 hours (Scenario 3). 157

6.1 Detail of implemented scenarios for power and current control. 173
6.2 A summary of the implemented optimization-based control approaches. . 174
6.3 Numerical values of control reference over four periods. 174

6.4 Numerical values of control parameters. 175
6.5 Statistical results in three phases over 24 hours (Scenario 1). 177
6.6 Statistical results of BILEVEL approach in three phases (Scenario 2). . . 180

7.1 Detailed implementation scenarios for phase-magnitude current control. . 194

List of Algorithms

4.1 Adaptive weight tuning 91

4.2 MPC scheme 106

5.1 Model-informed optimal rounding (MIOR) strategy 147

Nomenclature

The conventions and the notations used in the manuscript are classical in the field of electrical engineering and control automation. However, as many variables and parameters need to be used, a detailed description of the conventions and notations is provided to avoid potential confusion, improve accessibility of the variables, enhance coherence across chapters and facilitate the comparison of the techniques discussed.

Convention

Type	**Description**	**Example**
Vectors	Bold lowercase letters	$\mathbf{u}$
Matrices	Bold uppercase letters	$\mathbf{A}$
Number sets	Double-struck uppercase letters	$\mathbb{R}$
Special sets[1]	Calligraphic uppercase letters	$\mathcal{R}$
Vector spaces	n-dimensional vector	$\mathbb{R}^n$
Matrix spaces	n rows and m columns matrix	$\mathbb{R}^{n\times m}$
Electrical signals	Italic lowercase letters for instantaneous values	i
	Italic uppercase letters for magnitude values	I
	Bold italic lowercase for three-phase vectors	$\boldsymbol{i}$
Superscript	'p' for variables on primary side	$\boldsymbol{u}^{\boldsymbol{p}}$
	's' for variables on secondary side	$\boldsymbol{u}^{\boldsymbol{s}}$
	'e' for variables on electrode	$\boldsymbol{u}^{\boldsymbol{e}}$
Subscripts	'a', 'b', 'c' for phase order linked to transformers	i_a^s
	'1', '2', '3' for phase order linked to electrodes	i_1^e
	'12', '23', '31' for phase order linked to grid	u_{12}^p
Variable index	(t) for continuous time	$\mathbf{x}(t)$
	(k) for discrete time step	$\mathbf{x}(k)$
	$(s\|k)$ for prediction at s given information at k	$\mathbf{u}(s\|k)$
	$(\cdot\|k)$ for predicted sequence at step k	$\mathbf{u}(\cdot\|k)$

[1] See notation for "System and control design" for definitions.

Notations

Number sets, vector spaces, matrix spaces and operators

Notation	Definition
$\mathbb{C}$	set of complex numbers
$\mathbb{R}$	set of real numbers
$\mathbb{Z}$	set of integers
$\mathbb{Z}_+$	set of non-negative integers
$\mathbf{I}_n$	identity matrix of size $n \times n$
$\mathbf{I}_{n\times 1}$	column vector of ones of size n
$\mathbf{0}_{n\times m}$	null matrix of size $n \times m$
$e^{\jmath\theta}$	Euler's formula for real number θ : $\cos\theta + \jmath \sin\theta$
$\Re\{z\}$	real part of complex number z: a for $z = a + \jmath b$
$\Im\{z\}$	imaginary part of complex number z: b for $z = a + \jmath b$
$\angle\{z\}$	phase (angle) of complex number z: $\tan^{-1}(\Im\{z\}/\Re\{z\})$
z^*	complex conjugate of z: $\Re\{z\} - \jmath\,\Im\{z\}$
$\mathbf{z}^*$	complex conjugate of vector: $[z_1^*, \ldots, z_n^*]^\top$
$\mathbf{x}^\top$	transpose of vector $\mathbf{x}$
$\mathbf{x} \odot \mathbf{y}$	element-wise (Hadamard) product of vectors $\mathbf{x}$ and $\mathbf{y}$
$\mathrm{diag}(\mathbf{x})$	diagonal matrix with entries $x_1, \ldots, x_n$ for vector $\mathbf{x} \in \mathbb{R}^n$
$\lvert\mathbf{x}\rvert$	vector of absolute values: $[\lvert x_1\rvert, \ldots, \lvert x_n\rvert]^\top$ for vector $\mathbf{x} \in \mathbb{R}^n$
$\lvert\mathbf{z}\rvert$	vector of moduli: $[\sqrt{z_1\bar{z}_1}, \ldots, \sqrt{z_n\bar{z}_n}]^\top$ for vector $\mathbf{z} \in \mathbb{C}^n$
$\lVert\mathbf{x}\rVert_2$	euclidean (L2) norm of vector $\mathbf{x}$: $\sqrt{x_1^2 + \cdots + x_n^2}$
$\lVert\mathbf{x}\rVert_\infty$	infinity norm (maximum absolute) of vector $\mathbf{x}$: $\max(\lvert x_i\rvert)$
$\lVert\mathbf{x}\rVert_Q$	weighted norm: $\sqrt{\mathbf{x}^\top Q\mathbf{x}}$, with $Q \succeq 0$
$\lfloor\mathbf{x}\rfloor$	component-wise floor: rounds down each entry of $\mathbf{x}$
$\lceil\mathbf{x}\rceil$	component-wise ceiling: rounds up each entry of $\mathbf{x}$
$\arg\min_x f(\mathbf{x})$	value of $\mathbf{x}$ that minimizes the function $f(\mathbf{x})$

System and control design

Notation	Definition
$\mathcal{R}$	rounding set
$\mathcal{F}$	feasible set
$\mathcal{E}$	electrode set
$\mathbf{x}(\cdot)$	system state vector
$\mathbf{u}(\cdot)$	control input (decision) vector
$\mathbf{y}(\cdot)$	control output vector
$\Psi(\cdot)$	nonlinear dynamical function
$\overline{\Psi}(\cdot)$	linearized dynamical function
$B_{i,d,j}(\cdot)$	B-spline basis function
$p_{i,j}$	B-spline control points
d	B-spline degree
n	number of B-spline control points
$(\cdot)_{\mathbf{ub}}$, $(\cdot)_{\mathbf{lb}}$	upper bound and lower bound parameters
$(\cdot)_{\mathbf{max}}$	maximum parameters for control inputs
$(\cdot)_{\mathbf{0}}$	initial parameters
$(\cdot)^{\text{ref}}$	desired setpoint, reference
$J(\cdot)$, $L(\cdot)$	objective function
$\mathbf{A}$, $\mathbf{B}$, $\mathbf{C}$, $\mathbf{D}$	state-space matrices
$\mathbf{F}$, $\bar{\mathbf{F}}$, $\mathbf{G}$	constraint coefficient matrices
$\mathbf{q}$, $\bar{\mathbf{q}}$, $\mathbf{k}$	constraint coefficient vectors
$\mathbf{L}$	tap balancing constraint matrix
$\mathbf{Q}$	positive semi-definite penalty matrix for control output
$\mathbf{R}$	positive definite penalty for control input
N_p	prediction horizon
N_s	number of samples during simulation
$\boldsymbol{\epsilon}$	control tolerance
$\boldsymbol{\kappa}$	calibration vector for error accumulation
$\mathbf{E}$	accumulated error vector
δ	tap balancing tolerance
$\lambda_{\max}$	maximum penalty parameter for tap changer variation
μ	parameter for steepness of logistic function
ν	parameter for inflection point of logistic function
k_{log}	logistic growth rate
T_s	sampling time
k	discrete-time step
t	continuous time variable
s	prediction step in MPC

Furnace and electrical system

Notation	Definition	Unit
Δ	delta coupling	–
$\curlyvee$	star (wye) coupling	–
$\cos\phi$	power factor at 50 Hz	–
$\jmath$	imaginary unit	–
α_{ij}, β_i, ζ_i, η	coefficients in electrical models, $i, j \in \{1, 2, 3\}$	–
$\boldsymbol{f}^{\boldsymbol{m}}(\cdot)$, $f^m(\cdot)$	mapping function from tap position to ratio	–
$\boldsymbol{f}^{\boldsymbol{r}}(\cdot)$, $f^r(\cdot)$	mapping function from tap position to resistance	–
$\boldsymbol{f}^{\boldsymbol{x}}(\cdot)$, $f^x(\cdot)$	mapping function from tap position to reactance	–
$\boldsymbol{\gamma}^{\boldsymbol{r}}$, $\boldsymbol{\gamma}^{\boldsymbol{x}}$	gradient vectors of resistance and reactance with respect to electrode height vector	–
$\boldsymbol{\Gamma}^{\boldsymbol{r}}$, $\boldsymbol{\Gamma}^{\boldsymbol{x}}$	jacobian matrices of resistance and reactance vectors with respect to electrode height vector	–
$\boldsymbol{m}$, m	transformer ratio	–
$\boldsymbol{\delta h}$, δh	variation of electrode height	[m]
$\boldsymbol{\delta\tau}$, $\delta\tau$	variation of tap changer position	[step]
$\boldsymbol{\tau}$, τ	tap changer position	[step]
$\boldsymbol{h}$, h	electrode height	[m]
f	electrical frequency	[Hz]
$\boldsymbol{u}$, u, U	voltage	[V]
$\boldsymbol{i}$, i, I	current	[A]
$\boldsymbol{z}$, Z	impedance	[Ω]
$\boldsymbol{r}$, R	resistance	[Ω]
$\boldsymbol{x}$, X	reactance	[Ω]
S	apparent power	[VA]
Q	reactive power	[VAR]
$\boldsymbol{p}$, P	active power	[W]

Acronyms

Systems

Abbreviation	Definition
CAVs	connected and automated vehicles
I/O	input-output
MIMO	multiple input - multiple output system
SISO	single input - single output system
UAVs	unmanned aerial vehicles

Control

Abbreviation	Definition
GS	gain-scheduling
MPC	model predictive control
NMPC	nonlinear model predictive control
PLC	programmable logic controller
PID	proportional integral derivative
PIDD	proportional integral derivative second-derivative
PD	proportional derivative
RHC	receding horizon control
RB	rule-based

Optimization

Abbreviation	Definition
AD	algorithmic differentiation
ADMM	alternating direction method of multipliers
B&B	branch-and-bound
B-Hyb	hybrid outer-approximation based branch-and-cut
B-QG	Quesada-Grossmann's branch-and-cut
BFGS	Broyden-Fletcher-Goldfarb-Shanno algorithm
BIP	binary integer programming
DE	differential evolution
DAG	directed acyclic graph
GA	genetic algorithm
GBD	generalized Benders decomposition
IPM	interior point method
LP	linear programming
MIP	mixed-integer programming
MILP	mixed-integer linear programming
MINLP	mixed-integer nonlinear programming
MIOR	model-informed optimal rounding
MIQCP	mixed-integer quadratically constrained programming
MIQP	mixed-integer quadratic programming
MI-MPC	mixed-integer model predictive control
MISQP	mixed-integer sequential quadratic programming
NLP	nonlinear programming
NP	nondeterministic polynomial time
OA	outer approximation
OCP	optimal control problem
PDPMM	primal-dual proximal method of multipliers
PSO	particle swarm optimization
PTH	penalty term homotopy
QP	quadratic programming
RENS	relaxation enforced neighborhood search
SDP	semidefinite programming
SQP	sequential quadratic programming
SR	standard rounding
SR1	symmetric rank-1 method

Furnace and electrical systems

Abbreviation	Definition
AC	alternating current
DC	direct current
DRI	direct reduced iron
BF-BOF	blast furnace - basic oxygen furnace
EAF	electric arc furnace
EMF	electromotive force
ESF	electric smelting furnace
FeMn	ferro-manganese
FeCr	Ferro-chromium
FeNi	Ferro-nickel
FeSi	Ferro-silicon
OLTC	on-load tap changer
rms	root mean square
UHP	ultra-high power
SAF	submerged arc furnace
SiMn	silico-manganese

Computational tools

Abbreviation	Definition
AMPL	Mathematical Programming Language
CAS	Computer Algebra System
CasADi	Computer algebra system with Automatic Differentiation
GAMS	General Algebraic Modeling System
JuMP	Julia for Mathematical Programming
Pyomo	PYthon optimization modeling objects
YALMIP	Yet Another LMI Parser

Simulation

Abbreviation	Definition
CPU	computation time
CVR	constraint violation rate
OCT	outside current tolerance
OPT	outside power tolerance
RCD	reference current deviation
RPD	reference power deviation
SIL	software-in-the-loop

Chapter 1

Introduction

1.1 Sustainable electric arc furnaces

NOWADAYS, the electrical arc furnace (EAF) is widely used in metallurgy compared to classical furnaces such as induction furnaces, blast furnaces, etc. In fact, EAF plays an essential role in a wide range of metallurgical applications, including steelmaking and the manufacture of ferrous and non-ferrous alloys. In steelmaking, the EAF is necessary for producing various types of steel, primarily from recycled scrap or direct-reduced iron (DRI). In particular, EAF steel products can be carbon steel, alloy steel, or stainless steel used in construction, automotive, or medical applications. In addition, EAF is employed to produce ferroalloys, e.g., ferromanganese (FeMn), silico-manganese (SiMn), etc, which are crucial elements for enhancing steel properties. In non-ferrous industries, EAFs are used to melt and refine metals such as aluminum, copper, and nickel [Hariharan and Gunasekar, 1998, Brooks, 2001, Chatterjee and Pandey, 2001, Norgate et al., 2004].

Depending on the specific application, EAF comes in various configurations and designs (see Figure 1.1). In particular, the standard AC-EAF used in steelmaking typically has three vertical electrodes arranged in a triangular configuration, as shown in Figure 1.1a. In contrast, DC-EAF generally operates with either two electrodes or a single one, acting as cathode, while the load or furnace bottom serves as the anode, as illustrated in Figure 1.1d and Figure 1.1c. For ferroalloys production, the EAF is commonly referred to as a submerged arc furnace (SAF), whose three electrodes are submerged in the

melting ore, as shown in Figure 1.1b. In some large-scale SAFs, additional electrodes may be installed, bringing the total to six. This configuration allows for higher power input and improved energy distribution, although it is less common than the traditional three-electrode design. A detailed classification of EAF will be discussed in Section 2.1.2.

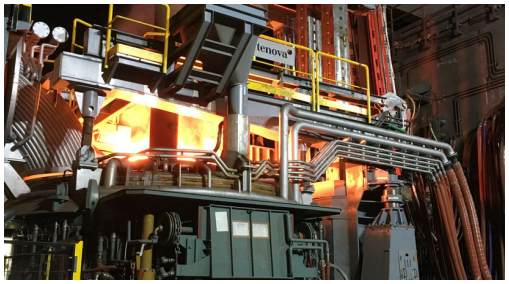

(A) 70 tonnes EAF at Valbruna ASW Inc. plant, Ontario, Canada.



(B) 34MW SAF at Comilog Dunkerque plant, Gravelines, France.



(C) 5.6MVA DC EAF with one electrode at Mintek, Randburg, South Africa. [Jones and Curr, 2006].



(D) 0.3MVA DC EAF with twin electrodes at Mintek, Randburg, South Africa. [Reynolds and Jones, 2006].

FIGURE 1.1: Different design of EAF, including AC-EAF with three electrodes (top) and DC-EAF with one or two electrodes (bottom).

1.1.1 Growth in recent years

In recent years, *EAF technology has shown steady growth in production capacity and share in the global steel market* compared to the other furnaces, mainly the traditional blast furnace-basic oxygen furnace (BF-BOF). According to the World Steel Association, global EAF steel production in 2024 accounted for 29.1% and had a capacity of 548.4 million tons per year [Worldsteel, 2025]. This represents approximately 11% relative growth over four years from 2020, when EAF's share was 26%. In Europe, over 44% of steel production is sustainably produced by EAFs, whereas this figure exceeds two-thirds for US production [Bishop et al., 2023, Eurofer, 2024]. Italy stands out among EU countries, with 89.3% of its steel produced in EAFs. Nevertheless, global EAF production is still dominated by the BF-BOF route because EAF-based production in China accounts for only about 10%. Moreover, China accounts for over 50% of global steel output. However, it is worth noting that China aims to increase the share of EAF in steel production to 20% by 2030 [Grigsby-Schulte et al., 2025]. Consequently, projections from [BigMint, 2024], shown in Figure 1.2, indicate that the EAF capacity is expected to have a growth rate of 24%, reaching up to 40% of the global steel production by 2030.

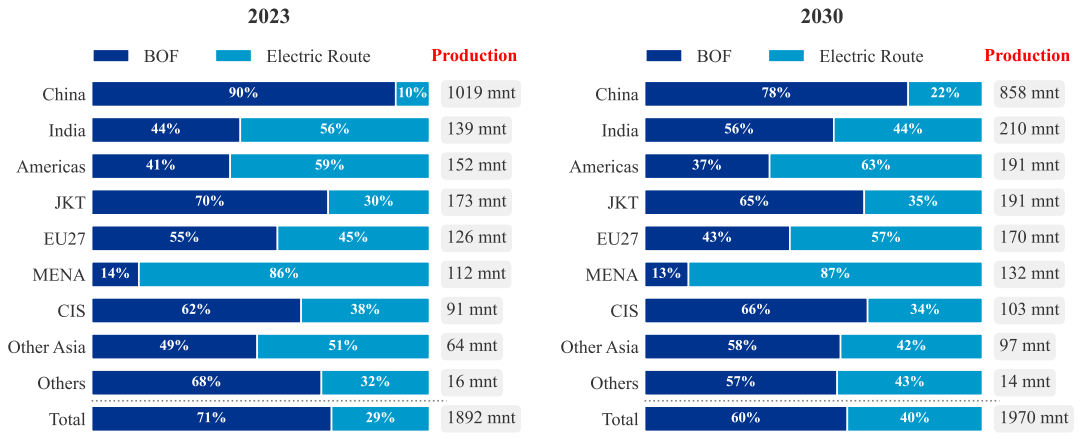

(A) 2023 steel production capacity and share (World Steel Association data).

(B) 2030 projected steel production capacity and share (Bigmint forecast).

FIGURE 1.2: The comparison of the production capacity and share in steelmaking between basic oxygen furnace (BOF) and electric arc furnace (EAF) across the countries and regions in based on data in 2023 and prediction in 2030 [BigMint, 2024].

The increasing share of EAF in global steel production is driven by *the growing demand for a high energy efficiency and environmentally friendly steel*. This becomes especially important in the context of the ambition to achieve net-zero greenhouse gas emissions by 2050 [Enrico et al., 2019, Graham, 2025] as the EAF requires less energy and also produces less carbon emissions than BOF. This comes from that fact that EAF can use scrap metal or direct-reduced iron (DRI) as its primary raw material. According to [Echterhof, 2021], the EAF route consumes 64.3% less energy and 90.9% less material than the blast-basic oxygen method. Additionally, it emits 2.6 times less CO_2 and 12 times less CO, making it a more energy-efficient and greener solution. As a result, this feature benefits the EAF route as a more sustainable option for steel production.

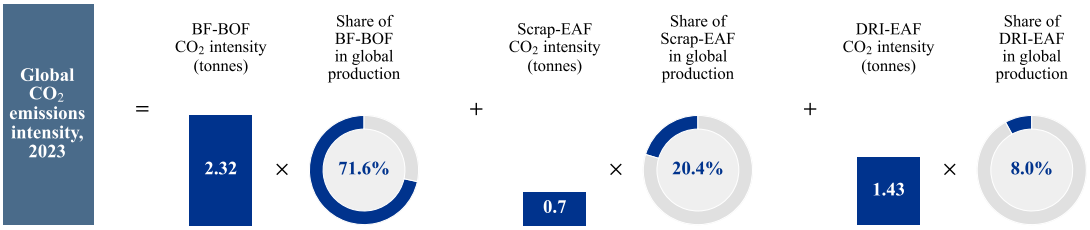

(A) Global CO_2 emissions intensity of steel production in 2023.

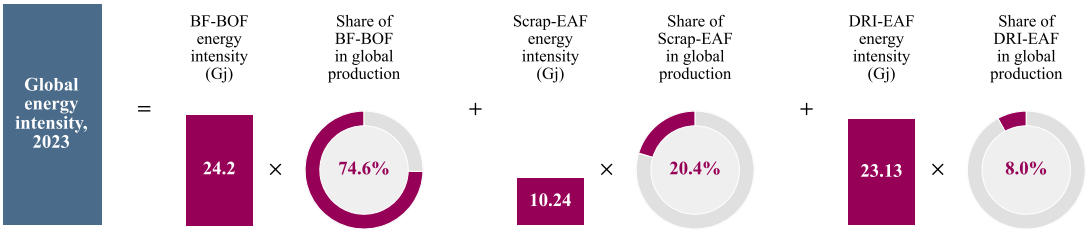

(B) Global energy intensity of steel production in 2023.

FIGURE 1.3: Global average value for CO_2 emissions and energy intensity including blast furnace-basic oxygen furnace (BF-BOF), direct reduced iron (DRI)-based and scrap-based electric arc furnace (EAF) steel production routes [Enrico et al., 2019].

The indicators presented in Figure 1.3, published by the World Steel Association, further reinforce the sustainability of the EAF route over the BF-BOF method in steelmaking. As shown in Figure 1.3a, we see that the BF-BOF route has an average emissions intensity of 2.32 tCO_2/tcs (tonnes of CO_2 per tonne of crude steel), whereas EAF-based production is significantly lower, with scrap-based at 0.7 tCO_2/tcs and DRI-based EAF at 1.43 tCO_2/tcs. Similarly, Figure 1.3b shows us the energy intensity required to produce crude steel by the BF-BOF is 24.2 GJ/tcs (gigajoules per tonne of crude steel), which is higher

compared to 10.24 GJ/tcs for scrap-based EAF and 23.13 GJ/tcs for DRI-based EAF. These indicators demonstrate that the EAF route is more sustainable and efficient than the BF-BOF route in terms of resource use and environmental impact.

Along with the growing capacity of EAF, *numerous technological innovations have been implemented in recent years to improve their operational efficiency and product quality* (see Toulouevski and Zinurov [2010], for details). These advancements draw significant attention from the metallurgical companies, who aims to increase competitiveness and align with sustainability goals. As a result, various investments in EAF research, innovation and technology development have continued in recent years. In particular, several EU-funded projects have brought together academic and industrial partners to develop advanced solutions to improve operations in the steelmaking industry. For instance, the MORSE project (2017-2022) focused on model-based optimization to improve resource and energy efficiency. As part of this initiative, MPC was tested on a 140-tonne EAF at Outokumpu Stainless to minimize batch time and energy consumption [Jawahery et al., 2021]. Similarly, the REVaMP project (2020-2023) aimed to enhance steel quality using low-grade scrap while reducing CO_2 emissions. At the Sidenor plant, an embedded MPC system incorporating a dephosphorization model was implemented to monitor heat conditions and predict setpoints for energy- and resource-efficient process control [Kleimt et al., 2023]. Lastly, the INEVITABLE project (2019-2023) focused on optimizing EAF operations with the operator in the loop, aiming to exceed the capabilities of conventional process automation and control systems [Tomažič et al., 2022]. In pursuit of this goal, the project introduced the data-driven modeling and optimization framework for EAF at SIJ Acroni steelworks.

To highlight, innovations in control systems are the key strategic priority for the metallurgical industry, driving competitiveness and alignment with global sustainability goals. For instance, an optimal control system has been successfully applied to ten fused magnesium furnaces (a similar type of SAF) in China. The result shows that from its implementation in May 2016 to its publication [Chai et al., 2017], the overall energy consumption per ton (ECPT) decreased by 2.28% and the product throughput increased by 1.6% with fewer abnormal conditions. This demonstrates the potential of advanced control techniques in enhancing operational efficiency and productivity, thus sustainability in metallurgical processes

1.1.2 Years in EAF automation and control

Over the past few decades, the electric arc furnace (EAF) has undergone significant technological advancements to improve operational efficiency and overall performance.

The automatic electrical control system was extensively investigated in earlier research. However, several limitations remain in the proposed control techniques and certain aspects of the control system have not yet been explored.

From 1950s to 1970s, several studies laid the foundation for the development of automatic control systems in the EAF, focusing on electrode positioning and arc regulation. Notably, [Andreae, 1950, Gosiewski and Wierzbicki, 1970, Nicholson and Roebuck, 1972, 1973, Billings and Nicholson, 1977, Billings et al., 1979] introduced an initial modeling framework and control strategies that inspired subsequent research. Particularly,

Andreae [1950] provided the first idea of automatic control for ferroalloy furnaces. The paper focused on regulating the electrode position using winch motors to maintain the desired current. It proposed straightforward rules for automatic adjustment of the electrodes.

However, electrical control still relied heavily on manual intervention, especially when disturbances last for a long time or during the recovery period after tapping operations. Andreae [1950] concluded that automatic control could not fully replace the manual operation, which requires constant attention, responsibility and extensive experience from skilled operators on the plant.

Gosiewski and Wierzbicki [1970] presented one of the first rigorous approaches to dynamic optimal control in electric arc furnaces. The paper focused on minimizing unit production cost, defined as a combination of energy and time costs, during the melting stage—the solution aimed to adjust the arc current dynamically. However, the paper did not address the control design of the arc current regulation. Furthermore, the transformer tap changer position was assumed to be constant at its maximum value and was neither considered in the control design nor in the optimization problem.

Nicholson and Roebuck [1972, 1973] explored different control strategies to regulate the arc impedance, through electro-hydraulic or electro-mechanical (winch) actuators. The first paper compared conventional analogue and direct digital control of electrode position, showing that four-mode PIDD control can significantly enhance transient response. While the second paper advanced the digital control framework by applying optimal control to a nonlinear furnace model that included electrode-position, transmission, generation system, etc. This also introduces multiple solution methods for the Riccati equation, e.g., dynamic programming, eigenvector and a novel unit P-matrix approach. Together, the papers show how combining model-based design with efficient control algorithms can improve transient behavior. However, the proposed control strategies were developed for a single phase of a three-phase EAF system, without accounting for interactions among the phases. Moreover, tap changer position control of the transformer was not discussed.

Billings and Nicholson [1977], Billings et al. [1979] focused on improving control of a three-phase EAF, using three-phase dynamical models. Therefore, they recognized the interaction effect among the phases. Particularly,

Billings and Nicholson [1977] compared arc impedance and arc current control strategies, showing that impedance control offers stable, non-interacting regulation. In contrast, current control enables faster disturbance correction but introduces phase interaction.

To address this, they proposed a dual control strategy that switches between the two based on operating conditions. Billings et al. [1979] was developed upon their previous contributions by further introducing a temperature-weighting adaptive controller and PD regulator to improve transient response. Additionally, it incorporated extended Kalman filtering for state estimation during the refining stage. While these papers demonstrated the issue of phase interaction, they did not explicitly address or resolve it.

The extensive studies of EAF electrical system and modeling laid a solid foundation for understanding the furnace dynamics and challenges. However, proposed control techniques were not clearly described and did not address existing problems.

Between the 1980s and the 1990s, several studies further advanced the understanding of EAF electrical dynamics and control. Some of them were intensively studied and documented in dissertations such as [Stewart, 1980, Valderhaug, 1992, Wasbø, 1996, R.P.Paiva, 1996]. These works provided more profound insights into the complex electrical behavior of EAFs, which later inspired our proposed control strategies.

Stewart [1980] provided an in-depth analysis of the electrical circuit in submerged-arc furnaces, particularly for ferroalloys production. His work presented problems of the control system in large furnaces, including dead-live phases, interaction effects, lack of sensitivity to electrode movement, measurement inaccuracies.

Moreover, it focused on analyzing and improving the electrical measurement system on a 48 MVA ferrochrome furnace. The study also modeled arcing conditions and the effect of geometry on reactance. The work provided a foundation for modeling the complex electrical system of an EAF using an equivalent electrical circuit. However, it did not address the electrical system's control design.

Valderhaug [1992] also conducted a detailed investigation of a submerged-arc furnace, particularly used for ferrosilicon production. The study first modeled the furnace's

electrical circuit, developed steady-state electrical models based on equivalent circuit representations and extended the analysis to dynamic models that capture transient electrical behavior.

In particular, Valderhaug [1992] discussed various electrical control strategies, ranging from conventional power control to distributing power between the three electrodes to electrode control using either current or resistance as the control variable. Notably, it proposed non-interacting current control by introducing a decoupling element, aiming to reduce phase interaction.

While the work provided a comprehensive and practical overview of the electrical modeling and control strategies, it did not delve into the design of specific control methods.

Wasbø [1996] presented an object-oriented modeling framework for high-carbon ferromanganese furnaces. The study includes a detailed coke-bed model that links metallurgical and electrical behavior, enabling the study of power distribution, resistivity, etc. It also includes an analysis of harmonics in high-frequency electrical measurements. More importantly, the work discussed both metallurgical and electrical control strategies, including resistance, power and slipping control for the electrodes. However, the control strategies were briefly discussed without in-depth analysis or specific control design.

R.P.Paiva [1996] focused on object-oriented modeling and impedance-based control design for EAF. The model incorporated detailed representations of the electrical system, electrode dynamics, arc behavior and disturbances. The control system is structured in three layers,i.e., power control (via tap changer positioning), impedance control (via electrode positioning), and hydraulic control (actuator dynamics). The work proposed implementing a fuzzy P-like impedance controller that adjusts electrode positions to maintain desired phase impedances, thereby indirectly controlling arc currents. However, the author did not address interaction effects. More interestingly, the discrete nature of tap changer operations in power control was first acknowledged in the work. However, it was not integrated into the control design or discussed further.

The more recent studies applied advancements in the field, along with a wide range of control techniques, to improve the automatic control of EAF's electrical systems. Nevertheless, they have not solved all the challenges, and there is still room for improvement.

From the 2000s, research on the control system of the EAF continued to focus on the electrode positioning system with a broader range of control techniques. These include classical control methods such as PID control approaches [Hauksdóttir et al., 2002, Boulet et al., 2003], fractional-order control [Feliu-Batlle et al., 2014, Feliu-Batlle and Rivas-Perez, 2016], and more advanced techniques such as sliding mode control [Ping et al., 2009], fuzzy logic, and neural networks [Khoshkhoo et al., 2011b, Moghadasian and Alenasser, 2011].

Hauksdóttir et al. [2002], Boulet et al. [2003] both studied the modeling and control of electrode current. Hauksdóttir et al. [2002] introduced a state-feedback decoupling controller that improves current distribution by accounting for electrode interactions. Boulet et al. [2003] investigated a simple proportional electrode current, which may not effectively handle nonlinearity in the system. Although the nonlinear circuit equations were derived, they were primarily used to model the system in Simulink and were not incorporated into the control design. As a result, the phase coupling still limited the performance of the proposed control strategies.

Furthermore, Boulet et al. [2003] claimed that current control would inherently lead to power control, a conclusion that only holds for the simplified model used in the paper. In practice, power regulation always involves tap-changer control in transformers, which was not addressed in their works.

Feliu-Batlle et al. [2014], Feliu-Batlle and Rivas-Perez [2016] proposed a robust fractional order PI^{α} controller designed to control the electric arc impedance by regulating the electrode position. Their approaches showed significant improvements in robustness compared to classical PI or PID controllers, particularly in handling system uncertainties and time delays. The fractional-order design provided greater tuning flexibility and maintained superior performance across varying operating conditions. However, practical implementation may be challenging due to the inherent complexity of fractional-order components. Again, the coupling characteristics among the phases were not addressed and the tap changer control was not discussed.

Ping et al. [2009] proposed a direct adaptive fuzzy sliding mode control for regulating the arc current through three-phase electrodes. This technique combined fuzzy logic with sliding mode control to address system nonlinearity, phase coupling and parameter

uncertainties. The fuzzy design approximated the equivalent control law without requiring an exact mathematical model of the system. Moreover, the switching control gain is dynamically adjusted using fuzzy rules, thereby mitigating chattering and enhancing the system's robustness. The proposed approach accounted for interaction effects through a rule-based fuzzy approximation, but its effectiveness may not generalize well across different operating conditions. Furthermore, the system constraints satisfaction could not be explicitly guaranteed in the approach.

Khoshkhoo et al. [2011b], Moghadasian and Alenasser [2011] both utilized artificial intelligence-based techniques to improve electrode position control. Khoshkhoo et al. [2011b] focused on an estimation scheme that evaluates the instantaneous inductance of the flexible cables based on cable swing angles and electrode positions. The paper used a feed-forward neural network (ANN) trained on a random dataset to estimate inductance variations, thereby enabling optimal regulation of the arc voltage. Although the ANN was trained on simulated data from a simplified model that may not fully capture the EAF system's complexity, the idea is worth further exploration. Moghadasian and Alenasser [2011] presented a fuzzy PI controller optimized via genetic algorithms for maintaining a constant arc length. The paper used a fuzzy PI controller with varying weights adapted by genetic algorithms to control the electrode position vertically and thus the arc length. However, the proposed control is specifically designed for the meltdown stage and does not fully capture the electrical dynamics of the furnace circuit. Additionally, genetic algorithm optimization introduced computational expenses.

In conclusion, most conventional control methods for EAFs lack coordination across the three phases and among system components, leading to undesirable behaviors, such as instability in multi-phase control or imbalance in power distribution [Barker and Stewart, 1980]. Although the advanced control approaches acknowledge phases interaction, their proposed solutions tend to be impractical. They consider unrealistic models that do not adequately represent the key electrical components. Moreover, none of the work addressed or integrated the discrete nature of tap changer operations into the power control problem, leading to suboptimal furnace performance. More importantly, no method explicitly guarantees compliance with operational constraints, e.g., transformer power and electrode current limits, thereby ensuring safe and stable furnace operation [De Waal et al., 1992]. As a result, many EAF plants still rely on simple rule-based control

systems that do not leverage model-based or optimization-based strategies, limiting their ability to operate the furnace efficiently.

In recent years, research efforts have been more focused on improving the metallurgical and off-gas systems, energy optimization, and economic control of the EAF, with less or even no consideration of electrical control system design.

Most recent studies have focused more on energy optimization [Saboohi et al., 2018, Shyamal and Swartz, 2019] or economic control strategies [Oosthuizen et al., 2004, Rashid et al., 2016]. Other research has delved into the detailed analysis of the off-gas system or metallurgical processes [Bekker et al., 1999, Kirschen et al., 2009, Opitz and Treffinger, 2016, Nam et al., 2022] which are important for metallurgical control. These works typically assume that the electrical system, which is regarded as the backbone of furnace operation, is well controlled. Therefore, there is less interest in addressing its control challenges or in improving its control design performance.

The energy optimization and economic control strategies aim to minimize energy consumption and production costs while maximizing operational productivity. For instance, Saboohi et al. [2018] proposed a multi-objective optimization framework that reduces production time and operational costs, thereby increasing efficiency in EAF operations. Shyamal and Swartz [2019] developed an economic MPC approach in a two-tiered control framework, aiming to satisfy the desired product endpoint specifications and minimize an economics-based cost function.

The economic control strategies are usually implemented in a hierarchical control structure, where the economic layer generates an optimal setpoint for the low-level electrical control system. As a result, even if energy consumption or economic costs are optimized, the outcomes remain dependent on the performance of the electrical control system, which is not fully addressed in these works.

Furthermore, it is well known that the metallurgical system is characterized by long time constants, whereas the electrical system has faster dynamics [Wasbø, 1996]. As a result, the metallurgical system is usually not under automatic control. Instead, it is indirectly regulated by experienced metallurgists, who rely on practical intuition to make decisions. This arises from the metallurgical process, which exhibits complex behavior,

time-varying disturbances and unmeasured parameters. Moreover, metallurgical control is often treated as a supervisory control that provides setpoints to the electrical control system. Consequently, an electrical control system remains essential for overall furnace operation.

1.1.3 Motivation for the thesis

Despite significant advancements in EAF technology, especially in electrical control design over the last few decades, as discussed in the previous subsection, several problems remain unsolved and numerous challenges have not yet been thoroughly addressed.

> The complex electrical models of the EAF system, characterized by *interaction among the three phases* and the *discrete nature of tap changer operations* in transformers, have been reported in the literature. However, to the best of our knowledge, there is no practical solution that adequately addresses these so far.

In terms of power control, previous studies only considered secondary voltages as continuous variables, which do not accurately reflect the discrete adjustments of OLTCs in transformers. These drawbacks have motivated us to explore model-based control frameworks that can systematically take into account interconnections among the phases and capture the integer nature of the decision variables. Moreover, the majority of the recent research on EAF has concentrated on *direct electric arc furnace*, which is typically used for the steelmaking industry [Boulet et al., 2003, Oosthuizen et al., 2004, Ping et al., 2009, Khoshkhoo et al., 2011b, Moghadasian and Alenasser, 2011, Feliu-Batlle et al., 2014, Feliu-Batlle and Rivas-Perez, 2016, Rashid et al., 2016, Saboohi et al., 2018, Shyamal and Swartz, 2019, Jawahery et al., 2021, Tomažič et al., 2022, Kleimt et al., 2023]. In contrast, SAF, which plays an important role in ferroalloy production, has received considerably fewer attention in the literature. The most recent studies with comprehensive analyses on SAF electrical control were around four decades ago [Barker and Stewart, 1980, Stewart, 1980, Valderhaug, 1992]. Consequently, this thesis aims to provide a comprehensive study of the SAF, contributing to the development of improved modeling and effective control strategies for the system.

Although our research focuses explicitly on SAFs, the methodological framework developed in this work can be extended to other types of furnaces, such as AC-EAFs or Electric Smelting Furnaces (ESFs), which are very similar to SAFs and can likewise benefit from the proposed modeling and control design.

In practice, some EAF plants still use a classical control system developed several decades ago, resulting in degraded operational performance. For instance, the 34 MW SiMn furnace at Comilog Dunkerque in France, with a production capacity of 70,000 tons per year, is currently operating based on such a system.

Particularly, this system often depends on simple rule-based strategies or manual control of experienced operators, as discussed in [Andreae, 1950]. This may provide greater operational reliability but significantly limits the ability to optimize furnace performance, as the furnace is forced to operate conservatively to avoid potential violations of operational constraints, such as electrode current limits.

This is because simple rule-based controls cannot effectively stabilize electrical responses nor guarantee satisfaction of operational constraints. They uses simple rules that do not consider the complex interactions of electrical system and inactively respond to disturbances. As a result, safety mechanism must be triggered in the event of a violation, leading to power cut-offs, production interruptions and increased operational costs. Consequently, switching to an advanced control system that can explicitly handle operational constraints would enhance stability and improve overall furnace performance.

Given the particular characteristics of the EAF electrical system, model-based control strategies, more specifically, optimization-based control, are the most suitable approach. In particular, by formulating the complex electrical models of a three-phase system and incorporating discrete decision variables, we can formulate Mixed-Integer Programming (MIP) problems in the Model Predictive Control (MPC) framework to optimize performance while ensuring operational constraints are satisfied. However, solving online optimization problems in MPC, especially MIP problems, remains infeasible in real time, even with state-of-the-art MIP solvers. As the MIP problem is known to be NP-hard[1],

[1] NP-hard (Non-deterministic Polynomial-time hard) in computational complexity theory is a class of problems considered at least as difficult as the hardest problems in NP [van Leuween, 1990].

it introduces significant computational complexity challenges for real-time applications [Prodan et al., 2015]. Therefore, it is crucial to explore approximation methods that can reduce computational complexity while preserving the high-quality solutions.

In the literature, several approximation methods have been proposed for practical applications to reduce the computational burden of solving MIPs, often accepting sub-optimal solutions. For instance, mixed-integer SQP or custom Branch & Bound were applied in the vehicle control problem [Quirynen and Di Cairano, 2021, 2023], and penalty term homotopy was proposed in Fusion Tokamaks [Orrico et al., 2023]. However, these approaches primarily tackle problems that are either binary or low-dimensional integer without involving continuous variables, and therefore do not pose a significant burden on the solvers. In contrast, our MIP formulation must account for multiple discrete tap changer configurations and nonlinear electrical dynamics, including tightly coupled continuous and integer decision variables, all of which must be handled under stringent real-time constraints. This results in a more challenging problem structure that limits the applicability of conventional MIP-solving techniques in the real world. This motivates us to investigate alternative methods that can effectively address our MIP formulations.

1.2 Thesis orientation

1.2.1 Study scope

From the literature review, it is clear that the challenges associated with the EAF system are immense and diverse, depending on the subsystems considered, e.g., electrical, measurement, control, and metallurgical processes. Thus, we narrow our focus to the electrical control problem of the AC-EAF, excluding issues related to the measurement system and metallurgical studies.

In addition, it is important to note that the electrical system of an EAF varies depending on its type. Typically, AC-EAFs are categorized into three types based on the heating method. Particularly, we have: i) direct arc furnace primarily used in steelmaking; ii) indirect arc furnace utilized for non-ferrous models and iii) submerged arc furnace (SAF) employed to produce various alloys [Abadi et al., 2024]. In alignment with the motivation presented in the previous section, we focus on a high-current submerged arc furnace (SAF)

used for silico-manganese production. This furnace has three electrodes deeply immersed in the burden, composed of ore, coke, and molten product, which is very conductive ($<1\,\mathrm{m}\Omega$), allowing the passage of high currents ($>100\,\mathrm{kA}$) through the furnace electrodes and resulting in substantial heat due to the Joule effect. Typically, in the SAF, energy is dissipated through a combination of resistive and arc heating [Barker and Stewart, 1980].

However, in certain furnaces where the conductivity of the furnace load is considerably high due to significant proportion of coke in the ore, no electric arc is generated during operation. In reality, this can be readily recognized from the acoustic characteristics of EAF operation, where the arc's presence produces a high level of noise [Guerra-Serrano et al., 2020]. Numerous studies have focused on the furnace that involves the arcing effect to study its contribution to the overall electrical performance of the furnace [R.P.Paiva, 1996, Boulet et al., 2003, Balan et al., 2007, Moghadasian and Alenasser, 2011, Shurygin, 2017, Luckins et al., 2022]. In this thesis, we consider the resistive heating as the sole electric energy dissipation, excluding any arcing effect.

1.2.2 Approaches

To conduct this thesis and achieve its objectives, the research methodology is structured into the following key steps:

1.2.2.1 System modeling

For system modeling, inspired by the foundational works [Barker, 1980, Stewart, 1980], we construct and adapt an equivalent electrical circuit for the SiMn SAF with lumped impedance, representing various sections on the circuit. Based on this equivalent circuit, we develop steady-state models of the SAF, which were also derived in analyses of the electrical environment in [Barker, 1980, Stewart, 1980, Valderhaug, 1992, R.P.Paiva, 1996, Boulet et al., 1997], but remain very different from each other. In here, Kirchhoff's current, voltage laws, Ohm's law and Faraday's law have been applied to analyze the circuit and derive the steady-state equations. Moreover, we approximate transformer ratio datasheet, given as look-up tables, using B-splines representation [Stoican et al., 2015]. Additionally, least-absolute-deviation regression is used to estimate the transformers

internal impedance, accounting for voltage drops across the transformer's secondary side. Finally, the electrode-process impedance, which is highly complex due to the unknown, time-varying nature of the furnace bath, is linearized using backward finite differences.

1.2.2.2 Control design

For control, we propose an EAF control system design inspired by optimization-based control techniques. In particular, we leverage the MPC framework [Rawlings et al., 2017] along with the MIP problem [Jünger et al., 2009] to formulate the SAF control problems. In addition to the explicit integration of furnace constraints, the approach effectively handles the complexity of the electrical models with multi-variable variables across the three phases and addresses the particularity of discrete tap changer operations in the transformers. However, the MIP formulation is inherently challenging to solve in real time. Therefore, we developed two different strategies to handle the computational complexity of the integer-based optimization problem in Section 5.2 and the MIP problem in Section 6.1 based on the idea of using heuristic methods [Berthold, 2015, Kronqvist et al., 2019]. We refer to them as a model-informed optimal rounding strategy and a bilevel optimization scheme. They are considered as approximation methods that aim to obtain sub-optimal solutions without finding exact solutions of the MIP problem, like in [Quirynen and Di Cairano, 2023, Orrico et al., 2023]. Both methods are based on rounding techniques and applied to the primal problems without introducing additional parameters.

1.2.2.3 Validation

To validate the proposed control strategies, we have developed a Software-In-the-Loop (SIL) simulation environment that replicates the behavior of a 34 MW SiMn furnace located at Comilog Dunkerque. This industrial-scale furnace has a production capacity of 66,000 tons, providing a realistic and robust testbed for evaluating the practicality and effectiveness of our control design.

1.3 Contributions of the thesis

This thesis presents comprehensive approaches for modeling and controlling the electrical system of a silicon-manganese (SiMn) submerged arc furnace (SAF). More precisely, we focus on the existing electrical challenges that have not been studied for decades and have not been adequately addressed in the literature. Particularly, we have developed and enhanced the electrical model of an industrial-scale Electric Arc Furnace (EAF), capturing the particularity of the SiMn furnace. Despite optimization-based control techniques not, to the best of our knowledge, having been explicitly investigated for the EAF electrical control, significant advances in this field in recent years have motivated us to propose a tailored control strategy. This strategy integrates the MPC technique with MIP formulation, aiming to address the particularity and optimize the performance of the electrical control system.

First, we developed and analyzed electrical models of the SAF, which is the foundation for control desig. In particular, we have:

- an electrical equivalent circuit of a high-current SAF, capturing its key electrical subsystems, i.e., the three-phase transformer and electrode-process system. The equivalent circuit describes the main electrical current paths within the furnace by lumped resistive and inductive elements. Even though it is simplified with respect to the actual system due to the unknown aspects, it still retains the essential information of the electrical system of the furnace [Dinh et al., 2024];
- mathematical models of the electrical variables in the system. The models are analytically developed based on fundamental electrical laws and regression techniques. As a result, we have established the prediction models that map the control variables, i.e., tap and electrode positions, to the output variables, e.g., electric currents. The secondary impedance model associated with integer taps in a three-phase transformer is particularly novel and has not been discussed in the literature. The electrode-process impedance model is estimated through linear regression [Dinh et al., 2024, 2025a];
- an open-loop system analysis based on the derived mathematical formulations to evaluate the electrical output behavior of the furnace, e.g., active power and current

magnitude variations across the three phases and provide insights on the complex coupling of the system, e.g, effect of tap changer movements and electrode height displacements on output variables. This analysis reveals interaction effects among the phases, leading to unresolved problems in large furnaces with high inductance [Dinh et al., 2025b].

Second, we propose advanced optimization-based control strategies for the SiMn furnace to enhance the performance of the electrical control system. In particular, we:

- design multi-variable current control strategies for the three-phase system within an MPC framework. This allows us to effectively control three current magnitudes while managing the interaction between the electrode positioning system and the furnace's operational constraints, a challenge that conventional control methods do not adequately address [Nguyen et al., 2025];
- formulate integer-based control problems to capture the discrete nature of tap changer operations in a three-phase transformer. This enables us to regulate transformer active powers while minimizing switching operations, which is not possible with traditional continuous control methods [Dinh et al., 2025a];
- construct a coordinated control strategy that combines these two previous control strategies, transformer active power and electrode current magnitude into a single MI-MPC framework. This novel approach, which has not been explored before, allows us to take into account the interactions not only among the phases but also between the two set of actuators [Dinh et al., 2024, 2025b];
- introduce tailored approximation methods to address the computational burden of solving MIP problems online: model-informed optimal rounding and bilevel optimization schemes. These methods aim to provide sub-optimal solutions with significantly reduced computation times, replacing the need of using state-of-the-art MIP solvers, which are often infeasible in real-time [Dinh et al., 2025b].

In addition to the modeling and control, we have also contributed to development of a digital twin simulation software to validate our proposed control strategies. Thus, we:

- integrate the electrical control layers into a SIL simulator that mimics the actual operation of a SiMn furnace. Additionally, we enhanced the software interface to support real-time monitoring and easy configuration of different study cases.
- develop a data logging and management framework using Optimistik to record simulation outputs. This enables us to have comprehensive analysis and visualization of results, particularly for long-term simulation studies.
- carry out various comparative studies of the proposed control strategies against both the classical control method existing on the industrial furnace and different state-of-the-art MIP implementations to highlight the performance improvements. [Nguyen et al., 2025]

In the sequel, we provide a list of accepted/submitted publications.

Journal/conference papers in preparation/review:

[J1] **M. T. Dinh**, I. Prodan, O. Lesage, E. Mendes: Computationally Efficient Mixed-Integer Predictive Control for a Three-Phase Electric Arc Furnace. *Control Engineering Practice*, 2025 (under review).

[C0] **M. D. Nguyen**, M. T. Dinh, I. Prodan, O. Lesage, E. Mendes: From Conventional to Optimization-based Control for Electric Arc Furnaces (under preparation).

Accepted conference papers:

[C1] **M. T. Dinh**, I. Prodan, O. Lesage, E. Mendes: Efficient Switching in Mixed-Integer Predictive Control for a Three-Phase Electric Arc Furnace. *2025 American Control Conference (ACC)*, Atlanta, USA, 2-5 July 2025, pp. 3409-3414.

[C2] **M. T. Dinh**, I. Prodan, O. Lesage, E. Mendes: Mixed-integer predictive control for a three-phase electric arc furnace producing Silico Manganese. *2024 European Control Conference (ECC)*, Stockholm, Sweden, 25-28 June 2024, pp. 1979-1984.

Accepted national workshop papers/presentations:

[N1] **M. T. Dinh**, I. Prodan, O. Lesage, E. Mendes: Efficient Switching in Mixed-Integer Predictive Control for a Three-Phase Electric Arc Furnace. *3ème Congrès Annuel de la SAGIP*, Mulhouse, France, 21-23 Mai 2025.

[N2] **M. T. Dinh**, I. Prodan, O. Lesage, E. Mendes: Mixed-integer predictive control for a three-phase electric arc furnace producing Silico Manganese. *CT Commande Prédictive Non-Linéaire*, Valence, France, 21th February 2024.

Also, I gave several presentations at Eramet Ideas company in front of industrial experts, researchers, managers and the CEO:

[P1] Approximated method for mixed-integer predictive control of a three-phase SiMn electric arc furnace. Presentation at Eramet Ideas, Trappes, France on February 26th, 2025.

[P2] Mixed-integer predictive control scheme for a three-phase SiMn electric arc furnace. Presentation at Eramet Ideas, Trappes, France on February 7th, 2024.

1.4 Organization of the manuscript

This thesis (not including this chapter) is organized into seven chapters as follows:

Chapter 2 introduces the high-current Submerged Arc Furnace (SAF), a particular type of the Electric Arc Furnace (EAF). Firstly, general features of an EAF are presented, including its classification, operational principles and typical control methodologies. Secondly, the SAF used for Silico-Manganese (SiMn) production is focused, detailing its components, process and electrical operating conditions. Finally, the chapter concludes with a discussion of the characteristics of both conventional and advanced control strategies for the furnace's electrical system.

Chapter 3 addresses the electrical modeling of the SiMn submerged arc furnace. Lumped impedance equivalent circuits are presented, focusing on two primary subsystems, i.e., the three-phase transformer and the electrode-process impedance. These subsystems are modeled to capture the furnace's essential electrical behavior. The

mathematical formulations of the electrical variables in the subsystem are analytically developed, encompassing both dynamic relationships and steady-state conditions. In the last part of the chapter, an open-loop system analysis is performed to evaluate the electrical behavior of the furnace and provide insights into the complex interactions within the system.

Chapter 4 explores the design of a control system for the SiMn furnace and the optimization tools that can be applied. First of all, the operational requirements, which include the control objectives and operating constraints, are explicitly described, which serve as the foundation for the optimization-based control design. A Software-In-the-Loop (SIL) simulation architecture is then introduced, providing a framework for validating under realistic conditions. After that, an overview of optimization-based control techniques, emphasizing Model Predictive Control (MPC) and Mixed-Integer Programming (MIP). Finally, the chapter concludes with a summary of state-of-the-art modeling languages and optimization solvers that support the implementation of these advanced control strategies.

Chapter 5 investigates “3-parameter” control strategies in the SiMn furnace. The first part focuses on the regulation of electrode current magnitude. The second part of the chapter addresses transformer active power control using integer-based formulations to handle multi-phase control, given the decision variables’ integer nature. Then, a model-informed optimal rounding strategy is designed to tackle the computational complexity of the integer programming problem. These approaches are validated through extended simulations and compared with MIP solvers.

Chapter 6 presents a "6-parameter" control strategy, a coordinated control framework that simultaneously manages transformer active power and electrode current magnitude. The multi-variable architecture of the control system is first provided, and the mixed-integer model predictive control (MI-MPC) problems are then formulated. From here, a bilevel optimization strategy is developed to effectively enhance the computational efficiency of solving the MIP problem. In the final part of the chapter, comparative simulation results demonstrate the performance of the coordinated control approach against a conventional strategy and benchmark it against state-of-the-art MIP solvers.

Chapter 7 completes the thesis with conclusions and discussions for future directions.

Chapter 2

High-intensity submerged-arc furnace

This chapter provides an overview of the electric arc furnace (EAF), with a particular focus on the silico-manganese (SiMn) submerged-arc furnace (SAF).

We begin with the historical development and comprehensive classification of the EAF. In the introduction of different types of furnaces, we present various DC and AC EAF applications operated by Mintek and Eramet groups, respectively, at both pilot and industrial scales. Among these, the furnace used for SiMn production at COMILOG Dunkerque, France, serves as the case study for this thesis. This furnace is classified as a high-intensity SAF, which is distinct from other SAFs due to the absence of electric arcs during operation. Subsequently, we provide detailed design and operation, which form the basis for modeling and control development in the following chapters.

Throughout the chapter, we also focus on the EAF control system, first highlighting the relationship between metallurgical and electrical control and emphasizing the importance of electrical automatic control. Moreover, we explore the main electrical control strategies, which include power regulation via tap changers and current or resistance management via the electrode positioning system. Subsequently, we present an overview of EAF control architectures, setting the stage for comparing existing SAF frameworks with the advanced architecture proposed for SiMn SAF in this thesis.

2.1 Electric arc furnace (EAF)

As we introduced in Chapter 1, in addition to the blast-basic oxygen furnace (B-BOF), the EAF is another main approach for steel production, using scrap-based or direct-reduced iron (DRI) as the primary feedstock. In this area, it accounts for approximately 29% of the global steel output [Worldsteel, 2025]. It is also well-known for ferro-alloy production, where a special type of EAF, known as a SAF, is used to produce SiMn, ferro-manganese (FeMn), ferro-chromium (FeCr), and ferro-nickel (FeNi), etc. A small percentage of EAF applications include non-ferrous production, e.g., aluminum, copper and nickel, etc.

2.1.1 History of development

The EAF has evolved significantly from its invention in the late 19th century. Particularly, EAF was initially invented by James Burgess Readman, with his first EAF patent for phosphorus production in 1889. However, the EAF was actually commercialized in 1907 by Paul Héroult, whose first industrial plant was established in the United States Fleming [1911]. His design featured an alternating-current (AC) furnace with three electrodes, which remains the standard configuration for most EAFs today. This furnace operates by generating an electric arc between the electrodes and the melting material, providing power to reduce and melt input materials. However, his original design faced several challenges, including uneven temperature distribution in the metal bath due to low transformer power and arc current. This resulted in very slow melting and high energy consumption, leading to low productivity due to heat losses.

To address this, Gironde and Nathusius increased convection in the furnace in 1915 by allowing the electric current to flow through the entire depth of the metal bath and the furnace hearth [Karbowniczek, 2021]. This was achieved by building a so-called conductive hearth with a water-cooled electrode embedded in it. While innovative, this approach resulted in a more complex, structurally weaker design. Consequently, it was then replaced by a nonconductive hearth furnace with a more durable design. This furnace includes a threaded carbon electrode, followed by a graphite electrode, which is a tuning point for the development of EAF. These electrodes enabled continuous and stable operation, thus improving operational efficiency.

In the 1960s, ultra-high power (UHP) furnaces were developed, significantly improving productivity and reducing tap-to-tap delays. The first UHP furnace was introduced in the United States in 1963. It had a capacity of a 135-ton furnace and was powered by 70-80 MVA transformers, delivering a specific power of 520-600 kVA/ton [Toulouevski and Zinurov, 2013]. By the early 1980s, the specific power of the UHP furnace had increased to approximately 1000 kVA/ton.

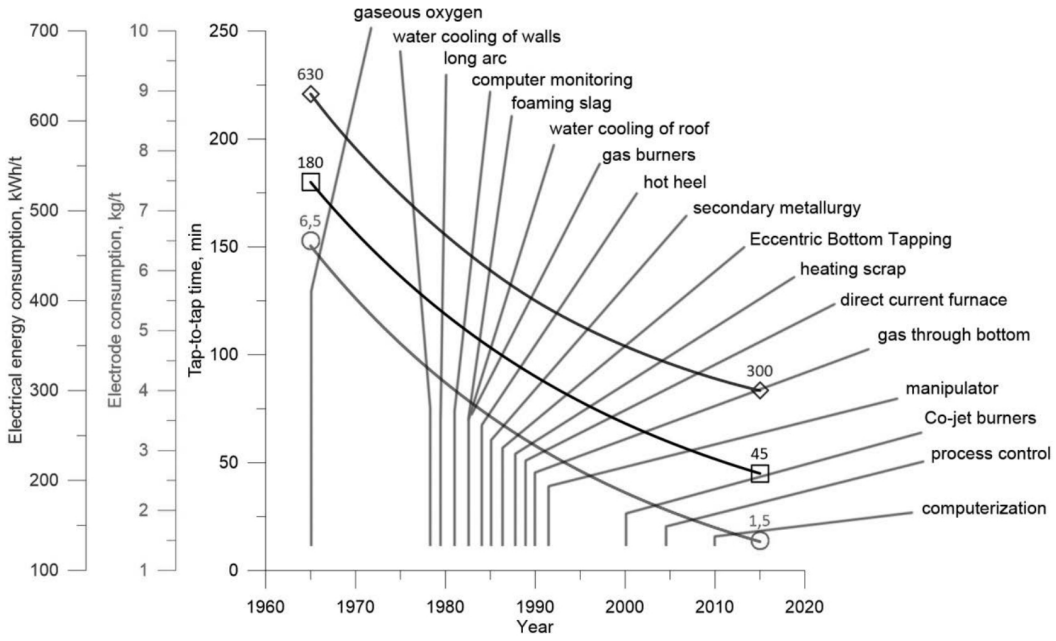

FIGURE 2.1: Evolution of the electric arc furnace technology including key milestones and advancements with performance indicators on energy consumption, electrode consumption and tap-to-tap time from 1960s to 2020s. [Karbowniczek, 2021].

In the 1980s-1990s, studies of the submerged arc furnace (SAF) focused on addressing production difficulties. In particular, a thorough investigation of the electrical behavior of a ferrochromium SAF was carried out by Barker and Stewart [1980], Stewart [1981], which laid the foundation for SAF modeling based on an equivalent electric circuit and for understanding operational challenges. These modeling frameworks were then extended to ferrosilicon SAF and used to analyze the electrode control system in Valderhaug [1992], thus providing a basis for the development of electrical control strategies with models in the following years.

In the same period, a direct current electric arc furnace (DC-EAF) with a single electrode was established, providing significant advantages over conventional AC furnaces at the

time. This is because it improves arc stability, reduces consumption of graphite electrodes and refractory materials, and mitigates the detrimental effects on the power grid. However, the DC-EAF is less common due to its higher construction costs and it is suitable only for smaller capacities [Reynolds and Jones, 2006].

Modern EAFs have seen remarkable improvements, primarily driven by advances in process control and automation, as we noted in Section 1.1.1. The global trajectory of this technological evolution is shown in Figure 2.1, which highlights the key milestones in EAF development since the 1960s. These modern advancements have always been aligned with the third and fourth industrial revolutions, during which the introduction of computerization, digital technologies, and artificial intelligence was significant. Indeed, the integration of automation technologies into EAF operations has improved safety and operational efficiency by enabling more precise process control, minimizing human error, and optimizing productivity.

As a result, EAF production performance has been considerably improved since the first EAF was invented. In particular, the tap-to-tap periods have been shortened and electrical energy and electrode consumption have been reduced.

2.1.2 Classification of EAF

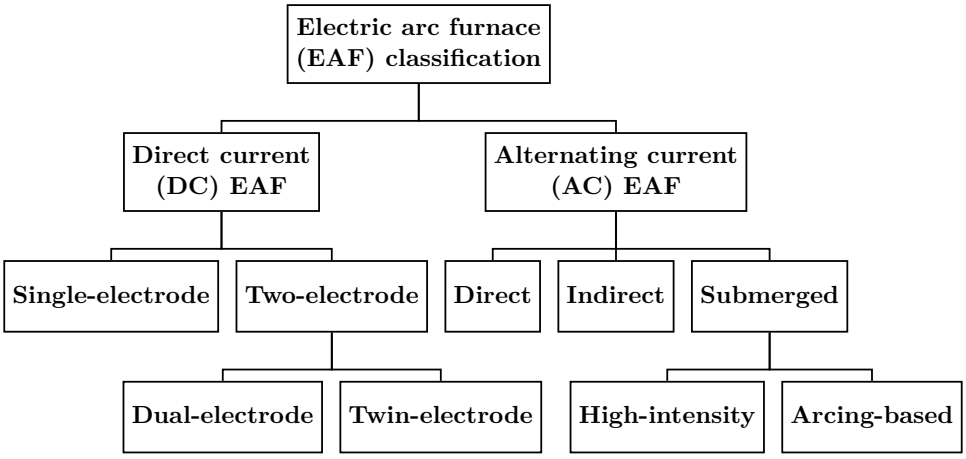

FIGURE 2.2: Classification of Electric Arc Furnaces (EAF).

Along with the development of EAF, various types of EAF have been designed to meet different applications. As a result, to have a clear overview of the EAF design, let us

first classify the EAF into different categories by the tree diagram shown in Figure 2.2. This classification provides a broad scope, covering almost all types of EAF based on different criteria such as power source, number of electrodes or heating method, etc.

As illustrated by Figure 2.2, we divide the EAF into direct current (DC) and alternating current (AC) EAF based on its power resource. The DC-EAF can then be classified, depending on the number of electrodes, into single-electrode and two-electrode furnaces. The AC-EAF can be further categorized, based on the heating method, into three main types, i.e., direct arc, indirect arc and submerged arc furnace Abadi et al. [2024].

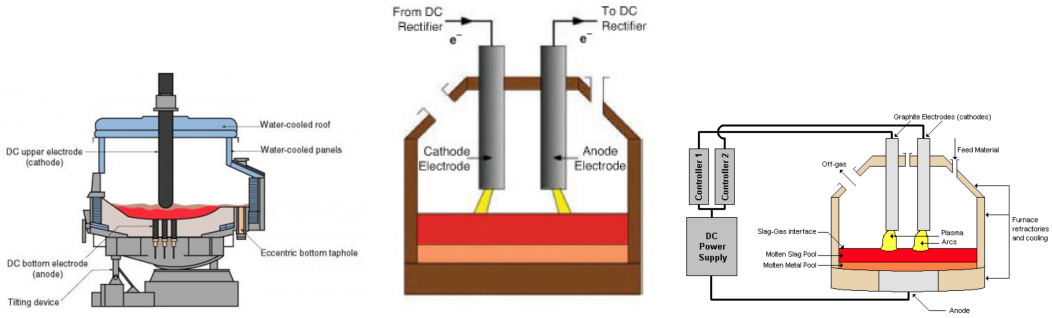

(A) DC EAF scheme with one electrode and bottom anode [Madias, 2014].

(B) DC EAF scheme with dual electrodes [Reynolds, 2012].

(C) DC EAF scheme with twin electrodes [Reynolds and Jones, 2006].

FIGURE 2.3: Schematic of different DC EAF configurations.

In DC EAF, the single-electrode furnace is the most common configuration. It features a single graphite electrode serving as the cathode and a conductive furnace bottom acting as the anode [Madias, 2014], as illustrated in Figure 2.3a. Alternatively, DC furnaces can be equipped with two electrodes, which can be arranged in a dual-electrode form, where one electrode is the anode and the other is the cathode, as shown in Figure 2.3b, or in a twin-electrode configuration, where both electrodes are cathodes and the furnace bottom serves as the anode, as displayed in Figure 2.3c. Each of them has its own features and therefore proposes different advantages, see [Reynolds and Jones, 2006, Reynolds, 2012] for more details. In Table 2.1, we introduce applications at industrial or pilot scale using DC-EAF, as demonstrated by the Mintek company.

Even though the DC-EAF is less common than the AC-EAF, it was actively pursued in the 1980s-1990s due to its advantages, including generally lower electrode and energy consumption, and reduced grid flicker. However, DC-EAF requires a high initial investment and more complex maintenance due to its configuration.

Besides DC-EAF, AC-EAF is more prevalent in the steelmaking and ferro-alloy industries. Direct and indirect EAF have electrodes above the molten bath, generating heat by arc heating. In contrast, SAF operates by submerging the electrodes deeply into the charge material, allowing heat to be generated through both direct arc heating and resistive heating (Joule effect). We provide a detailed comparison of these furnace types in Table 2.1, highlighting their characteristics and applications.

TABLE 2.1: Comparison of AC EAF types based on heating method.

Category	**Direct Arc Furnace**	**Indirect Arc Furnace**	**Submerged Arc Furnace (SAF)**
Heating	Direct arcing effect	Radiation of arcing	Direct arcing, Joule effect
Generation	- Heat is directly transferred to the charge via the arc. - Arc is formed between electrodes and the charge.	- Heat is transferred indirectly to the charge via arc radiation. - Arc is formed between two electrodes positioned above the charge.	Heat is generated by: - Arc between electrodes and the charge, - Joule heating due to current passing through the resistive charge.
Feature	- Fast melting. - Higher electrode wear. - Localized overheating. - Refractory damage. - Batch operation. - Significant harmonics.	- Lower operating temperatures. - More stable arc. - Less harmonics. - Limited size. - Batch operation. - Less common.	- Electrodes are deeply submerged in the charge. - Charge is more conductive. - High thermal efficiency. - Continuous operation. - Less or no harmonics.
Application	Smelting iron, cast iron, melting steel scrap, stainless steels.	Smelting non-ferrous metals such as copper, zinc and its alloys.	Smelting ferrous alloys such as FeMn, FeSi, SiMn, FeCr.

In Table 2.3, we summarize applications using AC-EAF technology operated by the Eramet group around the world. All of them are used for Manganese applications with different configurations, capacities and products. Interestingly, they are classified in a different way, which is also common in the field, based on the presence of the furnace roof, i.e., open, semi-open and closed furnaces [Wasbø, 1996]. Here, we do not focus on

this classification, as it is more interesting from a metallurgical perspective, e.g., the off-gas system.

TABLE 2.2: DC EAF applications demonstrated by Mintek [Jones and Curr, 2006].

Application	**Config.**	**Load**	**Products**	**Plant**
Chromite smelting	single	16 –> 40 MVA, 62 MVA.	Ferrochromium	Palmiet Ferrochrome, Middelburg Ferrochrome.
Ilmenite smelting	single	25 MW, 35 MW, 36 MW.	Titania slag, Pig iron	Namakwa Sands, Ticor SA.
Cobalt recovery from slag	single	3 MW pilot, 40 MW.	Cobalt-bearing alloy	Mintek, Thambishi Metals.
Zinc fuming	single	5.6 MVA pilot	Zinc vapour, treated slag	Mintek
Steel dust treatment	single	40 MVA	Cr-Ni alloy, Zinc vapour, safe slag	Mogale Alloys
Magnesium	single	50-100 kVA pilot	High-purity magnesium metal	Mintek
Ferronickel from laterites	twin	2 x 80 MW	Ferronickel	Koniambo (Falconbridge)
PGM smelting (UG2 ores)	single	1.6 MW pilot	Iron-based PGM alloy, clean slag	Mintek

PGM: Platinum Group Metals.

TABLE 2.3: AC EAF for manganese alloy production by Eramet [Folmo et al., 2010].

Plant	**Config.**	**Load**	**Capacity**	**Products**	**Country**
COMILOG Dunkerque	semi-open	34MW	70kt/year	Std SiMn	France
ERAMET Porsgrunn	close	30, 35MW	160kt/year	Std SiMn, Ref FeMn, HC FeMn	Norway
ERAMET Sauda	close	40, 42MW	250kt/year	Std SiMn, Ref FeMn, HC FeMn	Norway
TINFOS Jenverk Kvinesdal	close	3x30MW	160kt/year	Std SiMn, LC SiMn, Ref FeMn	Norway
ERAMET Marietta	semi-open	12, 20, 30MW	170kt/year	Std SiMn, Ref FeMn, HC FeMn	USA
Guilin COMILOG	open	9MW	150kt/year	HC FeMn, Std SiMn	China

Std = Standard, Ref = Refined, HC = High Carbon, LC = Low Carbon.

Among the AC-EAF furnaces in Table 2.3, we consider the SiMn furnace at COMILOG Dunkerque, France, as the case study for modeling and control in the following chapters. This furnace is often classified as a SAF furnace with a capacity of 34 MW, producing approximately 70 kt/year of standard SiMn. It is important to note that SiMn SAF is a high-intensity furnace type without electric arc.

As shown in Figure 2.2, SAF can be further divided into two different types, which are *high-intensity* and *arcing-based* SAF. The difference between them can be visually understood through the schematic representation in Figure 2.4, where the high-intensity SAF is characterized by a significantly conductive environment around the electrode tip, leading to no arc formation; thus, the thermal energy is mainly generated by resistive heating. In contrast, the arcing-based SAF operates in a less conductive environment; its electrode tip is also above the resistive area, so the arc forms between the charge and the foaming slag, resulting in strong plasma stabilization. Typical applications of this SAF type can be found in the production of FeNi or FeSi.

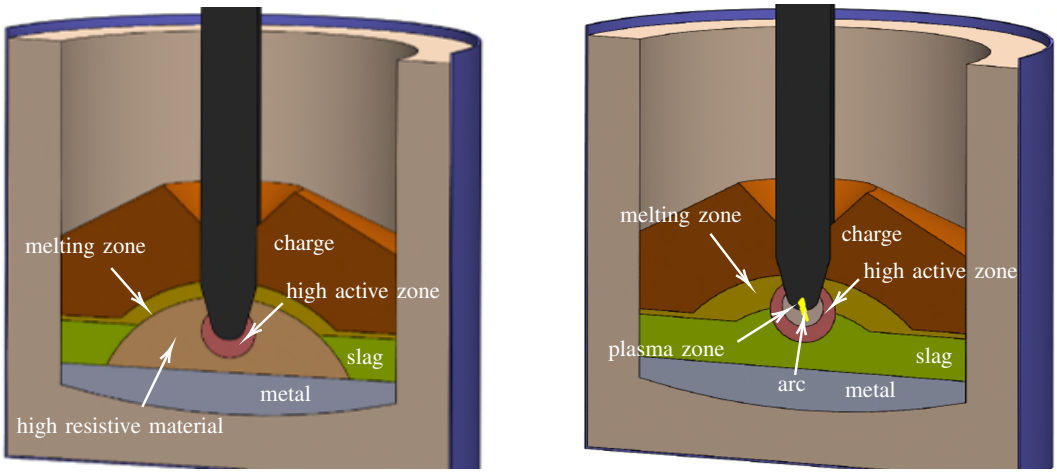

(A) High intensity SAF with full resistive heating and no arc.

(B) Arcing-based (normal) SAF with arc and resistive heating.

FIGURE 2.4: SAF schematic cross-section, showing difference between high-intensity SAF (left) and normal SAF (right). Reproduced with permission from Eramet Ideas.

2.1.3 Control of EAF

The operation of an EAF involves several subsystems. While the two main systems for process control are the metallurgical and electrical systems, other subsystems also require special attention, such as the Søderberg electrode baking and slipping, gas extraction and filtering or furnace refractory management, which includes temperature monitoring and slag chemistry control.

Here, we focus on metallurgical and electrical control systems, as they are the most critical systems for EAF operation. In particular, the metallurgical system is responsible for the physical transformations of the charge materials, e.g., solid ore and coke bed into molten metal, slag, or the chemical reactions, e.g., reduction of Mn ore to Mn, or thermal heat transfer, etc. The electrical system provides the necessary energy and appropriate power distribution to the furnace to support the metallurgical system. As a result, the EAF requires managing both metallurgical and electrical aspects to ensure efficient operation.

Metallurgical control is characterized by long time constants, often in the order of hours, whereas electrical control operates on a much faster time scale, typically seconds or even milliseconds. Consequently, electrical control is a fundamental basis for regulating metallurgical reactions, as it directly influences metallurgical aspects, e.g., thermal conditions, reaction zones, production rate, metal quality, etc, in a shorter time frame.

Therefore, the electrical control is often considered as the inner loop of the main EAF control system, while metallurgical control serves as the outer loop, providing setpoints and operational requirements for electrical control to follow.

2.1.3.1 Metallurgical control

Metallurgical control in an EAF refers to the regulation of chemical processes to ensure the quality of final products and optimize the energy consumption. This involves managing complex, harsh environments in the molten bath, where there is massive heat transfer, various emitted gases, diverse material flow patterns, complex compositions and phase changes, etc. Furthermore, the metallurgical parameters are usually unknown and cannot

be measured due to the extreme conditions inside the furnace. Moreover, the metallurgical processes are subject to various disturbances and uncertainty, such as raw material quality, charge distribution, emitted gases, etc.

As a result, metallurgical control remains a manual process that primarily relies on process knowledge and observations of metallurgical operators. Specifically, operators typically monitor and analyze key metallurgical properties of the product sample, e.g., temperature, composition, slag properties, etc. Based on these observations, they make adjustments to the process, such as modifying the charge weight or mix, adjusting feeding rates, changing casting schedules, etc. Therefore, an automatic control system for a metallurgical system is impractical. Moreover, it is indeed unnecessarycasting schedules, etc. Therefore, an automatic control system for a metallurgical system is impractical. Moreover, it is indeed unnecessary, as metallurgical processes operate on a much slower time scale than electrical processes, thus there is no argument for automating it over electrical control.

In this thesis, our focus is not on the metallurgical control, so it will not be discussed here. However, the metallurgical aspect is essential because it defines the overall objectives and setpoints for the electrical control system to follow. For more detail on this part, we refer readers to the works of Valderhaug [1992], which analyzed metallurgical control strategies of a FeSi SAF, or Wasbø [1996], which proposed a dynamical model of metallurgy based on mass and energy balances in a FeMn furnace.

2.1.3.2 Electrical control

Electrical control in an EAF involves regulating electrical parameters such as power, current, resistance, etc, to ensure efficient and stable operation. Unlike metallurgical control, the automatic control system of electrical systems is more developed and has been widely studied in the literature [Barker, 1980, Valderhaug, 1992, Hauksdóttir et al., 2002, Boulet et al., 2003, Balan et al., 2007, Ghiormez and Panoiu, 2015, Feliu-Batlle and Rivas-Perez, 2016]. One important reason is that electrical parameters can be measured or estimated in real time [Stewart, 1981]. Moreover, as mentioned above, electrical dynamics operate on a time scale of milliseconds to seconds, making it reasonable to implement automatic control, thereby improving operational efficiency in real time.

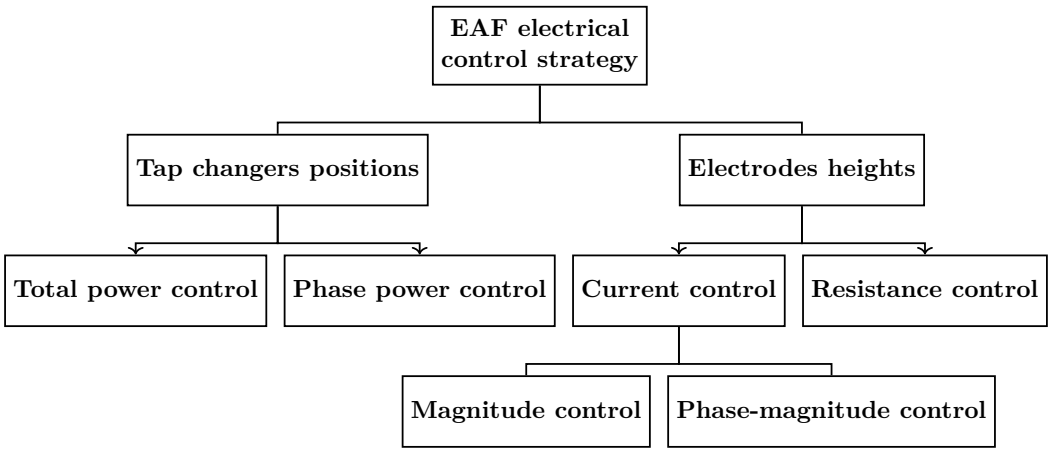

FIGURE 2.5: Classification of control strategies for an EAF.

In general, electrical control strategies depend on the desired variables to be controlled within the circuit, e.g., total furnace power, electrode currents in three phases, etc. However, these strategies can be alternatively classified into two main categories depending on actuator variables available in the system, i.e., transformer tap changers and electrode positioning systems. This classification arises from the strong relationship between these actuators and the controlled variables.

The classification of control strategies for an EAF in Figure 2.5 indicates that the power regulation strategies are typically associated with tap changer adjustments, whereas current or resistance control strategies are actually the means for electrode tips control in three three-phase furnace.

Power control

Tap changers are primarily used for power regulation in the furnace. This comes from the fact that power control requires significant changes in electrical parameters, which can be effectively achieved by adjusting the transformer tap positions in discrete steps. Each discrete adjustment results in large electrical variations. The integer nature of tap changers will be mentioned in Section 2.2.1. Moreover, power does not require exact regulation; i.e., a larger controlled tolerance band (or deadband) is acceptable; thus, tap changers are well-suited for implementation due to their limited number of switching operations during the working period, which will be discussed in Section 4.1.3.

Maintaining stable regulation of active power distribution is critical for efficient energy transfer to the furnace, as it directly affects the energy dissipated across the three electrodes and within the molten bath, thereby influencing the overall melting process [Valderhaug, 1992]. Power control can be implemented at the secondary side of the transformer or directly at the electrodes, depending on the specific furnace's available voltage and current measurement capabilities, as discussed in Section 2.3.1.

In principle, power control can be implemented in multivariable control, where each phase power is regulated individually. However, this approach is less common in practice due to the balanced requirements of the three-phase transformer configuration, see Section 4.1.4, and especially the complexity of discrete, independent tap changer regulations. As a result, power control is typically performed as single-variable control, in which the total power across all three phases is regulated by uniformly adjusting the tap positions of all three transformers. While this approach offers a simplified control mechanism, the literature lacks a detailed discussion of its implementation and coordination, particularly in relation to current and resistance control strategies.

Electrode control via current or resistance control

The electrode positioning system is better suited for current or resistance control, which typically requires higher-accuracy regulation. This is because electrodes can be continuously displaced vertically, adjusting electrical parameters on a finer scale, thereby achieving tighter tolerance. Furthermore, the electrode positioning system operates independently for each phase, meaning it does not rely on balanced conditions as required in tap changers; thus, the current or resistance control can be performed separately in each phase.

It is interesting to note that current or resistance control is, in fact, an implicit way to control the electrode tip's position in the molten bath, thereby ensuring effective heat dissipation in the intended zones. For instance, lower resistance or higher current control results in a lower electrode tip position, and vice versa. Therefore, by controlling current or resistance, we can indirectly manage the reaction zones, minimizing heat loss at the surface and preventing corrosion of the furnace refractories.

Given the power regulation, current and resistance control strategies are functionally equivalent, in the sense that specific current control values can be translated into specific

TABLE 2.4: Comparison of current and resistance control strategies.

Strategy	Advantages	Limitations
Current control	Current values can be accurately measured.	High interaction effect between the three phases due to the interconnection of the system.
Resistance control	No interaction effect as resistance in one phase is independently affected by its own electrode position.	Non-trivial resistance estimation due to unreliable voltage measurements. In classical techniques, electrode currents are not controlled and can exceed operational constraints. In the presence of arcing, resistances may not correctly reflect the information of the electrode tip.

resistance values, and vice versa. However, each method presents distinct advantages and limitations, as summarized in Table 2.4. In the literature, current control has been more studied due to the interest in avoiding interaction effects among three phases [Barker, 1980, Hauksdóttir et al., 2002, Boulet et al., 2003, Balan et al., 2007, Ghiormez and Panoiu, 2015, Feliu-Batlle and Rivas-Perez, 2016]. However, the design solutions were not so clear or did not effectively address the challenges.

While most current control strategies focus on regulating the magnitude (or intensity) of three-phase currents, we are also interested in controlling their phase angles. In particular, phase shifts among the three currents, when combined with magnitude control in a single phase, can be strategically employed to regulate energy distribution and thereby influence the heating area within the molten bath. However, this will be discussed in future work and thoroughly investigated thereafter.

2.2 Silico-manganese (SiMn) submerged-arc furnace (SAF)

In the steelmaking industry, manganese (Mn) is an essential and irreplaceable ingredient for deoxidation and mechanical enhancement. About 30% of the manganese serves as a deoxidizer and sulphide former. It reacts with sulphur to prevent the formation of

iron sulphides (FeS), which have low melting points and can cause surface cracks during hot rolling. The remaining 70% is used as an alloying element to enhance mechanical properties, i.e., strength and toughness. It is also the least expensive of the others, making it an indispensable and sustainable choice in steelmaking [Eramet, 2013].

Manganese is typically added to steel as FeMn or SiMn. The production of these ferro-alloys goes through a smelting-reduction of manganese ores, coke, and fluxes in a SAF. As SAF is the primary focus of this thesis, we will provide a detailed overview of its design and operation in the following subsections. Moreover, the electrical control strategies for SiMn SAF will also be presented. It is important to note that the main design of SiMn SAF is similar to that of other ferro-alloy SAFs or even scrap-based EAFs.

2.2.1 SiMn furnace design

The design of a SiMn SAF is essentially similar to that of a standard EAF. It is a combination of several components such as transformers, power transmission devices, electrodes, actuators, furnace as illustrated in Figure 2.6.

Here, we introduce the main components and their functions in the SiMn SAF.

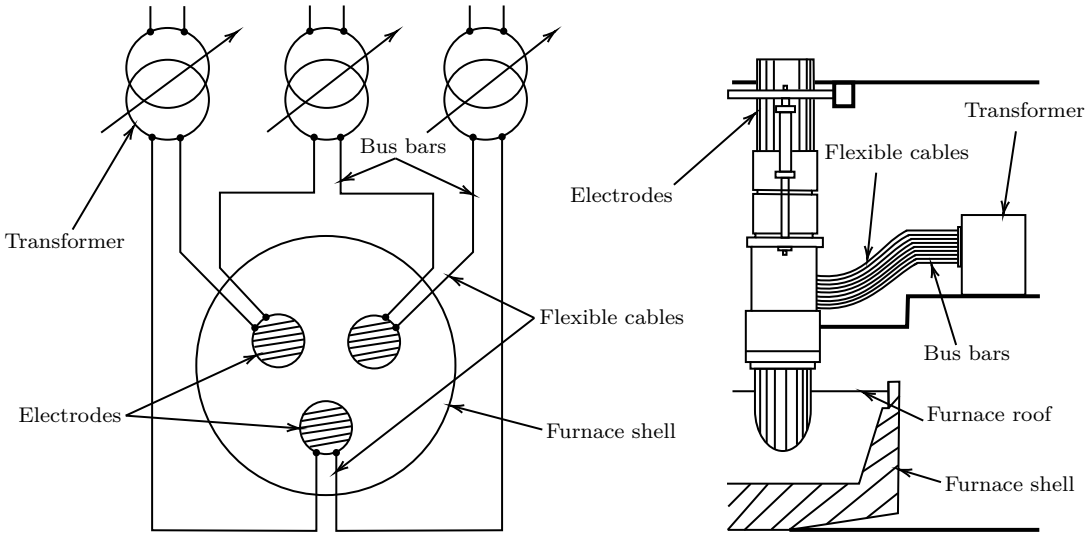

(A) Overview of three phases. (B) Side cross-sectional view of one phase.

FIGURE 2.6: Schematic of a SiMn submerged-arc furnace.

Transformers

In the furnace system, there are three furnace transformers, connected to three phases of the power supply either in a star or delta configuration. All of them are used to lower plant high voltage at primary side and adjust it to electrodes low impedances (<1mΩ) at secondary side. A furnace transformer differs from a standard power transformer in that its secondary windings are subject to significantly high currents at low voltages. As a result, it experiences significant electrical and thermal stress during regular operation; therefore, it is designed to be more durable than standard distribution transformers. A complete analysis of the power supply system in an electric arc furnace can be found in the literature Akdag et al. [2000].

An essential feature of the furnace transformer is its ability to adjust output voltage via an on-load tap changer (OLTC) on the primary winding. Like other SAFs, SiMn furnaces use OLTC, which allows the tap position to be continuously adjusted while the transformer remains energized and under load [Ram et al., 2014]. This is essential for furnace operation, as a prolonged interruption of the furnace power supply would cause the furnace to cool, potentially freezing the burden and damaging the refractory lining.

Technically, OLTC is used to switch between different tap positions, enabling the transformer to operate over a range of power levels. Primarily, the OLTC uses an switching mechanism to change the number of coil rotations on primary side of the furnace transformer, because it deals with lower currents, which makes it possible to change the number of turns on this coil. Therefore, the ratio of primary to secondary turns, also known as the transformer ratio, is modified, resulting in a change in the secondary voltage and consequently, the operating power. A schematic arrangement of OLTC is illustrated in Figure 3.3 of Section 3.2.1.

Bus bars and flexible cables

Transmission components such as bus bars and flexible cables serve as the electrical connection from transformers to electrodes. The bus bars are rigid conductors that can carry intensely high currents from the transformer outputs. The flexible cables connect the bus bars to the electrodes via a long, flexible electrical line, allowing vertical movement of the electrodes. Due to the considerably high currents carried on the cables, which induce substantial heat through resistive losses, these cables are typically water-cooled.

Electrodes

In a three-phase SiMn SAF, three electrodes are arranged in a triangular configuration, as shown in Figure 2.6a and vertically positioned above melt metals at furnace bottom, as depicted in Figure 2.6b. The electrodes are conductive elements, delivering electric current to furnace reaction zone, thereby generating significant heat via Joule heating. As a result, the electrode, particularly the electrode tip, may reach up to 3000 °C during furnace operation [White et al., 2024]. For illustration, we present a real image of SiMn SAF electrodes in Figure 2.7, where the electrodes are immersed in the molten bath, creating a high-temperature



FIGURE 2.7: SiMn SAF electrodes at COMILOG Dunkerque, France.

Regarding electrode properties, the SiMn furnace is typically equipped with Søderberg self-baking electrodes [Wilhelm, 1923] rather than pre-baked graphite electrodes, which are commonly used in scrap-based EAFs. In fact, pre-baked graphite electrodes were also used in older, smaller SAFs, but as furnaces become larger, the maximum available size of pre-baked electrodes become limited A.B.Stewart [1981]. Therefore, a self-baking electrode, illustrated in Figure 2.8, was invented by C.W. Søderberg, which is also cheaper than the pre-baked type, providing a means for making larger electrodes in continuous furnace operation. However cooking Søderberg electrodes is a delicate process itself, creating operation constraints to furnace conduct. The Søderberg electrode is merged into the molten burden and chemical reactions gradually consume its tip. Therefore, the new carbon paste (1) and casing (2) are continuously added from the head. Moreover, the electrode tip is not symmetric, as shown in the figure, and its position is unknown.

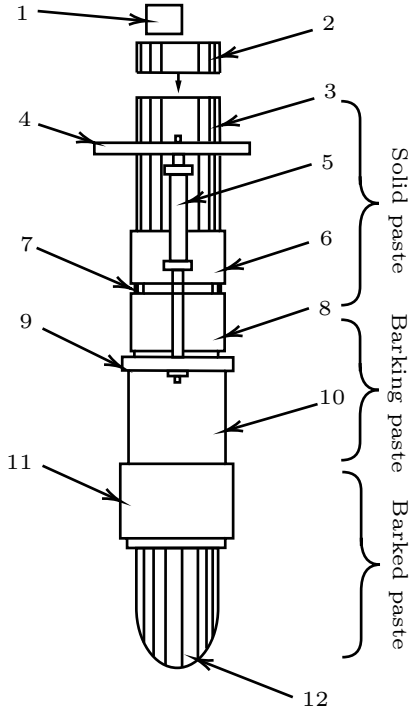

No.	Description
1	Carbon paste
2	New casing
3	Electrode casing
4	Upper-level floor
5	Hydraulic hoist
6	Top clamping ring
7	Slipping system
8	Bottom clamping ring
9	Hoist platform
10	Electrode holder
11	Contact shoes
12	Electrode tip

FIGURE 2.8: Søderberg electrode with hydraulic actuator systems.

Electrode positioning system

The electrode positioning system is a crucial component in the SiMn SAF, as it directly influences electrical parameters by vertically adjusting electrode positions via an actuator, typically hydraulic or electromechanical [Leopold Gmelin, 1984]. In large furnaces, hydraulic systems, shown in Figure 2.8, are generally preferred due to their ability to provide high force and precise control over electrode movements. From the figure, we can see that the Søderberg electrode casing (3), containing the carbon paste (1), is vertically clamped by the top clamping ring (6) and the electrode holder (10). They are both rigidly connected to the hydraulic platform (9); thus, the hydraulic cylinder (5). The current is transmitted from the flexible cables to the contact shoe (11), which is in direct contact with the electrode casing (3).

When the hydraulic system is activated, the hydraulic cylinder (5) moves vertically, thus raising or lowering the cylinder platform (9) and the entire electrode system. The upper-level floor (4) serves as a support structure for the hydraulic cylinder (5). The electrode's movement range is limited by the stroke length of the hydraulic cylinder (5).

The hydraulic actuator is typically controlled by a programmable logic controller (PLC).

Electrode slipping system

The electrode slipping allows the electrode holder (10) and its associated elements to glide upward with respect to the electrode casing (3) as the electrode is consumed at the tip (12) during furnace operation. As shown in Figure 2.8, the slipping system (7) is located between the top and bottom clamping ring (6) and (8).

The slipping mechanism periodically executes the slipping operation, which slightly loosens the top clamping ring (6) and the electrode holder (10) while keeping the bottom ring (8) clamped tightly. This allows the slipping system (7) to raise (6) and (9–11) by 1-2 cm, while the electrode casing (3) remains stationary. Once the slipping operation is completed, the top clamping ring (6) is re-tightened to hold the electrode casing (3). In general, the slipping operation is automated based on current positions of the electrode holders and an estimate of furnace's energy consumption.

Furnace

As SiMn is a semi-opened furnace, it consists of a spherical hearth, a cylindrical shell and a roof at 3 meters above its top. Furnace is where the energy is dissipated and the main chemical reactions take place. We briefly introduce the main components in the furnace:

- Hearth is the lower part of the furnace with a spherical shape, where the slag and molten alloys are produced and accumulated. It is covered by a refractory lining, which generally is composed of bricks and refractory rammed earth.
- Shell is made of steel, with additional carbon layers of lining. The carbon can withstand very high temperatures and also serves as an electrical conductor.
- The roof has three holes for electrode passage and is equipped with a fume-extraction system. It is designed to limit air intrusion into the furnace gases. It is also water-cooled and is lined with high-temperature refractory.

2.2.2 SiMn furnace operation

Operation of a SiMn furnace in particular, or a SAF in general, requires an uninterrupted power supply to maintain the molten bath at high temperatures throughout the process.

Unlike scrap-based EAFs, which operate in batch mode with periodic power-off events during feeding and casting, the SAF is designed for continuous operation. This mainly comes from the nature of the production, e.g., power supply interruptions can cause the molten bath to freeze, leading to operational difficulties or potential damage to the furnace lining. The overall operation of a SiMn SAF can be summarized as follows:

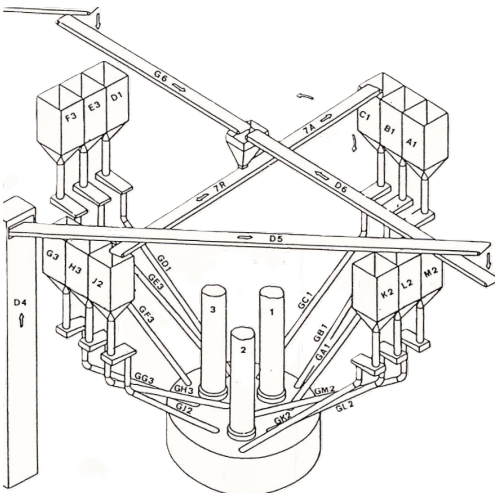

(A) Charging system in schematic.



(B) Charging system in operation.



(C) Stoking operation is done via a special truck with stoking rod.

FIGURE 2.9: Charging and stoking operations in SiMn SAF.

Feeding-stoking

The furnace is charged with a mixture of manganese ore, coke, and fluxes through a system of multiple feeding chutes and feeding tubes, as illustrated in Figure 2.9a and Figure 2.9b. The feeding chutes and tubes are located above the furnace roof and in different areas to ensure even distribution of the charge materials into the furnace. The

feeding process can be run continuously and coordinated with the smelting process, with materials added at regular intervals to maintain the desired level of raw material in the furnace. Different compositions of charge materials also result in different qualities of final products. As a result, they are carefully analyzed and mixed in accordance with metallurgical requirements.

During the feeding process, materials are usually stoked by a special truck equipped with a movable stoking rod, as shown in Figure 2.9c. Stoking typically refers to the manual process of managing the upper layer of the furnace burden to redistribute charge materials, push the charges towards the hot zone of the furnace and ensure uniform heating.

Controlling

The metallurgical aspect of the SiMn furnace is observed and controlled via the electrical control system. Given desired metallurgical conditions, electrical references, e.g., power, current, resistance, etc, are provided to the electrical control system. Then, the electrical control system, either manually or automatically, monitors electrical parameters and adjusts the actuators, i.e., transformer tap changers and electrode positioning system, to maintain the electrical parameters at their setpoints. The control system also operates continuously throughout furnace operation, and its behavior corresponds to the different operations, e.g., smelting versus casting.

Regarding electrode regulation, there is also a slipping operation that is periodically executed to compensate for electrode consumption, as mentioned in Section 2.2.1. However, it is challenging to determine the exact electrode consumption rate due to unknown conditions in the molten bath and the electrode tip's position; thus, the slipping operation is automated based on estimated energy consumption and real-time electrode holder positions.

Smelting

Smelting is the core process in the SiMn SAF, which involves reducing manganese ore to produce SiMn alloy in the presence of coke and fluxes. The smelting process is ignited by the significant thermal energy from resistive heating (Joule effect), generated by the intense electric current passing through the charges. The heat causes the charged materials to melt and react, triggering a series of chemical reactions that also produce

a large amount of heat. Eventually, the process results in the formation of a molten manganese alloy and slag at the bottom of the furnace. In here, the coke serves as a reducing agent, while the fluxes help to form slag, removing impurities from the alloy. Smelting is also a continuous process, with the molten alloy and slag maintained at high temperatures to prevent freezing until the casting step.

Casting

The casting is a discontinuous operation in the furnace, involving periodic tapping of the molten alloy and slag from the taphole into collecting vessels. The tapholes are typically located on the side of the furnace, near the bottom of the hearth, as shown in Figure 2.10. They are sealed with plugs, often made of clay, coke, and metal particles, so an electrical lance can melt them to open the taphole when it is time to cast. Appropriate casting timing also prevents excessive accumulation of molten alloy and slag in the furnace, which could lead to operational instability or damage to the furnace lining. In particular, the casting process of our target SiMn furnace takes around 20-30 minutes and is typically performed every 6-8 hours.



FIGURE 2.10: Casting operation in SiMn SAF.

2.3 SAF electrical control system

The electrical control of a SiMn SAF is indispensable for furnace operation, as it directly influences energy transfer to the molten bath and thus affects smelting. To ensure effective

electrical control, we must consider measurement capabilities and the control strategy. As a result, we will discuss these two aspects in the following.

2.3.1 Measurement system

In a SiMn SAF, accurate and reliable electrical measurements are crucial for controlling the furnace. In classical control, measurement values provide feedback to the control system, whereas in advanced control, such as MPC, they are also used to construct system models and predict future behavior.

Typically, the electrical measurement system in a SiMn SAF is considered to be the best indirect measurement of the operational state of the furnace, as direct measurements of metallurgical parameters are often impractical due to the harsh environment inside the furnace, as discussed in Section 2.1.3.1. Moreover, these electrical measurements are used to estimate important circuit parameters, e.g., resistance and reactance, which are essential for developing the prediction models in Chapter 3.

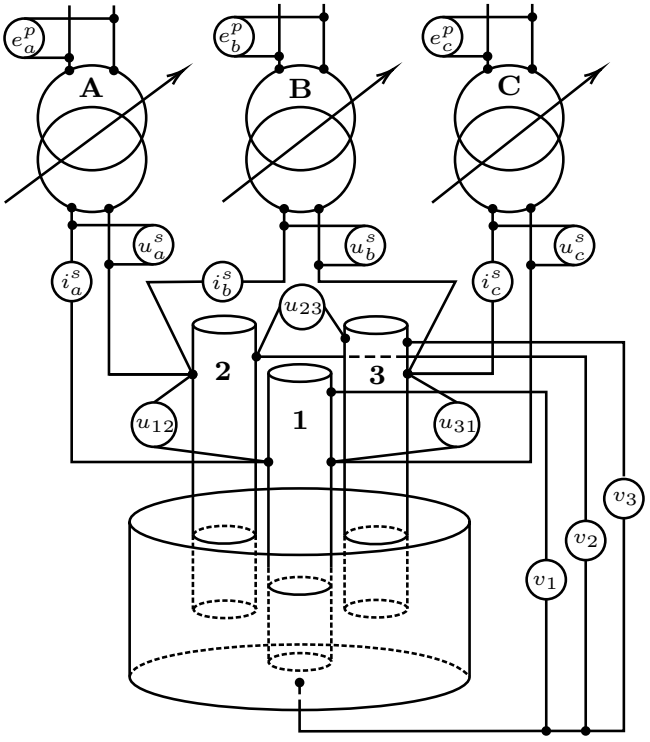

FIGURE 2.11: Electrical measurement system of a SiMn SAF.

The electrical measurements available in a SiMn SAF, illustrated in Figure 2.11 include:

- Primary voltages (e_a^p, e_b^p, e_c^p): are line voltages measured on the primary side of the furnace transformers for each phase. These represent the electrical input to the three-phase transformer system.
- Secondary voltages (u_a^s, u_b^s, u_c^s): are line voltages of the delta connection across the secondary windings of the furnace transformers. These represent the voltage supply levels to the electrodes.
- Secondary currents (i_a^s, i_b^s, i_c^s): are currents flowing through the secondary windings of the transformers, corresponding to each phase.
- Electrode-to-electrode head voltages (u_{12}, u_{23}, u_{31}): are head-to-head voltages measured between each pair of electrode heads. These can be used to estimate the impedances of transmission cables or correct the electrode-to-bottom voltages.
- Electrode-to-bottom voltages (v_1, v_2, v_3): are head-to-neutral voltages measured between each electrode head and the furnace hearth. These are critical for estimating the electrical parameters of the furnace loads, e.g., resistance and reactance.

It is important to note that, among all electrical measurements, electrode-to-bottom voltages are particularly difficult to measure accurately due to the induction effect in long, closed-loop measurement cables. This phenomenon arises from the extremely high magnetic fields surrounding the furnace, which vary with the vertical movement of the electrodes. As a consequence, the fluctuating magnetic flux generated in large geometric loops during the operation induces an electromotive force (EMF) in the voltage measurement cables, leading to significant measurement errors [Stewart, 1981].

Therefore, voltages at the electrode heads cannot be directly measured using standard methods. Instead, they are usually measured using a so-called Bockman method [Bockman, 1973], which employs a clever geometric arrangement of three measuring leads symmetrically extended from the furnace hearth and connected via calibration resistors in a low-magnetic field area. This configuration allows destructive interference of the induced EMF among the three leads. For more details on this method, we refer readers to Sparta et al. [2024].

In addition to the electrical measurements, we also need access to the real-time measurement of the physical actuator:

- Transformer tap positions: are positions of the tap changers in each transformer phase, indicating the transformer winding configuration and therefore, the voltage transformation ratio, which affects the secondary voltage levels.
- Electrode holder positions: are the relative positions of each electrode holder with respect to a fixed reference point, providing insight into the electrode immersion depth in the molten bath, which impacts the electrical parameters.

It is worth noting that the sampling rates for the transformer tap and electrode holder positions measurements differ from each other and also from the electrical measurements, due to the use of different sensors and measurement systems. As a consequence, this will be taken into account in the data processing to have a proper synchronization for the control design implementation.

2.3.2 Control architecture

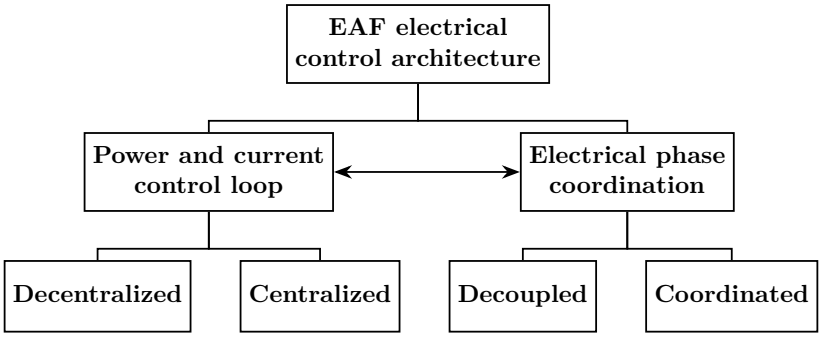

FIGURE 2.12: Control architectures of an EAF based on cooperation of submodules.

In addition to measurement, selecting an appropriate control architecture from existing strategies for a SiMn SAF is of great importance. As discussed in Section 2.1.3.2, the objectives are to ensure efficient energy transfer to the furnace to support the smelting process and to maintain an even distribution of energy across the layers of the molten bath. To this end, power control through tap positions and current (or resistance) control via electrode positions are employed.

In the classical framework, it is more common to have power and current (or resistance) regulations operate independently, resulting in two different control loops, even though they are interconnected in the overall system. This may lead to suboptimal performance due to a lack of coordination between the two control strategies. As a result, we would like to propose a centralized control scheme that simultaneously manages both power and current (or resistance).

Regarding the control within each loop, interactions among different phases are the primary concern. Similarly, conventional control uses decoupled control strategies that neglect coupling effects, whereas we propose advanced frameworks that account for these interactions to achieve more effective regulation.

Based on these considerations, the design of control architectures for the EAF can be approached from different perspectives, depending on whether we are considering the interaction between the main control strategies (power versus current) or the interaction among three electrical phases within a single control strategy, as illustrated in Figure 2.12. Hereinafter, we will analyze these perspectives in detail.

2.3.2.1 Decentralized and centralized control

In an EAF, for the control loop managing powers and currents (or resistances), we can use decentralized or centralized configurations, as shown in Figure 2.13.

In the *decentralized control architecture*, illustrated in Figure 2.13a, there are two independent controllers, each responsible for a specific control loop. In particular, while one controller manages power regulation by adjusting tap positions, the other is dedicated to regulating electrode currents (or resistances) via the electrode positioning system. Consequently, each controller operates based on its own setpoints and measurements, without accounting for the interactions with the other controller.

In contrast, the *centralized framework* shown in Figure 2.13b employs a single controller to manage both control loops. It takes all setpoints and measurements, subsequently provides control signals for power and current (or resistance) regulation. Consequently, the design of this controller must account for the effects of both tap variations and

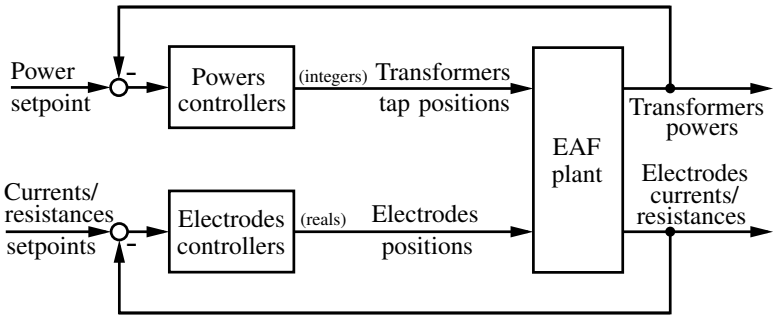

(A) Decentralized control architecture.

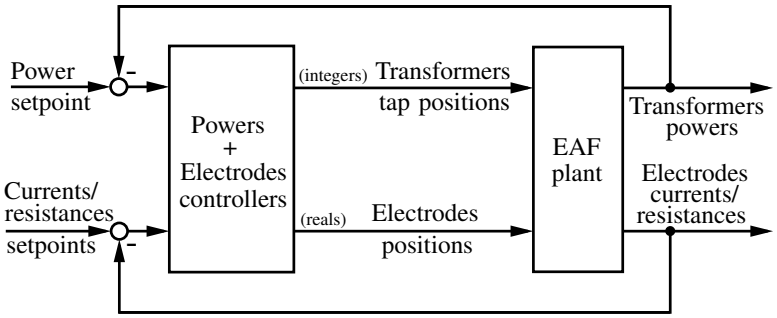

(B) Centralized control architecture.

FIGURE 2.13: Overall EAF control architectures.

electrode displacements across the entire system, thereby ensuring better coordination between tap adjustments and electrode displacements.

2.3.2.2 Conventional versus advanced control architecture

Most existing EAFs or SAFs, in particular, are currently operated under conventional control systems, which typically employ a decentralized framework, as shown in Figure 2.13a, as this architecture allows for the integration of simpler control methods, e.g., rule-based or proportional-integral-derivative (PID).

Conventional control

The SAF conventional control scheme usually consists of four separate feedback loops: one dedicated to power, and the remaining three for current regulation, as shown in Figure 2.14. In particular, Figure 2.14a presents the control scheme of a FeSi SAF

implemented at the Elkem plant, whereas we see in Figure 2.14b the corresponding scheme of a SiMn SAF at the COMILOG Dunkerque plant.

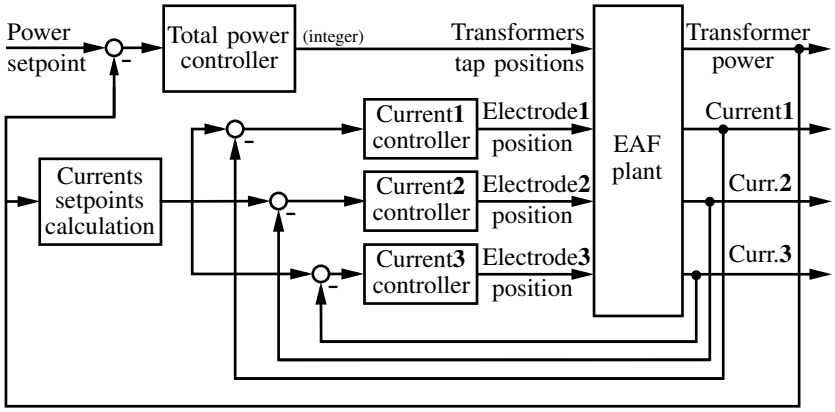

(A) Control scheme at Elkem Thamshavn, Norway [Valderhaug, 1992].

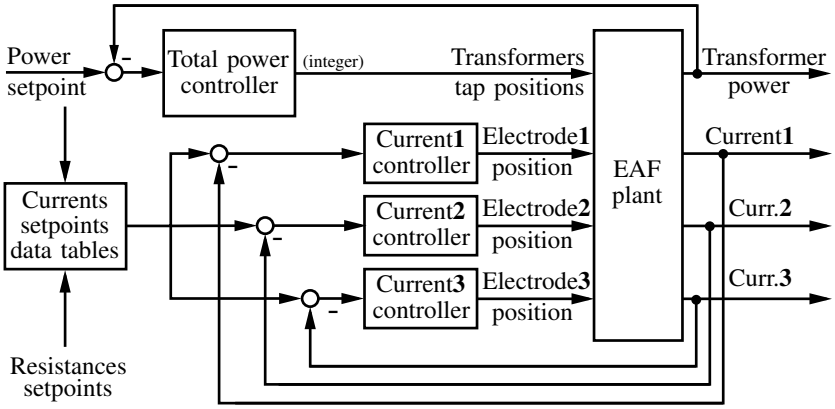

(B) Control scheme at COMILOG Dunkerque, France.

FIGURE 2.14: Conventional control with decentralized and decoupled architecture.

In both schemes, the power controller is responsible for the total power delivered to the furnace by adjusting together the three transformer taps, whereas three current controllers independently manage three electrode positions to maintain the desired current setpoints. The difference between the two schemes lies in how the current setpoint is generated. In the first case, current setpoints are computed from measurements of the controlled powers [Valderhaug, 1992], whereas in the second case, they are retrieved from the power and resistance setpoints provided by the metallurgical control layer.

It is important to note that the limitations of these approaches stem from a lack of coordination, both between tap movements and electrode displacements, as well as

among the three phases of the current control loop. As each controller acts solely on its own error signal, neglecting coupling interactions, this leads to slower disturbance response and instability in both power and current control. Moreover, only the total power is regulated, rather than the individual phase powers. This can result in the so-called "dead-and-live phase" problem, particularly in large furnaces, where one phase has significantly more power than another one [Barker and Stewart, 1980], due to the lack of individual regulation across three phases.

Advanced control

Therefore, accordingly with the motivation discussed in Section 1.1.3, we will employ advanced control architectures using model predictive control (MPC), an optimization-based control method, formulated within a (mixed)-integer programming (MIP) framework. Both MPC and MIP will be introduced in Chapter 4.3.

In addition to the advantages offered by MPC, this approach will provide the necessary flexibility to implement different control frameworks that effectively address the limitations of conventional control schemes such as coordination and phase interaction, thereby improving overall control performance. Specifically, we propose two control schemes, based on the concepts of overall EAF control architectures in Figure 2.13, namely decentralized MPC and centralized MPC, as shown in Figure 2.15.

In particular, Figure 2.15a illustrates a decentralized strategy, in which two MPC controllers operate in parallel but on different time scales. More specifically, we use an MI-MPC to regulate three transformer powers via discrete control signals for three tap variations, on a slower time scale, since power control typically requires less frequent adjustments, as also discussed in Section 2.1.3.2. In addition, we have a classical MPC managing electrode displacements for three-phase current control at a faster time scale, enabled by the continuous movement of the electrodes. Each MPC controller employs a different cost function tailored to its specific objectives. However, both rely on similar mathematical models that capture the complex interactions of the predicted state across the three phases. These models are also used for constraint handling, as both controllers share a standard set of system constraints that must be satisfied regardless of the control strategy considered. Since they can be operated independently, we present the designs of the MPC controllers separately in Section 5.1 and Section 5.2 for current and power

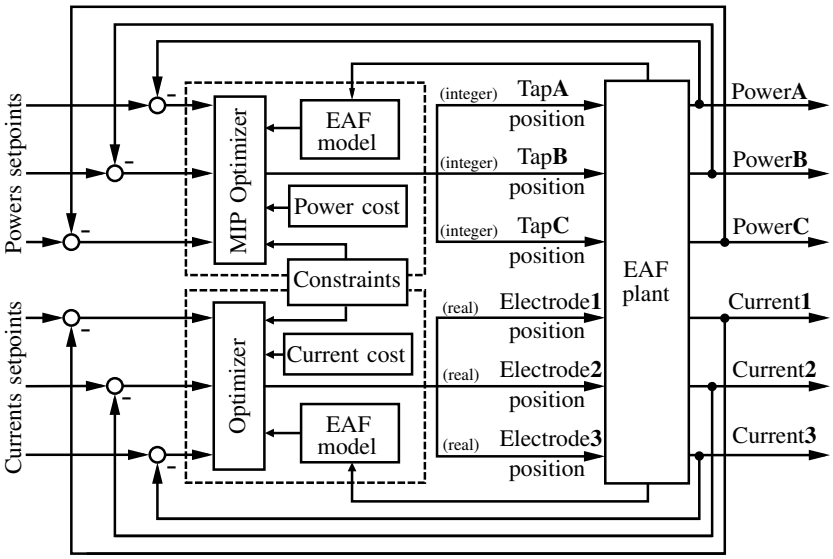

(A) Proposed decentralized MPC scheme for SiMn SAF.

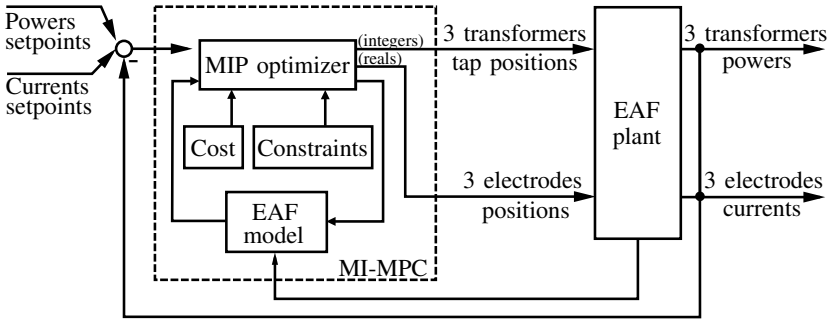

(B) Proposed centralized MPC scheme for SiMn SAF.

FIGURE 2.15: Model predictive control (MPC) with coordinated architecture.

regulation, respectively. However, the combination of both controllers in a decentralized framework will not be addressed in this thesis and left for future work.

In Figure 2.15b, we present another approach based on a centralized architecture, where a single mixed-integer MPC (MI-MPC) controller handles both power and current regulation simultaneously. This controller operates on a unified time scale, integrating both discrete and continuous control actions. The MI-MPC uses a comprehensive cost function that balances the objectives of power and current regulation, thus adapting the interactions between the two control loops. Similar to the decentralized scheme, the centralized controller uses the same mathematical model to predict the future behavior

of the entire system and thus ensure that its constraints are satisfied. The design and implementation of this MI-MPC controller will be detailed in Chapter 6.

Although these advanced control architectures with coordinated phase regulations offer significant potential to enhance the electrical regulation of SiMn SAF, there are still challenges to be addressed. From a real-time implementation perspective, these MPC-based architectures significantly increase computational complexity due to the need to solve the optimization problems online. This burden is particularly higher in the centralized scheme illustrated in Figure 2.15b, where MIP problems are formulated. The decentralized scheme 2.15a, in contrast, can reduce the computational burden to some extent by splitting the MIP problem into two smaller problem, e.g., a purely integer problem and a nonlinear problem NLP. However, it will require careful coordination between the two controllers. Otherwise, constraints might not be satisfied with two separate controllers operating on different time scales.

2.4 Concluding remarks

This chapter provided a comprehensive overview of the electric arc furnace (EAF), with a particular focus on the silico-manganese (SiMn) submerged-arc furnace (SAF), which will be studied throughout this thesis. Here, we emphasized the classification and control aspects of the EAF, especially electrical control strategies and architectures of the SAF.

In terms of classification, EAF can be categorized into different types based on their application, configuration, power source, or heating method, etc Wasbø [1996], Abadi et al. [2024]. The SiMn furnace we consider in this thesis is a high-intensity SAF type that uses resistive (Joule) heating as the primary heating source, distinguishing it from other SAF types that rely on arc heating.

Regarding the physical design, the SiMn furnace is similar to a standard EAF, consisting of several main components, such as transformers, cables, electrodes, and the furnace [Valderhaug, 1992]. Notably, SiMn has some features inherent to its SAF family, including the use of Søderberg electrodes and the continuous feeding-smelting process. As a result, the transformers are equipped with on-load tap changers (OLTC) to allow continuous voltage adjustment without interrupting the power supply [Ram et al., 2014]. The primary

operations of SiMn SAF involve key steps, i.e., feeding-stoking, controlling, smelting, and casting.

Regarding the control strategy, we highlighted the interconnection between metallurgical and electrical control in EAF operations. Metallurgy is manually controlled, providing setpoints for electrical control, which is automated and directly regulates the energy dissipated in the molten bath. Here, we emphasized electrical control strategies, including power regulation via tap changers and current (or resistance) control through an electrode positioning system. While the current control is well defined in the literature [Barker, 1980, Hauksdóttir et al., 2002, Boulet et al., 2003, Balan et al., 2007, Ghiormez and Panoiu, 2015, Feliu-Batlle and Rivas-Perez, 2016], the validity of existing approaches remains unclear, and there is still room for improvement. Power control, in contrast, is less studied and usually implemented in a simple manner, e.g., total power regulation without handling individual phase powers [Valderhaug, 1992].

Regarding the control architecture, we analyzed various configurations from different perspectives, i.e., decentralized versus centralized control. In existing frameworks, conventional control typically employs a decentralized architecture with decoupled controllers for power and current regulation, neglecting interactions between them and among the three phases, e.g., the classical control scheme in the FeSi furnace at the Elkem plant [Valderhaug, 1992] and in the SiMn furnace at the COMILOG Dunkerque plant. As a consequence, we proposed advanced control architectures based on MPC with coordinated controllers in both decentralized and centralized configurations.

Chapter 3

SiMn modeling in view of electrical control

In this chapter, we focus on modeling the electrical system of a silico-manganese (SiMn) submerged-arc furnace (SAF) using an equivalent circuit approach, inspired by the pioneering work of Barker [1980], Stewart [1981]. From here, we establish steady-state models cingpturing the interactions among the components in the three-phase circuit. Moreover, we develop empirical dynamic models that describe how the actuators affect the furnace's electrical characteristics. Finally, we provide a comprehensive understanding of electrical characteristics based on the derived models.

We consider the 34 MW SiMn SAF operated by Comilog in Dunkerque, France, as modeling case. Consequently, the equivalent circuits, model parameters and underlying assumptions presented herein are specific to this furnace configuration. Nevertheless, the modeling circuits and the derived electrical relations can be adapted to other EAFs.

The modeling process is crucial for control design, as it allows us to capture the intricate behavior of the furnace, including interactions across three phases and effects among the subsystems, i.e., transformers, electrodes and the molten bath. It provides a concrete framework for developing various control strategies for the furnace.

Using the derived analytic models, we analyze the furnace electrical characteristics via a set of visualizations. These graphical interpretations clarify the interconnections and

nonlinearities of the EAF system, providing insights into how the three-phase actuators jointly influence the furnace's key electrical characteristics. This also motivates the coordinated control strategies developed in the following chapter.

3.1 Electrical circuit

In modeling an EAF or a specific SiMn furnace, it is common to represent the electrical system using lumped impedance models. In particular, Barker [1980], Stewart [1981] laid the foundation with an equivalent electrical circuit of lumped impedance to represent the star representation in the furnace bath. The method was then used in various furnace designs with variant circuits in Valderhaug [1992], Boulet et al. [2003], Balan et al. [2007]. However, they both focused on the secondary side of the transformer and neglected the primary side, thereby ignoring the influence of transformer tap changers on the system and treating the secondary voltage as a direct input to the system.

In this work, we extend the modeling approach to include the entire three-phase circuit from the primary side of the transformer to the electrode-to-bath, accounting for impedance models along the circuit. These models simplify the complex electrical behavior into an equivalent circuit representation, as shown in Figure 3.1, retaining essential information about the furnace system's electrical characteristics.

The electrical circuit of an EAF can be configured in different ways depending on the furnace type or specific operational requirements. Here, we focus on a SiMn system that can be modeled by two equivalent circuits, depending on the configuration of the primary side of the three-phase transformer. They are denoted as delta (Δ) or wye ($\curlywedge$) configurations, as illustrated in Figure 3.1a or Figure 3.1b, respectively.

The configuration choice is determined by the plant's operational requirements, which affect the input voltages to the primary sides of the transformers. The delta configuration allows higher phase voltages than the wye configuration, providing more power to the furnace. As a result, the delta configuration is usually used during regular operation, while the wye configuration is occasionally used when the furnace needs to stop or reduce power consumption. Therefore, we will focus on the equivalent circuit in Figure 3.1a with Δ-configuration on the transformer's primary sides. However, the mathematical

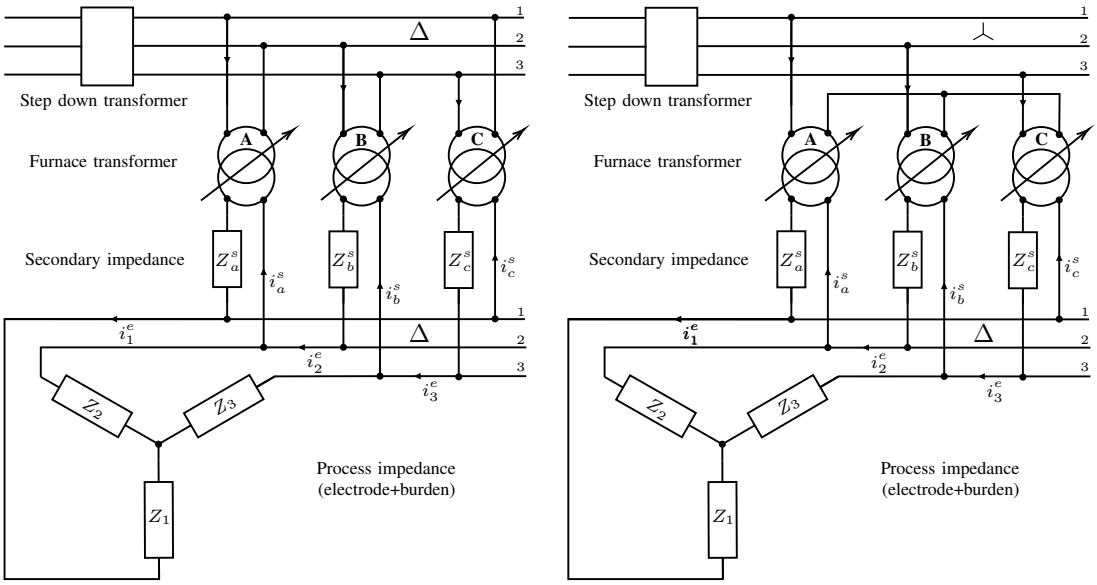

(A) Delta (Δ) configuration circuit. (B) Wye (Y) configuration circuit.

FIGURE 3.1: Electrical equivalent circuits for a SiMn electric arc furnace (EAF) system illustrating the two different transformer configurations in the primary side.

formulation of the system remains the same for both configurations, as long as the primary voltage inputs are correctly measured.

Besides the primary transformer coupling, the rest of the circuit is identical. The equivalent circuit starts with a step-down transformer that gets a three-phase alternating current (AC) supply from the power grid. Then, the electrical current passes through a three-phase transformer system consisting of three independent single-phase transformers, which further adjust the voltage and power distribution to the furnace reactor. The secondary side of furnace transformers is connected in a delta configuration to three vertical electrodes through the transmission subsystem, i.e., bus-bars and water-cooled flexible cables. Lastly, the electrodes are immersed in the raw materials inside the furnace bath, transmitting electrical currents to a floating neutral point within the burden, thus forming a closed circuit.

As discussed, the electrical equivalent circuit of the SiMn furnace is characterized by lumped impedances for the subsystems, i.e., the secondary transformer impedance and the process impedance. The secondary transformer impedance is represented by the equivalent impedances of the transformer windings and transmission subsystem across three phases,

denoted as (Z_a^s, Z_b^s, Z_c^s). The process impedance corresponds to the combination of electrode impedance and molten bath impedance, denoted as (Z_1, Z_2, Z_3). In addition to the lumped impedance models, we also account for the corresponding currents passing through the main subsystems in the three-phase circuit. These are denoted as (i_a^s, i_b^s, i_c^s) for the secondary side of the transformer and (i_1^e, i_2^e, i_3^e) for the electrode-to bath side.

It is important to note that the electrical frequency of this system is 50 Hz. Since there is no arc present in this type of furnace and no semi-conductors converters in its power system and no semi-conductors converters in its power system, harmonic effects can be neglected. Therefore, all impedances as well as other electrical values are evaluated at this fundamental frequency.

3.2 Modeling subsystem

In this section, we detail the modeling of the main subsystems in the equivalent circuit shown in Figure 3.1a, i.e., the three-phase transformer and electrode-process. The modeling facilitates the introduction of a mathematical formulation of the system in the next section.

3.2.1 Three-phase transformer

In the state-of-the-art, modeling transformer systems in an EAF is often focused solely on the secondary side, assuming the secondary impedance constant and the secondary voltage as control input [Barker, 1980, Valderhaug, 1992, Boulet et al., 2003, Balan et al., 2007].

However, this assumption does not hold in practice, as both secondary impedances and voltages vary with the tap changer positions. As a consequence, for more comprehensive modeling, we consider the effect of tap changers on the three-phase transformer subsystem in this thesis.

For the three-phase transformer circuit, we analyze the Δ-Δ configuration as illustrated in Figure 3.2. This setup features delta connections on both primary and secondary sides

of the transformers. Moreover, the circuit incorporates a transformer system with bus-bars and water-cooled, flexible cables on the secondary side, known as the transmission subsystem. In particular, the equivalent transformer circuit consists of three single-phase transformers (A, B, C), each one characterized by a distinct transformer ratio, denoted as (m_a, m_b, m_c) and lumped impedance of the transformer internal winding plus associated transmission components denoted as (Z_a^s, Z_b^s, Z_c^s). This impedance can be decomposed into resistance (R_a^s, R_b^s, R_c^s) and reactance (X_a^s, X_b^s, X_c^s).

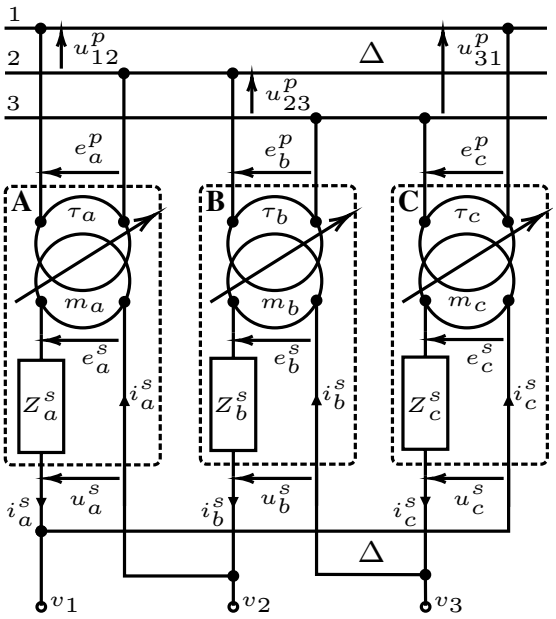

Para.	Description
u^p	Line voltage.
e^p	Transformer primary voltage.
τ	Tap position.
m	Transformer ratio, $m \triangleq f^m(\tau)$.
e^s	Ideal transformer secondary voltage.
Z^s	Secondary side lumped impedance, $Z^s = Z^t + Z^l$.
Z^t	Transformer internal impedance, $Z^t = R^t + \jmath X^t \triangleq f^r(\tau) + \jmath f^x(\tau)$.
Z^l	Transmission line impedance.
R^t	Transformer internal resistance.
X^t	Transformer internal reactance.
u^s	Secondary line voltage.
i^s	Transformer secondary current.
v	Electrode head voltage.

$f^m(\cdot)$, $f^r(\cdot)$, $f^x(\cdot)$: regression functions (3.3.1).

FIGURE 3.2: Schematic representation of a delta-delta three-phase transformer model, illustrating the primary and secondary windings connected in a Δ-Δ configuration.

The transformer ratio defines the ratio of the primary voltage (e_a^p, e_b^p, e_c^p) to the secondary voltage (e_a^s, e_b^s, e_c^s) of the transformers, which is determined by the on-load tap changer (OLTC) devices as discussed in Section 2.2.1. For simplicity, we refer to OLTC as a tap changer throughout the thesis.

In the three-phase transformer system, each transformer has its own tap changer, which is used to alter the number of primary-side coils in n *discrete steps*, as shown in Figure 3.3, thus allowing adjustment of the secondary voltage. We refer to these steps as tap changer positions, denoted by (τ_a, τ_b, τ_c).

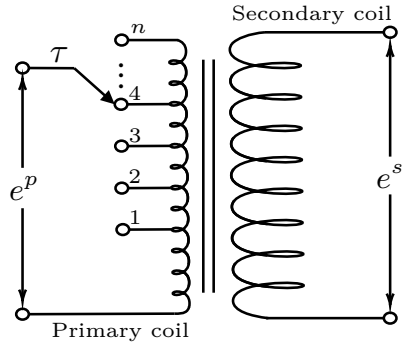

Para.	Description
e^p	Transformer primary voltage.
τ	Tap position.
n	Maximum number of position.
e^s	Transformer secondary voltage.

FIGURE 3.3: Schematic winding arrangements of OLTC in the furnace transformer.

The values of the ratio (m_a, m_b, m_c) in three transformers vary with their corresponding tap changer positions (τ_a, τ_b, τ_c) and are provided by the manufacturer in the form of look-up tables. In addition to the ratio, we model the transformer internal impedances (Z_a^t, Z_b^t, Z_c^t), which represent the voltage drops on both sides of the transformer and vary with the tap position. This modeling also helps account for the mismatch between look-up table data and real measurements. Due to a lack of detailed manufacturer data and measurement capability, we neglect magnetization and iron losses impedances. This is justified for furnace transformers, which are usually operated at nominal intensity.

We consider the impedances of the transmission subsystem (Z_a^l, Z_b^l, Z_c^l), which are generally larger in resistance. As is known, the cables are equipped with water-cooling systems and are specifically designed to carry intensive currents (i_a^s, i_b^s, i_c^s) to the electrodes. Consequently, their electrical resistance corresponds to their current-carrying capability. Moreover, the cables are designed to move flexibly together with the electrodes. These movements, combined with high-intensity currents passing through the cables and the presence of a strong magnetic field, can cause significant variations in their inductance.

Since transformer internal and transmission cables impedances are in serial, we collectively refer to them as the secondary impedance (Z_a^s, Z_b^s, Z_c^s) in the equivalent circuit 3.2.

3.2.2 Electrode-process model

Regarding the electrode-process model, which is more complex due to the uncertainty of the environment, we consider a simplified representation in Δ-人 configuration, as

shown in Figure 3.4. This circuit captures the combined electrical behaviors of the three vertical electrodes and the burden in the molten bath, without including the electric arc as discussed previously. Specifically, each phase is characterized by its lumped impedance, denoted respectively as (Z_1, Z_2, Z_3), representing the electrodes because we can not accurately measure. Moreover they are relatively small compared to the self-inductances of the electrodes according to the estimation and the burden (process) impedances in series. This representation assumes that the electrode currents in the molten bath cancel out at a neutral point at the furnace bottom. Moreover, we neglect the mutual inductances present among the electrodes because we can not accurately measure. Moreover they are relatively small compared to the self-inductances of the electrodes according to the estimation.

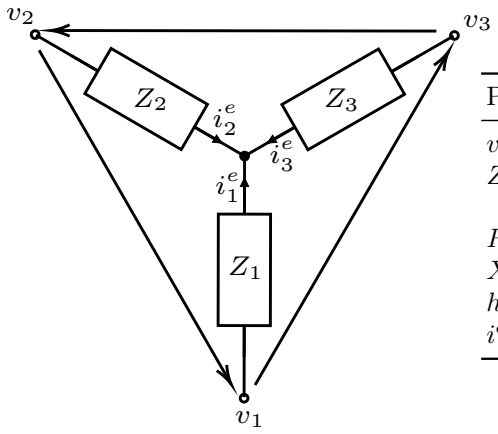

Para.	Description
v	Electrode head voltage.
Z	Electrode-process lumped impedance, $Z = R + \jmath X$.
R	Electrode-process lumped resistance, $R \propto h$.
X	Electrode-process lumped reactance, $X \propto h$.
h	Electrode holder height.
i^e	Electrode current.

FIGURE 3.4: Schematic representation of a delta-wye electrode-process model, illustrating lumped impedance of electrodes and process burden in the molten bath.

The electrode-process impedance (Z_1, Z_2, Z_3) which consists of resistance (R_1, R_2, R_3) and reactance (X_1, X_2, X_3), is a complex and dynamic parameter. They can be influenced by various factors, including the vertical position of the electrode, burden properties, e.g., particle size, burden composition, density, etc, and operating conditions in the molten bath, e.g., thermal dynamics, temperature, etc. Among those factors, the electrode position is the direct way to actively control the electrode-process impedance, thereby determining the current (i_1^e, i_2^e, i_3^e) passing through the impedance.

As is known, the three electrodes are arranged in a triangle and vertically held above the furnace by the electrode holder mechanism. Therefore, their positions are determined by the heights of their respective holders, denoted (h_1, h_2, h_3), measured from a specific

reference point. For simplicity, we refer to this height as the electrode position. These positions can be raised and lowered by their hydraulic system. As a result, vertical movement of the electrodes is used to alter the distance between electrode tips and furnace bottom, thereby changing the quantity and geometric distribution of the burden between them. These changes, in turn, affect the process's electrical impedance. Moreover, the graphite furnaces are consumed over time by the process, leading to changes in their actual lengths, thus their impedance. Additionally, the electrode's movements affect the geometric configuration of the entire current path, causing inductive variations in the furnace. In general, the electrode-process impedance is highly dependent on the electrode movement.

It is important to note that our electrode-process modeling does not include the electric arc model, which is well-established and commonly found in the literature [R.P.Paiva, 1996, Moghadasian and Alenasser, 2011, Shurygin, 2017, Luckins et al., 2022]. As explained in Section 2.1.2, the SiMn furnace, which is considered a high-intensity SAF, operates without an electric arc. Therefore, arc modeling is not necessary in this case.

3.3 Mathematical model formulation

In this section, we formulate the mathematical models of the electrical system using both empirical approaches derived from data regressions and fundamental electrical laws based on equivalent circuit analysis. The models capture the dynamic relationships between actuators and essential circuit parameters, as well as the steady-state behaviors of the interest output variables, which will be described in Section 3.3.1 and Section 3.3.2, respectively. These models serve as a foundation for understanding the complex interactions in the furnace system in the Section 3.4. Moreover, it is apparently indispensable for the design of optimization-based control strategies in Chapter 5-6.

Before delving into details, let us summarize the notations of the most essential variables considered in the transformation and formulation of the following subsections. Particularly, we define in Table 3.1 the main output vectors of interest for control design.

TABLE 3.1: Electrical output variables of interest in the SiMn SAF system.

Output	Description	Domain
$\boldsymbol{p^s}$	Transformer output active power	$\mathbb{R}^3$
$\lvert\boldsymbol{i^s}\rvert$	Secondary transformer current magnitude	$\mathbb{R}^3$
$\lvert\boldsymbol{i^e}\rvert$	Electrode current magnitude	$\mathbb{R}^3$

The instantaneous values of these variables can be measured or computed in real-time using the measurement system installed on the furnace as indicated in Section 2.3.1. In particular, the active power $\boldsymbol{p^s} \in \mathbb{R}^3$ at the secondary side of the transformer is calculated based on the corresponding measured voltage and current signals. The secondary transformer current $\boldsymbol{i^s} \in \mathbb{C}^3$ is directly measured, while the electrode current $\boldsymbol{i^e} \in \mathbb{C}^3$ is derived from the secondary current using Kirchhoff's law. Accordingly, their magnitudes $|\boldsymbol{i^s}|$ and $|\boldsymbol{i^e}| \in \mathbb{R}^3$ can be computed.

Moreover, these outputs are systematically dependent on other circuit parameters and can be analytically expressed as functions of them. For clarity, let us summarize the vectors representing these important circuit parameters in Table 3.2.

TABLE 3.2: Electrical parameter vectors in the SiMn SAF system.

Parameter	Description	Domain
$\boldsymbol{u^p}$	Input primary voltage	$\mathbb{C}^3$
$\boldsymbol{m}$	Transformer ratio	$\mathbb{R}^3$
$\boldsymbol{z^s}$	Secondary impedance	$\mathbb{C}^3$
$\boldsymbol{z^l}$	Transmission line impedance	$\mathbb{C}^3$
$\boldsymbol{z}$	Electrode-process impedance	$\mathbb{C}^3$

Herein, the instantaneous values of the input voltage $\boldsymbol{u^p}$ are directly measured from the power grid, while the other parameters are estimated from the measurement data or transformer specifications. Specifically, we have the transmission line impedance $\boldsymbol{z^l}$ computed from measurements of secondary currents and the voltage drops across the transmission cables.

While values of transformer ratio $\boldsymbol{m}$ and secondary impedance $\boldsymbol{z}^s$ can be derived by regression from tap positions using the models in Section 3.3.1, the instantaneous value of electrode-process impedance $\boldsymbol{z}$, estimated from the electrode currents and voltages, is necessary for linearized models defined in Section 3.3.2.

Finally, we define in Table 3.3 the control actuator vectors of the system that will be manipulated to achieve the desired output performance. Particularly, these actuator variables correspond to the physical positions of the subsystems in the furnace, i.e., tap changer position $\boldsymbol{\tau}$ and electrode holder height $\boldsymbol{h}$. These positions can also be directly measured in real-time, which is necessary for constraint handling in the control design.

TABLE 3.3: Control actuator variables of the SiMn SAF system.

Actuator	Description	Domain
$\boldsymbol{\tau}$	Tap changer position	$\mathbb{Z}^3$
$\boldsymbol{h}$	Electrode holder height	$\mathbb{R}^3$

3.3.1 Dynamic relationships with actuators

As discussed in Section 3.2, the transformer ratio (m_a, m_b, m_c) and secondary impedance (Z_a^s, Z_b^s, Z_c^s) are directly affect by the tap positions (τ_a, τ_b, τ_c) in the transformers. Meanwhile, the electrode-process impedance (Z_1, Z_2, Z_3) across the three phases is influenced by the electrode positions (h_1, h_2, h_3). Therefore, we consider these six variables as the actuators of the system. In the following, we establish their mathematical relationships to predict the impacts these actuators have on the electrical variables.

3.3.1.1 Three-phase transformer tap changer

The modeling of transformer ratio and secondary impedance is dependent on both reference data provided by the manufacturer and historical measurement data collected from the plant. We start with the relationship between transformer tap changer positions $\boldsymbol{\tau} \triangleq [\tau_a, \tau_b, \tau_c]^\top \in \mathbb{Z}_+^3$ and transformer ratios $\boldsymbol{m} \triangleq [m_a, m_b, m_c]^\top \in \mathbb{R}^3$, which the transformer's manufacturer provides in form of look-up tables.

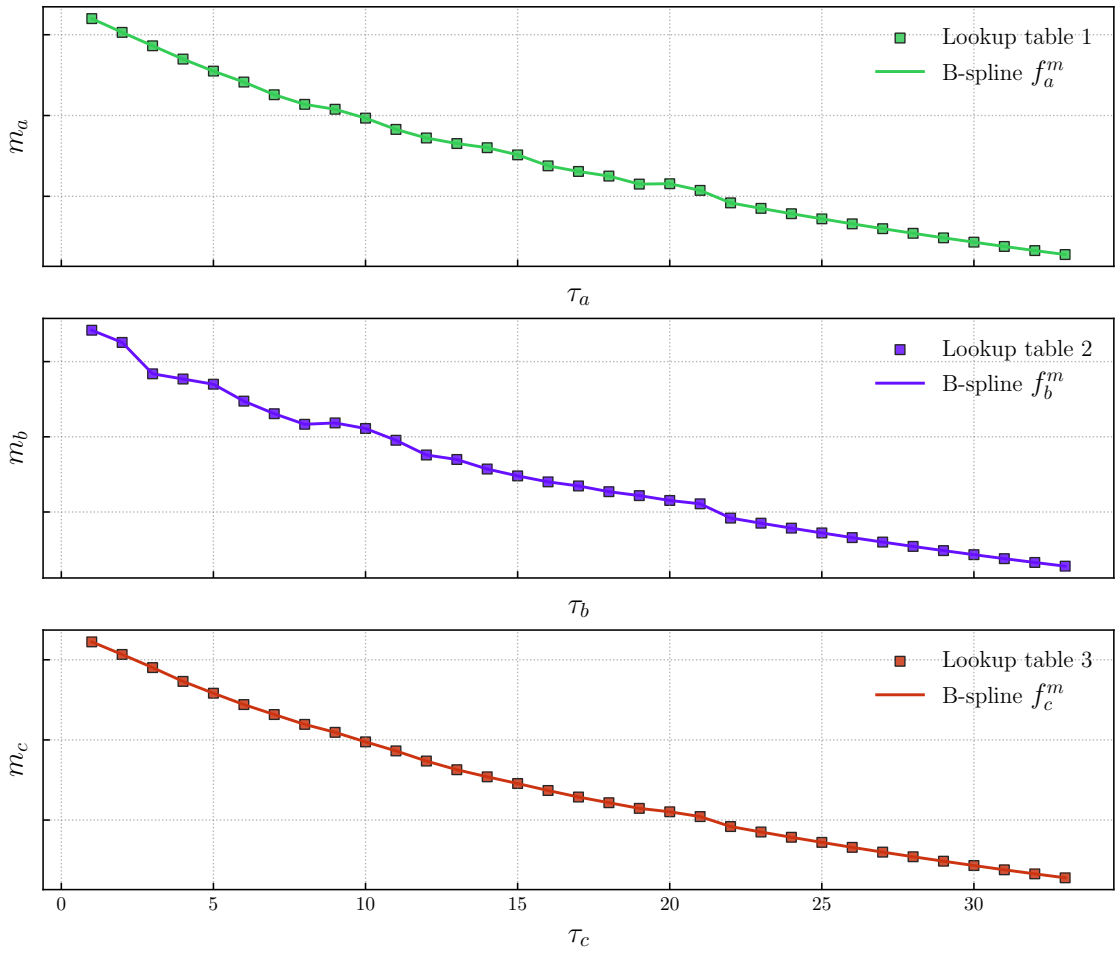

FIGURE 3.5: Visualization of the transformer ratio parameters (m_a, m_b, m_c) as functions of the respective tap changer positions (τ_a, τ_b, τ_c) for all three phases using B-spline interpolation.

However, straightforward integration of this look-up table in the optimization-based control design is not feasible, as such methods typically require differentiable equations. As a result, we propose a robust interpolation model using B-splines to ensure differentiability and provide smooth interpolation:

$$m_j = \sum_{i=0}^{n} B_{i,d,j}(\tau_j) p_{i,j} \triangleq f_j^m(\tau_j), \quad j \in \{a, b, c\}, \tag{3.1}$$

where the order d, knot vector of the basis function $B_{i,d}(\cdot)$ and associated control points

p_i are determined based on the look-up table data[1]. Accordingly, the ratio vector can be defined through the vectorized functions:

$$\boldsymbol{m} \triangleq [f_a^m(\tau_a),\, f_b^m(\tau_b),\, f_c^m(\tau_c)]^\top \triangleq \boldsymbol{f^m}(\boldsymbol{\tau}), \qquad \boldsymbol{f}^m : \mathbb{Z}_+^3 \to \mathbb{R}^3, \tag{3.2}$$

where $\boldsymbol{f}^m(\cdot)$ denotes the nonlinear mapping from the discrete tap positions $\boldsymbol{\tau}$ to the continuous transformer ratio values $\boldsymbol{m}$. Figure 3.5 visually shows the transformer ratio models $(f_a^m,\, f_b^m,\, f_c^m)$ in three phases obtained by the B-spline scheme (3.1).

In the following, we consider the relationship between tap positions and secondary impedances, denoted by $\boldsymbol{z^s} \triangleq [Z_a^s,\, Z_b^s,\, Z_c^s]^\top \in \mathbb{C}^3$, where we have:

$$\boldsymbol{z^s} = \boldsymbol{z^t} + \boldsymbol{z^l}, \tag{3.3}$$

with $\boldsymbol{z^t} \in \mathbb{C}^3$ is the transformer internal impedance and $\boldsymbol{z^l} \in \mathbb{C}^3$ presents the transmission line impedance. Note that the secondary impedance $\boldsymbol{z^s}$ only vary with the tap position $\boldsymbol{\tau}$ due to the internal impedance $\boldsymbol{z^t} \triangleq [Z_a^t,\, Z_b^t,\, Z_c^t]^\top$, whereas the transmission impedance $\boldsymbol{z^l} \triangleq \left[Z_a^l,\, Z_b^l,\, Z_c^l\right]^\top$ is considered independent of the tap position. As a result, we concentrate on formulating the models of transformer apparent impedance:

$$\boldsymbol{z^t} = \boldsymbol{r^t} + \jmath \boldsymbol{x^t}, \tag{3.4}$$

where $\boldsymbol{r^t} \triangleq [R_a^t,\ R_b^t,\ R_c^t]^\top$, $\boldsymbol{x^t} \triangleq [X_a^t,\ X_b^t,\ X_c^t]^\top \in \mathbb{R}^3$ denotes resistance and reactance.

In particular, we approximate the resistance $\boldsymbol{z^t}$ and reactance $\boldsymbol{x^t}$ profiles in three phases as second-degree polynomial functions of the tap position. The resistance and reactance values at each tap position are estimated based on regression analysis of historical measurement data. Consequently, these values inherently include noise resulting from measurement errors or operating disturbances in the furnace. Therefore, to mitigate overfitting or oscillatory behavior, we fit the models using least absolute deviation regression, which is more robust to outliers than the standard least-squares approach.

[1]The B-spline interpolation is automatically optimized using CasADi [Gillis, 2018].

This yields the following models for resistance and reactance in each phase:

$$R_j^t = \sum_{i=0}^{2} \alpha_{i|j} \tau_j^i \triangleq f_j^r(\tau_j), \quad j \in \{a, b, c\}, \tag{3.5}$$

$$X_j^t = \sum_{i=0}^{2} \beta_{i|j} \tau_j^i \triangleq f_j^x(\tau_j), \quad j \in \{a, b, c\}. \tag{3.6}$$

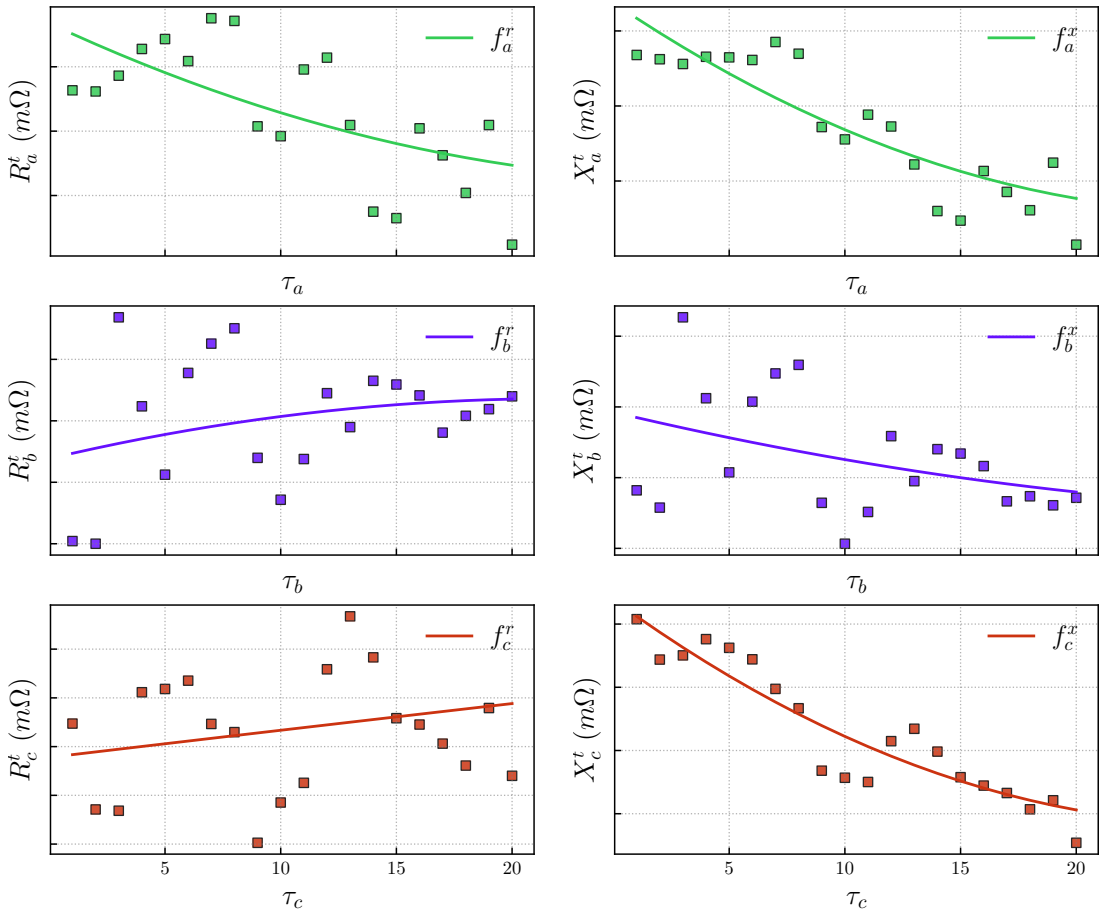

(A) Transformer resistance (R_a^t, R_b^t, R_c^t). (B) Transformer reactance (X_a^t, X_b^t, X_c^t).

FIGURE 3.6: Visualization of the transformer internal impedance (Z_a^t, Z_b^t, Z_c^t) as functions of the respective tap changer positions (τ_a, τ_b, τ_c) for all three phases using least absolute deviation regression.

Here, the coefficients α and β are determined by minimizing the L1-norm of the difference between the regression data at each tap and the corresponding second-degree polynomial model. Accordingly, we can denote the secondary resistance and reactance through:

$$\boldsymbol{r}^{\boldsymbol{t}} \triangleq [f_a^r(\tau_a),\, f_b^r(\tau_b),\, f_c^r(\tau_c)]^\top \triangleq \boldsymbol{f}^{\boldsymbol{r}}(\boldsymbol{\tau}), \quad \boldsymbol{f}^r : \mathbb{Z}_+^3 \to \mathbb{R}^3, \tag{3.7}$$

$$\boldsymbol{x}^{\boldsymbol{t}} \triangleq [f_a^x(\tau_a),\, f_b^x(\tau_b),\, f_c^x(\tau_c)]^\top \triangleq \boldsymbol{f}^{\boldsymbol{x}}(\boldsymbol{\tau}), \quad \boldsymbol{f}^x : \mathbb{Z}_+^3 \to \mathbb{R}^3, \tag{3.8}$$

where $\boldsymbol{f}^r(\cdot)$ and $\boldsymbol{f}^x(\cdot)$ denote the nonlinear mappings from the discrete tap position $\boldsymbol{\tau}$ to the transformer internal resistance $\boldsymbol{r}^{\boldsymbol{t}}$ and reactance $\boldsymbol{x}^{\boldsymbol{t}}$, respectively. A visual representation of the polynomial impedance model is provided in Figure 3.6, which illustrates the model's approximation to the data across the three phases. As shown, the accuracy of the approximated models depends on the quality of the regression data, as irregular or noisy data patterns tend to result in higher errors.

3.3.1.2 Electrode positioning system

In addition to the furnace transformer system, the electrode positioning system is of great importance in the SiMn furnace. The dynamic response to vertical movement of electrode position $\boldsymbol{h} \triangleq [h_1,\, h_2,\, h_3]^\top \in \mathbb{R}^3$ can be characterized by changes in electrode-process impedance $\boldsymbol{z} \triangleq [Z_1,\, Z_2,\, Z_3]^\top \in \mathbb{C}^3$. As electrode movements change the distance from the electrode tips to the furnace bottom, the composition, quantity, and geometry of the burden in between, thus the associated resistance. Moreover, their movements affect the geometry of the entire current path, causing the inductive variations discussed. Moreover, we know that the electrode-process impedance defines the furnace system circuit; thus, any change in the impedance affects the entire electrical system. Therefore, it is essential to analyze how the electrode displacements influence the electrode-process impedance.

However, the dynamical model of the electrode-process impedance is difficult to formulate accurately due to the complex metallurgical characteristics and the significant disturbances in the furnace bath. The resistivity of the burden considerably depends on the status of the molten pool, i.e., the material composition, the particle sizes of the charges, the geometry or distribution of the burden, temperature, etc. Moreover, the resistance of the electrodes depends on their actual lengths, which are unknown as they are deeply immersed in the molten bath and consumed over time. Additionally, the inductive characteristics of the electrode-process impedance are also affected by the magnetic field caused by the currents in the surrounding structure. All these factors are difficult to capture with precision or measured in real-time.

Therefore, we propose a simplified dynamic model that approximates electrode-process impedance locally around the operating points due to *its quasi-static behavior over a small variation*:

$$R_j = R_{0|j} + \boldsymbol{\gamma}_j^{\boldsymbol{r}\top}(\boldsymbol{h} - \boldsymbol{h_0}), \quad j \in \{1, 2, 3\}, \tag{3.9}$$

$$X_j = X_{0|j} + \boldsymbol{\gamma}_j^{\boldsymbol{x}\top}(\boldsymbol{h} - \boldsymbol{h_0}), \quad j \in \{1, 2, 3\}, \tag{3.10}$$

where, R_0, $X_0 \in \mathbb{R}$ and $\boldsymbol{h_0} \in \mathbb{R}^3$ indicate the instantaneous measurements of resistance, reactance and electrode relative position, while $\boldsymbol{\gamma}_j^{\boldsymbol{r}}$, $\boldsymbol{\gamma}_j^{\boldsymbol{x}} \in \mathbb{R}^3$ are the gradients computed in real-time using backward finite difference on historical data, representing the sensitivity of impedance to electrode position. However, this local approximation becomes increasingly inaccurate as the system deviates further away from the operating point.

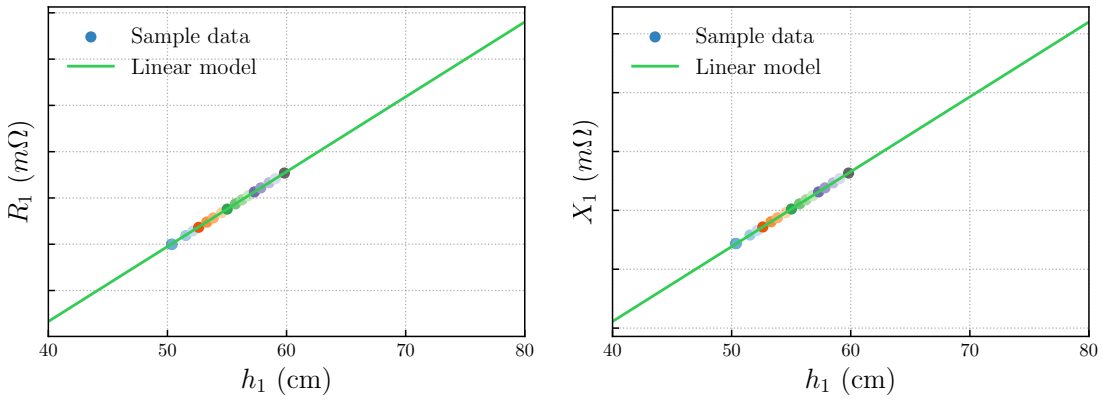

(A) Electrode-process resistance R_1.

(B) Electrode-process reactance X_1.

FIGURE 3.7: Visualization of the electrode-process impedance estimation in phase one using backward difference finite with 17 sample data and sampling is 1s.

We provide in Figure 3.7 a visual representation of the linear electrode-process impedance model in phase one at the operating point. The data points exhibit a linear correlation between electrode displacement and impedance variation over a short time interval during regular operation, assuming there are no disturbances. As a consequence, we observe that the linear model provides a reasonable approximation of the impedance dynamics.

Nevertheless, this relationship may become highly nonlinear or unpredictable under different operating conditions, such as during casting, when the metal is cast and the

resistance changes rapidly. During such periods, the linear model may not accurately capture impedance dynamics.

For control design, given the affine impedance models obtained in (3.9) and (3.10), we consider the electrode displacement $\boldsymbol{\delta h} \triangleq [\delta h_1,\, \delta h_2,\, \delta h_3]^\top \in \mathbb{R}^3$ as the control decision variable. To ensure consistency in the control strategy, the transformer tap deviation vector $\boldsymbol{\delta \tau} \triangleq [\delta \tau_a,\, \delta \tau_b,\, \delta \tau_c]^\top \in \mathbb{Z}^3$ is also included as a decision variable. Thus, these variables can be defined at each discrete time step k as follows:

$$\boldsymbol{\delta h}(k) = \boldsymbol{h}(k+1) - \boldsymbol{h}(k), \tag{3.11}$$

$$\boldsymbol{\delta \tau}(k) = \boldsymbol{\tau}(k+1) - \boldsymbol{\tau}(k), \tag{3.12}$$

From here, to compactly express the models in (3.9) and (3.10) at a particular time step k, we rewrite them in a vector form. This allows us to represent the impedance changes for all three phases as an affine function of the three electrode position deviations:

$$\boldsymbol{r}(k+1) = \boldsymbol{r}(k) + \boldsymbol{\Gamma^r}(k)\ \boldsymbol{\delta h}(k), \tag{3.13}$$

$$\boldsymbol{x}(k+1) = \boldsymbol{x}(k) + \boldsymbol{\Gamma^x}(k)\ \boldsymbol{\delta h}(k), \tag{3.14}$$

where, the two vectors $\boldsymbol{r} \triangleq [R_1,\ R_2,\ R_3]^\top$, $\boldsymbol{x} \triangleq [X_1,\ X_2,\ X_3]^\top \in \mathbb{R}^3$ represent the electrode-process resistance and reactance respectively. The jacobian matrices $\boldsymbol{\Gamma^r} \triangleq [\boldsymbol{\gamma}_1^{\boldsymbol{r}},\ \boldsymbol{\gamma}_2^{\boldsymbol{r}},\ \boldsymbol{\gamma}_3^{\boldsymbol{r}}]^\top$ and $\boldsymbol{\Gamma^x} \triangleq [\boldsymbol{\gamma}_1^{\boldsymbol{x}},\ \boldsymbol{\gamma}_2^{\boldsymbol{x}},\ \boldsymbol{\gamma}_3^{\boldsymbol{x}}]^\top \in \mathbb{R}^{3\times 3}$ are computed locally at every time step k, as mentioned in (3.9)–(3.10), capturing the quasi-static impedance dynamics. Their off-diagonal elements capture the interaction effects, i.e., how the movement of one electrode in one phase affects the impedance in the other phases. These models will be used for control design presented in Chapter 5–6.

3.3.2 Steady state electrical models

In the following, we derive the steady-state electrical SiMn SAF models based on the equivalent circuits of the three-phase transformer in Figure 3.2 and electrode-process in Figure 3.4. The idea is to analyze the equivalent circuits using fundamental electrical laws, i.e., Ohm's law and Kirchhoff's law and subsequently, establish the mathematical

relationships between the main electrical output variables in Table 3.1 and the electrical parameters of the system in Table 3.2.

In particular, we present the analytical transformation of the electrical steady-state model, which is systematically derived from the equivalent circuits in Figure 3.1a. The transformation starts with Ohm's and Kirchhoff's laws applied to the first phase of the equivalent circuit shown in Figure 3.2. In particular, we have the primary voltage e_a^p of transformer **A** is related to the secondary voltage e_a^s by the transformer ratio m_a:

$$e_a^p = m_a\, e_a^s \tag{3.15}$$

$$\Leftrightarrow u_{12}^p = m_a\,(u_a^s + Z_a^s\, i_a^s), \tag{3.16}$$

where e_a^p is equivalent to u_{12}^p because the primary side is connected in delta configuration and e_a^s can be expressed in term of $u_a^s + Z_a^s\, i^s{}_a$ due to the voltage Kirchhoff's laws. Here, u_{12}^p, m_a and Z_a^s are considered as known parameters. Whereas, the secondary current i_a^s is the unknown variable and the voltage between two electrode heads u_a^s can be expressed in terms of two individual voltages in electrode one v_1 and electrode two v_2 as follows:

$$u_a^s = v_1 - v_2. \tag{3.17}$$

From here, we apply Ohm's law on the equivalent circuit shown in Figure 3.4 to express the electrode voltages v_1 and v_2 as functions of electrode currents i_1^e and i_2^e, respectively. Note that we do not consider the mutual inductances among the three electrodes; thus, the electrode voltages are represented by their own impedance and current as follows:

$$v_1 = Z_1\, i_1^e, \tag{3.18}$$

$$v_2 = Z_2\, i_2^e. \tag{3.19}$$

Whereas, Z_1 and Z_2 are the known parameters of the model, while i_1^e and i_2^e are the unknown variables. After, we combine the equations in (3.16), (3.17), (3.18) and (3.19) to obtain the expression that contains the secondary and electrode currents as follows:

$$(Z_1\, i_1^e - Z_2\, i_2^e) + Z_a^s\, i_a^s = \frac{u_{12}^p}{m_a}. \tag{3.20}$$

We repeat the same procedure applied to have (3.20) for the second and third phases of the equivalent circuit shown in Figure 3.2, thus obtaining the following expressions:

$$(Z_2\, i_2^e - Z_3\, i_3^e) + Z_b^s\, i_b^s \;=\; \frac{u_{23}^p}{m_b}, \tag{3.21}$$

$$(Z_3\, i_3^e - Z_1\, i_1^e) + Z_c^s\, i_c^s \;=\; \frac{u_{31}^p}{m_c}. \tag{3.22}$$

Additionally, we apply Kirchhoff's current law at each node of the delta coupling in the secondary side of Figure 3.2 to obtain the relationship between the electrode currents i_1^e, i_2^e, i_3^e and the secondary currents i_1^s, i_2^s, i_3^s as follows:

$$i_1^e \;=\; i_a^s - i_c^s, \tag{3.23}$$

$$i_2^e \;=\; i_b^s - i_a^s, \tag{3.24}$$

$$i_3^e \;=\; i_c^s - i_b^s. \tag{3.25}$$

From here, we derive systems of electric current models based on the circuit parameters. The transformation computes the electrode current $\boldsymbol{i^e}$ and then obtains the secondary current $\boldsymbol{i^s}$. Note that, in the Appendix A.1, we also provide an equivalent transformation that starts with the secondary current $\boldsymbol{i^s}$ and obtains the electrode current $\boldsymbol{i^e}$.

In particular, we express the secondary currents i_a^s, i_b^s and i_c^s from equations (3.20)–(3.22) in terms of the electrode currents i_1^e, i_2^e and i_3^e. First, we rearrange the factors of those equations to isolate the secondary currents i_a^s, i_b^s and i_c^s as follows:

$$i_a^s \;=\; \frac{1}{Z_a^s}\frac{u_{12}^p}{m_a} - \frac{1}{Z_a^s}(Z_1\, i_1^e - Z_2\, i_2^e), \tag{3.26}$$

$$i_b^s \;=\; \frac{1}{Z_b^s}\frac{u_{23}^p}{m_b} - \frac{1}{Z_b^s}(Z_2\, i_2^e - Z_3\, i_3^e), \tag{3.27}$$

$$i_c^s \;=\; \frac{1}{Z_c^s}\frac{u_{31}^p}{m_c} - \frac{1}{Z_c^s}(Z_3\, i_3^e - Z_1\, i_1^e). \tag{3.28}$$

Then, we substitute the secondary current expressions (3.26)–(3.28) into the node relations (3.23) and (3.24). This eliminates the secondary currents and produces two linear

equations that relate the electrode currents directly to the known primary voltages:

$$i_1^e = \left[\frac{1}{Z_a^s}\frac{u_{12}^p}{m_a} - \frac{1}{Z_a^s}(Z_1\, i_1^e - Z_2\, i_2^e)\right] - \left[\frac{1}{Z_c^s}\frac{u_{31}^p}{m_c} - \frac{1}{Z_c^s}(Z_3\, i_3^e - Z_1\, i_1^e)\right], \tag{3.29}$$

$$i_2^e = \left[\frac{1}{Z_b^s}\frac{u_{23}^p}{m_b} - \frac{1}{Z_b^s}(Z_2\, i_2^e - Z_3\, i_3^e)\right] - \left[\frac{1}{Z_a^s}\frac{u_{12}^p}{m_a} - \frac{1}{Z_a^s}(Z_1\, i_1^e - Z_2\, i_2^e)\right], \tag{3.30}$$

By rearranging (3.29) and (3.30) to isolate all electrode current terms on the left-hand side and grouping their coefficients, we obtain the following expressions:

$$\left(1 + \frac{Z_1}{Z_a^s} + \frac{Z_1}{Z_c^s}\right) i_1^e - \frac{Z_2}{Z_a^s} i_2^e - \frac{Z_3}{Z_c^s} i_3^e = \frac{1}{Z_a^s}\frac{u_{12}^p}{m_a} - \frac{1}{Z_c^s}\frac{u_{31}^p}{m_c}, \tag{3.31}$$

$$-\frac{Z_1}{Z_a^s} i_1^e + \left(1 + \frac{Z_2}{Z_b^s} + \frac{Z_2}{Z_a^s}\right) i_2^e - \frac{Z_3}{Z_b^s} i_3^e = \frac{1}{Z_b^s}\frac{u_{23}^p}{m_b} - \frac{1}{Z_a^s}\frac{u_{12}^p}{m_a}. \tag{3.32}$$

Next, we clear the fractional coefficients by multiplying both sides by the least common multiple of the denominators Z_a^s, Z_b^s and Z_c^s, thus it yields:

$$\Big(Z_a^s Z_c^s + Z_1 Z_c^s + Z_1 Z_a^s\Big) i_1^e - \Big(Z_2 Z_c^s\Big) i_2^e - \Big(Z_3 Z_a^s\Big) i_3^e = Z_c^s \frac{u_{12}^p}{m_a} - Z_a^s \frac{u_{31}^p}{m_c}, \tag{3.33}$$

$$-\Big(Z_1 Z_b^s\Big) i_1^e + \Big(Z_b^s Z_a^s + Z_2 Z_b^s + Z_2 Z_a^s\Big) i_2^e - \Big(Z_3 Z_a^s\Big) i_3^e = Z_a^s \frac{u_{23}^p}{m_b} - Z_b^s \frac{u_{12}^p}{m_a}. \tag{3.34}$$

Moreover, we apply Kirchhoff's current law at the neutral point of the star in Figure 3.4 to obtain the third equation that relates the electrode currents:

$$i_1^e + i_2^e + i_3^e = 0. \tag{3.35}$$

Finally, (3.33)–(3.35) are combined to yield complex electrode current model $\boldsymbol{i}^{\boldsymbol{e}} \triangleq [i_1^e,\ i_2^e,\ i_3^e]^\top \in \mathbb{C}^3$ in three phases at steady state as a vector solution of a linear system:

$$\boldsymbol{i}^{\boldsymbol{e}} \;=\; \mathbf{A}_{\mathbf{e}}^{-1}\,\mathbf{b}_{\mathbf{e}}, \tag{3.36}$$

where coefficient matrix $\mathbf{A}_{\mathbf{e}} \in \mathbb{C}^{3\times 3}$ and vector $\mathbf{b}_{\mathbf{e}} \in \mathbb{C}^{3}$ are explicitly defined as:

$$\mathbf{A}_{\mathbf{e}} = \begin{bmatrix} Z_{ac} & -Z_2 Z_c^s & -Z_3 Z_a^s \\ -Z_1 Z_b^s & Z_{ba} & -Z_3 Z_a^s \\ 1 & 1 & 1 \end{bmatrix}, \quad \mathbf{b}_{\mathbf{e}} = \begin{bmatrix} Z_c^s \dfrac{u_{12}^p}{m_a} - Z_a^s \dfrac{u_{31}^p}{m_c} \\ Z_a^s \dfrac{u_{23}^p}{m_b} - Z_b^s \dfrac{u_{12}^p}{m_a} \\ 0 \end{bmatrix},$$

$$Z_{ac} \triangleq Z_a^s Z_c^s + Z_1(Z_c^s + Z_a^s), \quad Z_{ab} \triangleq Z_b^s Z_a^s + Z_2(Z_b^s + Z_a^s).$$

Thus, the model of electrode current magnitude is derived by applying the element-wise modulus operator $|\cdot|$ to (3.36), which yields a nonlinear function:

$$|\boldsymbol{i}^{\boldsymbol{e}}| \;=\; |\mathbf{A}_{\mathbf{e}}{}^{-1}\mathbf{b}_{\mathbf{e}}|. \tag{3.37}$$

From the coefficient $\mathbf{A}_{\mathbf{e}}$ and $\mathbf{b}_{\mathbf{e}}$, we can see that the electrode current model (3.36) is described as a function of input voltage $\boldsymbol{u}^{\boldsymbol{p}}$, transformer ratio $\boldsymbol{m}$, secondary impedance $\boldsymbol{z}^{\boldsymbol{s}}$ and electrode-process impedance $\boldsymbol{z}$ which are all parameters of the circuit. Thus, its magnitude model (3.37) is also an explicit analytic function of the circuit parameters and allows for the use of the algorithmic differentiation technique in the subsequent linearization.

Next, by substituting the solution of the electrode current system (3.36) into the secondary current expressions (3.26)–(3.28), we can express the complex model of secondary current $\boldsymbol{i}^{\boldsymbol{s}} \triangleq [i_a^s,\ i_b^s,\ i_c^s]^\top \in \mathbb{C}^3$ and its magnitude model by the following expression:

$$\boldsymbol{i}^{\boldsymbol{s}} = \mathbf{M_e}\mathbf{A_e}^{-1}\mathbf{b_e} + \mathbf{n_e}, \tag{3.38}$$

$$|\boldsymbol{i}^{\boldsymbol{s}}| = |\mathbf{M_e}\mathbf{A_e}^{-1}\mathbf{b_e} + \mathbf{n_e}|. \tag{3.39}$$

Here, $\mathbf{M_e} \in \mathbb{C}^{3\times3}$ and $\mathbf{n_e} \in \mathbb{C}^3$ denote the coefficients that express the secondary currents in (3.26)–(3.28) as an affine function $\boldsymbol{i}^{\boldsymbol{s}} = \mathbf{M_e}\,\boldsymbol{i}^{\boldsymbol{e}} + \mathbf{n_e}$:

$$\mathbf{M_e} = \begin{bmatrix} -\frac{Z_1}{Z_a^s} & \frac{Z_2}{Z_a^s} & 0 \\ 0 & -\frac{Z_2}{Z_b^s} & \frac{Z_3}{Z_b^s} \\ \frac{Z_1}{Z_c^s} & -\frac{Z_3}{Z_c^s} & 0 \end{bmatrix}, \quad \mathbf{n_e} = \begin{bmatrix} \frac{1}{Z_a^s}\frac{u_{12}^p}{m_a} \\ \frac{1}{Z_b^s}\frac{u_{23}^p}{m_b} \\ \frac{1}{Z_c^s}\frac{u_{31}^p}{m_c} \end{bmatrix}.$$

Similarly, the secondary current magnitude model (3.39) is also addressed as a function of the input voltage $\boldsymbol{u}^{\boldsymbol{p}}$, transformer ratio $\boldsymbol{m}$, secondary impedance $\boldsymbol{z}^{\boldsymbol{s}}$ and electrode-process impedance $\boldsymbol{z}$ because of their presence in the coefficient matrices and vectors.

Furthermore, the transformer secondary active power in three phases is also of great interest. So, we express the active power at the transformer secondaries as an explicit function of circuit parameters. First, we have the secondary impedances Z_a^s, Z_b^s, Z_c^s being the lumped impedances that represent the transformer internal impedances Z_a^t, Z_b^t, Z_c^t and the transmission line impedances Z_a^l, Z_b^l, Z_c^l:

$$Z_a^s = Z_a^t + Z_a^l, \tag{3.40}$$

$$Z_b^s = Z_b^t + Z_b^l, \tag{3.41}$$

$$Z_c^s = Z_c^t + Z_c^l. \tag{3.42}$$

We start by applying Kirchhoff's voltage law to the transformer circuit Figure 3.2 to obtain the voltages u_a^t, u_b^t, u_c^t at the output of the transformers, which are given by:

$$u_a^t = u_a^s + Z_a^l\, i_a^s, \tag{3.43}$$

$$u_b^t = u_b^s + Z_b^l\, i_b^s, \tag{3.44}$$

$$u_c^t = u_c^s + Z_c^l\, i_c^s. \tag{3.45}$$

Then, we substitute (3.17)–(3.19) and expressions which can be drawn from similar analysis of phase two and phase three into (3.43)–(3.45), to express the transformer output voltages in terms of the electrode currents and secondary currents:

$$u_a^t = (Z_1\, i_1^e - Z_2\, i_2^e) + Z_a^l\, i_a^s, \tag{3.46}$$

$$u_b^t = (Z_2\, i_2^e - Z_3\, i_3^e) + Z_b^l\, i_b^s, \tag{3.47}$$

$$u_c^t = (Z_3\, i_3^e - Z_1\, i_1^e) + Z_c^l\, i_c^s. \tag{3.48}$$

From here, we express the transformer output voltage vector $\boldsymbol{u^t} \triangleq [u_a^t,\ u_b^t,\ u_c^t]^\top \in \mathbb{C}^3$ in terms of electrode and secondary current vectors by the matrix operations as follows:

$$\begin{bmatrix} u_a^t \\ u_b^t \\ u_c^t \end{bmatrix} = \begin{bmatrix} Z_1 & -Z_2 & 0 \\ 0 & Z_2 & -Z_3 \\ -Z_1 & 0 & Z_3 \end{bmatrix} \begin{bmatrix} i_a^e \\ i_b^e \\ i_c^e \end{bmatrix} + \begin{bmatrix} Z_a^l & 0 & 0 \\ 0 & Z_b^l & 0 \\ 0 & 0 & Z_c^l \end{bmatrix} \begin{bmatrix} i_a^s \\ i_b^s \\ i_c^s \end{bmatrix} \tag{3.49}$$

or:

$$\boldsymbol{u^t} = \mathbf{Z_e}\, \mathbf{A_e^{-1}} \mathbf{b_e} + \mathbf{Z_l} \left(\mathbf{M_e} \mathbf{A_e^{-1}} \mathbf{b_e} + \mathbf{n_e} \right), \tag{3.50}$$

where $\mathbf{A_e^{-1}}$, $\mathbf{b_e}$, $\mathbf{M_e}$ and $\mathbf{n_e}$ are defined in (3.36) and (3.38), while $\mathbf{Z_e}$, $\mathbf{Z_l}$ are defined by:

$$\mathbf{Z_e} = \begin{bmatrix} Z_1 & -Z_2 & 0 \\ 0 & Z_2 & -Z_3 \\ -Z_1 & 0 & Z_3 \end{bmatrix}, \quad \mathbf{Z_l} = \begin{bmatrix} Z_a^l & 0 & 0 \\ 0 & Z_b^l & 0 \\ 0 & 0 & Z_c^l \end{bmatrix}, \tag{3.51}$$

Next, we compute the active powers at the transformer secondaries, whose values are based on the transformer output voltages $\boldsymbol{u^t} \in \mathbb{C}^3$ and corresponding currents $\boldsymbol{i^s} \in \mathbb{C}^3$:

$$P_a^s = \Re\{u_a^t\, i_a^{s*}\} = |u_a^t|\, |i_a^s|\, \cos(\angle u_a^t - \angle i_a^s), \tag{3.52}$$

$$P_b^s = \Re\{u_b^t\, i_b^{s*}\} = |u_b^t|\, |i_b^s|\, \cos(\angle u_a^t - \angle i_a^s), \tag{3.53}$$

$$P_c^s = \Re\{u_c^t\, i_c^{s*}\} = |u_c^t|\, |i_c^s|\, \cos(\angle u_a^t - \angle i_a^s), \tag{3.54}$$

where $\{\cdot\}^*$ is the complex conjugate operator and $\angle\{\cdot\}$ denote the angle operator. Then, we substitute (3.38) and (3.50) into (3.52)–(3.54) to express the active power vector $\boldsymbol{p^s} \triangleq [P_a^s,\ P_b^s,\ P_c^s]^\top \in \mathbb{R}^3$ as an explicit function of circuit parameters:

$$\boldsymbol{p}^{\boldsymbol{s}} = \left|\mathbf{Z_e}\,\mathbf{A_e^{-1}}\mathbf{b_e} + \mathbf{Z_l}\,(\mathbf{M_e}\mathbf{A_e^{-1}}\mathbf{b_e} + \mathbf{n_e})\right| \odot \left|\mathbf{M_e}\mathbf{A_e^{-1}}\mathbf{b_e} + \mathbf{n_e}\right| \odot \cos\boldsymbol{\phi}_{\boldsymbol{ui}}, \quad (3.55)$$

where $\odot$ is the element-wise multiplication operator and $\phi_{ui} \in \mathbb{R}^3$ is the angle difference vector between the transformer secondary voltages and their corresponding currents:

$$\boldsymbol{\phi}_{\boldsymbol{ui}} = \angle\Big(\mathbf{Z_e}\,\mathbf{A_e^{-1}}\mathbf{b_e} + \mathbf{Z_l}\,(\mathbf{M_e}\mathbf{A_e^{-1}}\mathbf{b_e} + \mathbf{n_e})\Big) - \angle\Big(\mathbf{M_e}\mathbf{A_e^{-1}}\mathbf{b_e} + \mathbf{n_e}\Big). \quad (3.56)$$

In addition to mentioned parameters, i.e., input voltage $\boldsymbol{u}^{\boldsymbol{p}}$, transformer ratio $\boldsymbol{m}$, secondary impedance $\boldsymbol{z}^{\boldsymbol{s}}$ and electrode-process impedance $\boldsymbol{z}$, the active power model (3.55) also depends on the transmission line impedance $\boldsymbol{z}^{\boldsymbol{l}}$ by the diagonal matrix $\mathbf{Z_l}$.

Noticeably, all output models of interest for control design, i.e., (3.37), (3.39), and (3.55), are nonlinear because of the modulo or the angle operators on complex vectors. They also contain inherent phase coupling due to the presence of circuit parameters from all three phases, including $\boldsymbol{u}^{\boldsymbol{p}}$, $\boldsymbol{m}$, $\boldsymbol{z}^{\boldsymbol{s}}$, $\boldsymbol{z}^{\boldsymbol{l}}$ and $\boldsymbol{z}$.

3.3.3 Output linearized model

The steady-state models derived in Subsection 3.3.2 form a comprehensive and nonlinear representation of the SiMn SAF electrical system. Some are indispensable for the control design, particularly, active power $\boldsymbol{p}^{\boldsymbol{s}}$, current magnitude $|\boldsymbol{i}^{\boldsymbol{s}}|$ of the three-phase transformer and electrode current magnitude $|\boldsymbol{i}^{\boldsymbol{e}}|$, as they are subject to operational constraints, as discussed in Section 4.1.4. Thus, we refer to these as the key electrical outputs of the system, denoted by $\mathbf{y} \triangleq [\boldsymbol{p}^{\boldsymbol{s}},\ |\boldsymbol{i}^{\boldsymbol{s}}|,\ |\boldsymbol{i}^{\boldsymbol{e}}|]^\top \in \mathbb{R}^9$. As noted in the previous subsections, they depend on the circuit parameters, some of which are affected by the actuators.

For instance, the ratio $\boldsymbol{m} \in \mathbb{R}^3$, secondary impedance $\boldsymbol{z}^{\boldsymbol{s}} \in \mathbb{C}^3$ can be analytically determined by the tap changer positions $\boldsymbol{\tau} \in \mathbb{Z}_+^3$ through (3.2), (3.3), (3.7)–(3.8), while the electrode-process resistance and reactance $\boldsymbol{r}$, $\boldsymbol{x} \in \mathbb{R}^3$ is linearly determined based on the electrode movements as indicated in (3.13)–(3.14). As a consequence, for compactness, we describe these equations at a discrete time step k, representing the system outputs as:

$$\mathbf{y}(k) \triangleq \Psi(\boldsymbol{\tau}(k), \boldsymbol{r}(k), \boldsymbol{x}(k)), \tag{3.57}$$

where, function $\Psi(\cdot) : \mathbb{R}^9 \mapsto \mathbb{R}^9$ stands for a mapping function established from combining all equations in (3.2), (3.7), (3.8), (3.37), (3.39), and (3.55).

Given that the electrical dynamics of the SiMn SAF system are relatively slow, we constrain tap switching and electrode displacement to small variations within their physical limits. Thus, it allows us to linearize the nonlinear model (3.57) around a steady-state operating point. Accordingly, we consider small deviations in tap positions and electrode heights, as defined in (3.11) and (3.12). Using the linearized dynamics described by (3.13) and (3.14), we derive a linear approximation:

$$\begin{aligned}
\mathbf{y}(k+1) &= \Psi\Big(\boldsymbol{\tau}(k) + \boldsymbol{\delta\tau}(k),\ \boldsymbol{r}(k) + \boldsymbol{\Gamma}^{\boldsymbol{r}}(k)\boldsymbol{\delta h}(k),\ \boldsymbol{x}(k) + \boldsymbol{\Gamma}^{\boldsymbol{x}}(k)\boldsymbol{\delta h}(k)\Big) \\
&\approx \underbrace{\Psi\Big(\boldsymbol{\tau}(k), \boldsymbol{r}(k), \boldsymbol{x}(k)\Big)}_{\mathbf{y}(k)} + \underbrace{\left.\frac{\partial \Psi}{\partial \boldsymbol{\tau}}\right|_{(k)}}_{\mathbf{J}^{\boldsymbol{\tau}} \in \mathbb{R}^{9\times 3}} \boldsymbol{\delta\tau}(k) + \underbrace{\left(\left.\frac{\partial \Psi}{\partial \boldsymbol{r}}\right|_{(k)} \boldsymbol{\Gamma}^{\boldsymbol{r}}(k) + \left.\frac{\partial \Psi}{\partial \boldsymbol{x}}\right|_{(k)} \boldsymbol{\Gamma}^{\boldsymbol{x}}(k)\right)}_{\mathbf{J}^{\boldsymbol{h}} \in \mathbb{R}^{9\times 3}} \boldsymbol{\delta h}(k) \\
&\triangleq \overline{\Psi}(\mathbf{y}(k),\ \boldsymbol{\delta\tau}(k),\ \boldsymbol{\delta h}(k)),
\end{aligned} \tag{3.58}$$

where the Jacobian matrices $\partial\Psi/\partial\boldsymbol{\tau}$, $\partial\Psi/\partial\boldsymbol{r}$, and $\partial\Psi/\partial\boldsymbol{x}$ are evaluated at every time step k. $\boldsymbol{\Gamma}^{\boldsymbol{r}}$ and $\boldsymbol{\Gamma}^{\boldsymbol{x}}$ are coefficient matrices defined in (3.13) and (3.14), respectively. Since the function $\Psi(\cdot)$ is an explicit analytical function, these Jacobians can be exactly computed using the algorithmic differentiation (AD) technique. This technique will be further discussed in Section 4.3.3.2. The resulting affine model $\overline{\Psi}(\cdot)$ provides a computationally efficient approximation for optimization-based control design, capturing the essential SiMn dynamics within a small neighborhood of the operating point.

3.4 Open-loop system analysis based on models

In this section, we introduce four-dimensional (4D) visualizations as a tool for open-loop analysis of the SiMn electrical system. These visual representations are designed to provide deeper insight into the complex electrical behavior of the SiMn furnace, which motivates optimization-based control design efforts. Furthermore, it can be used to

validate the developed mathematical models by comparing simulated behavior with historical operational data.

This analysis builds upon the mathematical framework developed in Section 3.3, which provided the relationships and models within the SiMn electrical system. Specifically, we leverage the formulation capturing the dependency between the transformation ratio, secondary impedance and tap changer position presented in (3.2), (3.7) and (3.8); the linear approximation model of electrode-process impedance formulated in (3.13) and (3.14); the steady state output models for transformer active power and electrode current magnitude derived in (3.55) and (3.37), respectively. Together, these models provide an analytical framework for simulating the performance of the SiMn electrical system, thereby facilitating open-loop analysis, which is usually unrealistic to conduct in real-time operation.

Given the mathematical framework, we have simulated and visualized the predicted electrical outputs, i.e., transformer active power $\boldsymbol{p}^{\boldsymbol{s}} \in \mathbb{R}^3$ and electrode current magnitude $|\boldsymbol{i}^{\boldsymbol{e}}| \in \mathbb{R}^3$, in Figure 3.8. This procedure involves simultaneously perturbing the control actuators across all three phases, i.e., tap changer positions $\boldsymbol{\tau} \in \mathbb{Z}_+^3$ and electrode positions $\boldsymbol{h} \in \mathbb{R}^3$, starting from a specific operating point of the furnace. The perturbations are applied within specific ranges around the actuators' operating points, e.g., ± 8 steps for tap positions and ± 50 cm for electrode heights. The considered operating point of the entire system is represented by the detailed variables in Table 3.4.

TABLE 3.4: SiMn electrical variables at specific operating point for open-loop analysis.

Vars	Numerical value	Unit
	Parameters	
$\boldsymbol{u}^{\boldsymbol{p}}$	$[63e^{\jmath 0^\circ},\ 63e^{\jmath 120^\circ},\ 63e^{-\jmath 120^\circ}]^\top$	(kV)
$\boldsymbol{z}$	$[525+\jmath 857.1,\ 525+\jmath 857.1,\ 525+\jmath 857.1]^\top$	(μΩ)
	Actuators	
$\boldsymbol{\tau}$	$[15,\ 15,\ 15]^\top$	(step)
$\boldsymbol{h}$	$[50,\ 50,\ 50]^\top$	(cm)
	Outputs	
$\boldsymbol{p}^{\boldsymbol{s}}$	$[8.46,\ 8.62,\ 8.81]^\top$	(MW)
$\lvert\boldsymbol{i}^{\boldsymbol{e}}\rvert$	$[126.91,\ 128.12,\ 129.53]^\top$	(kA)

Electric values are considered at $f = 50\,\text{Hz}$.

In this circumstance, some might question why a reliable analysis of the actual SiMn furnace at COMILOG Dunkerque cannot be conducted instead of a model-based analysis. We will address this concern with the following explanation. First of all, this furnace is a production furnace, whose operation is delicate and the quality of the products depends on long-term process equilibrium. Therefore, furnace operation and production can not be put at risk for the sake of testing. The tests could only be conducted during the dead time of the operation, which does not reflect system behavior during the onload operation. Secondly, the SiMn furnace system operates in a continuous rather than batch process, which means it rarely stops during operation. As a result, there are far fewer opportunities to perform open-loop tests, aside from occasional stops for inspection or furnace maintenance. Lastly, even if we are allowed to test during active operation for a short period of time, it is still infeasible to isolate and investigate the effects because many variables vary considerably with the environment and are tightly coupled with uncertainty.

Therefore, model-based analysis provides a safe and systematic way to analytically explore electrical behavior without risk or limitations. It allows for a wide range of exploration over the operating conditions and perturbations that are not feasible to set up in a real furnace system. Moreover, this analysis can further facilitate the validation of the developed mathematical models, thereby enabling adjustments and improvements. The validation can be conducted by comparing simulation results with historical data collected from the plant under specific operating conditions within a limited range. This is a crucial step in establishing the credibility and reliability of the models' predictive capability.

The detailed visualizations are presented in Figure 3.8a and Figure 3.8b, where the first figure illustrates the influence of tap position deviations on transformer active power and electrode current magnitude, while the second one demonstrates the impact of electrode position deviations on the same electrical outputs. The four-dimensional visualizations display the three axes representing deviations in tap or electrode position for each phase, while the fourth dimension, the color gradient, captures the predicted output behavior for each phase.

In particular, the left plot of Fig. 3.8a illustrates that the transformer power (e.g., P_a^s) is not only directly affected by the tap position of the corresponding phase (τ_a), but also indirectly influenced by the tap positions of other phases (τ_b, τ_c). As indicated by the

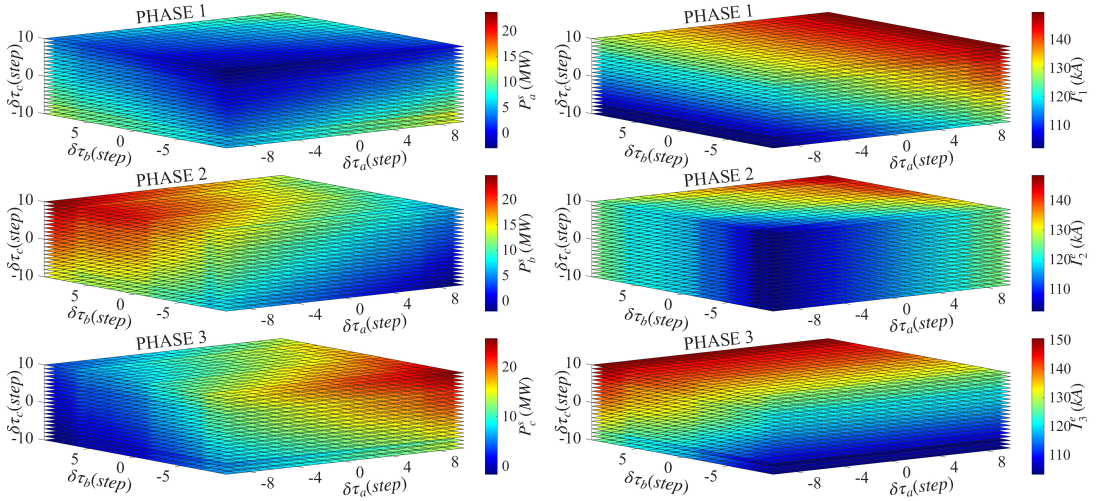

(A) Transformer powers (P_a^s, P_b^s, P_c^s) and electrode currents ($|i_1^e|$, $|i_2^e|$, $|i_3^e|$) with respect to the movement of three separate transformer taps ($\delta\tau_a, \delta\tau_b, \delta\tau_c$).

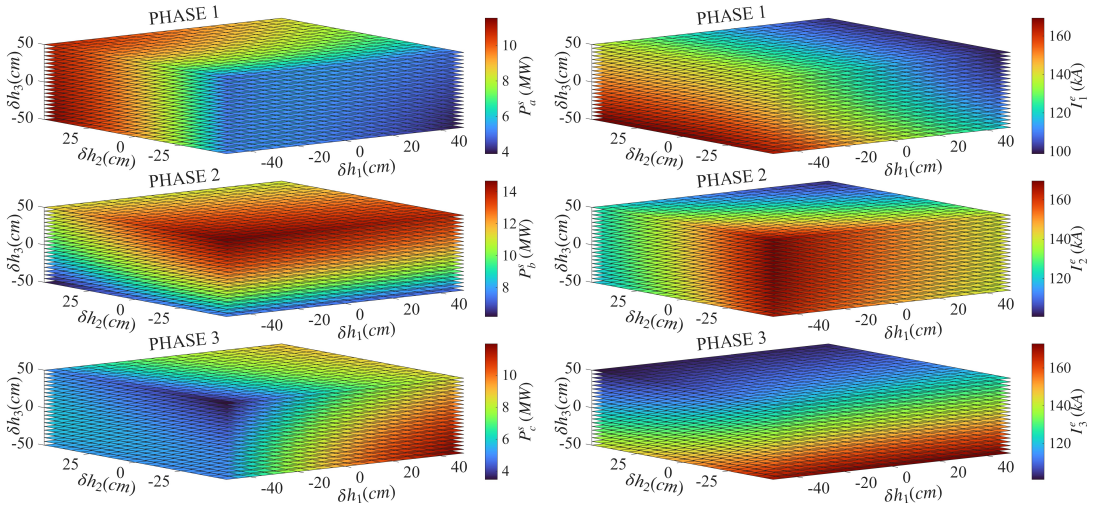

(B) Transformer powers (P_a^s, P_b^s, P_c^s) and electrode currents ($|i_1^e|$, $|i_2^e|$, $|i_3^e|$) with respect to the movement of three separate electrodes ($\delta h_1, \delta h_2, \delta h_3$).

FIGURE 3.8: Dynamic response of transformer power (left) and electrode current (right) to control signal variations. The 4D plots demonstrate the effect of control action, i.e., transformer tap variation and electrode displacement on secondary active power of the transformer and the current magnitude in the electrode.

color gradient, variations in transformer tap positions across phases affect transformer power. The electrode current is also influenced by tap positions, as shown in the right plot of Fig. 3.8a. However, the electrode intensity in one phase (e.g., I_1^e) depends on its own tap position (τ_a) and the preceding phase (τ_c) but not the following phase (τ_b), as illustrated by the constant color along the axis of independent tap (y-axis).

In more detail, each plot in the four-dimensional figures indicates the correlation between three inputs and a single output. We can observe that transformer power (e.g., P_a^s) is proportional to the tap positions of the corresponding and the following phase ($\propto \tau_a, \tau_b$), while inversely proportional to the tap position of the previous phase ($\propto 1/\tau_c$). As shown in the first left figure, extreme blue (minimum P_a^s) is located at the minimum of the xy-axis ($\delta\tau_a, \delta\tau_b$) and maximum of the z-axis ($\delta\tau_c$). In contrast, the electrode current (e.g., I_1^e) is proportional to the tap positions of the corresponding phase and the previous phase ($\propto \tau_a, \tau_c$) while remaining constant in the other phase of the three-phase rotation.

Similarly, the influence of electrode movement can be observed in Fig. 3.8b, where the electrical behaviors of control outputs exhibit distinct behaviors. As indicated by the left plots, the transformer power (e.g., P_a^s) varies inversely with the electrode displacement of the corresponding phase ($\propto 1/h_1$) and proportionally with the subsequent phase ($\propto h_2$), while it tends to remain approximately constant with respect to the preceding phase. Regarding electrode current (e.g., I_1^e), the impact of electrode displacement varies, as shown in the right plots. The current shows minimal sensitivity to the electrode movement of the subsequent phase, but is inversely related to the displacements of the corresponding and the preceding phase($\propto 1/h_1$, $1/h_3$). The inverse relationship within one phase can be interpreted as an inverse relationship between current and impedance.

To conclude, this analysis offers a practical solution for analyzing complex interactions within the SiMn furnace system while ensuring safety and reliability. The observations highlight the complex interdependencies among tap positions, electrode positions, and system outputs across three phases of the EAF system, providing a broader and more intuitive explanation of the interaction problem raised in [Barker and Stewart, 1980]. Moreover, these highlight the limitations of decoupled control strategies, in which each phase is controlled independently without considering interactions with other phases, emphasizing the need for coordinated control strategies in EAF operations, which will be developed in the following chapters.

3.5 Concluding remarks

This chapter introduced an electrical model of a submerged-arc furnace based on a particular 34MW SiMn furnace in Dunkerque, France. The distinct difference in the

modeling of this work compared to the existing literature, e.g., Barker [1980], Stewart [1981], Valderhaug [1992], Boulet et al. [2003], Balan et al. [2007] lies in the comprehensive consideration of the entire electrical system, including tap changers and their associated elements in the transformer circuit and the absence of the arc in the electrode-process circuit. Regarding the model formulation, we have developed more details of the empirical relationships between the actuators and the electrical parameters. The steady-state models are also well-formulated as explicit analytical functions of the circuit parameters.

According to the specific characteristics of the SiMn furnace and the objectives of the optimization-based control design, we also had the following assumptions in this chapter:

1. The electrical system operates at 50 Hz and harmonics are negligible.
2. Transmission line impedances are considered constant and are not affected by the electrode movements.
3. Electrode-process impedances are quasi-static over minor deviations during regular operation, so a local approximation around the operating point is valid.
4. Mutual inductances among the electrodes are neglected.
5. Look-up table data for transformer ratios provided by the manufacturer are smooth and match actual transformer characteristics.

Based on the assumptions above, to obtain the mathematical formulation, we have:

i) represented the three-phase electrical circuit of the SiMn furnace by the lumped impedance equivalent circuits that explicitly model the transformer secondary side, transmission lines, electrodes and molten bath.

ii) combined B-splines interpolation for look-up tables, robust regression on historical data and backward difference finite on real-time measurements data to build the differentiable relationships between the actuators (tap and electrode) and the electrical parameters (transformer ratio, secondary impedance, etc).

iii) derived the steady-state electrical models based on the equivalent circuit analysis, providing explicit analytical relationships between the electrical outputs (transformer power, secondary and electrode currents) and the system parameters.

Last but not least, based on the obtained analytical models, we generate four-dimensional visualizations by simultaneously perturbing the tap positions and the electrode heights around a chosen operating point. The resulting plots show that changes in tap positions or electrode heights affect not only their own phases but also those of the other phases, producing phase-coupled, nonlinear responses in transformer powers and electrode currents. The result motivates coordinated control strategies developed in the next chapter.

Chapter 4

SiMn control design and optimization tools

This chapter presents the operational control problems and simulation environment that will be used to design and evaluate advanced control strategies for a three-phase silico-manganese (SiMn) submerged arc furnace (SAF). The goal is to provide a clear view of the operational objectives, the practical constraints that a real plant requires, along with the simulation structure utilized to reproduce those conditions. Moreover, the chapter introduces the optimization-based control techniques, including MPC formulations, MIP methods and the numerical tools employed to implement and solve the resulting optimal control problems.

For SAF, the control objectives vary depending on the control strategies and involve:

1. Managing the active power delivered to the furnace.
    a) The total power is controlled by using the same tap positions in three phases.
    b) The phase powers are controlled by adjusting separately the three tap positions.
2. Regulating the distribution of electrical power dissipation in the furnace.
    a) The phase currents are regulated by the movements of the three electrodes.
    b) The phase resistances are controlled by the movements of the three electrodes.

The tap changer positions are constrained to be discrete variables with a minimized number of switches during the operation to avoid the "hunting problem". The control system must ensure that the operational constraints, including physical conditions of the actuators and electrical constraints of the circuit variables, are satisfied to maintain safe and efficient operation.

Note that in such an application, it is not easy to implement the practical test on a real system, especially an industrial-scale furnace. Consequently, we leverage a developed software-in-the-loop (SIL) simulation environment to support the design and evaluation of the proposed control strategies. This environment has been built based on a high-fidelity electrical model of the SAF, which captures the essential operational events and disturbances of the furnace. Herein, we also present the structure of the SIL simulation environment briefly.

Finally, we summarize the optimization-based control tools central to the advanced strategies presented in the following chapters.

4.1 Operational requirements

In this first section, we present control objectives and practical constraints that a real SiMn SAF plant requires.

4.1.1 Control objective

The main objective of the electrical control system in a SAF is to stabilize key electrical variables according to predefined setpoints. As discussed in Section 2.1.3, its control strategy is typically classified into managing the active powers delivered to the furnace or regulating the distribution of energy dissipation via the electrode tip's positions. As a result, we focus on two primary control strategies, i.e., power and current that can be operated in a decentralized or centralized framework as indicated in Section 2.3.2.

4.1.1.1 Power control

In the classical control techniques, power control usually refers to controlling the powers of the three phases combined; thus, the tap positions are always treated similarly across phases. In this work, we extend this power control to multiple dimensions, i.e., controlling the active power in each phase independently, with the tap changers are allowed to be adjusted individually. Particularly, we focus on the active power control at the secondary side of the furnace transformer, $\boldsymbol{p}^{\boldsymbol{s}} \in \mathbb{R}^3$, defined in (3.55).

This new idea provides more flexibility in managing the power distribution in the furnace. On one hand, it enables the separated power regulation of each phase under unbalanced loads, while still accounting for the interaction effect between the phases. On the other hand, it allows for any desired degree of restriction on balanced secondary transformer voltages by incorporating a balancing constraint on the tap variables.

Given the predefined active power reference in three phases, defined by a vector $\boldsymbol{p}^{\boldsymbol{s},\text{ref}} \triangleq [P_a^{s,\text{ref}}, P_b^{s,\text{ref}}, P_c^{s,\text{ref}}]^\top \in \mathbb{R}^3$, we aim to stabilize the active powers around this reference. More specifically, we minimize the deviations of $\boldsymbol{p}^{\boldsymbol{s}}$ from $\boldsymbol{p}^{\boldsymbol{s},\text{ref}}$ at each sampling time k:

$$J_P(k) = Q_a^P \Big[P_a^{\boldsymbol{s}}(k) - P_a^{s,\text{ref}}(k)\Big]^2 + Q_b^P \Big[P_b^{\boldsymbol{s}}(k) - P_b^{s,\text{ref}}(k)\Big]^2 + Q_c^P \Big[P_c^{\boldsymbol{s}}(k) - P_c^{s,\text{ref}}(k)\Big]^2, \quad (4.1)$$

where Q_a^P, Q_b^P and $Q_c^P \in \mathbb{R}$ are weighting coefficients that determine the relative importance of power cost in each phase.

4.1.1.2 Current control

In addition to the power control, we consider the regulation of power dissipation in the molten bath or, equivalently, the electrode tip's position control. As discussed in Section 2.1.3.2, this can be achieved implicitly via the electrode current regulation or resistance control, which can be alternative to each other under the power control. Herein, we focus on the electrode current magnitude control.

In the literature, three-phase current magnitudes $|\boldsymbol{i}^{\boldsymbol{e}}| \in \mathbb{R}^3$, defined in (3.37), are usually controlled but in a decoupled manner, i.e., current in each phase is regulated independently without considering the interaction between phases. This approach can lead to some

sub-optimal performance, e.g., longer settling times and potential instability during the steady-state period. This is one of the main reasons why optimization-based approaches are proposed to overcome this limitation. Similar to power control, we introduce a cost function of the deviations of current magnitude $|\boldsymbol{i}^{\boldsymbol{e}}|$ from its predefined reference in three phases $\boldsymbol{I}^{\boldsymbol{e},\text{ref}} \triangleq [I_1^{e,\text{ref}}, I_2^{e,\text{ref}}, I_3^{e,\text{ref}}]^\top \in \mathbb{R}^3$, as follows:

$$J_I(k) = Q_1^I\Big[|i_1^e(k)| - I_1^{e,\text{ref}}(k)\Big]^2 + Q_2^I\Big[|i_2^e(k)| - I_2^{e,\text{ref}}(k)\Big]^2 + Q_3^I\Big[|i_3^e(k)| - I_3^{e,\text{ref}}(k)\Big]^2, \quad (4.2)$$

where Q_1^I, Q_2^I and $Q_3^I \in \mathbb{R}$ are weighting coefficients that determine the relative importance of intensity cost in each phase. The interconnection of current magnitude between phases is taken into account by the prediction models that define $\boldsymbol{i}^{\boldsymbol{e}}$.

4.1.1.3 Combined power and intensity control

Instead of controlling power and current separately, we consider a combined control objective that integrates both objectives. In particular, we propose the control objective that stabilizes the active power at the secondary side of the transformer and regulates the electrode current magnitude simultaneously, both applied in three phases. This approach allows for coordinated management of the electrical variables, ensuring that both the power delivered to the furnace and the distribution of current among the electrodes are optimized simultaneously. As a consequence, we design the following cost function, combined from both objective functions (4.1) and (4.2), thus we obtain:

$$J_{PI}(k) = \underbrace{\left\|\boldsymbol{p}^{\boldsymbol{s}}(k) - \boldsymbol{p}^{\boldsymbol{s},\text{ref}}(k)\right\|^2_{\mathbf{Q}^{\boldsymbol{P}}}}_{\text{Power deviations}} + \underbrace{\left\||\boldsymbol{i}^{\boldsymbol{e}}(k)| - \boldsymbol{I}^{\boldsymbol{e},\text{ref}}(k)\right\|^2_{\mathbf{Q}^{\boldsymbol{I}}}}_{\text{Intensity deviations}} w \quad (4.3)$$

with weighting matrices $\mathbf{Q}^{\boldsymbol{P}} \in \mathbb{R}^{3\times3} \succeq 0$ and $\mathbf{Q}^{\boldsymbol{I}} \in \mathbb{R}^{3\times3} \succeq 0$ defined as:

$$\mathbf{Q}^{\boldsymbol{P}} = \begin{bmatrix} Q_a^P & 0 & 0 \\ 0 & Q_b^P & 0 \\ 0 & 0 & Q_c^P \end{bmatrix}, \quad \mathbf{Q}^{\boldsymbol{I}} = \begin{bmatrix} Q_1^I & 0 & 0 \\ 0 & Q_2^I & 0 \\ 0 & 0 & Q_3^I \end{bmatrix}.$$

4.1.2 Tolerance ranges

In practice, precise reference tracking of electrical variables may not always be necessary. Therefore, we prefer to avoid unnecessary control actions as long as the controlled variables are close enough to their reference, thus preventing the chattering phenomenon and enhancing the control stability. To achieve this, we define different tolerance ranges (deadbands) around the setpoint corresponding to control objectives in Section 4.1.1, in which the control actions are not required. Specifically, we have tolerance ranges for:

- Transformer active power control: $\left[\boldsymbol{p}^{\boldsymbol{s},\text{ref}} - \boldsymbol{\epsilon}^{\boldsymbol{p}}, \boldsymbol{p}^{\boldsymbol{s},\text{ref}} + \boldsymbol{\epsilon}^{\boldsymbol{p}}\right]$,
- Electrode current magnitude control: $\left[\boldsymbol{I}^{\boldsymbol{e},\text{ref}} - \boldsymbol{\epsilon}^{\boldsymbol{i}}, \boldsymbol{I}^{\boldsymbol{e},\text{ref}} + \boldsymbol{\epsilon}^{\boldsymbol{i}}\right]$,

where $\boldsymbol{\epsilon}^{\boldsymbol{p}} \in \mathbb{R}^3$ and $\boldsymbol{\epsilon}^{\boldsymbol{i}} \in \mathbb{R}^3$ are vectors defining tolerances for power and current magnitude control, respectively in three phases. The values of these tolerance vectors are selected based on the specific operational requirements of the furnace plant.

4.1.3 Hunting problem

In addition to the main control objectives that stabilize electrical variables in the furnace under predefined references, it is of great importance to mitigate a so-called *hunting problem*[1], i.e., reduce the number of switching operations performed by on-load tap changers (OLTCs) devices in the transformers [Smith et al., 2003, Maataoui et al., 2023].

As is known, power regulation is indispensable in the EAF operation. To this end, OLTCs are employed to allow for the addition or subtraction of steps from the winding as shown in Figure 3.3, adjusting the transformer voltage ratio, thus the power delivered to the furnace. As a result, OLTCs are frequently switched up or down in discrete steps to change power level or maintain power stability under varying loads in the furnace bath. [Redfern and Handley, 2001], which can lead to an undesired hunting phenomenon.

[1]The term "hunting" describes an oscillatory behavior where the tap changer hunts for correct position.

The *hunting phenomenon* in transformers equipped with OLTCs refers to the frequent and often unnecessary switching of tap positions. This issue typically arises from overly sensitive regulation and poorly coordinated control strategies.

Such frequent fluctuations can lead to several negative consequences for the transformers. For instance, it not only undermines power stability but also accelerates mechanical wear and electrical degradation of tap changer components. Over time, this leads to reduced lifespan of the transformers, early maintenance, or even failure in the transformers, thus increasing operational costs. Moreover, excessive tap operations can propagate disturbances across the electrical network, affecting power quality.

With MPC framework, we can effectively mitigate the hunting problem by incorporating in the control objective, a quadratic cost $J_\tau(k)$, given the tap deviation variables in three phases $\boldsymbol{\delta\tau} \triangleq [\delta\tau_a, \delta\tau_b, \delta\tau_c]^\top$ at every time step k, as follows:

$$J_\tau(k) = \left\| \boldsymbol{\delta\tau}(k) \right\|^2_{\mathbf{R}(k)}. \tag{4.4}$$

This quadratic cost penalizes tap switching in each phase through a time-varying weighting matrix $\mathbf{R}(k) \in \mathbb{R}^3$. This matrix is designed to appropriately adapt to the furnace operating conditions, so that the frequent switching operations of the tap changers are discouraged.

In particular, we introduce in Algorithm 4.1, the adaptive weight tuning strategy to adjust $\mathbf{R}(k)$. This strategy employs a sigmoidal function to periodically change the penalty weight based on the switching history of the tap changer positions and the accumulated tracking errors of the control output. The algorithm runs independently of the optimization, with a faster sampling time than the control sampling time.

From Algorithm 4.1, we briefly explain the dual-mode technique used, which is handled by an if-else statement. In the first mode, when a sequence of switching finishes, i.e., $\boldsymbol{\delta\tau}^*(k+1)$ is non-zero and $\boldsymbol{\delta\tau}^*(k)$ become null, the algorithm restarts the error accumulator $\mathbf{E}(k)$ and resets the weight $\lambda(k) \in \mathbb{R}$ to the maximum $\lambda_{\max} \in \mathbb{R}$ to force the taps hold. Otherwise, when no switching occurs, it creates a vector of tracking error $\mathbf{e}(k) \in \mathbb{R}^6$, which is then integrated over sampling time Δ_t into the accumulator $\mathbf{E}(k)$. Depending on the specific control strategy, either power control in Section 5.2.2 or coordinated power-current control in Section 6.1.2, the dimension of the tracking error

$\mathbf{e}(k)$ is different and so is $\mathbf{E}(k)$. In case of power and current control, the error vector is appropriately scaled by a calibrated vector $\boldsymbol{\kappa} \in \mathbb{R}^6$ such that it balances the relative error between power and current tracking with respect to their tolerances, i.e., $\boldsymbol{\epsilon}^{\boldsymbol{p}}$ and $\boldsymbol{\epsilon}^{\boldsymbol{i}}$. The accumulated error vector $\mathbf{E}(k)$ is then converted into the weight value $\lambda(k)$ through the logistic function:

$$\lambda(k) = \frac{\lambda_{\max}}{1 + \exp\left[\underbrace{\frac{10\mu}{\lambda_{\max}}}_{k_{log}}\left(\|\mathbf{E}(k)\|_\infty - \frac{\lambda_{\max}}{\nu}\right)\right]}. \tag{4.5}$$

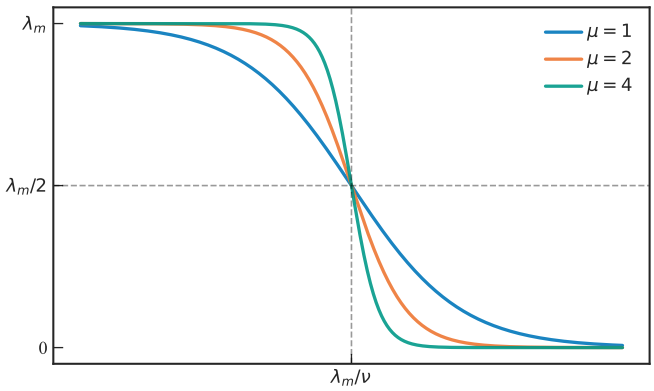

FIGURE 4.1: Logistic function (4.5) behavior based on $\|\mathbf{E}(k)\|_\infty$.

The logistic weighting function ensures smooth decreasing transitions from the upper bound penalty $\lambda_{\max}$, with a logistic growth rate determined by $k_{log} = 10\mu/\lambda_{\max}$ and exponent computed based on the maximum accumulated error in $\mathbf{E}(k)$. The parameter μ governs the steepness of the transition between the lower and upper bounds, determining the decreasing rate of the weight $\lambda(k)$. Whereas, ν influences the amount of the accumulated error, at which the weight $\lambda(k)$ decreases to half of its maximum value $\lambda_{\max}$. This behavior is illustrated through Fig. 4.1.

Given the value of $\lambda(k)$ from the previous step of the Algorithm 4.1, we construct a diagonal matrix $\mathbf{R}(k) \triangleq \text{diag}(\lambda(k), \lambda(k), \lambda(k)) \in \mathbb{R}^{3\times3}$ with uniform weights across three dimensions where each element is ensured to be positive and bounded by the value $\lambda_{\max}$. The penalty is periodically updated at every time step k for the next optimization.

Algorithm 4.1: Adaptive weight tuning

Input: Optimal variable $\boldsymbol{\delta\tau}^*(\cdot|k)$, parameters $\lambda_{\max}, \mu, \nu, \boldsymbol{\kappa}$ in (4.5)
Output: Weighting matrix $\mathbf{R}(k)$ for cost function (4.4)

Function `LogisticWeight(`$\mathbf{E}, \lambda_{\max}, \mu, \nu$`):`

Compute logistic rate: $k_{log} \leftarrow \dfrac{10\mu}{\lambda_{\max}}$

Calculate exponent: $a \leftarrow k_{log}\Big(\|\mathbf{E}\|_\infty - \dfrac{\lambda_{\max}}{\nu}\Big)$

return $\dfrac{\lambda_{\max}}{1+\exp(a)}$

if $\exists u \in \boldsymbol{\delta\tau}^*(k-1) : u \neq 0$ ***and*** $\exists u \in \boldsymbol{\delta\tau}^*(k) : u = 0$ **then**

Initialize error accumulator: $\mathbf{E}(k) \leftarrow \mathbf{0}$

Reset to maximum weight: $\lambda(k) \leftarrow \lambda_{\max}$

else

Compute calibrated tracking error vector:

$$\mathbf{e}(k) \leftarrow \begin{cases} \Big[\boldsymbol{p}^s(k) - \boldsymbol{p}^{s,\mathrm{ref}}(k)\Big] & \text{in Section 5.2.2} \\ \boldsymbol{\kappa} \odot \Big[\boldsymbol{p}^s(k) - \boldsymbol{p}^{s,\mathrm{ref}}(k),\ |\boldsymbol{i}^e(k)| - \boldsymbol{I}^{e,\mathrm{ref}}(k)\Big]^\top & \text{in Section 6.1.2} \end{cases}$$

Accumulate errors over time: $\mathbf{E}(k) \leftarrow \mathbf{E}(k-1) + \Delta t \cdot \mathbf{e}(k)$

Update adaptive weight: $\lambda(k) \leftarrow$ `LogisticWeight` $(\mathbf{E}(k), \lambda_{\max}, \mu, \nu)$

end

return $\mathbf{R}(k) \leftarrow diag(\lambda(k), \lambda(k), \lambda(k))$

4.1.4 Operational constraints

Constraint handling is crucial in EAF operation due to the presence of various physical and electrical limitations of the system. To prepare for the MPC control design, we consider a set of practical constraints that must be satisfied during the control process.

4.1.4.1 Tap positions and variations

The tap changer of the furnace transformer is subject to a limited operational range, depending on the mechanical configuration of the transformer design. As a consequence, tap positions are constrained within a bounded range. Moreover, depending on the sampling time, we have restrictions on the tap variations between consecutive time steps. Most importantly, tap positions are discrete variables by their nature as indicated in

Section 3.2.1, thus tap deviations must be integer values:

$$\boldsymbol{\tau}_{\mathbf{lb}} \leq \boldsymbol{\tau}(k) \leq \boldsymbol{\tau}_{\mathbf{ub}}, \tag{4.6}$$

$$-\boldsymbol{\Delta\tau}_{\mathbf{max}} \leq \boldsymbol{\delta\tau}(k) \leq \boldsymbol{\Delta\tau}_{\mathbf{max}}, \tag{4.7}$$

$$\boldsymbol{\delta\tau}(k) \in \mathbb{Z}^3, \tag{4.8}$$

where $\boldsymbol{\tau}_{\mathbf{lb}}$, $\boldsymbol{\tau}_{\mathbf{ub}} \in \mathbb{Z}^3$ are the lower and upper bounds of tap positions, respectively. $\boldsymbol{\Delta\tau}_{\mathbf{max}} \in \mathbb{Z}^3$ is the maximum allowable tap variation between two consecutive steps.

4.1.4.2 Tap balancing

To maintain voltage symmetry and avoid phase imbalance across the three phases in the transformers, we can constrain the differences in tap positions between any two phases of the transformer within a specified tolerance:

$$\Big\| \big[(\tau_a(k) - \tau_b(k)),\ (\tau_b(k) - \tau_c(k)),\ (\tau_c(k) - \tau_a(k)) \big] \Big\|_\infty \leq \gamma, \tag{4.9}$$

where, $\| \cdot \|_\infty$ denotes the infinity norm. The constant value $\gamma \in \mathbb{R}$ is the maximum allowable tap difference between any two phases at time k. So, this formulation allows us to flexibly manage the balance in the transformer by adjusting the value of γ. For instance, setting $\gamma = 0$ enforces a strict balance across phases, while a larger value of γ does the opposite, accommodating unbalanced load conditions.

4.1.4.3 Electrode holder positions and displacements

The vertical positions of the electrode holders are limited by the mechanical range of the hydraulic system, specifically the stroke length of the hydraulic hoists as indicated in Section 2.2.1. Additionally, the displacement between two consecutive time steps is restricted by the maximum speed of the hydraulic system. Consequently, we have the constraints on electrode holder positions and their displacement range as follows:

$$\boldsymbol{h}_{\mathbf{lb}} \leq \boldsymbol{h}(k) \leq \boldsymbol{h}_{\mathbf{ub}}, \tag{4.10}$$

$$-\boldsymbol{\Delta h}_{\mathbf{max}} \leq \boldsymbol{\delta h}(k) \leq \boldsymbol{\Delta h}_{\mathbf{max}}, \tag{4.11}$$

where, $\boldsymbol{h}_{\mathbf{lb}}$, $\boldsymbol{h}_{\mathbf{ub}} \in \mathbb{R}^3$ are the lower and upper bounds of electrode holder positions, respectively and $\boldsymbol{\Delta h}_{\mathbf{max}} \in \mathbb{R}^3$ is the maximum allowable electrode displacement.

4.1.4.4 Operational impedance

Impedances of the electrode and molten bath should be kept within acceptable ranges to ensure safe and proper operations. In particular, we impose constraints on electrode-bath resistances and reactances with their physical limits $\boldsymbol{r}_{\mathbf{lb}}$, $\boldsymbol{r}_{\mathbf{ub}}$, $\boldsymbol{x}_{\mathbf{lb}}$ and $\boldsymbol{x}_{\mathbf{ub}} \in \mathbb{R}^3$:

$$\boldsymbol{r}_{\mathbf{lb}} \leq \boldsymbol{r}(k) \leq \boldsymbol{r}_{\mathbf{ub}}, \tag{4.12}$$

$$\boldsymbol{x}_{\mathbf{lb}} \leq \boldsymbol{x}(k) \leq \boldsymbol{x}_{\mathbf{ub}}, \tag{4.13}$$

4.1.4.5 Electrical safety

In the furnace operation, no matter what control strategy is applied, essential electrical variables in the circuit, e.g., powers and currents, must always be kept within the safety limits to avoid any undesired consequences. In classical control approaches, this is not addressed within the control algorithm itself but rather by the external mechanism, which often leads to suboptimal performance, as discussed in Section 1.1.3. As a result, in the MPC design, we explicitly account for these constraints by defining bounds on *secondary transformer active power*, *secondary transformer current magnitude* and *electrode current magnitudes*, all of which are critical variables to ensure practical safety for furnace operation.

$$\boldsymbol{p}^{\boldsymbol{s}}_{\mathbf{lb}} \leq \boldsymbol{p}^{\boldsymbol{s}}(k) \leq \boldsymbol{p}^{\boldsymbol{s}}_{\mathbf{ub}}, \tag{4.14}$$

$$\boldsymbol{I}^{\boldsymbol{s}}_{\mathbf{lb}} \leq |\boldsymbol{i}^{\boldsymbol{s}}(k)| \leq \boldsymbol{I}^{\boldsymbol{s}}_{\mathbf{ub}}, \tag{4.15}$$

$$\boldsymbol{I}^{\boldsymbol{e}}_{\mathbf{lb}} \leq |\boldsymbol{i}^{\boldsymbol{e}}(k)| \leq \boldsymbol{I}^{\boldsymbol{e}}_{\mathbf{ub}}, \tag{4.16}$$

where $\boldsymbol{p}^{\boldsymbol{s}}_{\mathbf{lb}}$, $\boldsymbol{p}^{\boldsymbol{s}}_{\mathbf{ub}} \in \mathbb{R}^3$ are the lower and upper bounds of transformer active power, respectively. Similarly, $\boldsymbol{I}^{\boldsymbol{s}}_{\mathbf{lb}}$, $\boldsymbol{I}^{\boldsymbol{s}}_{\mathbf{ub}} \in \mathbb{R}^3$ are the lower and upper bounds of transformer current magnitude at the secondary side. Finally, $\boldsymbol{I}^{\boldsymbol{e}}_{\mathbf{lb}}$, $\boldsymbol{I}^{\boldsymbol{e}}_{\mathbf{ub}} \in \mathbb{R}^3$ are the lower and upper bounds of electrode current magnitude. All of them are constant variables and are provided in accordance with the operational requirements of the plant.

4.2 Validation frameworks

This section outlines a validation framework used to assess the effectiveness of our control designs. We first define a set of performance metrics to quantify control strategy performance. Next, we provide a description of a high-fidelity simulation environment that replicates the behavior of an industrial SAF. This allows us to test and validate the proposed strategies under realistic operating conditions.

4.2.1 Performance metrics

Herein, we define in Table 4.1 a set of performance metrics that will be used to evaluate and compare the effectiveness of different control strategies applied to the SAF, which will be demonstrated in Chapter 5 and Chapter 6.

TABLE 4.1: Definitions of the performance metrics used for evaluation.

Metric	Description	Unit
Reference Deviation		
RPD	Reference Power Deviation	%
RCD	Reference Current Deviation	%
Outside Tolerance		
OPT	Outside Power Tolerance	%
OCT	Outside Current Tolerance	%
Input Effort		
Tap Switch	Number of tap switching operations	–
Controller Performance		
CVR	Constraint Violation Rate	%
CPU	Average CPU time	ms

These metrics can be divided into four main categories according to requirements on different aspects, i.e., reference tracking performance, i.e., tracking accuracy and operational stability; ability to mitigate hunting problem, i.e., number of tap changer switches; and controller performance, i.e., feasibility and computational efficiency. Accordingly:

1. **Reference Deviation** measures the percentage of variation of the controlled variables from their predefined setpoints, as defined in Section 4.1.1. Particularly,

they are reserved to calculate the variation of active power (RPD) and electrode current magnitude (RCD), providing an indication of tracking accuracy. The metrics are computed for each phase using the following formulas:

$$\mathrm{RPD}_j \triangleq \sqrt{\frac{1}{N_s}\sum_{k=1}^{N_s}\left(\frac{P_j^s(k)-P_j^{s,\mathrm{ref}}(k)}{P_j^{s,\mathrm{ref}}(k)}\right)^2}, \quad j\in\{a,b,c\}, \tag{4.17}$$

$$\mathrm{RCD}_j \triangleq \sqrt{\frac{1}{N_s}\sum_{k=1}^{N_s}\left(\frac{|i_j^e(k)|-I_j^{e,\mathrm{ref}}(k)}{I_j^{e,\mathrm{ref}}(k)}\right)^2}, \quad j\in\{1,2,3\}, \tag{4.18}$$

2. **Outside Tolerance** represents the percentage of simulation time that the controlled variables are outside their specified tolerance bands, defined in Section 4.1.2. This includes metrics for power (OPT) and current (OCT), measuring the controller's ability to keep variables within acceptable limits. The detailed formulas are:

$$\mathrm{OPT}_j \triangleq \frac{1}{N_s}\sum_{k=1}^{N_s}\begin{cases}1 & \text{if } \left|P_j^s(k)-P_j^{s,\mathrm{ref}}(k)\right|>\epsilon_j^p\\ 0 & \text{otherwise}\end{cases}, \quad j\in\{a,b,c\}, \tag{4.19}$$

$$\mathrm{OCT}_j \triangleq \frac{1}{N_s}\sum_{k=1}^{N_s}\begin{cases}1 & \text{if } \left|\,|i_j^e(k)|-I_j^{e,\mathrm{ref}}(k)\,\right|>\epsilon_j^i\\ 0 & \text{otherwise}\end{cases}, \quad j\in\{1,2,3\}. \tag{4.20}$$

In these formulations, N_s is the total number of samples and j is the index of the electrical phase. To have the mean value of the metrics over three phases, we define $\mathrm{RPD_M}$ and $\mathrm{RCD_M}$ as:

$$\mathrm{RPD_M} \triangleq \frac{\mathrm{RPD}_a+\mathrm{RPD}_b+\mathrm{RPD}_c}{3}, \tag{4.21}$$

$$\mathrm{RCD_M} \triangleq \frac{\mathrm{RCD}_1+\mathrm{RCD}_2+\mathrm{RCD}_3}{3}. \tag{4.22}$$

For power control, because we also implement total-power control in Section 5.2.4 instead of just individual phase power, we define an additional metric $\mathrm{RPD_T}$ and

$\mathrm{OPT_T}$ to evaluate the tracking performance of the total power:

$$\mathrm{RPD_T} \triangleq \sqrt{\frac{1}{N_s}\sum_{k=1}^{N_s}\left(\frac{\sum_j P_j^s(k) - \sum_j P_j^{s,\mathrm{ref}}(k)}{\sum_j P_j^{s,\mathrm{ref}}(k)}\right)^2}, \tag{4.23}$$

$$\mathrm{OPT_T} \triangleq \frac{1}{N_s}\sum_{k=1}^{N_s}\begin{cases}1 & \text{if } \left|\sum_j P_j^s(k) - \sum_j P_j^{s,\mathrm{ref}}(k)\right| > \sum_j \epsilon_j^p \\ 0 & \text{otherwise}\end{cases}. \tag{4.24}$$

3. **Input Effort** focuses on the total number of tap changer switching operations (tap switch) during the simulation. This metric is crucial for evaluating the effectiveness of the controller in mitigating the hunting problem.

4. **Controller Performance** assesses the controller capability through:

   - CVR: stands for constraint violation rate, which represents the percentage of time operational constraints on a certain variable are violated. This metric is used to evaluate the safety and feasibility of the algorithm. For instance, we have:
   $$\mathrm{CVR}_{|i_a^s|} \triangleq \frac{1}{N_s}\sum_{k=1}^{N_s}\begin{cases}1 & \text{if } |i_a^s(k)| < I_{\mathrm{lb}}^s \text{ or } |i_a^s(k)| > I_{\mathrm{ub}}^s \\ 0 & \text{otherwise}\end{cases}.$$
   - CPU: indicates the average computation time required to solve the optimization problem at each control step. This is essential for assessing the real-time feasibility of the controller.

4.2.2 Software-in-the-loop (SIL) environment

For a safe and flexible validation of the proposed control approaches, we employ a software-in-the-loop (SIL) environment, developed by Eramet Ideas[2] (and improved by the candidate), which provides a primary platform before the real system deployment.

In general, the SIL simulator architecture is designed to mimic the real-world operation of an industrial SiMn SAF with the most fundamental features. This involves several subsystems, e.g., electrical, metallurgical, operational, measurement, actuator and control

[2]Eramet Ideas is the innovation center of the Eramet Group dedicated to the development and industrialization of innovative concepts in mining extractive metallurgy and recycling.

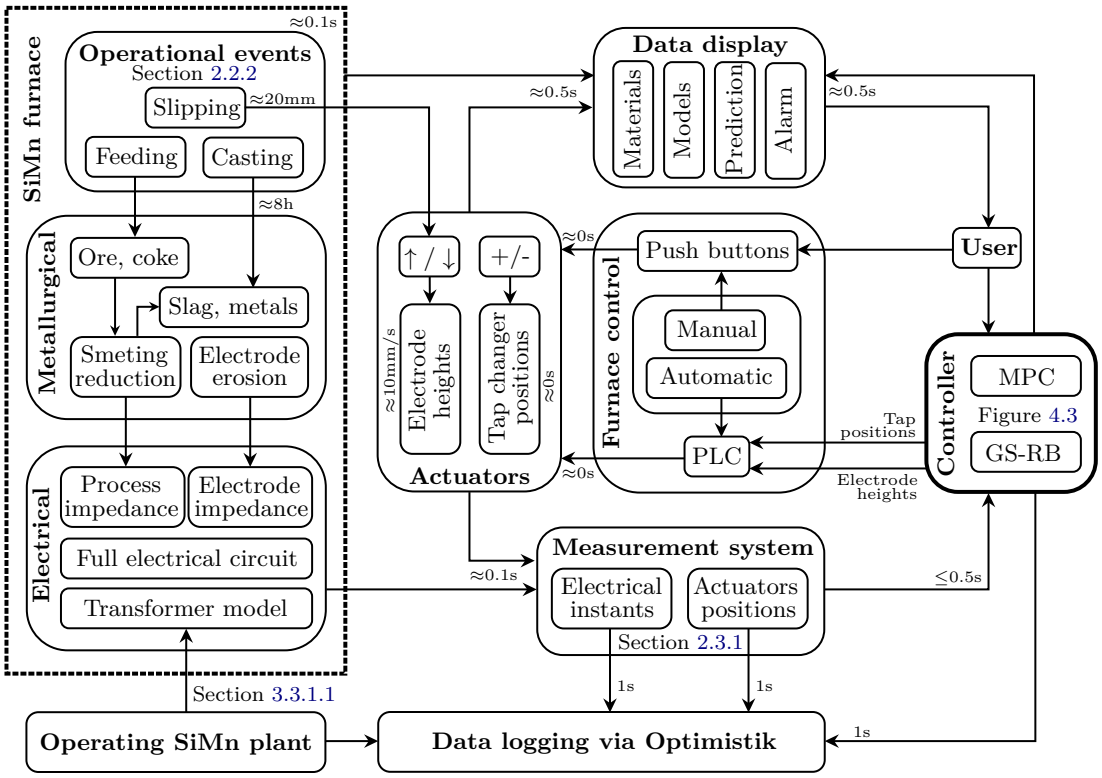

FIGURE 4.2: The SiMn software-in-the-loop (SIL) simulation architecture.

systems. The overall architecture of the SIL is illustrated in Figure 4.2, showing the interaction among subsystems within the furnace simulator and its connection with the control system. Particularly:

i) The metallurgical system represents the evolving chemical conditions inside the furnace. It models the quantity and distribution of burden materials such as ore, coke, slag, and molten metals. Moreover, it simulates smelting reduction and electrode erosion, which govern the process behavior. These characteristics affect the electrical impedances of the furnace, key parameters for electrical modeling.

ii) The electrical system provides a detailed representation of the SiMn electrical circuit, from the power grid to the furnace bottom. Unlike the simplified model used for control design in Section 3.3, this subsystem describes the full electrical circuits of the furnace, including more complex impedance in reaction zones and a dynamical electrode impedance model. Additionally, it incorporates a transformer

model, which is calibrated with measurements from the COMILOG Dunkerque plant.

iii) Operational system simulates real operational events such as electrode slipping, raw material feeding and casting of slag or molten metal. These events interact with the metallurgical and actuator systems, creating disturbances that propagate to the electrical system. Noticeably, the casting event is triggered every 8 hours, causing sudden changes in furnace load, followed by the feeding operations. The slipping event periodically occurs, raising the electrode holder positions by 0.2 mm each time. These allow us to assess the robustness of the control algorithms.

iv) Measurement system replicates the measurement devices used in the real furnace to record the measures of electrical values, e.g., currents, voltages, and actuator positions, i.e., electrode heights, tap positions in approximately 0.1 ms. These measurements provide real-time feedback to the control system. Also, all recorded data are systematically logged and stored on Optimistik[3] database.

v) The actuator system implements physical actions commanded by the furnace control system, including both manual and automatic modes through push buttons and the PLC system, respectively. Specifically, it simulates the electrode movements by raising or lowering the electrode heights. The electrode speed is limited to $10\,\mathrm{mm\,s^{-1}}$. It also handles the on-load transformer tap changers switching by increasing or decreasing the discrete tap positions with immediate response.

vi) The control system consists of a furnace control interface with both manual and automatic designs. While the manual mode allows users to directly manipulate the actuator system, i.e., switch transformer tap positions or adjust electrode heights, the automatic mode relies on the design of a dedicated controller module, that provides desired positions of the actuators to the PLC system. The design incorporates the MPC framework developed in this work and classical methods, which closely resemble the strategies employed in practice. This module interfaces with the measurement subsystem to acquire feedback signals every 0.5 ms. Moreover, it concurrently executes the selected algorithm and sends commands to the PLC system.

[3]Optimistik is an industrial data platform, allowing for the collection, contextualization and use of industrial data with ease and autonomy.

vii) Data monitoring includes the display and logging subsystems. The data display module is used to provide visualization in real-time for material states, electrical dynamics, control predictions, and alarms related to operational events or controller issues. The data logging is performed during the simulation and connected to the Optimistik platform. These allow us to flexibly observe real-time data or retrieve data run over days and weeks for observation and evaluation later on.

The SIL platform aims to replicate the SiMn furnace operation as closely as possible. However, the actual furnace operation itself remains a "black box" that has not been completely understood even by the experts in the field due to the complex metallurgical and thermal phenomena. As a result, this SIL platform focuses on essential functionalities with several assumptions as follows:

- Metallurgical processes are represented in a simplified manner and thermodynamic effects are disregarded. For example, the reduction of manganese oxides is modeled with constant parameters, without accounting for temperature gradients.
- Electrical model captures the primary dynamics of the furnace circuit but does not include all components present in the real system. For instance, mutual inductances between phases are neglected.
- Operational scenarios are modeled based on typical cases, which may not encompass all situations encountered in practice. For example, shutdowns for maintenance are not considered.
- Certain operational uncertainties and disturbances are not represented. Events such as explosions in the burden, electrode breakage, or gas eruptions can unexpectedly affect electrical variables but are excluded from the SIL simulator.
- Measurement system is assumed to be ideal; thus, noise and measurement errors are not fully modeled in the SIL simulator.
- Actuator behavior is simplified by assuming an ideal response to control commands, without considering mechanical delays. In reality, electrode movements are influenced by hydraulic system dynamics, and tap changers have switching delays with unknown intermediate positions during transitions.

Even though the SIL may not represent exactly the real furnace operation due to the above assumptions, it provides a comprehensive platform and more realistic conditions for testing and validating control strategies than simplified models.

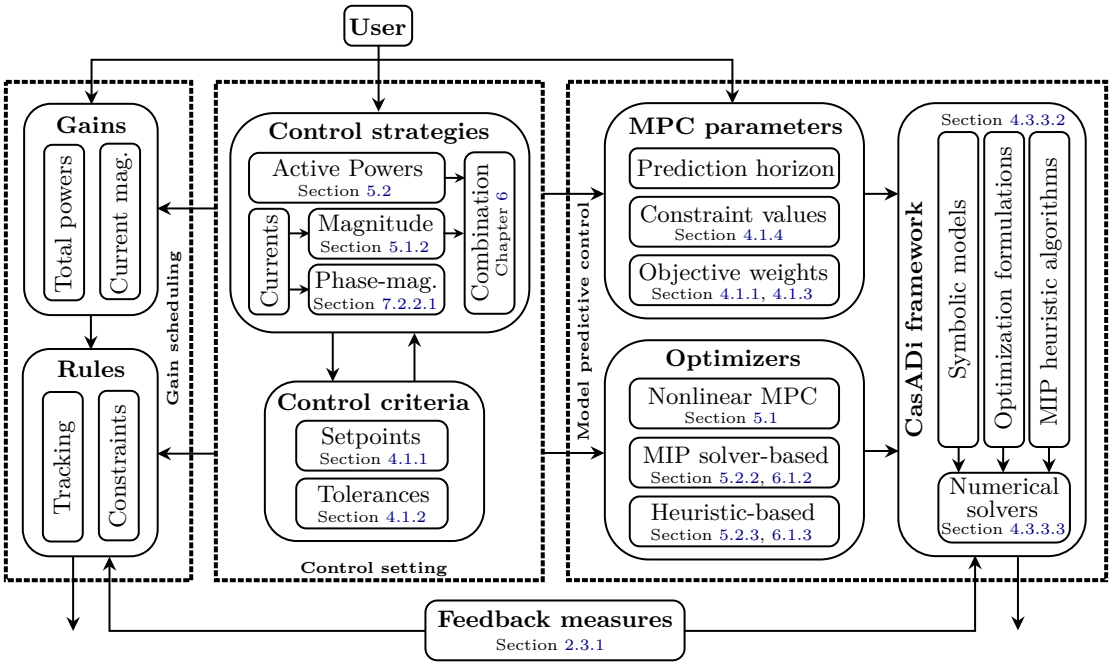

FIGURE 4.3: Architectural diagram of the automatic control interface for the SIL.

In this SIL setup, the design of the controller module in control system and its seamless integrations with the other subsystems represent one of the main contributions of this thesis. We present in Figure 4.3 its detailed configuration, which can be organized into:

- Control setting module provides multiple control strategy interfaces and the corresponding control criteria as discussed in Section 4.1.1. Moreover, this module allows users to switch between different control strategies and adapt control parameters at runtime, enabling flexible testing of various scenarios.
- Advanced controller module implements MPC framework with multiple control strategies studied in this thesis, i.e., active power control in Section 5.2; current magnitude in Section 5.1 or phase-magnitude control in future work; combined active power and current magnitude control in Section 6. It integrates the CasADi toolbox,

introduced in Section 4.3.3.2, to formulate and solve the corresponding optimization problems. This enables configuration of MPC parameters, i.e., prediction horizon, constraint, and objective values, as well as selection of appropriate optimizers for specific problem types, e.g., linear, nonlinear, and mixed-integer formulations.

- Classical controller module implements gain-scheduling (GS) approaches for electrode control combined with a simple rule-based (RB) algorithm to handle integer tap switching in the transformers. Constraints on maximum currents are also enforced through heuristic rules. This module imitates the classical controller currently used in the real system. In here, its integration serves as a benchmark for comparing the performance with our proposed MPC strategies; thus, its detailed design will not be focused on and will be briefly presented in the scenario setup subsection of each control strategy in Chapter 5 and Chapter 6.

The control system, illustrated by Figure 4.3, runs in a separate process from the simulator, allowing for real-time interaction with the other subsystems and parallel computation of optimal control actions alongside the furnace operation.

The SIL platform has been developed in Python and packaged in a user-friendly graphical interface to facilitate the interaction between users and the simulation environment. Moreover, it serves as a monitoring tool for real-time simulator operation, providing visualizations of various important subsystems, e.g., electrical system, metallurgical system, control system, etc. For instance, Figure 4.4 demonstrates a part of the dedicated SIL interface, focusing on the metallurgical system of the SiMn furnace.

4.3 Optimization-based control tools

Optimization-based control refers to a class of control techniques that use mathematical optimization to determine the best control actions to achieve some desired behaviors. In this work, we consider this terminology as a control strategy that solves an optimization criterion *online* while satisfying a set of constraints on the system dynamics and operational conditions, by the resolution techniques to compute the parameters of the control law [Murray et al., 2009, Faulwasser and Pannocchia, 2019]. The strategy offers a property

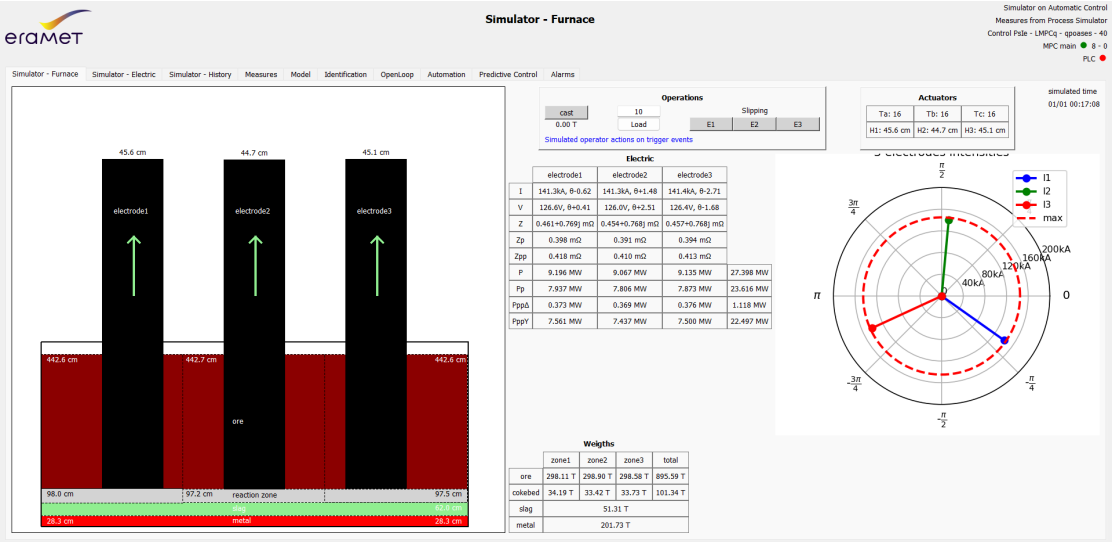

FIGURE 4.4: SIL SiMn furnace interface with a focus on metallurgical system.

so-called *optimality* which is generally equivalent to certain desired characteristics of the closed-loop system, e.g., stability, feasibility, reactivity, or robustness.

4.3.1 Model predictive control (MPC)

In the optimization-based control framework, *model predictive control*[4] (MPC), also called *receding horizon control*[5] (RHC), stands out as one of the most popular and powerful methods [Garcia et al., 1989, Qin and Badgwell, 2003, Rawlings et al., 2017]. MPC has existed since the 1970s Propoi [1963] and became widely used and matured in process industries around the late 1990s to early 2000s [Cutler, 2007, Richalet and O'Donovan, 2009, Wang et al., 2017, Vaccari et al., 2021, Grancharova et al., 2023, Horvath et al., 2025].

> MPC is not only an optimization-based control strategy, but also a model-based control technique and a feedback control algorithm.

[4] *predictive model* refers to the use of a model to predict the future behavior of the system.
[5] *receding horizon* comes from the fact that the prediction horizon, while typically fixed in length, recedes forward in time as the system evolves.

The core idea of MPC is to utilize an *explicit mathematical model* of a system to predict its future response over a *finite time horizon*. At each control interval, it attempts to optimize the predicted behavior, i.e., minimizing *control objectives* and satisfying *system constraints*, by computing an optimal sequence of control actions based on *current state measurements*. The first control action from this sequence is applied to the system. The process is then repeated at the next time step, with the horizon shifting forward in time.

4.3.1.1 MPC formulation

In the following, we present the standard formulation of a discrete-time MPC problem. Consider a discrete-time system described by the following dynamical model at time k:

$$\mathbf{x}(k+1) = f\big(\mathbf{x}(k), \mathbf{u}(k)\big), \tag{4.25}$$

where $\mathbf{x}(k) \in \mathbb{R}^n$ is a state vector, $\mathbf{u}(k) \in \mathbb{R}^m$ is a control input vector and $f : \mathbb{R}^n \times \mathbb{R}^m \to \mathbb{R}^n$ is a function that describes the system dynamics. Then, a typical MPC problem at time step k can be formulated in a minimization form as follows:

$$\min_{\mathbf{u}(0|k),\ldots,\mathbf{u}(N_p-1|k)} \quad \ell_N\big(\mathbf{x}(N_p|k)\big) + \sum_{s=0}^{N_p-1} \ell\big(\mathbf{x}(s|k), \mathbf{u}(s|k)\big) \tag{4.26a}$$

$$\begin{aligned}
\text{s.t.} \quad & \mathbf{x}(s+1|k) = f\big(\mathbf{x}(s|k), \mathbf{u}(s|k)\big), && s = 0, \ldots, N_p - 1, && \text{(4.26b)}\\
& \mathbf{x}(s|k) = \mathbf{x}(k), && s = 0, && \text{(4.26c)}\\
& h\big(\mathbf{x}(s+1|k), \mathbf{u}(s|k)\big) \le 0, && s = 0, \ldots, N_p - 1, && \text{(4.26d)}\\
& h_f\big(\mathbf{x}(s+1|k)\big) \le 0, && s = N_p - 1, && \text{(4.26e)}
\end{aligned}$$

where N_p represents the prediction horizon length, which is the number of future time steps considered during the optimization process. The optimization variable is the predicted sequence of control inputs $\mathbf{u}(0|k), \mathbf{u}(1|k), \ldots, \mathbf{u}(N_p - 1|k)$ at time k over the prediction horizon N_p. The notation $\mathbf{x}(s|k)$ and $\mathbf{u}(s|k)$ denote the predicted state and control input at future time step s based on the information available at current time k.

The objective (or cost) function (4.26a) to be minimized, consists of two basic components; namely a *terminal cost* function $\ell_N(\cdot) : \mathbb{R}^n \to \mathbb{R}$, evaluated at the end of the prediction horizon and a *cost-per-stage* function $\ell(\cdot) : \mathbb{R}^n \times \mathbb{R}^m \to \mathbb{R}$, accumulated over the prediction horizon. Here, the cost function $\ell(\cdot)$ is designed to penalize deviations of the predicted states $\mathbf{x}(s+1|k)$ and inputs $\mathbf{u}(s|k)$ from their desired values. Whereas, $\ell_N(\cdot)$ penalizes further the final predicted state $\mathbf{x}(N|k)$ to ensure the system's *stability*. Typically, these cost functions are chosen as quadratic functions, i.e., the penalized values are quadratically weighted. For instance, we present below the general forms:

$$\begin{aligned} \ell(\mathbf{x}(s|k), \mathbf{u}(s|k)) &\triangleq \|\mathbf{x}(s|k)\|^2_{\mathbf{Q}} + \|\mathbf{u}(s|k)\|^2_{\mathbf{R}} \\ &= \mathbf{x}(s|k)^\top \mathbf{Q}\mathbf{x}(s|k) + \mathbf{u}(s|k)^\top \mathbf{R}\mathbf{u}(s|k), \qquad (4.27a) \\ \ell_N(\mathbf{x}(N_p|k)) &\triangleq \|\mathbf{x}(N_p|k)\|^2_{\mathbf{P}} \\ &= \mathbf{x}(N_p|k)^\top \mathbf{P}\mathbf{x}(N_p|k), \qquad (4.27b) \end{aligned}$$

where $\mathbf{Q} \in \mathbb{R}^{n\times n} \succeq 0$, $\mathbf{R} \in \mathbb{R}^{m\times m} \succ 0$ are weighting matrices that determine the *relative importance* of the state and input variables in the cost function, respectively. $\mathbf{P} \in \mathbb{R}^{n\times n} \succeq 0$ is a weighting matrix for the terminal cost. The choice of these matrices significantly influences the closed-loop performance and stability of the MPC controller.

In addition to the cost functions, we have optimization constraints that are *explicitly* treated in (4.26b)–(4.26e). Respectively, the continuity of state evolution is ensured by system dynamics $f(\cdot)$ defined in (4.25), the initial state condition is taken from the *current state measurement* $\mathbf{x}(k)$, the general state and input constraints are defined by $h(\cdot) : \mathbb{R}^n \times \mathbb{R}^m \to \mathbb{R}^p$, while terminal constraint is represented by $h_f(\cdot) : \mathbb{R}^n \to \mathbb{R}^{p_f}$. The constraints in (4.26d) can be written in more explicit forms in (4.28a), (4.28b), stated in terms of hard constraints on the internal state variables and input control action, respectively, whereas, terminal constraint (4.26e) can be expressed as (4.28c):

$$\begin{aligned} x(s+1|k) &\in \mathcal{X} \subset \mathbb{R}^n, \qquad s = 0, \dots, N_p - 1, \qquad (4.28a) \\ u(s|k) &\in \mathcal{U} \subset \mathbb{R}^m, \qquad s = 0, \dots, N_p - 1, \qquad (4.28b) \\ x(N_p|k) &\in \mathcal{X}_f \subset \mathcal{X} \qquad (4.28c) \end{aligned}$$

where $\mathcal{X}$ and $\mathcal{U}$ are usually convex sets, defining the feasible regions for the system states and control inputs, respectively. $\mathcal{X}_f$ is a terminal set which is a subset of $\mathcal{X}$, ensuring

the system's stability and feasibility. This set is often designed as a positively invariant set for the system under a specific control law, see Section 4.3.1.3 for more details.

Remark 4.1. *The MPC formulation* (4.26) *is presented in a general form, which can be applied to both linear and nonlinear systems. In the case of linear system, the dynamics* $f(\cdot)$ *in* (4.26b) *is represented by a linear state-space model, i.e.,* $\mathbf{x}(k+1) = \mathbf{A}\mathbf{x}(k)+\mathbf{B}\mathbf{u}(k)$*, where* $\mathbf{A} \in \mathbb{R}^{n\times n}$ *and* $\mathbf{B} \in \mathbb{R}^{n\times m}$ *are constant matrices. In this case, the optimization problem* (4.26)*, given cost functions are as in* (4.27) *and the constraints* (4.26d)-(4.26e) *are linear, becomes a convex quadratic programming (QP) problem. Conversely, for nonlinear systems, i.e.,* $f(\cdot)$ *is a nonlinear function or the constraints are nonlinear, the problem* (4.26) *becomes a nonlinear programming (NLP) problem.*

Remark 4.2. *Note that the MPC formulation* (4.26) *can become a mixed-integer programming (MIP) problem if some of the optimization variables are considered as integer or binary values. This situation often arises in problems that have hybrid dynamics, switching operations, or control mode selections. In this case, the optimization problem* (4.26) *is referred to as MI-MPC. More details about MIP formulation and solving methods are discussed in Section 4.3.2.*

4.3.1.2 MPC principle

In the following, we describe the operational principle of the MPC technique. At each time step k, the optimization problem (4.26) is formulated and solved for the current state $\mathbf{x}(k)$, yielding an optimal control sequence $\mathbf{U}^*(k) = \{\mathbf{u}^*(0|k), \ldots, \mathbf{u}^*(N_p-1|k)\}$. Subsequently, we have the corresponding optimal state sequence $\mathbf{X}^*(k) = \{\mathbf{x}^*(1|k), \ldots, \mathbf{x}^*(N_p|k)\}$. In accordance with the receding horizon principle, only the first element of the control sequence is applied to the system; thus, the resulting MPC control law is:

$$\mathbf{u}(k) = \mathbf{u}^*(0|k) \triangleq \mu(\mathbf{x}(k)). \tag{4.29}$$

Here, $\mu(\cdot) : \mathbb{R}^n \to \mathbb{R}^m$ defines an implicit state-feedback control law that maps the current state $\mathbf{x}(k)$ to the corresponding control action $\mathbf{u}(k)$. So, the MPC control law can be viewed as a feedback mechanism that continuously adjusts the control input based on the current state of the system. Subsequently, the nominal closed-loop system under the

MPC law (4.29) is described by:

$$\mathbf{x}(k+1) = f(\mathbf{x}(k), \mu(\mathbf{x}(k))). \tag{4.30}$$

This process is repeated at each time step with the receding horizon shifted forward as illustrated in Figure 4.5. The overall MPC algorithm is summarized in Algorithm 4.2.

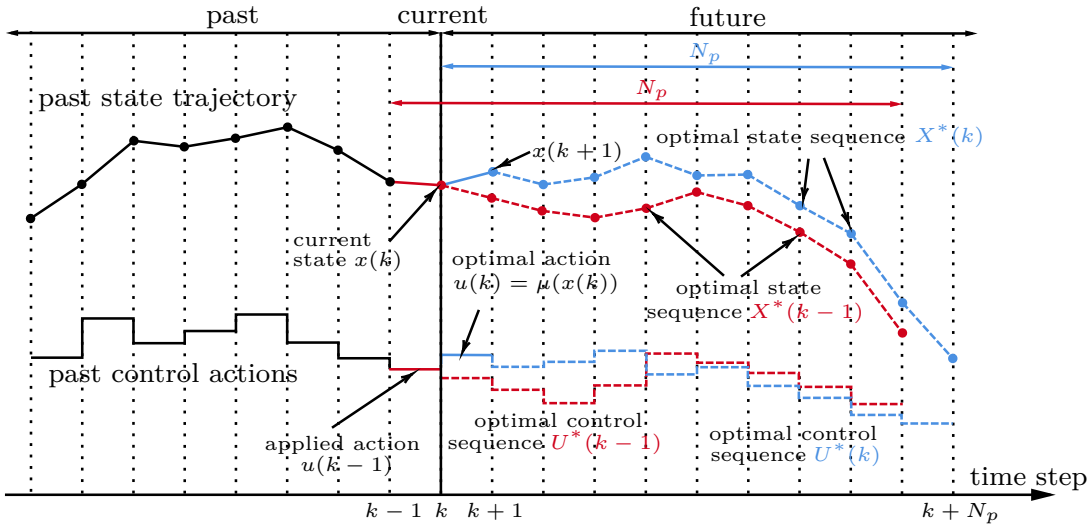

FIGURE 4.5: The receding horizon principle of MPC.

Algorithm 4.2: MPC scheme

Input: Sampling time T_s.

1 At time step k, measure or estimate the current state $\mathbf{x}(k)$;
2 Solve the MPC optimization problem (4.26) to find the optimal control sequence $\mathbf{U}^*(k) = \{\mathbf{u}^*(0|k), \ldots, \mathbf{u}^*(N_p - 1|k)\}$;
3 Apply the first element of this control sequence, $\mathbf{u}(k) = \mathbf{u}^*(0|k)$ to the system over the sampling interval T_s;
4 Advance to the next time step $k+1$ and repeat step 1.

4.3.1.3 Feasibility and stability guarantees in MPC

Terminal constraint (4.26e) represented by $\mathcal{X}_f$ and terminal cost function $\ell_N(\cdot)$ in (4.26a) is crucial to guarantee the closed-loop stability of the MPC design.

If we solve the constrained optimization problem (4.26) over a finite horizon N_p, at every time step k, without considering the *terminal ingredients*, i.e., terminal constraint (4.26e) and terminal cost in (4.26a), we may lose the guarantees of *recursive feasibility*, i.e., the existence of a solution to the problem (4.26) at every time step k and *asymptotic stability*, i.e., the closed-loop system (4.30) converges to a desired equilibrium point. Therefore, we present below sufficient conditions using the terminal cost and constraint to ensure recursive feasibility and asymptotic stability in MPC.

Theorem 4.1 (**Closed-loop system stability under MPC**). *[Mayne et al., 2000] Consider the MPC problem (4.26) with the following conditions:*

i) The cost-per-stage function $\ell(\cdot)$ in (4.26a) is positive definite:

$$\ell(0,0) = 0 \text{ and } \ell(\mathbf{x},\mathbf{u}) > 0, \quad \forall (\mathbf{x},\mathbf{u}) \neq (0,0); \tag{4.31}$$

*ii) The terminal set $\mathcal{X}_f$ (4.28c) is **positively invariant** under local control law $\kappa(\cdot)$:*

$$\mathbf{x}(k+1) = f(\mathbf{x}(k), \kappa(\mathbf{x}(k))) \in \mathcal{X}_f, \quad \forall \mathbf{x}(k) \in \mathcal{X}_f, \tag{4.32}$$

which satisfy all state and input constraints in $\mathcal{X}_f$:

$$\mathcal{X}_f \in \mathcal{X}, \ \kappa(\mathbf{x}(k)) \in \mathcal{U}, \quad \forall \mathbf{x}(k) \in \mathcal{X}_f; \tag{4.33}$$

*iii) The terminal cost $\ell_N(\cdot)$ is a **Lyapunov function** in terminal set $\mathcal{X}_f$ and satisfies:*

$$\ell_N(f(\mathbf{x}(k), \kappa(\mathbf{x}(k)))) - \ell_N(\mathbf{x}(k)) \leq -\ell(\mathbf{x}(k), \kappa(\mathbf{x}(k))), \quad \forall \mathbf{x}(k) \in \mathcal{X}_f. \tag{4.34}$$

Then, if the MPC problem (4.26) is feasible at time step $k = 0$, it is recursively feasible, i.e., feasible for all $k \in \mathbb{Z}_+$. Moreover, the closed-loop system (4.30) under the MPC control law obtained by solving the problem (4.26) is asymptotically stable. □

Proof. See Chen and Allgöwer [1998]. For positive invariance notions, Lyapunov stability and the like see Khalil [2009] □

Remark 4.3. *Note that Theorem 4.1 is a sufficient condition for the closed-loop stability. There are alternative approaches to guarantee the closed-loop stability without the terminal*

ingredients. One common approach in the literature is to use a sufficiently long prediction horizon N_p in combination with a certain controllability assumption. This assumption can be stated by either a suitable upper bound on the optimal cost value [Reble and Allgöwer, 2012] or an unbounded optimal cost value with a slow growth rate [Müller and Worthmann, 2017]. The choice of prediction horizon N_p in such a case is provided in [Worthmann et al., 2014].

By appropriately designing the terminal set $\mathcal{X}_f$ and terminal cost function $\ell_N(\cdot)$ such that the conditions in Theorem 4.1 are satisfied, the recursive feasibility and asymptotic stability of the closed-loop system under the MPC law is ensured. The specific design of these terminal components, especially the positively invariant set, depends on the system dynamics and can be constructed using various existing methods. For linear systems, a common approach is to compute a polyhedral maximal positively invariant (MPI) set using backward reachability [Alessio et al., 2006, Gheorghe et al., 2024] or ellipsoidal invariant sets by analytical construction via Lyapunov functions [Chen and Allgöwer, 1998, Nguyen et al., 2020]. For nonlinear systems, the computation of invariant sets is more complicated; thus, approximated invariant sets are also considered [Wang et al., 2020].

In practice, the control system is much more complex with high-dimensional state and input spaces, nonlinear dynamics and various constraints. Therefore, designing the terminal cost and terminal constraint may not be realistic due to the complex and intensive computation of these sets. Moreover, it might lead to conservative control designs, which affect the overall performance of the closed-loop system. Therefore, we do not address the theoretical guarantee in this work, but rather focus on the real performance of the closed-loop system through extensive simulations.

4.3.1.4 MPC characteristics

Based on the MPC formulation and principles that we have discussed so far, it is evident that MPC possesses various interesting characteristics. Among those, we present below the most significant ones which should be taken into consideration when it comes to the control design of practical systems.

- Multi-variable: MPC handles MIMO systems, i.e., the system in (4.25) that has multiple inputs $\mathbf{u}(k) \in \mathbb{R}^m$ and multiple outputs $\mathbf{x}(k) \in \mathbb{R}^n$. As a result, it can incorporate the couplings among the system variables and effectively manage the coordination of the control variables. However, controlling large MIMO results in a large-scale optimization problem (4.26); hence, cascaded or hierarchical MPC structures can be considered to reduce the size of the optimization.

- Nonlinearity: MPC can be applied to not only linear systems but also nonlinear systems, i.e., system dynamics $f(\cdot, \cdot)$ in (4.25) can be either linear or nonlinear, which results in nonlinear model predictive control (NMPC). This helps to capture more accurately the system dynamics but also leads to an increase in the complexity of the optimization problem (4.26). Therefore, a nonlinear model can be locally approximated by a linear model around an operating point to reduce the complexity.

- Constraints: MPC explicitly takes into consideration various types of constraints on both states and inputs, by defining the inequality condition $h(\mathbf{x}(k), \mathbf{u}(k)) \leq 0$ in (4.26d) or the feasible state $\mathcal{X}$ and input $\mathcal{U}$ in (4.28a)-(4.28b). This is one of the features making MPC particularly appealing for practical applications, especially in situations where physical limitations and safety conditions of the control systems must be strictly respected. However, an increasing number of constraints also increases the complexity of the optimization problem (4.26), thus redundant constraints should be avoided in the optimization formulation.

- Trade-off: MPC offers flexibility in specifying the control objectives and adjusting the relative importance of the control goals, e.g., tracking performance and control effort. This is achieved by appropriately designing the cost-per-stage function $\ell(\cdot)$ in (4.26a), more specifically, the weighting matrices in the quadratic cost (4.27a). For instance, increasing the weight matrix $\mathbf{Q}$ enhances the convergence of the system state $\mathbf{x}(k)$, whereas increasing the matrix $\mathbf{R}$ reduces the control effort $\mathbf{u}(k)$ [Alamir, 2024].

- Preview: By using the dynamical model $f(\cdot, \cdot)$ in (4.25) to predict the future behavior of the system over the predefined horizon N_p, MPC can anticipate the future sequence of system state $\mathbf{x}(k), \ldots, \mathbf{x}(k + N_p)$ and therefore adjust control actions $\mathbf{u}(k), \ldots, \mathbf{u}(k + N_p - 1)$, accordingly. Moreover, MPC allows for the incorporation of disturbances into the predictive model, thus considering the

uncertainties or disturbances along the prediction horizon. However, the accuracy of the anticipation significantly depends on the quality of the model and the length of the prediction horizon N_p. On one hand, the inaccurate model in (4.25) results in unreliable prediction, making the control actions $\mathbf{u}(k)$ potentially infeasible for the real system. On the other hand, a longer horizon with an accurate model may provide better anticipation but also increases the computational burden of (4.26).

- Optimality: By solving online the optimization problem (4.26) at each time step k, MPC provides an optimal control sequence $\mathbf{U}^*(k)$, allowing for the achievement of optimal control performance, i.e., minimizes the cost function while satisfying all constraints. In other words, MPC ensures that the control actions are chosen in a way that they are optimal with respect to some control requirements. Nevertheless, this brings challenges in terms of computational complexity to the control method in real-time implementation. As a result, it is important to choose appropriate optimization algorithms that can efficiently solve the problem (4.26). One can be considered is approximated method which provide suboptimal solutions while significantly reducing the computational burden. In addition, for embedded systems, the optimization problem (4.26) should be formulated and solved in such a way that it can be implemented within limited memory.

In industry, despite the presence of advanced control methods, classical control strategies, e.g., proportional integral derivative (PID) control, simple rule-based control, etc, have been widely used for decades due to their simplicity and ease of implementation. However, these control techniques may not necessarily fulfill the performance requirements for complex systems and people tend to accept these inefficiencies. Because they would rather focus on the stability and reliability of the automatic control system and partially rely on the manual control with human experience to handle the complex situations. However, with the advancement of computing technologies, optimization-based control like MPC has been intensively explored and successfully implemented to overcome the limitations of the classical approaches [Kozák, 2016, Schwenzer et al., 2021]. Subsequently, we present in Table 4.2 a comprehensive comparison between classical and advanced control methods in practice to clarify this point.

In addition, it is also worth mentioning the essential tuning ingredients in MPC design, which are the core of MPC characteristics [Alamir, 2024]. The main tuning parameters

TABLE 4.2: Comparison of Classical PID and Modern MPC Control.

Criteria	Classical PID Control	Modern MPC Control
	System	
Model	Model-free	Online model
Dimension	SISO	MIMO
Coupling	No	Explicitly accounted
Linearity	Linear	Linear, Nonlinear
Time	Time-invariant	Time-invariant, time-varying
	Control	
Design	Easy	Complex
Input constraint	Indirectly by anti-windup	Explicitly accounted
Output constraint	No	Explicitly accounted
Trade-off	Implicitly by gain	Explicitly by weight cost
Optimality	No	Yes
Reactivity	Reactive	Proactive
Hierarchical ability	Low-level	Multi-level
	Implementation	
Computation	Cheap	Expensive
Measurement	Less	More
Hardware	Simple	Powerful, large memory
Embedded	Yes	Challenging
Performance	Satisfactory	Optimal
Manual control	Common	Rare
Investment	Low	High
Industry adoption	Very high	Increasing

Green indicates advantages, red indicates limitations, Blue can be both.

include the sampling time T_s for Algorithm 4.2, the prediction horizon N_p for problem (4.26), and the weighting matrices $\mathbf{Q}$ and $\mathbf{R}$ for the cost function (4.27a).

- Sampling time T_s: The sampling time T_s is the time interval at which the controller takes a new measurement and computes the corresponding control signals. A shorter sampling time allows for faster reaction to the disturbances. Nevertheless, it increases the frequency of computing the optimization, thus requiring high-performance computational algorithms. Moreover, it also demands a longer prediction horizon to cover the same time span of the system's dynamics.

- Prediction horizon N_p: A longer horizon allows for farther prediction, increasing the feasibility and stability of the closed-loop system. However, it also increases the size of the optimization problem, leading to a greater computational burden. Conversely, a shorter horizon reduces the computational load but may compromise the control performance and stability. The choice of N_p should take into consideration the system dynamics, constraints, and available computational resources.
- Weighting matrices $\mathbf{Q}, \mathbf{R}$: The weighting matrices offer an explicit balance between the regulation performance and the control effort, more specifically:
  - A larger $\mathbf{Q}$ relative to $\mathbf{R}$, penalizes the state deviation $\mathbf{x}(k)$ more heavily, resulting in faster response and better converge or tracking performance, but obviously obtain the more aggressive and costly control action $\mathbf{u}(k)$.
  - A larger $\mathbf{R}$ relative to $\mathbf{Q}$, in contrast, emphasizes more on the control effort $\mathbf{u}(k)$, leading to smoother and lest aggressive control signals, but potentially result in a slower system response and larger state deviations $\mathbf{x}(k)$.

In practice, the T_s and N_p parameters are often chosen based on the system dynamics, prediction models and computational capabilities, whereas the weighting matrices $\mathbf{Q}$ and $\mathbf{R}$ are initially selected based on the control objectives on site and then refined by the trial-and-error approaches, in which their values are iteratively adjusted by evaluating the feedback control performance through simulations or closed-loop experiments.

4.3.2 Mixed-integer MPC

For more than 60 years, MIP problems have been playing a key role in building the bridge between academia and industrial life [Jünger et al., 2009]. MIP has been intensively used across various domains to address complex decision-making problems, particularly MPC problems where binary or integer decisions are essential.

Examples span many domains: i) logistics and supply chains, such as cash distribution and inventory routing Osorio and Toro [2012], Dong et al. [2014]; ii) finance, for portfolio optimization with discrete constraints Esmaeily and Loge [2023]; iii) robotics including collision avoidance, safe trajectory planning, task allocation, unmanned aerial vehicles

(UAVs), connected and automated vehicles (CAVs) decision making Prodan et al. [2013], Mancuso et al. [2014], Stoican et al. [2022], Suriyarachchi et al. [2023], Quirynen et al. [2024], Samada et al. [2025], Atay and Bayazit [2006]; iv) energy systems, including micro-grid management, fusion reactors Prodan and Zio [2014], Orrico et al. [2023] and hydrogen production Vijayshankar et al. [2025]; v) chemical engineering, for production scheduling Liu et al. [2011], Velez and Maravelias [2013].

These examples collectively highlight the broad applicability of MIP in solving real-world problems, usually involving complex structural, logical and combinatorial requirements.

4.3.2.1 Mixed-integer programming (MIP) problems

MIP is an optimization framework for problems where some or all decision variables are restricted to be integer values, in addition to continuous variables [Ioan et al., 2021].

In the context of control system design, MIP is particularly leveraged for the sake of modeling and solving control problems that involve switching dynamics, logical conditions or discrete decisions.

The general solving methods for MIP problems can be categorized into exact algorithms and heuristic procedures depending on the nature of the solution obtained. However, due to the complexity of MIP and the diversity of problem structures, MIP solvers often combine multiple techniques to enhance performance [Jünger et al., 2009]. The foundation of exact algorithms is mainly based on two fundamental techniques, i.e., *branch-and-bound* and *cutting plane* algorithms, which were introduced by the pioneering works of Land and Doig [1960] and Gomory [1957], respectively, in the mid-20th century. Let us consider the general form of a mixed-integer linear programming (MILP) problem:

$$J = \min_{\mathbf{x}} \mathbf{c}^T \mathbf{x}, \tag{4.35a}$$

$$\text{s.t.} \quad \mathbf{A}\mathbf{x} \leq \mathbf{b}, \ \mathbf{x} \leq 0 \tag{4.35b}$$

$$\mathbf{x}_j \in \mathbb{Z}, \quad \forall j \in \mathcal{I}, \tag{4.35c}$$

where, $\mathbf{x} \in \mathbb{R}^n$ is the decision variable, $\mathbf{c} \in \mathbb{R}^n$, $\mathbf{A} \in \mathbb{R}^{m \times n}$, $\mathbf{b} \in \mathbb{R}^m$ are constant variables and $\mathcal{I} \subseteq \{1, \ldots, n\}$ is the index set of integer variables.

The branch-and-bound algorithm, proposed by Land and Doig [1960], systematically explores subproblems by relaxing integer constraints and branching on fractional variables with bound comparison to find the optimum. In contrast, the cutting plane method, introduced by Gomory [1957], iteratively refines the feasible region of the LP relaxation problem by adding linear constraints, also known as *cuting planes* that cut off fractional solutions. A more detailed explanation of these methods is provided in Appendix A.2.

As is known, because of the NP-hard nature of the problem, solving MIP problems to optimality is computationally challenging. Because we want to always have the "true" incumbents for convergence in branch-and-bound, we have to pay for the extremely computational effort to explore nodes in the search tree. In practical scenarios, this is usually unrealistic and unnecessary because certain problems can not be solved to provable optimality within restricted time constraints, while for others, a high-quality solution is sufficient rather than exact optimality. As a result, heuristic methods are employed with the exact methods in the primal problems to find good feasible solutions quickly. Some common heuristic methods which have been intensively studied include rounding, feasibility pump, local branching, etc [Berthold, 2015]. These methods do not guarantee optimality but can provide good solutions in a reasonable time interval.

4.3.2.2 MIP formulation in MPC framework

Mixed-integer optimization provides a powerful framework for modeling and solving MPC problems that involve both continuous and discrete decision variables. The MPC formulation (4.26) can be extended to handle mixed-integer variables, resulting in a formulation of discrete-time *mixed-integer model predictive control* (MI-MPC) problem, where we do not consider the terminal ingredients for simplicity. Let us reconsider the system (4.25), whose control vector $\mathbf{u}(k) \in \mathbb{R}^m$ consists of both continuous part $\mathbf{u}_c(k) \in \mathbb{R}^{m_c}$ and integer part $\mathbf{u}_i(k) \in \mathbb{Z}^{m_i}$, explicitly written as:

$$\mathbf{u}(k) = \begin{bmatrix} \mathbf{u}_c(k) \\ \mathbf{u}_i(k) \end{bmatrix} \quad \in \mathbb{R}^{m_c} \times \mathbb{R}^{m_i}, \tag{4.36}$$

where m_c and m_i are the dimensions of the continuous and integer control inputs, respectively, with $m = m_c + m_i$, we have an MI-MPC problem at time step k that can be formulated as the following MIP problem:

$$\min_{\substack{\mathbf{u}_c(0|k),\ldots,\mathbf{u}_c(N_p-1|k)\\ \mathbf{u}_i(0|k),\ldots,\mathbf{u}_i(N_p-1|k)}} \quad \sum_{s=0}^{N_p-1} \ell\big(\mathbf{x}(s|k), \mathbf{u}_c(s|k), \mathbf{u}_i(s|k)\big) \tag{4.37a}$$

$$\begin{aligned}
\text{s.t.} \quad & \mathbf{x}(s+1|k) = f\big(\mathbf{x}(s|k), \mathbf{u}_c(s|k), \mathbf{u}_i(s|k)\big), && s = 0,\ldots,N_p-1, && \text{(4.37b)}\\
& \mathbf{x}(0|k) = \mathbf{x}(k), && && \text{(4.37c)}\\
& h\big(\mathbf{x}(s+1|k), \mathbf{u}_c(s|k), \mathbf{u}_i(s|k)\big) \le 0, && s = 0,\ldots,N_p-1, && \text{(4.37d)}\\
& \mathbf{u}_c(s|k) \in \mathbb{R}^{m_c}, && s = 0,\ldots,N_p-1, && \text{(4.37e)}\\
& \mathbf{u}_i(s|k) \in \mathbb{Z}^{m_i}, && s = 0,\ldots,N_p-1, && \text{(4.37f)}
\end{aligned}$$

where the optimization variables are the sequences of continuous control inputs $\mathbf{u}_c(s|k)$ and integer control inputs $\mathbf{u}_i(s|k)$ over the prediction horizon N_p. The constraint (4.37e) is written only to emphasize the distinction between continuous and integer variables and is not presented in standard MIP formulations. Whereas, the constraint (4.37f) explicitly enforces the integer nature of the variables $\mathbf{u}_i(s|k)$. If there are no continuous variables appearing in the optimization problem (4.37), i.e., $m_c = 0$, the problem is referred to as a pure *integer programming* (IP) problem. Moreover, if the integer variables are restricted to binary values, i.e., the constraint (4.37f) is rewritten as $\mathbf{u}_i(s|k) \in \{0,1\}^{m_i}$, the problem is called a *binary-integer programming* (BIP) problem.

TABLE 4.3: Classification of main types of MIP problems.

MIP (4.37)	**Cost** (4.37a)	**Dynamics** (4.37b)	**Constraints** (4.37d)
MILP	Linear	Linear	Linear
MIQP	*Quadratic*	Linear	Linear
MIQCP	Linear/Quadratic	Linear	*Quadratic*
MINLP	*Any**, with at least one function must be nonlinear		

*Linear, Quadratic or Nonlinear.

As shown in Table 4.3, the MIP problem (4.37) can be classified into different types of MIP problems, based on the nature of the cost function $\ell(\cdot)$ defined in (4.37a), the

system dynamical model $f(\cdot)$ defined in (4.37b) and the constraint function $h(\cdot)$ defined in (4.37d). Among those, the mixed-integer nonlinear programming (MINLP) problem is the most challenging to solve due to the non-convexity and discrete decision spaces involved in the problem formulation. In the following, we detail the main solving methods for MINLP problems in the state of the art.

4.3.2.3 MIP solving methods

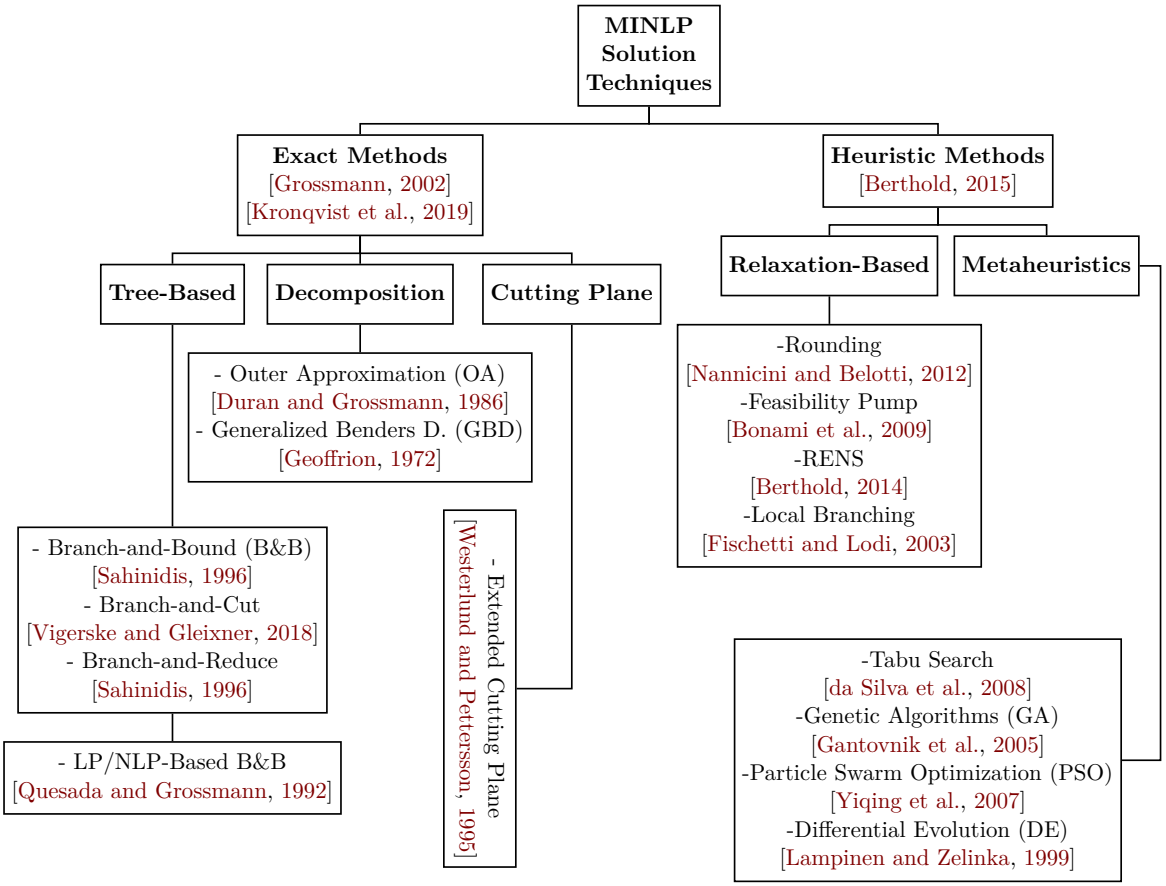

FIGURE 4.6: Classification of solution techniques for MINLP.

The classical exact methods, branch-and-bound and cutting-plane are employed for MILP problems, but can also be extended to solve MINLP problems. To effectively handle the nonlinearities in the MIP, there are alternatives are based on the decomposition strategy of the original problem [Grossmann and Ruiz, 2011]. Figure 4.6 delineates the taxonomy of the main solving methods for MINLP.

The exact methods are categorized in three main classes, i.e., tree-based methods, decomposition techniques and cutting plane methods [Kronqvist et al., 2019]. Note that tree-based NLP branch-and-bound and extended cutting-plane methods are direct adaptations of the classical MILP algorithms. The decomposition technique, including outer approximation (OA) and generalized Benders decomposition (GBD) divides the original problem into NLP subproblems and MILP master problems. While the OA method solves NLP first and then generates linearization (outer approximations) around the NLP solution to update the MILP master problem, the GBD method uses Benders cuts from the dual multipliers of solving NLP to refine the MILP master problem. Both methods iteratively solve these subproblems and master problems until convergence to the global optimum is achieved.

Heuristic methods, in contrast, offer approximate solutions without guarantees of optimality, but they are computationally efficient. They are especially designed for non-convex problems where exact methods struggle to find the optimal solution. The heuristic-based methods, which consist of rounding, feasibility pump, relaxation enforced neighborhood search (RENS) local branching [Berthold, 2015], etc, start with solutions to primal problems and apply heuristic rules to obtain best feasible integer solutions. Metaheuristic approaches draw inspiration from stochastic optimization problems and can be applied to explore the optimum in the MIP problem. They rely on a list of gradient-free optimization methods, e.g., Tabu search, genetic algorithms (GA), particle swarm optimization (PSO), and differential evolution (DE). All heuristic methods are designed to quickly generate good-quality solutions by exploiting the relaxed problem and employing the heuristic rules to guide the search process without the need to compute derivative information.

4.3.3 Modeling languages and solvers

In optimization-based control design, once the problem is formulated, it is essential to choose efficient modeling language and solvers that can reliably handle its specific characteristics. This subsection briefly reviews popular modeling languages and state-of-the-art optimization solvers relevant for our control problem.

4.3.3.1 Modeling languages

There are numerous well-established modeling languages available, providing users a high-level interface for defining optimization problems, e.g., AMPL [Fourer et al., 1990], GAMS [Brook et al., 1988], Pyomo [Hart et al., 2011], JuMP [Dunning et al., 2017], YALMIP [Lofberg, 2004], CasADi [Andersson et al., 2019], etc. They allow users to define optimization variables, control objectives and constraints using a concise and natural syntax, then solve the obtained formulations by various solvers without requiring a deep understanding of the underlying solver algorithms.

For gradient-based optimization algorithms, derivative information is significantly important as it is used to guide the search for optimal solutions. For instance, in Newton-type methods, the gradient and Hessian are used to determine the search direction:

$$\Delta \mathbf{x} = -[\nabla^2 f(\mathbf{x})]^{-1} \nabla f(\mathbf{x}), \tag{4.38}$$

where $\nabla f(\mathbf{x})$ is the gradient and $\nabla^2 f(\mathbf{x})$ is the hessian of the objective function $f(\mathbf{x})$ at the current point $\mathbf{x}$. In quasi-Newton methods such as BFGS or SR1, approximation of the inverse Hessian is iteratively updated using gradient information. As a consequence, one of the key features of a modeling language is its ability to provide derivative computation to support these underlying algorithms. Although some (mostly commercial) solvers can internally compute derivatives using either numerical or algorithmic differentiation, this process still incurs significant overhead in the optimization, especially for large-scale problems. Modeling languages that provide efficient and accurate derivative information can greatly enhance the performance of solving the optimization.

There are four common approaches when it comes to computing derivatives computation Boyd et al. [2004], Nocedal and Wright [2006], Griewank and Walther [2008]:

i) Analytical differentiation, i.e., manually deriving the mathematical expressions.

ii) Numerical differentiation, e.g., using finite difference methods.

iii) Symbolic differentiation, i.e., manipulating mathematical expressions via computer algebra system (CAS) to obtain exact derivative formulas.

iv) Algorithmic differentiation (AD), also known as automatic differentiation, i.e. the application of the chain rule of calculus to compute exact derivatives efficiently.

To briefly summarize their features: i) analytical differentiation gives exact derivatives but becomes difficult for complex or large systems; ii) numerical differentiation is easy but often unstable and error-prone; iii) symbolic differentiation is exact but can suffer from expression swell. To address these limitations, iv) algorithmic differentiation (AD) has been developed to provide exact, efficient and stable derivatives.

Regarding the native AD capability, AMPL, JuMP and CasADi offer built-in AD. Particularly, AMPL provides AD based on static expression graphs [Gay, 1991], whereas JuMP utilizes forward and reverse mode AD through the Julia packages [JuMP, 2024] and CasADi allows for efficient AD interactively on its expression graphs [Andersson et al., 2012]. YALMIP does not explicitly provide information on whether or not it uses AD. In contrast, native AD is not inherently supported in Pyomo and GAMS, but derivative information can still be provided with external AD tools like AMPL library or CasADi (for Pyomo) and C++ library (for GAMS) [Nicholson et al., 2018, GAMS, 2025].

Although AMPL and GAMS are long-established, they are commercial tools with proprietary syntax, while JuMP is open-source but limited to Julia. These options are less convenient for us compared with Python or MATLAB based tools in terms of flexibility, efficiency, derivative computation and solver integration. We therefore focus on the modeling frameworks used in our work, CasADi, YALMIP, the MPC Toolbox and SciPy.optimize, and summarize their key features in Table 4.4, highlighting the advantages of CasADi.

To provide some insights, YALMIP, accessible only through MATLAB, is still a great option for academic use, although it has been less frequently updated in recent years. MPC Toolbox in MATLAB is tailored for only for MPC with numerous easy-tuning features via a graphical interface, but it has less flexibility in terms of modeling and solving. SciPy.optimize is a lightweight, general-purpose optimization library in Python with basic features and limited solver options, thus suitable for simple problems. CasADi, which can be used in both Python and MATLAB, in our view, it offers the most comprehensive support for advanced optimization, with powerful features and active development.

TABLE 4.4: Modeling tools comparison for optimization and control used in this thesis.

Feature	**CasADi** [Andersson et al., 2019]	**YALMIP** [Lofberg, 2004]	**MPC Toolbox** [Morari and Ricker, 1994]	**SciPy.optimize** [Virtanen et al., 2020]
Version	3.7.2	R20250626	24.1	1.16.2
License	Free (LGPL).	Free.	Commercial or Academic license.	Free (BSD).
Language	C++, Python, MATLAB/Octave.	MATLAB/Octave.	MATLAB, Simulink.	Python.
Purpose	Optimal control, NLP, AD.	MPC, semidefinite programming (SDP).	MPC applications.	General-purpose optimization.
Target	Academia, Industry	Academia.	Academia.	Scientific computing.
Maintain	Actively developed and improved by KU research team.	Infrequent updates by Johan Löfberg.	Professionally maintained by MathWorks.	Maintained by developer community.
Problem	LP, QP, NLP, MINLP.	LP, QP, NLP, MILP, MIQP, SDP.	Linear/nonlinear MPC.	LP, QP, NLP, Global Opt.
Modeling	Symbolic expression graphs (SX/MX)[6].	Symbolic expressions via MATLAB object.	MATLAB functions, Simulink blocks.	Python functions (callables).
Native AD	Forward, reverse with graph coloring.	Not mentioned.	No.	No.
Solvers	Interfaces numerous external solvers.	Interfaces external solvers.	Built-in QP/NLP, custom solvers.	Only built-in solvers.
MIP	Yes (MINLP).	Yes (MILP, MIQP).	Yes (MIQP-MPC).	No.

[1] SX: *scalar expression* type; MX: *matrix expression* type.

It is also worth mentioning `acados` [Verschueren et al., 2022], a software package with a collection of solvers for fast and embedded optimization. It provides interfaces to higher-level languages and can seamlessly work with CasADi to provide optimal control algorithms in embedded devices. However, since our thesis does not specifically involve embedded systems, we do not consider this tool here.

4.3.3.2 CasADi framework

CasADi is an open-source framework designed for numerical optimization, with a strong focus on modeling and solving the NLP problems or optimal control problems (OCP) with a large degree of flexibility [Andersson et al., 2019].

CasADi stands for Computer Algebra System (CAS) with Algorithmic Differentiation (AD) feature, highlighting its core capabilities in *symbolic computation* and *efficient derivative evaluation*, which are significant elements in modeling and solving an optimization problem.

To clarify the tools used in our implementation, we constructed Figure 4.7 as our own architectural overview of the CasADi framework, synthesized from various sources since no such unified illustration exists in the literature.

CasADit is confirmed by [Andersson et al., 2012] that it is not a traditional CAS, as its symbolic capabilities are specialized for optimization. Moreover, it is not a conventional AD tool that can retrieve derivatives from arbitrary code, we need to reimplement the models in CasADi syntax to leverage its AD feature. Lastly, CasADi is not a standalone optimization solver but rather a framework that provides interfaces to solvers. As shown in Figure 4.7, CasADi acts as a bridge connecting high-level languages, e.g., Python or MATLAB with various state-of-the-art numerical solvers, e.g., ipopt, gurobi, etc. This architecture offers flexibility for optimization at any complexity, enables seamless implementation of methods and leverages the strengths of different algorithms.

The first layers in Figure 4.7, as a user, we can interact with CasADi core written in self-contained C++ through its front-ends in Python, MATLAB or Octave which are fully featured and auto-generated using Simplified Wrapper and Interface Generator (SWIG) tool on code C++. This provides us the ease of use in higher-level programming languages, while still benefiting from the performance of C++ in the backend. However, if computational performance is tightly considered, using these front-end interfaces still results in some losses of efficiency. To address this, we can implement the optimization problem directly in C++ to fully leverage the performance of CasADi.

Symbolic computation in CasADi is based on the construction of expression graphs as shown in Figure 4.8, where mathematical expressions are represented as directed acyclic graphs (DAGs), each node of the graph is either a symbolic primitive, a constant, a unary or binary operation. The symbolic primitive can be defined by scalar expression type, i.e., SX or matrix expression type, i.e., MX. While the SX expression allows for more efficient computation but requires larger memory, the MX expression does the opposite. DM type is similar to SX, but is mainly used for storing matrices whose nonzero elements

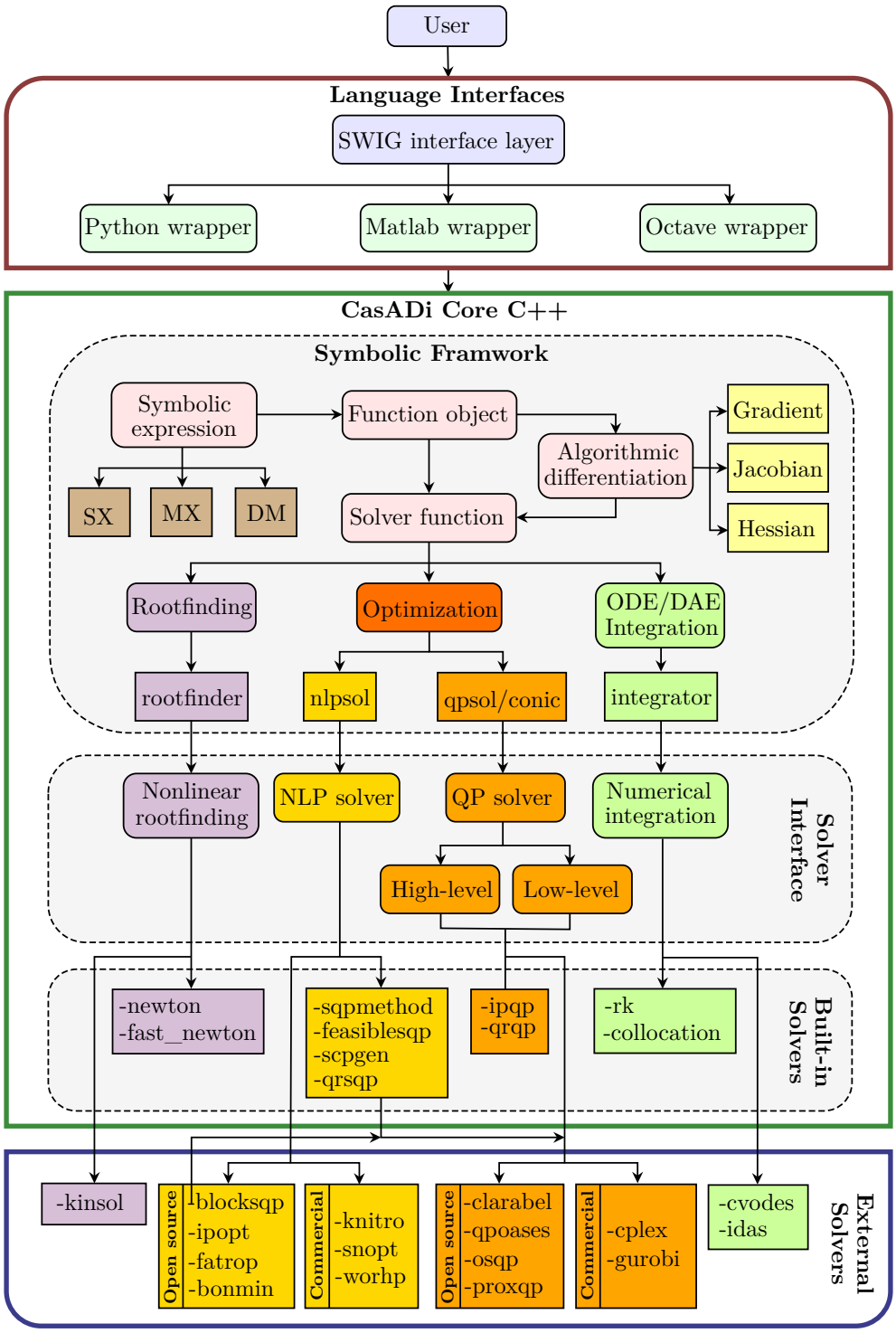

FIGURE 4.7: Architectural overview of the CasADi framework, illustrating its role as an interface between high-level modeling languages and high-performance numerical optimization solvers. A representative set of the supported solvers is also illustrated.

are numerical values rather than symbolic expressions. This simple graph representation enables CasADi to efficiently manipulate and evaluate complex numerical expressions.

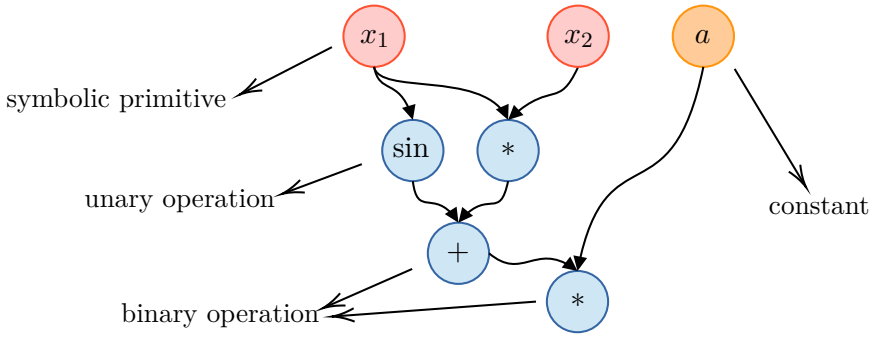

FIGURE 4.8: An example of CasADi expression graph representing the mathematical expression $f(x_1, x_2) = a(\sin x_1 + x_1 x_2)$, where x_1, x_2 are inputs, a is constant.

CasADi's AD capabilities are built on top of this symbolic framework, allowing for the efficient computation of derivatives using the chain rule of calculus. CasADi supports both forward and reverse mode AD [Barth et al., 2005], allowing us to compute the gradient, Jacobian, and Hessian of any functions defined in CasADi, thus providing the necessary derivative information to the solving algorithms. While forward mode is efficient for functions with significantly more outputs than inputs, reverse mode is better for computing gradients of functions with a larger number of inputs. Both modes have the same computational cost as evaluating the original function. However, reverse mode can be memory-intensive for large symbolic expressions, since it needs to store and access intermediate results in reverse order. To address this, we can break large expressions into smaller, separate ones.

Last but not least, CasADi offers several built-in solvers written in C++ or the interfaces to various external solvers. Thus, the solver interface allows us to address different types of problems, including nonlinear systems of equations, which are handled through the rootfinding interface, optimization handled by NLP or QP interfaces, and ODE/ADE integration through the integrator interface. Depending on the supported interfaces, we can choose appropriate solvers to solve the formulated problems. For instance, for NLP problems, we can use either the built-in solver `sqpmethod` or external solvers like `ipopt`, etc. For MIP problems, we can solve the MINLP problems through NLP interface using `bonmin`, or solve MIQP problems through QP interface using `gurobi`, `cplex`, etc. Some detailed information about the solvers is presented in the following subsection.

4.3.3.3 Numerical solvers

CasADi provides a variety of built-in and external solvers for different types of optimization problems, including QP, NLP and MIP. We summarize in Table 4.5 and Table 4.6, some well-known solvers that can be integrated with CasADi through NLP and QP interfaces. This helps us to understand their characteristics, advantages and limitations, thus choosing the appropriate ones for our control design purpose.

Algorithms for QP

Constrained QP problems without inequality constraints can be analytically solved through Karush-Kuhn-Tucker (KKT) conditions [Nocedal and Wright, 2006]. In contrast, the problems with inequality constraints become more complex due to the complementary slackness condition and require numerical methods to find the optimal solution: *active-set* methods [Wolfe, 1959] and *penalty-function* methods. Penalty-function is a broader category for methods that handle inequality constraints by incorporating them into the objective function through barrier functions, aka *interior-point* methods [Wright, 1997] or quadratic penalty terms, aka *augmented Lagrangian*-based methods [Fortin and Glowinski, 2000].

The active-set method was initially extended from the simplex method, which is used for linear programming (LP) [Dantzig et al., 1955]. It selects and iteratively updates the set of active constraints based on the current dual variables and the feasibility of the primal variables. It then solves a sequence of reduced equality-constrained QP problems to find the optimal solution. The active-set method can easily be warm-started to reduce the number of iterations. This is particularly useful for solving cascades of QP problems, .e.g., in sequential quadratic programming (SQP) methods or in MPC. The drawback of this method is that it inherently relies on the polyhedral structure of the feasible region and may require more iterations to converge as the number of half-spaces increases. Active-set methods can be implemented as dual type in `daqp` solver, primal-dual type in `qrqp` or parametric type in `qpoases`, etc.

Interior-point method was also first developed for the LP problems and later extended for convex QPs of a primal-dual type. It approaches the optimal solution from within the feasible region by using barrier functions to handle inequality constraints and iteratively

TABLE 4.5: Overview of solvers can be used via CasADi QP interface (`qpsol`/`conic`).

Solver	Brief description	Principal algorithmic features
	Active-set methods [Wolfe, 1959]	
`daqp`	Dual Active-set QP [Arnström et al., 2022]	Dual active-set method with warm-starting.
`qpoases`	QP Online Active-SEt Strategy [Ferreau et al., 2014]	Parametric active-set method.
`qrqp`	QR-based QP (built-in solver) [Andersson and Rawlings, 2018]	Primal-dual active set method with sparse QR factorization.
	Interior-point methods [Wright, 1997]	
`clarabel`	Interior-point solver for conic programs with quadratic objectives [Goulart and Chen, 2024]	Primal-dual interior-point using novel homogeneous embedding formulation.
`hpipm`	High-Performance Interior-Point Method [Goulart and Chen, 2024]	Primal-dual interior-point with dense and structure exploitation.
`ipqp`	Interior Point QP (built-in solver)	Basic primal-dual interior-point method
`ooqp`	Object-Oriented QP [Gertz and Wright, 2003]	Primal-dual interior point algorithms.
	Augmented Lagrangian-based methods [Fortin and Glowinski, 2000]	
`proxqp`	Proximal QP [Bambade et al., 2022]	PDPMM[7], combined bounded constraint Lagrangian strategy with a (primal-dual) proximal method of multipliers.
`osqp`	Operator Splitting QP [Stellato et al., 2020]	ADMM[8]with novel splitting requiring the solution of a quasi-definite linear system.
	Commercial solvers	
`cplex`[9]	IBM ILOG CPLEX Optimization Studio [Bliek1ú et al., 2014]	Simplex, barrier and mixed integer optimizers.
`gurobi`[10]	Gurobi Optimizer [Gurobi Optimization, 2023]	Similar to `cplex` with presolve techniques, built-in heuristics.

[2]PDPMM: Primal-Dual Proximal Method of Multipliers [De Marchi, 2022].
[3]ADMM: Alternating Direction Method of Multipliers [Boyd et al., 2011].
[4]CPLEX: C refers to the C programming language, PLEX is short for Simplex method.
[5]Gurobi: is named after its founders, Gu Zonghao, Rothberg Edward and Bixby Robert.

solves a series of modified problems that gradually approximate the original problem. Unlike active-set methods, interior-point methods can handle non-polyhedral (conic) constraints and easily exploit the sparsity structure of the problem. Moreover, it inherits more robust convergence guarantees than active-set methods. However, it is harder to

warm-start when solving a sequence of related QPs due to its homotopy-based structure. Primal-dual interior-point methods have been improved and integrated in many solvers we can use in CasADi, e.g., `clarabel`, `hpipm`, `ipqp`, or `osqp`, etc.

The augmented Lagrangian method is another penalty-function approach, similar to interior-point methods, but it handles inequality constraints by augmenting the Lagrangian with a quadratic penalty term. The classical implementation of this method is the method of multipliers (MM), which iteratively updates the primal and dual variables to minimize the augmented Lagrangian function [Hestenes, 1969]. An extension of MM with stronger convergence guarantees is the proximal method of multipliers (PMM), where an additional proximal regularization on primal variables [Rockafellar, 1976] is added. An alternative formulation of PMM, primal-dual PMM, provides robustness to ill-conditioned problems with warm-starting, sparsity exploiting, and is integrated in `proxqp` solver. Alternating direction method of multipliers (ADMM) splits the problem such that each variable is alternately updated by solving independent subproblems, coordinated by dual variables [Boyd et al., 2011]. ADMM is typically suited to problems that have separable objectives with separate variables and do not require highly accurate solutions, as it is known to be prone to poor convergence at high precision. Because it is simple, scalable and offers fast convergence with warm-starting and sparsity exploitation, ADMM is widely used in embedded applications with less accuracy requirements. A well-known primal-dual ADMM solver is `osqp`.

Algorithms for NLP

For NLP optimization, algorithms fall into gradient-based and derivative-free categories. We focus on the gradient-based methods used in practical solvers, as summarized in Table 4.6. Similar to the QP problems, equality-constrained NLP problems are solved through KKT conditions, reducing to the task of finding the roots of a nonlinear system of equations. Note that this task is not trivial and usually requires numerical methods, e.g., Newton's method, to derive solutions. In contrast, inequality-constrained NLP problems are more complex due to the complementary slackness condition in KKT and require more advanced numerical methods to find the optimal solution.

To handle the inequalities in NLP problems, the existing approaches are grouped into two main strategies, which are: *sequential quadratic programming* (SQP) [Barclay et al., 1998]

TABLE 4.6: Overview of some solvers can be used via CasADi NLP interface (`nlpsol`).

Solver	Description	Principal algorithmic features
	IPM methods (IPM)	
`ipopt`	Interior Point OPTimizer [Biegler and Zavala, 2009]	Primal–dual barrier (IPM) with filter line-search.
`fatrop`	Fast constrained optimal [Vanroye et al., 2023]	Inspired from `ipopt` with structure exploiting.
	Sequential quadratic programming (SQP)	
`sqpmethod`	Classical SQP framework (built-in solver)	SQP with L1 line-search, BFGS[11]Hessian approximation.
`feasiblesqpmethod`	Feasible-point SQP variant (built-in solver)	Maintains (or enforces) feasibility during iterations.
`scpgen`	Sequential convex programming (built-in solver)	Structure exploiting SQP which projects a block sparse QP to a smaller, dense QP.
`qrsqp`	QR-enhanced SQP (built-in solver)	SQP using QR factorization for improved numerical stability.
`blocksqp`	Block-structured SQP [Janka, 2015]	SQP with filter line-search and a blockwise hybrid BFGS/SR1[12] Hessian approximation.
	Mixed-integer NLP (MINLP)	
`bonmin`	Basic Open-source Mixed INteger [Bonami et al., 2008]	Hybrid strategies: B-BB, B-OA, B-QG, B-Hyb.[13]
	Commercial solvers	
`knitro`	Nonlinear Interior point Trust Region Optimization [Byrd et al., 2006]	IPM, sequential linear-quadratic programming (SLQP).
`snopt`	Sparse Nonlinear OPTimize [Gill et al., 2005]	SQP with limited-memory quasi Newton Hessian and line-search.
`worhp`	We Optimize Really Huge Problems [Büskens and Wassel, 2012]	SQP, IPM, augmented Lagrangian for structured problems.

[6]BFGS: Broyden-Fletcher-Goldfarb-Shanno algorithm [Nocedal and Wright, 2006].
[7]SR1: Symmetric Rank-1 method [Nocedal and Wright, 2006].
[8]B-BB: branch-and-bound; B-OA: outer approximation; B-QG: Quesada–Grossmann's branch-and-cut; B-Hyb: hybrid outer-approximation based branch-and-cut.

and *penalty-function* methods. Penalty-function methods for NLP problems can include nonlinear *interior-point* methods [El-Bakry et al., 1996, Vanderbei and Shanno, 1999], *augmented Lagrangian*-based methods [Bertsekas, 2014] and the combination of both [Cao

et al., 2016]. The resulting unconstrained NLP problem or its corresponding KKT system is then numerically solved by different methods. Depending on the search direction: *steepest descent* methods, i.e., the search direction is the negative of the gradient [Meza, 2010], *conjugate gradient* methods, i.e., the search direction is a linear combination of the current gradient and the previous search direction [Hager and Zhang, 2006], *Newton's methods*, i.e., gradient and exact Hessian are used to determine the search direction or *quasi-Newton methods* such as BFGS or SR1, where approximation of the inverse Hessian is iteratively updated using gradient information [Nocedal and Wright, 2006]. Moreover, unlike QP problems, global convergence, i.e., convergence to a stationary point, is not inherently guaranteed in the numerical methods for NLP problems due to the nonlinearity of the problem. As a result, solving NLP problems must also take into account the globalization strategies, such as *line search* or *trust region* methods, which help to decide the step size along the search direction, thus ensuring convergence from arbitrary initial points [Omesa et al., 2025, Yuan, 2015].

SQP methods approximate the original NLP problem by a sequence of QP subproblems, where the solution at each iteration corresponds to the optimum of its quadratic approximation. Specifically, at each iteration, the objective function is approximated by a quadratic function and the constraints are linearized around the current point. The resulting QP subproblem is then solved by QP algorithms to obtain the search direction. Because of this property, CasADi employs the SQP method in many built-in solvers to address specific structural and numerical challenges. For instance, `sqpmethod` exploits L1 line-search and BFGS Hessian approximation, `scpgen` improves efficiency by projecting block-sparse QPs into smaller dense ones, `qrsqp` enhances numerical stability by employing QR factorization. Additionally, external SQP solvers, such as `blocksqp` and `snopt`, use hybrid strategies to enhance algorithm convergence.

Interior-point methods for NLP problems extend the QP approach, keeping inequality constraints to be strictly within the feasible region using barrier functions. In another words, they approximate the complementary slackness condition by gradually reducing the barrier parameter to zero. One of the most popular and robust open-source NLP solvers is `ipopt`, which uses the primal-dual interior-point algorithm combined with a filter line-search strategy [Wächter and Biegler, 2006]. `knitro`, `worhp` are well-known commercial NLP solvers that implement interior-point methods with various advancements to enhance

the convergence and robustness of the algorithm. It is also worth mentioning `fatrop` and `bonmin`, which have been built on top of `ipopt` to leverage properties of interior-point methods. `fatrop` is designed for large-scale problems with a focus on exploiting sparsity and structure; a reformulation of the problem is needed to benefit from the advances of the solver in terms of computational efficiency. Whereas `bonmin` combines with different methods to handle MINLP problems, e.g., branch-and-bound, outer-approximation, etc.

The advantages and limitations of these two methods are similar to those in QP problems. SQP methods are based on solving a sequence of QP subproblems, their characteristics also depend on the sub-algorithms used. Generally, they can easily be warm-started and exploit the problem structure, thus having fast convergence. However, they can be sensitive to the initial guess and may struggle with large-scale problems. Interior-point methods are known for their robustness and ability to handle large, sparse problems. However, their warm-starting is not straightforward and may require more iterations to converge, thus more computationally intensive [Forsgren et al., 2002, Gill et al., 2015].

4.4 Concluding remarks

This chapter provided a comprehensive overview of the optimization-based control design framework. It laid the theoretical and practical groundwork for the advanced control strategies that will be designed and validated in Chapter 5 and Chapter 6.

We started the chapter by defining the practical operational requirements of the SiMn SAF with the formulations of control objectives and system constraints based on Chapter 2 and Chapter 3. The control objectives employ quadratic cost functions, including different terms for setpoint tracking, i.e., minimizing the deviations of the controlled variables from their references or for mitigation of the hunting problem, i.e., minimizing the number of actuator switches. Whereas, the constraints involve both physical conditions of the actuators, e.g., tap ranges, tap balancing, etc and safety requirements of the electrical parameters, e.g., electrode current limits, impedance ranges, etc.

Then, we focused on describing the validation frameworks for control algorithms developed in the subsequent chapters. In particular, we introduced performance metrics that will be used to evaluate the effectiveness of the designed control strategies. Additionally,

we presented a software-in-the-loop (SIL) environment developed for implementing and validating the control algorithms. This features a high-fidelity simulator of the SiMn SAF, replicating the behavior of the real plant and integrating various subsystems such as electrical, operational modules, etc. Notably, the control module is implemented as a separate process running in parallel with the simulator, allowing for online computation of the optimization problem and real-time interaction with other subsystems.

In the context of SAF control design, including the furnace models presented in Chapter 3, the control objectives and system constraints involving integer-valued tap variables discussed herein, it is essential to adopt MI-MPC strategies, which are particularly well-suited for addressing the particularity of this control problem. As a result, we explored the theoretical foundations and practical implementation aspects of MI-MPC.

Thus, we focused on MPC, MIP and CasADi modeling framework as the core components of our implementation. Specifically, we presented the principles of MPC, emphasizing its strengths in handling multivariable, nonlinear and constrained systems [Rawlings et al., 2017]. We also highlighted the importance of terminal ingredients for recursive feasibility and closed-loop stability guarantee [Mayne et al., 2000]. Then, we introduced MIP as a powerful framework for addressing the discrete decision variables and provided an overview of solution techniques, including exact as well as heuristic methods [Grossmann, 2002, Berthold, 2015]. Finally, we reviewed the available modeling languages and numerical solvers, highlighting CasADi for its flexibility, efficient algorithmic differentiation and seamless integration with state-of-the-art solvers for quadratic, nonlinear, and mixed-integer programming problems [Andersson et al., 2019].

Chapter 5

Independent power and current control

This chapter presents two control designs, one for transformer active power and the other for electrode currents in the three-phase SAF. This framework enables the development of a coordinated control system in the next chapter.

Based on the detailed electrical model presented in Chapter 3 and the operational requirements outlined in Section 4.1, we propose two different MPC strategies. The first scheme controls transformer active power by adjusting tap changer positions, while the second scheme regulates electrode currents by adjusting electrode heights.

In Section 5.1, we propose a multi-phase magnitude current control framework, designed to regulate currents in all three phases. Additionally, Section 5.2 presents the design of an MI-MPC for three-phase active power regulation. This design captures the nature of discrete tap changer positions via a MINLP formulation. To reduce the number of tap changer switches and address the computational burden of the MIP problem, we introduce an adaptive penalty strategy and a model-informed optimal rounding (MIOR) heuristic.

Each section includes implementation details and performance evaluation via various simulations using the SIL simulator described in Section 4.2.2. Our proposed control strategies are compared with classical methods and also the state-of-the-art MIP solvers.

5.1 Electrode current control

This section presents a centralized predictive control strategy for regulating the electrode currents in a three-phase SAF by manipulating the electrode positions. We describe the control architecture, followed by constrained optimization formulations using nonlinear and linearized models. Lastly, we evaluate their performance through SIL simulations.

5.1.1 Multi-phase current control architecture

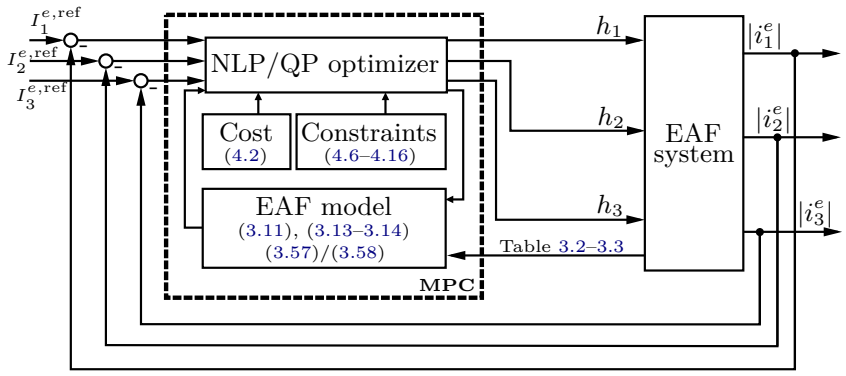

FIGURE 5.1: Proposed centralized MPC architectures to control electrode currents in all three phases by adjusting electrode heights.

The detailed MPC architecture for current control is illustrated in Figure 5.1. It employs a centralized framework where the controller adjusts the three electrode heights $\boldsymbol{h}$ to track the desired current magnitude references $\boldsymbol{I}^{\boldsymbol{e},\mathrm{ref}}$. By leveraging the detailed electrical model developed in Chapter 3, the controller accounts for the interaction effects between phases, which cannot be achieved in a decoupled controller.

The control strategy penalizes the cost function (4.2) to regulate the magnitude of the three electrode currents $|\boldsymbol{i}^{\boldsymbol{e}}|$. This is the most common approach for current control in industrial furnace operation. Depending on the electrical output model used, the problem can be formulated as either a nonlinear program (NLP) with nonlinear model (3.57) or a quadratic program (QP) with linearized model (3.58).

The controller explicitly incorporates the operational constraints defined in Chapter 4, which must be satisfied at all times. In the following, we will detail the formulation of the control problem and evaluate its performance through long-term simulations.

5.1.2 Magnitude control formulation

Given the dynamical models described in Section 3.3.1, steady-state models presented in 3.3.2, objectives and constraints introduced in Section 4.1, the magnitude predictive control problem is formulated as an NLP problem (5.1) at each sampling instant k over a finite prediction horizon N_p. The optimization variable is the sequence of electrode displacements $\boldsymbol{\delta h}(\cdot|k) = [\boldsymbol{\delta h}(0|k), \boldsymbol{\delta h}(1|k), \ldots, \boldsymbol{\delta h}(N_p-1|k)] \in \mathbb{R}^{3\times N_p}$. The objective function (5.1a) minimizes the current magnitude cost $J_I(\cdot)$ from (4.2). The optimization is subject to initial conditions (5.1b) and constraints including the system dynamics (5.1c), the nonlinear output relation (5.1d) and all operational constraints (5.1e)–(5.1g).

- NLP problem for current magnitude control (NMPC):

$$\delta\mathbf{h}^*(\cdot|k) = \arg\min_{\delta\mathbf{h}(\cdot|k)} \underbrace{\sum_{s=0}^{N_p-1} \overbrace{J_I(s+1|k)}^{(4.2)}}_{L_I\left(|\boldsymbol{i}^e(s+1|k)|\right)}, \tag{5.1a}$$

s.t. $\forall s \in [0,\, N_p-1]$:

$$\boldsymbol{h}(0|k), \boldsymbol{r}(0|k), \boldsymbol{x}(0|k) = \boldsymbol{h_0}, \boldsymbol{r_0}, \boldsymbol{x_0}, \tag{5.1b}$$

Linear dynamics (3.11), (3.13)–(3.14), (5.1c)

Nonlinear outputs (3.57), (5.1d)

Electrode holder position constraint (4.10), (5.1e)

Electrode-process impedance constraints (4.12)–(4.13), (5.1f)

Electrical output constraints (4.14)–(4.16), (5.1g)

Electrode displacement constraint (4.11). (5.1h)

From here, we can see that the output (5.1d) is nonlinear, which makes the control problem (5.1) become a nonlinear MPC problem. For the interest of solving the approximated QP of this NLP problem, we replace the nonlinear output equation (5.1d) by its linearized version around the current operating point. This leads to:

- QP problem for current magnitude control (LMPC):

$$\delta\mathbf{h}^*(\cdot|k) = \arg\min_{\delta\mathbf{h}(\cdot|k)} L_I(\cdot) \text{ in (5.1a)}, \tag{5.2a}$$

$$\text{s.t. } \forall s \in [0,\, N_p - 1]:$$

$$\mathbf{x}(s+1|k) = \mathbf{A}\mathbf{x}(s|k) + \mathbf{B}(k)\delta\mathbf{h}(s|k), \tag{5.2b}$$

$$\mathbf{F}\mathbf{x}(s+1|k) - \mathbf{q} \leq 0,\ \mathbf{x}(0|k) = \mathbf{x_0}, \tag{5.2c}$$

$$\mathbf{G}\delta\mathbf{h}(s|k) - \mathbf{k} \leq 0. \tag{5.2d}$$

In the QP formulation (5.2), the state vector is defined as $\mathbf{x}(s|k) \triangleq [\boldsymbol{h},\, \boldsymbol{r},\, \boldsymbol{x},\, \mathbf{y}]^\top \in \mathbb{R}^{18}$. The objective function (5.2a) remains the same quadratic cost on current deviation. The system is described by the linearized model (5.2b), where $\mathbf{A} = \mathbf{I}_{18}$ is an identity matrix and $\mathbf{B}(k) \triangleq \left[\mathbf{I}_3,\, \boldsymbol{\Gamma}^{\boldsymbol{x}}(k),\, \boldsymbol{\Gamma}^{\boldsymbol{r}}(k),\, \mathbf{J}^{\boldsymbol{h}}(k)\right]^\top \in \mathbb{R}^{18\times 3}$ is a time-varying matrix combining (3.13), (3.14) and (3.58) linearized at every operating point. The operational limits are compactly represented by the linear inequality constraints on the state (5.2c) and the control input (5.2d), with the corresponding coefficients defined as:

$$\mathbf{F} \triangleq \begin{bmatrix} \mathbf{I}_{18} \\ -\mathbf{I}_{18} \end{bmatrix}, \quad \mathbf{q} \triangleq \begin{bmatrix} [\boldsymbol{h}_{\mathbf{ub}},\, \boldsymbol{r}_{\mathbf{ub}},\, \boldsymbol{x}_{\mathbf{ub}},\, \boldsymbol{p}^{\boldsymbol{s}}_{\mathbf{ub}},\, \boldsymbol{I}^{\boldsymbol{s}}_{\mathbf{ub}},\, \boldsymbol{I}^{\boldsymbol{e}}_{\mathbf{ub}}]^\top \\ [\boldsymbol{h}_{\mathbf{lb}},\, \boldsymbol{r}_{\mathbf{lb}},\, \boldsymbol{x}_{\mathbf{lb}},\, \boldsymbol{p}^{\boldsymbol{s}}_{\mathbf{lb}},\, \boldsymbol{I}^{\boldsymbol{s}}_{\mathbf{lb}},\, \boldsymbol{I}^{\boldsymbol{e}}_{\mathbf{lb}}]^\top \end{bmatrix},$$

$$\mathbf{G} \triangleq \begin{bmatrix} \mathbf{I}_3 \\ -\mathbf{I}_3 \end{bmatrix}, \quad \mathbf{k} \triangleq \begin{bmatrix} \boldsymbol{\Delta h}_{\mathbf{max}} \\ \boldsymbol{\Delta h}_{\mathbf{max}} \end{bmatrix},$$

These bound vectors are detailed in Section 4.1.4. The initial state vector $\mathbf{x_0} \in \mathbb{R}^{18}$ in (5.2c) is taken from the measurement system at each sampling instant k. In addition to the initial values used in (5.1b), the initial outputs $\mathbf{y_0} \in \mathbb{R}^9$ are also needed for the linearized output (3.58). As the constraints are linear and the cost is quadratic, the problem is a QP, which can be solved by standard QP solvers, e.g. `qpOASES`, `OSQP`.

5.1.3 Long-term simulation analysis

To evaluate the performance of the proposed MPC strategies for electrode current control, we implemented a series of long-term simulations using the SIL simulator described in Section 4.2.2. Consequently, we show and analyze the simulation results below.

5.1.3.1 Scenario setup

Let us define in Table 5.1 the information of two scenarios running over 24 hours to compare the proposed magnitude predictive control developed in Section 5.1.2 against a conventional controller, which will be briefly described in the following.

TABLE 5.1: Details of implemented scenarios for electrode current control.

Scenario	Approach	Reference Value	Ref. Characteristics	Run Time
1	Table 5.2	140−140−140kA	Balanced	24 hours
2		135−130−140kA	Unbalanced	

TABLE 5.2: A brief explanation of the control approaches for electrode current regulation.

No.	Approach	Problem	Solver	Strategy
i	GS	–	–	Classical GS controller.
ii	NMPC	(5.1)	`IPOPT`	Solves the original NLP problem directly.
iii	LMPC	(5.2)	`qpOASES`	Solves the QP approximation of the NLP.

Here, we have the simulations in scenario one run under balanced setpoints of 140 kA per phase, while scenario 2 extends to unbalanced setpoints of 135, 130 and 140kA for three electrode currents, respectively. The implemented approaches for both scenarios include solving the NLP (5.1) and QP (5.2) formulations using the corresponding solvers in Table 5.2. Accordingly, they are denoted as NMPC and LMPC to distinguish the nonlinear and linearized models used in each optimization problem.

Additionally, GS is also implemented for comparison with MPC methods. This conventional control strategy mimics the industrial controller by employing a simplified, decoupled strategy. Particularly, at each time step k, $\delta\mathbf{h}(k)$ is determined by:

$$\delta\mathbf{h}(k) = -\mathbf{K} \cdot \left(\boldsymbol{I}^{e}(k) - \boldsymbol{I}^{e,\mathrm{ref}}(k) \right), \tag{5.3}$$

where the gain matrix $\mathbf{K} \in \mathbb{R}^{3\times3}$ determine the proportional gains for the three currents.

Table 5.3 details the numerical values of the controller parameters used consistently throughout the simulations in this section. These include the sampling time T_s, horizon N_p, objective values $\boldsymbol{\epsilon}^{i}$, $\boldsymbol{I}^{e,\mathrm{ref}}$, $\mathbf{Q}^{\mathbf{I}}$. All constraint-related variables are also included.

TABLE 5.3: Numerical values of control parameters for electrode current control.

Parameter	Value	Unit	Parameter	Value	Unit
Time			**Constraint**		
T_s	500	ms	$[\boldsymbol{h_{\text{lb}}}, \boldsymbol{h_{\text{ub}}}]$	$[5, 105]\,\mathbf{I_{3\times1}}$	cm
N_p	1	–	$[\boldsymbol{r_{\text{lb}}}, \boldsymbol{r_{\text{ub}}}]$	$[0.2, 2\times10^3]\,\mathbf{I_{3\times1}}$	mΩ
Objective			$[\boldsymbol{x_{\text{lb}}}, \boldsymbol{x_{\text{ub}}}]$	$[0.2, 2\times10^3]\,\mathbf{I_{3\times1}}$	mΩ
$\boldsymbol{\epsilon^i}$	$0.5\,\mathbf{I_{3\times1}}$	kA	$[\boldsymbol{p^s_{\text{lb}}}, \boldsymbol{p^s_{\text{ub}}}]$	$[1, 25\times10^3]\,\mathbf{I_{3\times1}}$	kW
$\boldsymbol{I}^{\boldsymbol{e},\text{ref}}$	Defined in Table 5.1	–	$[\boldsymbol{I^s_{\text{lb}}}, \boldsymbol{I^s_{\text{ub}}}]$	$[10, 84.2]\,\mathbf{I_{3\times1}}$	kA
$\mathbf{Q^I}$	$\mathbf{I_{3\times1}}$	–	$[\boldsymbol{I^e_{\text{lb}}}, \boldsymbol{I^e_{\text{ub}}}]$	$[17, 145]\,\mathbf{I_{3\times1}}$	kA
			$\boldsymbol{\Delta h_{\text{max}}}$	$5\,\mathbf{I_{3\times1}}$	cm

5.1.3.2 Performance evaluation

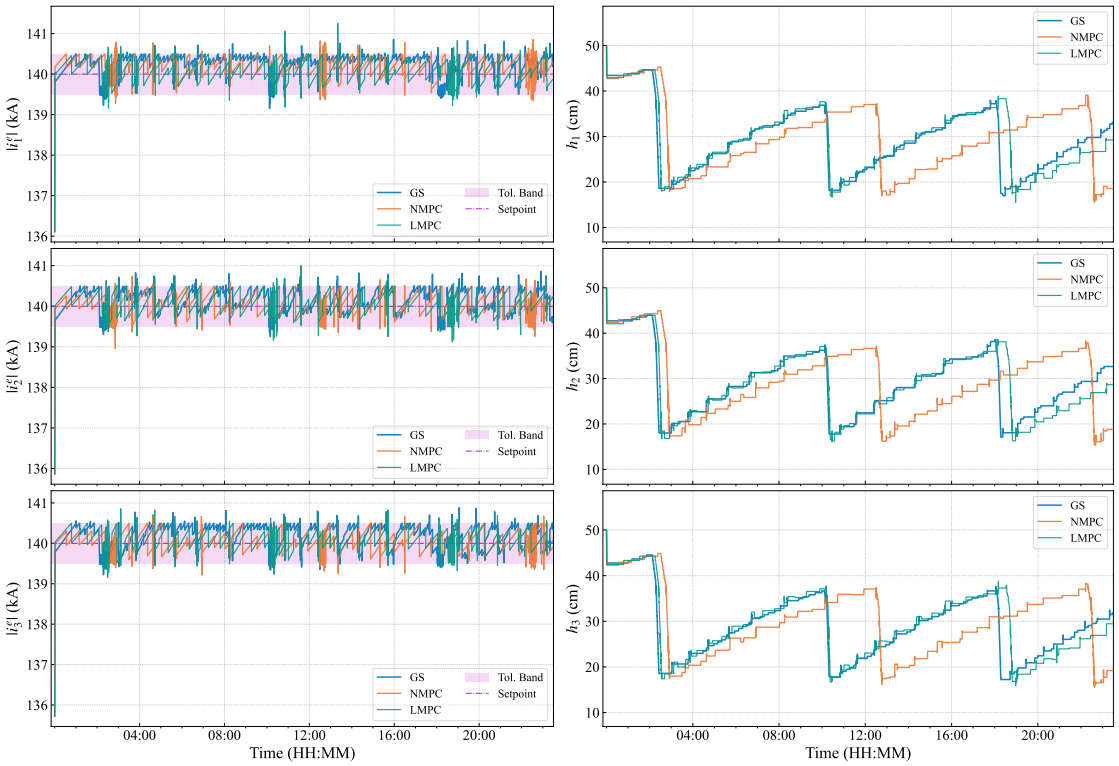

(A) Electrode current magnitudes. (B) Electrode positions.

FIGURE 5.2: Controlled output and input performance comparison between GS (blue), NMPC (orange) and LMPC (green) approaches under balanced setpoints (Scenario 1).

Here, we present the simulation results in several figures and summarize the overall performance using the metrics defined in Section 4.2.1.

In particular, Figure 5.2 shows both controlled outputs and control signals over the 24-hour simulation of scenario 1 with balanced current setpoints. The left figures illustrate the electrode current magnitudes $|\boldsymbol{i}^{\boldsymbol{e}}|$ tracking the reference $\boldsymbol{I}^{\boldsymbol{e},\mathrm{ref}}$ for all three control approaches, i.e., GS, NMPC and LMPC. The right-hand figures show the corresponding electrode heights $\boldsymbol{h}$ for all three phases sent to the PLC system.

The results demonstrate that both MPC-based strategies achieve good tracking performance around the setpoints, with values mainly remaining within the tolerance band. In contrast, the GS controller exhibits noticeable steady state offsets due to the neglect of phase interactions and the choice of unoptimized gain in (5.3). This is further shown by the metric values in Table 5.4, where NMPC and LMPC have lower RCD and OCT in every phase than GS.

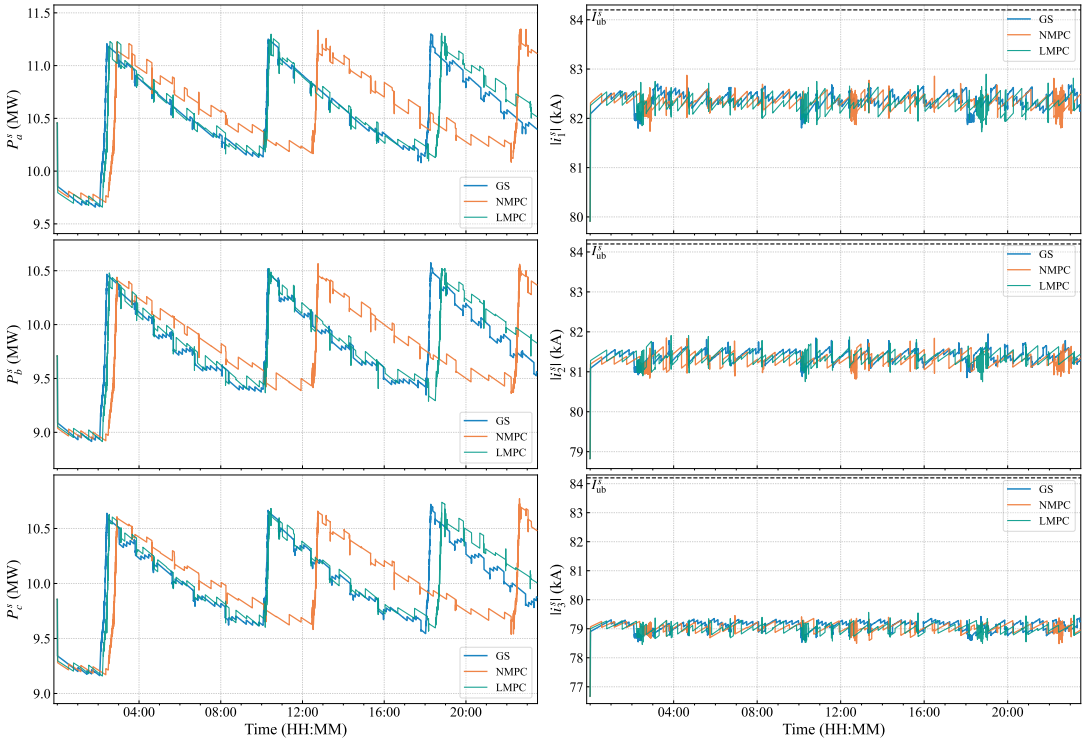

(A) Active powers in three phases. (B) Secondary current magnitudes.

FIGURE 5.3: Electrical outputs under operational constraints (Scenario 1).

In addition, Figure 5.3 illustrates the other outputs of interests in scenario one including secondary active powers $\boldsymbol{p^s}$ and current magnitudes $|\boldsymbol{i^s}|$, which are not directly controlled but are required to remain within operational limits, e.g., $p^s_{\text{ub}} = 25\,\text{MW}$, $I^e_{\text{ub}} = 84.2\,\text{kA}$. In this scenario, the system does not have to operate very close to the constraints; hence, all three controllers always maintain these variables within the feasible regions.

Similar observations on the tracking performance can be made for scenario 2. Figure 5.4 presents the electrode current magnitudes tracking over unbalanced current setpoints and the corresponding electrode heights $\boldsymbol{h}$. Both NMPC and LMPC effectively stabilize these variables around their desired setpoints at 135 kA, 130 kA and 140 kA for the three phases, respectively. At the same time, the GS controller still induces an offset at the upper tolerance bounds. Due to the slight deviation from the setpoints, the GS approach causes the electrode to move over shorter distances but more frequently. This is why we can see sharper deviations in the electrode heights compared to the smoother movements from the two MPC-based controllers in Figure 5.4b.

Moreover, Figure 5.5 also demonstrates the behavior of the electrode-process resistance $\boldsymbol{r}$ and reactance $\boldsymbol{x}$, which are essential variables reflecting the process condition. Their behaviors are conversely related: when the resistance is lowered by the enhanced conductivity of the molten bath, the reactance increases, and vice versa. Under power control, current can be indirectly regulated via resistance control, as explained in Section 2.1.3.2. This can be further investigated in future work.

It is worth mentioning that the sudden increase of powers, resistance in Figure 5.3a, in Figure 5.5a and decrease of reactance in Figure 5.5b are caused by the casting operation, which was introduced in Section 2.2.2. When the molten metal and slag are cast from the furnace, the bath level drops suddenly, increasing the process impedance and causing the electrode currents to drop sharply. Therefore, the controllers reduce the electrode heights to compensate for the current drop.

Regarding the computation time, GS is obviously more efficient as the solution is straightforward. In contrast, both NMPC and LMPC require solving optimization problems online at each sampling instant. Figure 5.6 presents the CPU time needed for two approaches at every time step, whereas Table 5.4 summarizes the average CPU time over the entire 24-hour simulation period. The results indicate that the computation

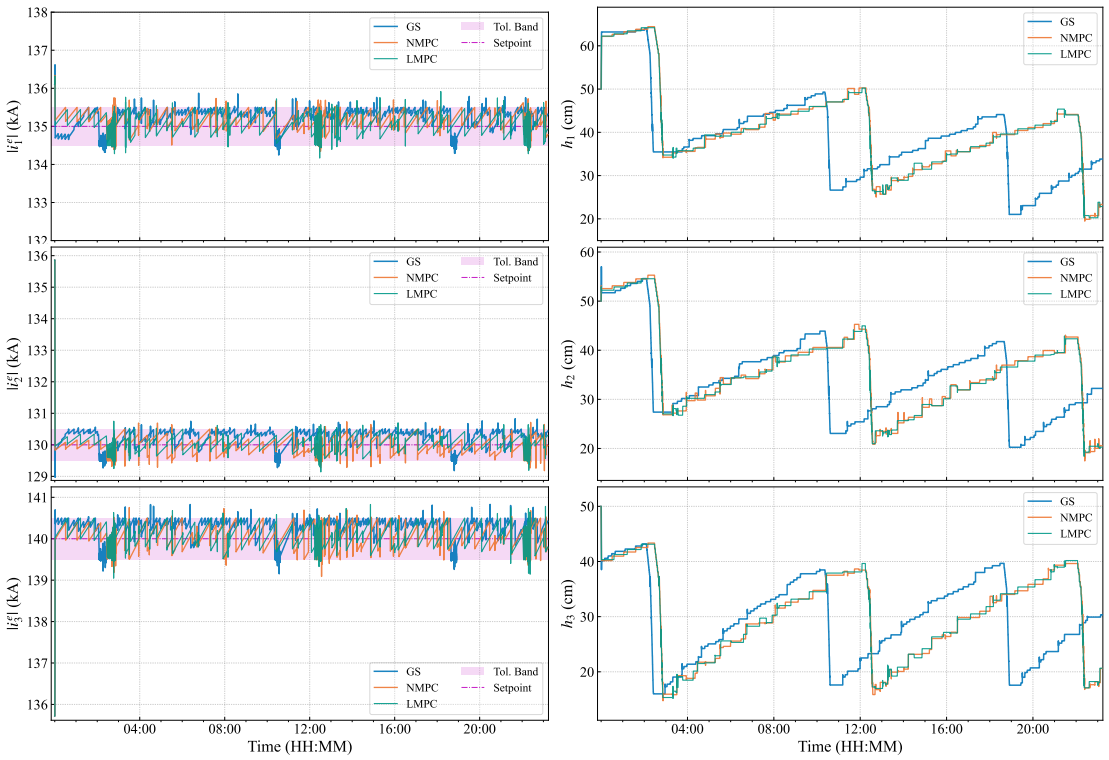

(A) Electrode current magnitudes. (B) Electrode positions in three phases.

FIGURE 5.4: Current magnitude control performance comparison between GS (blue), NMPC (orange) and LMPC (green) approaches under unbalanced setpoints (Scenario 2).

time of LMPC is always less than 2 ms, while NMPC is approximately 10 and 30 times slower in scenarios 1 and 2, respectively.

The other tracking comparison among the three approaches is also displayed in Table 5.4. Overall, we can see that LMPC achieves the best performance. Despite NMPC also outperforming GS across all metrics, it is less effective than LMPC, especially in CPU time. This highlights the advantage of using linearized models to reduce computational burden while maintaining control performance.

5.1.3.3 Discussion

The simulation results validate the effectiveness of the proposed MPC strategies for electrode current control with a very short predictive horizon, $N_p = 1$. This is due to

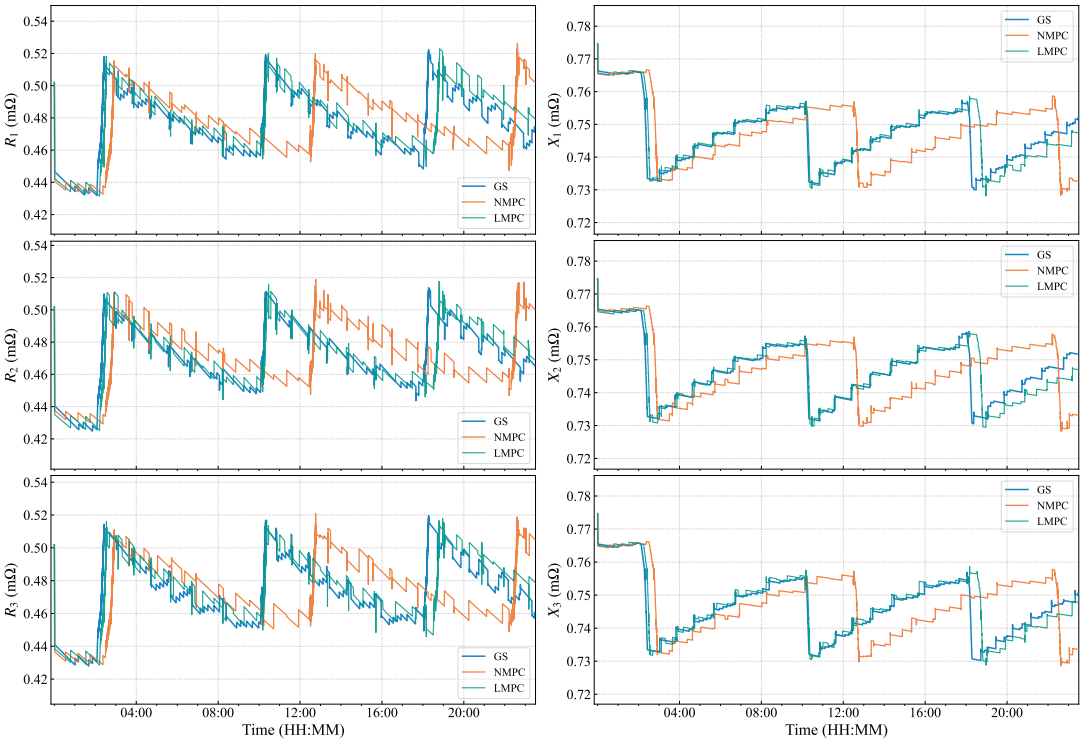

(A) Electrode-process resistances. (B) Electrode-process reactances.

FIGURE 5.5: Electrode-process impedance behaviors (Scenario 2).

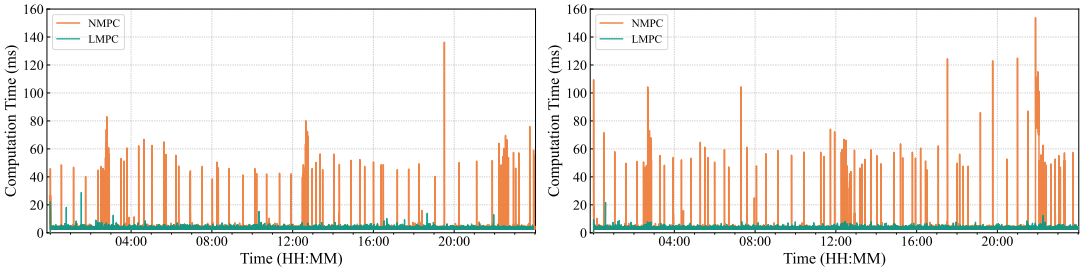

(A) Scenario 1 (B) Scenario 2.

FIGURE 5.6: Comparison of computation time per time step.

TABLE 5.4: Statistical results across three phases over 24 hours (Scenario 1 & 2).

Approach	**Reference Deviation** (%)				**Outside Tolerance** (%)				**CPU**
	RCD_1	RCD_2	RCD_3	$\mathbf{RCD_M}$	OCT_1	OCT_2	OCT_3	$\mathbf{OCT_M}$	(ms)
Scenario 1									
GS	0.25	0.22	0.24	**0.24**	0.69	0.70	0.74	**0.71**	–
NMPC	0.19	0.17	0.16	**0.17**	0.37	0.27	0.25	**0.30**	21.34
LMPC	0.18	0.18	0.17	**0.18**	0.27	0.31	0.26	**0.28**	1.85
Scenario 2									
GS	0.25	0.28	0.26	**0.26**	0.83	0.80	0.85	**0.83**	–
NMPC	0.19	0.18	0.18	**0.18**	1.02	0.43	0.32	**0.59**	50.79
LMPC	0.18	0.17	0.18	**0.18**	0.33	0.21	0.27	**0.27**	1.75

Lower value represents better performance.

the linear models of electrode-process impedance (3.13)–(3.14), which can not accurately capture the impedance dynamics over longer horizons as explained in Section 3.3.1.2.

However, even with such a short horizon, both NMPC and LMPC approaches outperform the conventional GS controller in tracking performance, thanks to their model-based, centralized frameworks that account for interaction effects among phases. Moreover, they can handle complex constraints systematically, ensuring safe operation. The importance of constraint handling, however, is not highlighted here but will be further emphasized in the MIP control design in the following sections.

The tracking performance between NMPC and LMPC is quite similar. The difference lies in the computational effort required to solve the respective optimization problems. With linearized models, LMPC offers a significantly lower computational cost than NMPC.

5.2 Integer-based power control

In the following, we present the design of an MI-MPC for three active power regulation. First, we present the control scheme and formulate the control problem as an MINLP to handle the integer nature of the tap deviations explicitly. Then, we incorporate an MIQP formulation using linearized models to improve computational efficiency. To further

reduce the computational cost, we introduce a heuristic strategy, so-called model-informed optimal rounding (MIOR).

5.2.1 Multi-phase power architecture

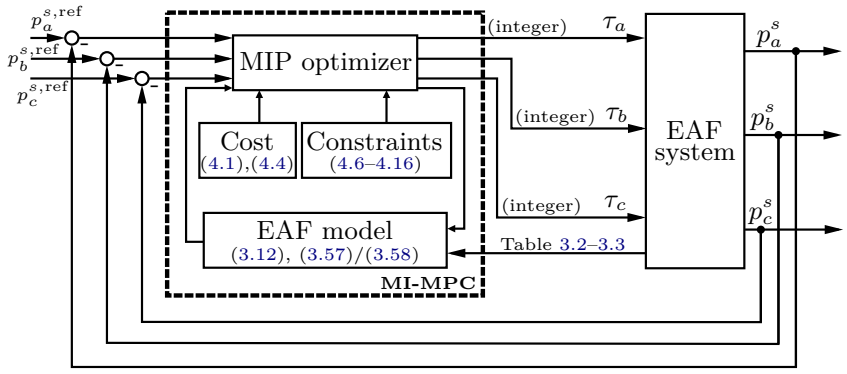

FIGURE 5.7: Proposed centralized MI-MPC architecture to control the transformer active powers in all three phases by adjusting tap positions.

The proposed MI-MPC architecture for power control is illustrated in Figure 5.7. This scheme employs a centralized framework in which the controller adjusts the transformer tap positions $\boldsymbol{\tau}$ across all three transformers to track desired active power setpoints $\boldsymbol{p}^{\boldsymbol{s},\mathrm{ref}}$.

Similar to current control schemes, the MI-MPC can account for interactions between phases through models constructed in Chapter 3. This is particularly interesting, as such interactions also occur in power regulation but are not studied in the literature. Moreover, MI-MPC penalizes the power deviation cost (4.1) to regulate the three active powers $\boldsymbol{p}^{\boldsymbol{s}}$ and tap switching cost (4.4) to reduce the number of tap changes. It also explicitly incorporates the operational constraints defined in Chapter 4, which must be satisfied in furnace operation, regardless of the control objectives.

Additionally, the approach allows for the direct handling of tap changer variations as integer variables within the control problem. As there are no continuous variables in the optimization, the problems become purely integer problems as indicated in Section 5.2.2. Consequently, it increases computational complexity, which must be addressed by efficient algorithms developed in Section 5.2.3.

5.2.2 Integer programming formulation

Given the system models from Chapter 3 and the operational requirements from Section 4.1, we formulate the integer-based power control problem as a MINLP problem (5.4) over a prediction horizon N_p.

- MINLP-based MPC for multi-phase power control (MINLP):

$$\boldsymbol{\delta\tau}^*(\cdot|k) = \arg\min_{\boldsymbol{\delta\tau}(\cdot|k)} \underbrace{\sum_{s=0}^{N_p-1} \overbrace{J_P(s+1|k)}^{(4.1)} + \overbrace{J_\tau(s+1|k)}^{(4.4)}}_{L_{P\tau}\left(\boldsymbol{p}^s(s+1|k),\, \boldsymbol{\delta\tau}(s|k)\right)}, \tag{5.4a}$$

s.t. $\forall s \in [0,\, N_p - 1]$:

$$\boldsymbol{\tau}(0|k) = \boldsymbol{\tau_0}, \tag{5.4b}$$

Linear dynamics (3.12), (5.4c)

Nonlinear outputs (3.57), (5.4d)

Tap position constraints (4.6) and (4.9), (5.4e)

Electrical output constraints (4.14)–(4.16), (5.4f)

Tap deviation and integer constraints (4.7)–(4.8). (5.4g)

The optimization variable is the sequence of tap variations $\delta\tau(\cdot|k) \in \mathbb{Z}^{3\times N_p}$. The objective (5.4a) is a quadratic function, minimizing the power regulation cost $J_P(\cdot)$ from (4.1) and the tap switching penalty $J_\tau(\cdot)$ from (4.4). The optimization is subject to initial tap position (5.4b) and constraints including the system dynamics (5.4c), the nonlinear output (5.4d) and complete operational constraints (5.4e)–(5.4g).

The presence of integer constraints in (5.4g) and the nonlinear output (5.4d) makes (5.4) become a MINLP problem. Even if the problem is purely integer, solving it directly using standard MINLP solvers, e.g., `Bonmin`, remains complicated in real-time optimization. As a result, we propose to approximate the MINLP problem by applying the Taylor series expansion on (3.57). This results in using the linear form (3.58) in the following MIQP.

- MIQP-based MPC for multi-phase power control (MIQP):

$$\boldsymbol{\delta\tau}^*(\cdot|k) = \arg\min_{\boldsymbol{\delta\tau}(\cdot|k)} L_{P\tau}(\cdot) \text{ in (5.4a)}, \tag{5.5a}$$

$$\text{s.t. } \forall s \in [0,\, N_p - 1]:$$

$$\mathbf{x}(s+1|k) = \mathbf{A}\mathbf{x}(s|k) + \mathbf{B}(k)\boldsymbol{\delta\tau}(s|k), \tag{5.5b}$$

$$\mathbf{F}\mathbf{x}(s+1|k) - \mathbf{q} \leq 0,\ \mathbf{x}(0|k) = \mathbf{x_0}, \tag{5.5c}$$

$$\mathbf{G}\boldsymbol{\delta\tau}(s|k) - \mathbf{k} \leq 0, \tag{5.5d}$$

$$\boldsymbol{\delta\tau}(s|k) \in \mathbb{Z}^3. \tag{5.5e}$$

In the MIQP formulation (5.5), the state vector is defined as $\mathbf{x}(s|k) \triangleq [\boldsymbol{\tau},\, \mathbf{y}]^\top \in \mathbb{R}^{12}$. The objective (5.5a) remains the same. The system is characterized by the linearized model (5.5b), where $\mathbf{A} = \mathbf{I}_{12}$ is an identity matrix and $\mathbf{B}(k) \triangleq [\mathbf{I}_3,\, \mathbf{J}^{\boldsymbol{\tau}}(k)]^\top \in \mathbb{R}^{12\times 3}$ is a time-varying matrix. $\mathbf{J}^{\boldsymbol{\tau}}(k)$ denoted in (3.58), is the Jacobian of the output model (3.57) with respect to the tap positions $\boldsymbol{\tau}$, evaluated at the current operating point.

The operational limits are compactly represented by the linear inequality constraints on the state (5.5c) and the control input (5.5d), with the corresponding coefficients:

$$\mathbf{F} \triangleq \begin{bmatrix} \mathbf{I}_{12} \\ -\mathbf{I}_{12} \\ \mathbf{L} \quad \mathbf{0_{6\times 18}} \end{bmatrix}, \quad \mathbf{q} \triangleq \begin{bmatrix} [\boldsymbol{\tau}_{\mathbf{ub}},\, \boldsymbol{p}^{\boldsymbol{s}}_{\mathbf{ub}},\, \boldsymbol{I}^{\boldsymbol{s}}_{\mathbf{ub}},\, \boldsymbol{I}^{\boldsymbol{e}}_{\mathbf{ub}}]^\top \\ [\boldsymbol{\tau}_{\mathbf{lb}},\, \boldsymbol{p}^{\boldsymbol{s}}_{\mathbf{lb}},\, \boldsymbol{I}^{\boldsymbol{s}}_{\mathbf{lb}},\, \boldsymbol{I}^{\boldsymbol{e}}_{\mathbf{lb}}]^\top \\ \gamma \times \mathbf{I_{6\times 1}} \end{bmatrix}, \ \mathbf{L} \triangleq \begin{bmatrix} 1 & -1 & 0 \\ -1 & 1 & 0 \\ 0 & 1 & -1 \\ 0 & -1 & 1 \\ 1 & 0 & -1 \\ -1 & 0 & 1 \end{bmatrix}$$

$$\mathbf{G} \triangleq \begin{bmatrix} \mathbf{I}_3 \\ -\mathbf{I}_3 \end{bmatrix}, \quad \mathbf{k} \triangleq \begin{bmatrix} \boldsymbol{\Delta\tau_{max}} \\ \boldsymbol{\Delta\tau_{max}} \end{bmatrix},$$

The scalar γ representing maximum tap difference among the phases and all operational bound vectors are defined in Section 4.1.4. The initial state vector $\mathbf{x_0} \in \mathbb{R}^{12}$ in (5.5c), including tap positions and interested outputs, is fully provided by the measurement system at each sampling instant k.

5.2.3 Model-informed optimal rounding

Solving the MINLP problem (5.4) directly is computationally expensive, while its MIQP approximation (5.5) slightly improves the efficiency but may be subject to undesirable behaviors due to linearization errors. To further enhance computational efficiency and ensure safety, we introduce model-informed optimal rounding (MIOR).

This heuristic approach approximates the MINLP solution by combining a relaxed QP problem with a guided search using optimal rounding. The concept is similar to relax-and-round techniques commonly used in integer programming. However, MIOR incorporates the original nonlinear model into the feasibility and optimality checks to enhance rounding quality and, consequently, the final solution.

The MIOR strategy is designed to efficiently handle problems involving only integer variables. It also serves as the foundation for the more advanced Bilevel strategy, presented in Section 6.1.3, which addresses the mixed-integer problem. Herein, we present the basic MIOR procedure in Algorithm 5.1, while a more detailed discussion on heuristic design and enhancement techniques will be provided in Section 6.1.3.

QP Relaxation : relax the MIQP problem (5.5) into a so-call QP-relaxation problem by removing the integer constraint (5.5e), thus we have (5.6). Solving this QP relaxation yields a continuous optimal control sequence $\boldsymbol{\delta\check{\tau}}(\cdot|k) \in \mathbb{R}^{3\times N_p}$:

$$\boldsymbol{\delta\check{\tau}}(\cdot|k) = \arg\min_{\boldsymbol{\delta\tau}(\cdot|k)} L_{P\tau}(\cdot) \text{ in (5.4a)}, \tag{5.6a}$$

$$\text{s.t. } \forall s \in [0,\, N_p - 1]:$$

$$\text{Linear dynamics (5.5b)}, \tag{5.6b}$$

$$\text{State and input constraints (5.5c), (5.5d)}, \tag{5.6c}$$

Heuristic Search : apply a three-step heuristic strategy to derive a feasible and sub-optimal integer solution $\boldsymbol{\delta\tilde{\tau}}(\cdot|k) \in \mathbb{Z}^{3\times N_p}$ from the continuous solution $\boldsymbol{\delta\check{\tau}}(\cdot|k)$:

- *Dual Rounding*: Determine the rounding set $\mathcal{R}(k)$ by applying downward $\lfloor\cdot\rfloor$ and upward rounding $\lceil\cdot\rceil$ to the continuous decision $\boldsymbol{\delta\breve{\tau}}(\cdot|k) \in \mathbb{R}^{3\times N_p}$:

$$\mathcal{R}(k) \triangleq \left\{\boldsymbol{\delta\hat{\tau}}(\cdot|k) \in \mathbb{Z}^{3\times N_p} \;\middle|\; \forall s, j:\ \delta\hat{\tau}_j(s|k) \in \left\{\lfloor \delta\breve{\tau}_j(s|k)\rfloor, \lceil \delta\breve{\tau}_j(s|k)\rceil\right\}\right\}, \tag{5.7}$$

  This step produces a set of $2^{3\times N_p}$ integer candidates by considering all possible combinations of rounding for each element in the continuous solution.

- *Feasibility Searching*: Evaluate each integer candidate $\boldsymbol{\delta\hat{\tau}}(\cdot|k)$ from the rounding set $\mathcal{R}(k)$ against the operational constraints. This step filters out any candidates that would violate the constraints in (5.4), thus yielding set $\mathcal{F}(k)$:

$$\mathcal{F}(k) \triangleq \{\boldsymbol{\delta\hat{\tau}}(\cdot|k) \in \mathcal{R}(k) \mid \text{constraints in (5.4b–5.4g) are satisfied}\}. \tag{5.8}$$

- *Optimality Searching*: The final integer solution $\boldsymbol{\delta\tilde{\tau}}(\cdot|k)$ is selected from the feasible set $\mathcal{F}(k)$ by searching for the candidate that minimizes the original quadratic cost function $L_{P\tau}(\cdot)$ from (5.4a):

$$\boldsymbol{\delta\tilde{\tau}}(\cdot|k) = \arg\min_{\boldsymbol{\delta\hat{\tau}}\in\mathcal{F}} L_{P\tau}(\cdot).$$

This MIOR algorithm provides the suboptimal solution $\boldsymbol{\delta\tilde{\tau}}(\cdot|k)$ to the MIP problem by avoiding the use of exact methods integrated into MIP solvers. Instead, it leverages the continuous solution from the QP relaxation and uses the simple heuristics to guide the search. Thus, it significantly reduces the computational burden of solving the original MINLP problem (5.4). We will validate MIOR's effectiveness in the following subsection.

5.2.4 Long-term simulation analysis

This section evaluates the performance of the proposed integer-based power control strategies. Moreover, it assesses the effectiveness of the adaptive switching cost function and the MIOR algorithm through a series of long-term simulations using the SIL simulator.

Algorithm 5.1: Model-informed optimal rounding (MIOR) strategy

Input: MINLP (5.4) and MIQP (5.5)
Output: Suboptimal integer solution $\boldsymbol{\delta\tilde{\tau}}(\cdot|k)$.

`/* Phase 1: QP Relaxation */`
Relax (5.5) by removing integer constraint (5.5e).
Solve the QP relaxation to obtain $\boldsymbol{\delta\breve{\tau}}(\cdot|k) \in \mathbb{R}^{3\times N_p}$.

`/* Phase 2: Heuristic Search */`
Step 1 `DualRounding(`$\boldsymbol{\delta\breve{\tau}}$`):`
  if $\boldsymbol{\delta\breve{\tau}}(\cdot|k) \in \mathbb{Z}^{3\times N_p}$ **then**
    $\boldsymbol{\delta\tilde{\tau}}(\cdot|k) \leftarrow \boldsymbol{\delta\breve{\tau}}(\cdot|k)$
  else
    $\mathcal{R}(k) \leftarrow \emptyset$.
    for $s \in \{0, \ldots, N_p - 1\}$ **do**
      for $j \in \{a, b, c\}$ **do**
        $\mathcal{R}_{s,j} \leftarrow \{\lfloor \delta\breve{\tau}_j(s|k) \rfloor, \lceil \delta\breve{\tau}_j(s|k) \rceil\}$
      end
      $\mathcal{R}_s \leftarrow \mathcal{R}_{s,a} \times \mathcal{R}_{s,b} \times \mathcal{R}_{s,c}$
    end
    $\mathcal{R}(k) \leftarrow \mathcal{R}_0 \times \mathcal{R}_1 \times \cdots \times \mathcal{R}_{N_p-1}$
  end
Step 2 `FeasibilitySearching(`$\mathcal{R}(k)$`):`
  $\mathcal{F}(k) \leftarrow \emptyset$.
  foreach $\boldsymbol{\delta\hat{\tau}}(\cdot|k) \in \mathcal{R}(k)$ **do**
    for $s \in \{0, \ldots, N_p - 1\}$ **do**
      $\hat{\boldsymbol{\tau}}(s+1|k) \leftarrow \hat{\boldsymbol{\tau}}(s|k) + \boldsymbol{\delta\hat{\tau}}(s|k)$.
      $\hat{\mathbf{y}}(s+1|k) \leftarrow \Psi(\hat{\boldsymbol{\tau}}(s+1|k))$ using (3.57).
      if $\mathbf{F}\begin{bmatrix}\hat{\boldsymbol{\tau}}(s+1|k)\\ \hat{\mathbf{y}}(s+1|k)\end{bmatrix} \not\leq \mathbf{q}$ **then**
        goto *Line 16*
      end
    end
    $\mathcal{F}(k) \leftarrow \mathcal{F}(k) \cup \{\boldsymbol{\delta\hat{\tau}}(\cdot|k)\}$.
  end
Step 3 `OptimalitySearching(`$\mathcal{F}(k)$`):`
  if $\mathcal{F}(k) \neq \emptyset$ **then**
    $\boldsymbol{\delta\tilde{\tau}}(\cdot \mid k) \leftarrow \arg\min_{\boldsymbol{\delta\hat{\tau}}(\cdot|k)\in\mathcal{F}(k)} L_{P\tau}\big(\hat{\mathbf{y}}(\cdot \mid k), \boldsymbol{\delta\hat{\tau}}(\cdot \mid k)\big)$
  end
return $\boldsymbol{\delta\tilde{\tau}}(\cdot|k)$

5.2.4.1 Scenario setup

First, we define three scenarios in Table 5.5 that run for 24 hours. The objective is to compare, in scenario one, the performance of our proposed approaches with that of a

conventional approach currently used in practice. In the last two scenarios, we implement different solving techniques for the optimization-based approaches, described in Table 5.6, to evaluate our proposed approach against state-of-the-art MIP solvers and a simple heuristic.

TABLE 5.5: Details of implemented scenarios for transformer active power regulation.

Scenario	Approach	Reference Value	Ref. Characteristics	Run Time
1	RB vs. MINLPs	30MW vs. 3×10MW	Normal, equal	24 hours
2	RB vs Table 5.6	36MW vs. 3×12MW	High, equal	24 hours
3	Table 5.6	$10-6-8$MW	Unequal	24 hours

Here, scenario one focuses on the comparison between simple RB and standard MPC approach, where MINLP formulations are solved using the `Bonmin` MIP solver. In addition, we would like to highlight the importance of the adaptive weight algorithm associated with switching cost in the control problem. Therefore, we implement two different MINLPs:

- MINLP*: solving the original problem (5.4).
- MINLP: solving the problem (5.4) without switching cost (4.4).

Regarding the RB method, unlike previous electrode current control scenarios, the power controller regulates the total active power across three phases rather than each phase independently, due to the complexity of integer tap positions. This also reflects the common industrial practice of specifying setpoints as total power and thus, simultaneously adjusting tap changers across all phases. As a result, the RB controller is implemented using simple rules as follows:

$$\boldsymbol{\delta\tau}(k) = \begin{cases} +\mathbf{I_{3\times 1}} & \text{if } e_{\mathrm{T}}(k) > \quad \epsilon^p_{\mathrm{T}} \\ -\mathbf{I_{3\times 1}} & \text{if } e_{\mathrm{T}}(k) < -\epsilon^p_{\mathrm{T}} \\ \mathbf{0_{3\times 1}} & \text{otherwise} \end{cases}, \tag{5.9}$$

where $e_{\mathrm{T}}(k) = \sum_j p^s_j(k) - \sum_j p^{s,\mathrm{ref}}_j(k)$ is the total power error and $\epsilon^p_{\mathrm{T}} = \sum_j \epsilon^p_j$ is the tolerance for the total power. The rule is to increase or decrease together the tap positions in three phases based on the comparison between the total power error and the tolerance band. Due to the discrete nature of tap changers, whose switching steps significantly affect

power levels, the RB controller can easily lead to oscillatory behavior if individual-phase power control is considered.

This highlights one of the key limitations of conventional controllers in handling multi-phase powers. In particular, they cannot independently control active power in all three phases at different setpoints. Consequently, under unbalanced load conditions, power cannot be evenly distributed among phases, even when the total power is regulated effectively.

In scenario 2, we extend the comparison to include different optimization-based approaches, listed in Table 5.6. In this scenario, we intentionally set the power setpoint much higher than the normal operating level, which is usually set at $< 30\,\text{MW}$ for the sum of three phases. Therefore, this scenario provides insight into the method's ability to ensure strict furnace operational safety, e.g., electrode current limits under high-power operating conditions.

The control objective of the RB method differs from that of the optimization-based approaches defined in the previous subsection. As the RB controller only regulates the total active power, while the optimization-based approaches control each phase power directly. With the difference, we ensure a fair comparison by supposing the loads are balanced across three phases; thus, the powers should be evenly distributed when the total power is controlled. Moreover, in the performance evaluation, we consider tracking metrics computed from total power, e.g., RPD_M and OPT_M, in addition to the individual phase powers. These metrics were introduced in Section 4.2.1.

In scenario 3, we introduce a more challenging condition in which power setpoints differ across phases, i.e., 10 MW, 15 MW, and 20 MW for three phases, respectively. This requires tap changers to operate at different positions, which the conventional RB controller can not handle. As we presented, the RB controller can only manage the total power; thus, taps are always adjusted simultaneously. Therefore, this scenario is primarily used to compare optimization-based techniques. To facilitate the tracking of unequal setpoints, we increase the tap difference limit to $\gamma = 4$ steps.

Regarding optimization-based methods, we implement two standard MPC approaches, using MINLP (5.4) and MIQP (5.5) formulations. While MINLP is solved using the

TABLE 5.6: A summary of optimization-based approaches for power control.

No.	Approach	Problem without (4.4)	Solver	Strategy
i	MINLP	(5.4)	`Bonmin`	Solves the original MINLP problem directly.
ii	MIQP	(5.5)	`Gurobi 12.0.3`	Solves the MIQP formulation directly.
iii	SR	(5.6)	`qpOASES`	Solves the relaxed problem and round to the nearest integer.
iv	MIOR	(5.6)	`qpOASES`	Applies the MIOR strategy detailed in Section 5.2.3.

open-source `Bonmin` solver, MIQP is solved by the commercial solver `Gurobi`, version 12.0.3, which is known to be one of the fastest MIP solvers. In addition to these exact methods, we also implement relaxation-based heuristic approaches. In addition to our proposed MIOR in Algorithm 5.1, we also consider a relax-and-round strategy with standard rounding (SR) as a baseline heuristic for comparison. The SR method rounds the continuous solution obtained from the QP relaxation in (5.6) to the nearest integer. This helps emphasize MIOR's advantages in terms of feasibility.

In the optimization-based methods, we do not include switching costs in the control problem, as we want to clearly observe the switching behavior of each approach without the influence of adaptive weights. Moreover, the focus in these scenarios is on comparing different solution techniques rather than on the impact of the switching cost function.

TABLE 5.7: Numerical values of control parameters for Ps control.

Parameter	Value	Unit	Parameter	Value	Unit
Time			**Constraint**		
T_s	500	ms	γ	1 (scenario 1&2)	step
N_p	1	–	γ	4 (scenario 3)	step
Objective			$[\boldsymbol{\tau}_{\mathbf{lb}}, \boldsymbol{\tau}_{\mathbf{ub}}]$	$[1, 33]\,\mathbf{I}_{3\times1}$	step
$\boldsymbol{\epsilon}^{\boldsymbol{p}}$	$0.5\mathbf{I}_{\mathbf{3\times1}}$	MW	$[\boldsymbol{p}^{\boldsymbol{s}}_{\mathbf{lb}}, \boldsymbol{p}^{\boldsymbol{s}}_{\mathbf{ub}}]$	$[1, 25]\,\mathbf{I}_{3\times1}$	MW
$\boldsymbol{p}^{\boldsymbol{s},\mathrm{ref}}$	Defined in Table 5.5	–	$[\boldsymbol{I}^{\boldsymbol{s}}_{\mathbf{lb}}, \boldsymbol{I}^{\boldsymbol{s}}_{\mathbf{ub}}]$	$[10, 84.2]\,\mathbf{I}_{3\times1}$	kA
$\mathbf{Q}^{\mathbf{p}}$	$\mathbf{I}_{\mathbf{3\times1}}$	–	$[\boldsymbol{I}^{\boldsymbol{e}}_{\mathbf{lb}}, \boldsymbol{I}^{\boldsymbol{e}}_{\mathbf{ub}}]$	$[17, 145]\,\mathbf{I}_{3\times1}$	kA
$\lambda_{\max}, \mu, \nu$	$10^{11}, 1, 2$	–	$\boldsymbol{\Delta\tau}_{\mathbf{max}}$	$\mathbf{I}_{\mathbf{3\times1}}$	step
$[\lambda_{\max},\ \mu,\ \nu]$	$[10^{11},\ 1,\ 2]$	–			

The numerical values for simulation, detailed in Table 5.7, will be consistently used across scenarios except for the values of γ mentioned above. We use the same sampling time as in the electrode current control, i.e., $T_s = 500\,\text{ms}$, and keep the prediction horizon short, $N_p = 1$. All control objective and constraint variables needed are presented in the table.

5.2.4.2 Simulation evaluation

Here, we analyze the simulation results for three scenarios defined in Table 5.5. The results include figures of interest variables and tables of overall performance metrics.

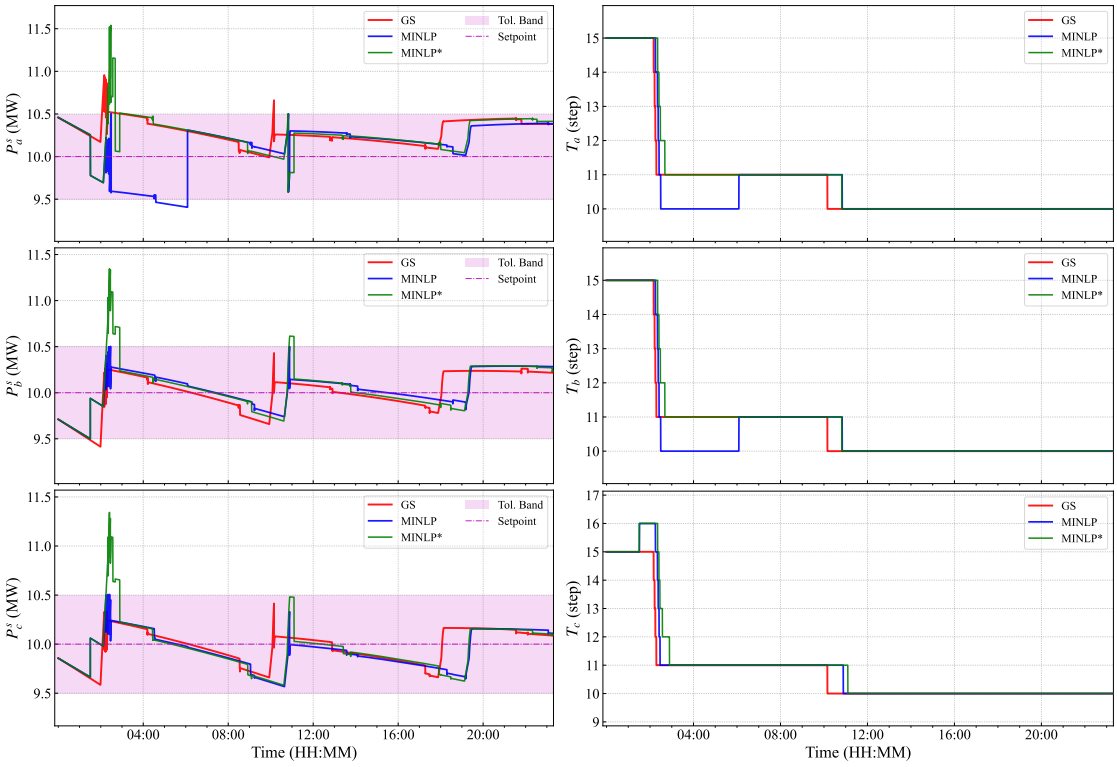

(A) Transformer active power. (B) Tap positions in three phases.

FIGURE 5.8: Controlled active power across three phases and corresponding control actions as tap changer positions under normal and equal setpoints (Scenario 1).

In Figure 5.8, first scenario, the MINLP controller, represented by blue curves, effectively manages the active powers within the tolerance band around the setpoints. Similarly, under balanced load conditions, the total power control by the RB approach (red curves) results in slightly better regulation of individual phase powers. However, the active power

in phase one, i.e., P_a^s, cannot be effectively controlled and is shifted towards the upper limit of the tolerance band. The MINLP* controller with switching cost (green curves) lets the powers exceed the tolerance range for a while during the casting period. This is expected due to the delay in tap changer switching induced by the switching cost (4.4) in the optimization formulation.

Table 5.8 shows more insights with detailed performance metrics. Without penalizing tap changes, MINLP achieves better tracking performance than RB with less reference deviation in total power, i.e., 1.48% vs. 1.83% and less outside tolerance band in phase power, i.e., 2.10% vs. 2.19%. The trade-off is that more tap switching is required to compensate for the tracking error, i.e., 21 vs. 15. This is reasonable because MINLP controls each phase's power independently. When incorporating switching cost, MINLP* slightly degrades tracking performance compared to MINLP, by reducing the number of tap changes from 21 to 17. The degradation occurs particularly during casting periods, when the tap changers are prevented from consecutive switching. This shows the effectiveness of the adaptive switching algorithm in terms of energy error over time.

TABLE 5.8: Statistical results of power control over 24 hours (Scenario 1).

Approach	**Reference Deviation** (%)		**Outside Tolerance** (%)		**Tap Switch**	**CPU** (ms)
	$\mathbf{RCD_M}$	$\mathbf{RCD_T}$	$\mathbf{OCT_M}$	$\mathbf{OCT_T}$		
RB	2.34	1.83	2.19	0.01	15	–
MINLP	2.34	1.48	2.10	0.00	21	184.87
MINLP*	2.68	2.16	3.04	1.7	17	171.50

Lower value represents better performance.

The upside of the RB controller is its simplicity, which only requires simple rules to compute control actions; thus, it is computationally efficient. In contrast, MINLP needs to solve complex optimization problems online at each sampling instant. As shown in Table 5.8, the average CPU time of solving the MINLP formulations is around 172−185 ms, which accounts for almost two-fifths of the sampling time $T_s = 500$ ms. This motivates the comparison of more efficient algorithms in the following scenarios.

Figure 5.9 shows the power tracking performance of the optimization-based approaches in the second scenario, where setpoints are set to 12 MW for each phase. In this scenario, the RB approach was also implemented, but is not shown in the figure. In fact, RB failed to maintain power levels within the tolerance band due to its limitations in handling

operational constraints. In particular, at high power setpoints, the RB controller cannot satisfy current constraints and also makes the system unstable, leading to significant tap variations, as indicated in Table 5.9. Even though constraints can also be passively managed through rule-based logic, there is no straightforward way to integrate them into the rule-based control of power to ensure safe and stable operation.

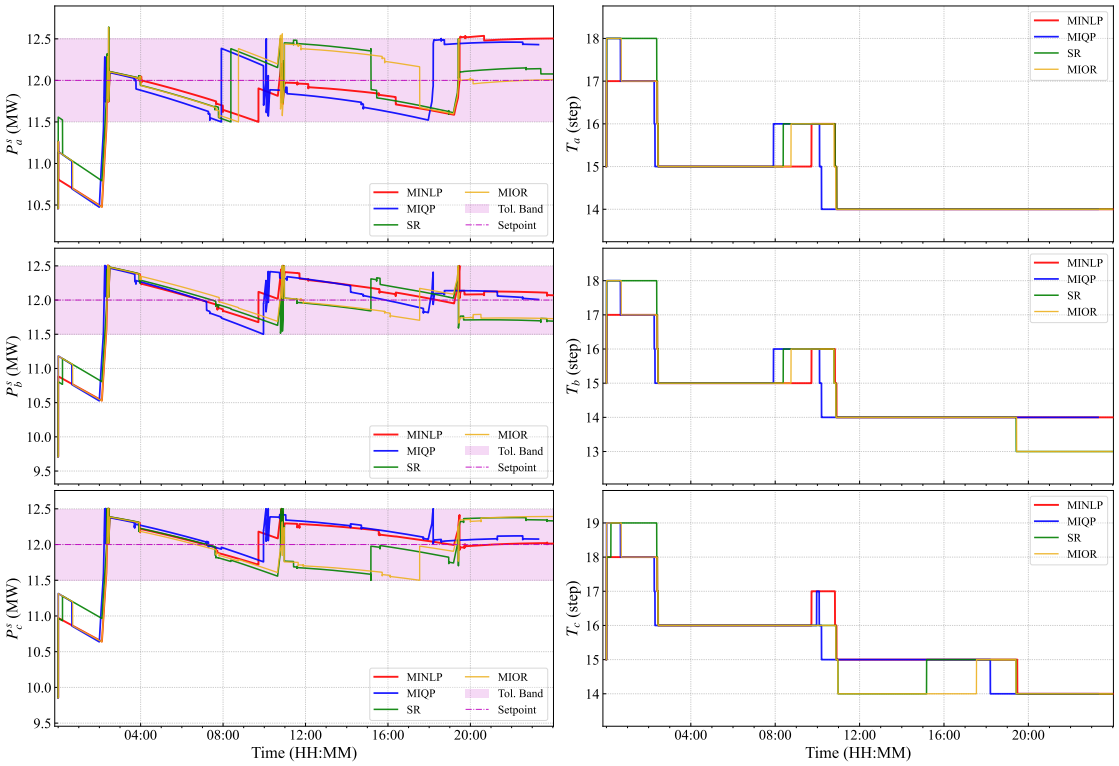

(A) Transformer active powers. (B) Tap positions in three phases.

FIGURE 5.9: Controlled active power across three phases and corresponding control actions as tap changer positions under high and equal setpoints (Scenario 2).

In contrast, we can see in Figure 5.9a that all optimization-based methods effectively track the powers setpoints. The right side, Figure 5.9b, shows the corresponding tap positions adjusted by each method. In general, tap changers are required to operate more frequently than in the first scenario to maintain high power levels. As a result, powers are mostly kept within the tolerance band, except for the first two hours of the beginning of the simulation. Power levels in this period cannot reach the tolerance band and continue to decrease gradually due to the formation of slag and metal in the furnace.

This behavior can be explained if we look at the electrical current evolution illustrated in Figure 5.10. During this period, both secondary and electrode currents are very close to their upper limits; thus, most optimization-based controllers avoid increasing the tap positions to prevent them from exceeding those limits. Notably, in addition to the RB controller, which completely fails to respect the current limits, the SR method (green curves) also allows the currents to violate the constraints. Especially, the transformer and electrode currents in phases one and three clearly get beyond their upper limits, e.g., $|i_c^s| > I_{\text{ub}}^s = 84.2\,\text{kA}$ and $|i_1^e|, |i_3^e| > I_{\text{ub}}^e = 145\,\text{kA}$.

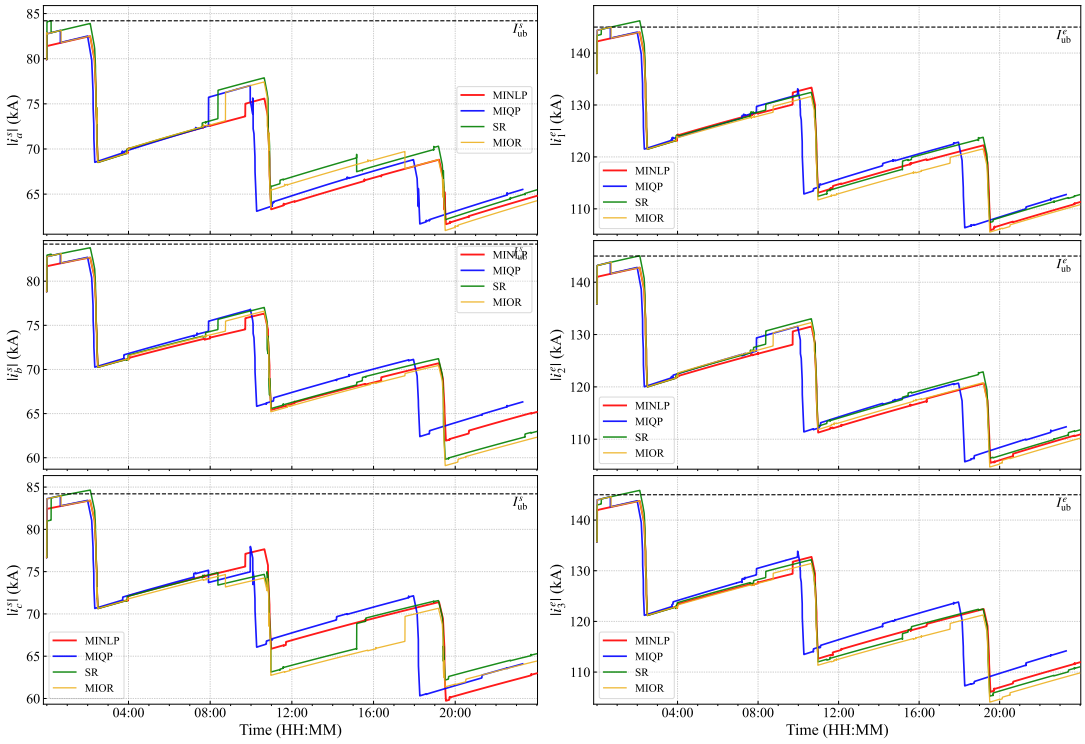

(A) Secondary current magnitudes. (B) Electrode current magnitudes.

FIGURE 5.10: Electrical currents under operational constraints (Scenario 2).

As shown in Table 5.9 and Table 5.10, we compare the statistical metrics across all approaches. The SR method demonstrates the best tracking performance with the lowest RPD_M of 3.27%, OPT_M of 9.16% and the most computational efficiency with the average CPU time is 1.54 ms, this comes at the cost of constraint violations with CVR is up to 6.2%. In contrast, the solution of exact methods, i.e., MINLP and MIQP, ensures no constraint violations with 0% CVR. The MINLP approach has the fewest tap changer

switches of 23, resulting in the highest OPT_M of 13.36%. The computation time for the MINLP approach with the `Bonmin` solver is 225 ms on average, accounting for almost half of the sampling time. Whereas the MIQP approach with `Gurobi` solver, the fastest commercial MIP solver, provides a good balance of performance and computational speed. Our proposed MIOR heuristic also effectively satisfies all constraints, achieving 0% CVR. It achieves better tracking performance than MINLP and comparable results to MIQP, with RPD_M of 3.73% and OPT_M of 9.73%. More importantly, MIOR significantly reduces the computation time with an average of 3.65 ms, i.e., 60 times faster than MINLP and 2.5 times faster than MIQP.

TABLE 5.9: Statistical results of power control over 24 hours (Scenario 2).

Approach	**Reference Deviation** (%)				**Outside Tolerance** (%)				**Tap Switch**	**CPU**	**CVR**
	RPD_1	RPD_2	RPD_3	$\mathbf{RPD_M}$	OPT_1	OPT_2	OPT_3	$\mathbf{OPT_M}$		(ms)	(%)
RB	–	–	–	–	–	–	–	–	∞	–	> 60
MINLP	4.24	3.69	3.37	**3.77**	20.70	9.72	9.65	**13.36**	23	224.99	Table 5.10
MIQP	4.13	3.58	3.27	**3.66**	9.34	9.30	9.24	**9.29**	29	8.95	
SR	3.38	3.22	3.20	**3.27**	8.66	9.46	9.35	**9.16**	30	1.54	
MIOR	3.88	3.59	3.72	**3.73**	9.84	9.71	9.64	**9.73**	30	3.65	

∞ indicates uncontrollable tap operations.
Lower value represents better performance.

TABLE 5.10: Constraint violation rate among approaches (Scenario 2).

Approach	**CVR transformer current (%)**			**CVR electrode current (%)**		
	$\lvert i_a^s \rvert$	$\lvert i_b^s \rvert$	$\lvert i_c^s \rvert$	$\lvert i_1^e \rvert$	$\lvert i_2^e \rvert$	$\lvert i_3^e \rvert$
MINLP	0	0	0	0	0	0
MIQP	0	0	0	0	0	0
SR	0.0035	0	4.22	6.20	0.28	4.33
MIOR	0	0	0	0	0	0

Lower value represents better performance.

The third scenario introduces unequal power setpoints, 10 MW, 6 MW, and 8 MW, respectively, in three phases, a challenging task that conventional RB controllers cannot handle. As a result, we only consider the power tracking and control signals behaviors among all considered optimization-based methods in Figure 5.11. Here, we observe that all optimization-based methods successfully track the unequal power setpoints in all three phases. The tap positions in Figure 5.11b behave differently across the phases to accommodate the unequal power demands. Specifically, the tap position in phase one

ranges from 15 to 7, while in phases two and three it drops to 5 and 3, respectively. The difference in tap positions across phases is always kept within the limit of $\gamma = 4$ steps.

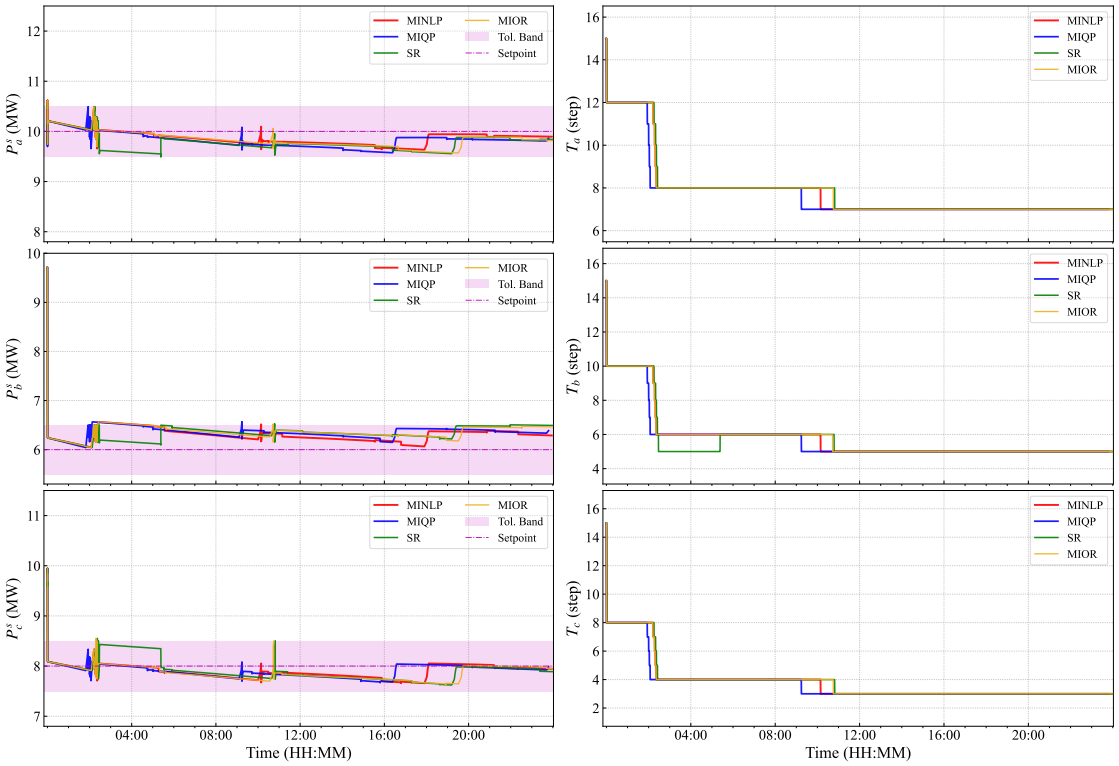

(A) Transformer active powers. (B) Tap positions in three phases.

FIGURE 5.11: Controlled active power across three phases and corresponding control actions as tap changer positions under unequal setpoints (Scenario 3).

The performance metrics of this third scenario are summarized in Table 5.11. The tracking performance trends are very similar to those in the second scenario. The statistical results show that the MINLP method achieves the lowest RPD_M of 3.08%, while the SR method achieves the best OPT_M of 1.44%. The performance of the MIQP approach lies between the two metrics. It also provides a good balance between tracking performance and computational efficiency with an average CPU time of 13.67 ms. However, our MIOR heuristic once again stands out for its overall performance. While having a satisfactory tracking performance with RPD_M of 3.62% and OPT_M of 3.09%, MIOR naturally requires fewer tap switches, i.e., 30 times compared to MIQP, which reaches up to 42 times and SR, which has 32 times. The MINLP exhibits the same number of tap operations as

MIOR, but MIOR still outperforms MINLP in computation time, with an average of 7.34 ms, over 20 times faster than MINLP (153.4 ms).

TABLE 5.11: Statistical results of power control over 24 hours (Scenario 3).

Approach	**Reference Deviation** (%)				**Outside Tolerance** (%)				**Tap Switch**	**CPU** (ms)
	RPD_1	RPD_2	RPD_3	$\mathbf{RPD_M}$	OPT_1	OPT_2	OPT_3	$\mathbf{OPT_M}$		
MINLP	1.85	5.37	2.00	**3.07**	0	9.21	0.02	**3.08**	30	153.58
MIQP	2.24	6.15	1.90	**3.43**	0	8.60	0.03	**2.88**	42	11.80
SR	2.80	5.86	2.8	**3.82**	0	4.30	0.03	**1.44**	32	1.59
MIOR	2.22	6.24	2.41	**3.62**	0	9.25	0.02	**3.09**	30	7.34

Lower value represents better performance.

5.2.4.3 Discussion

The three simulation scenarios presented above provide necessary insights into our proposed integer-based power control strategies using the MPC framework. It compares and validates the effectiveness of our contributions to designing the adaptive weight-tuning algorithm in Section 4.1.3 and the MIOR heuristic algorithm in Section 5.2.3.

Regarding the adaptive weights associated with switching cost, the results from scenario 1 demonstrate its benefits in reducing the number of tap operations in the MINLP formulation. By penalizing tap switching with time-varying weights computed from accumulated power error, the cost effectively balances the trade-off between power regulation accuracy and tap operation. Thus, the number of switches is reduced compared to the case without switching cost, but still higher than that of the RB controller. Nevertheless, this is reasonable because the MINLP formulation accounts for the independent-phase power control strategy. Moreover, the results also rely on the choice of the fixed parameters in the algorithm, i.e., $\lambda_{\max}$, μ and ν. The choice varies depending on specific furnace operation, thus it requires proper selection when put into practice. Lastly, the algorithm's effectiveness will be more realistic when considering with the electrode current control. As a result, its benefits will be further validated in the coordinated control in the next chapter.

The RB controller, a classical, straightforward controller that mimics industrial practice, has shown satisfactory performance in regulating the total active power at normal levels.

However, it shows the restriction in handling the multi-phase power control problem, which is the primary purpose of validation in scenario 3. Moreover, the RB controller cannot handle operational constraints, as shown in scenario 2. This explains why EAFs are often operated far below their maximum power levels in practice, as operators prefer to avoid the risk of constraint violations and their consequences.

In contrast, optimization-based methods with exact solving techniques such as MINLP and MIQP effectively manage these constraints while achieving optimal tracking performance. The MINLP approach solved by `Bonmin` provides the most robust results with the low tracking error and minimal tap switches. However, its computational burden is significant with respect to the sampling time. The MIQP formulation solved by `Gurobi` offers a good compromise between performance and computational efficiency, but it produces significantly more tap switches in scenario three, which should be avoided.

Moreover, we implement and evaluate the heuristic approaches, including SR and MIOR. While both methods significantly reduce computation time compared to exact methods, they exhibit distinct performance. The SR method, despite its simplicity, cannot guarantee the feasibility of the solution in scenario two due to its simple rounding scheme. In practice, this may not be realized if the furnace operates at low power levels where constraints are less likely to be violated. Moreover, the SR can degrade tracking performance when it comes to control problems involving continuous variables, where the rounding solution may deviate substantially from the optimal one. Therefore, although it offers competitive tracking and computational performance, it lacks reliability.

On the other hand, our proposed MIOR heuristic, by combining a relaxed QP problem with an optimal rounding heuristic, provides high-quality solutions that are slightly less optimal than those of exact methods. The trade-off is much lower computational efficiency, with around a few milliseconds for each computation. Moreover, it strictly ensures operational safety under high-power conditions in scenario two or when unequal setpoints are present in scenario three, which neither the RB controller nor the SR heuristic can effectively handle. Lastly, the MIOR approach applies simple strategies without introducing any additional tuning parameters.

While the MIOR shows improvements in computational efficiency, it was validated over a short prediction horizon, e.g., $N_p = 1$. For a longer horizon, the size of the search

space can exponentially grow with respect to the number of fractional variables in the QP relaxation solution. However, this can be mitigated with parallel computation or other enhancement techniques, which will be discussed in the next chapter, where we extend the MIOR concept to mixed-integer problems involving both continuous and integer variables.

5.3 Concluding remarks

In this chapter, we presented our contributions to developing predictive control strategies to regulate either transformer active powers or electrode currents, establishing the foundational framework for the coordinated control presented in the next chapter. We have formulated specialized MPC problems for each control problem, addressing the computational challenges associated with nonlinearities and integer variables.

For electrode current control, as detailed in Section 5.1, we proposed two MPC-based approaches, denoted as NMPC and LMPC, as shown in Figure 5.1. The simulation results verify that both approaches provide better tracking performance than the classical GS method. In addition, using the linearized model for the interest outputs, LMPC significantly reduces computational effort, computing the solution 30 times faster than NMPC while achieving even better control performance.

For active power regulation, presented in Section 5.2, we developed integer-based MPC formulations to account for the discrete nature of the tap changer, as shown in the control scheme of Figure 5.7. To reasonably reduce the number of tap operations, we designed an adaptive weight tuning in Algorithm 4.1 for the switching cost, effectively balancing power tracking accuracy with the hunting problem of tap changers. Moreover, to address the burden of solving integer problems, we introduced MIOR in Algorithm 5.1, a heuristic-based method that efficiently approximates the solution of MIP problems. As demonstrated in our SIL simulations, the MIOR strategy provided a good balance between control performance and computational feasibility. It inspired the development of improved heuristic techniques for mixed-integer problems in the next chapter.

In conclusion, this chapter demonstrated the advantages of the MPC-based method in controlling the SAF. By leveraging the furnace models, we can flexibly design different

control strategies according to specific control objectives and systematically handle operational constraints. The preliminary results provide necessary insights for the combined control architecture developed in the subsequent chapter.

Chapter 6

Coordinated power and current control

This chapter presents our proposed control design, strategically coordinating both power and current regulation developed in Chapter 5 in a centralized framework.

Building upon the mathematical models established in Chapter 3 and the formulation of control objectives and constraints in Chapter 4, we formulate a mixed-integer power and current predictive control problem that incorporates both continuous electrode displacement and integer decision tap changer variables. To effectively mitigate the hunting problem, we incorporate an adaptive penalty strategy as in Section 5.2.

To address the computational challenges of solving MINLP problems in real-time, we introduce a novel bilevel optimization strategy, developed from MIOR in Section 5.2.3. This approach approximates the MINLP solution by decomposing it into QP subproblems and combining them via a heuristic search, enabling efficient online implementation while maintaining satisfactory control performance.

Subsequently, we demonstrate the effectiveness and real-time feasibility of our proposed control approach through extensive SIL simulations and compare it with both conventional methods and optimization-based approaches using state-of-the-art MIP solvers under various operating scenarios.

6.1 Mixed-integer power and current predictive control

This section uses the MI-MPC framework, which combines Section 5.1 and Section 5.2 to formulate a coordinated power and current control problem as a MINLP problem. Due to the high computational cost of solving MINLPs in real time, the problem is first approximated as an MIQP. To further enhance computational efficiency while maintaining control performance, a novel bilevel strategy is introduced.

6.1.1 Coordinated power and current architecture

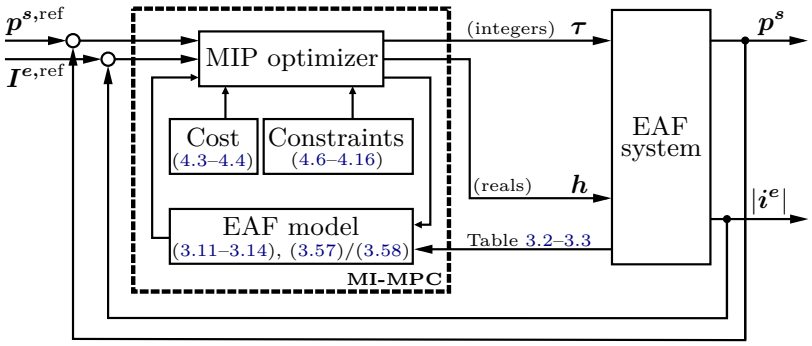

FIGURE 6.1: Proposed centralized MI-MPC architectures to coordinately control both the active powers and current magnitudes in all three phases by adjusting tap positions and electrode heights.

The proposed MI-MPC architecture, illustrated in Figure 6.1, presents in detail the equations and variables used for the centralized control framework presented in Figure 2.15b. This scheme simultaneously and coordinately adjusts both transformer tap positions $\boldsymbol{\tau}$ and electrode heights $\boldsymbol{h}$ across all three phases to have the system track the desired reference of transformer active powers $\boldsymbol{p}^{s,\mathrm{ref}}$ and electrode magnitude currents $\boldsymbol{I}^{e,\mathrm{ref}}$.

Similar to other MPC schemes presented, the key advantage of this architecture is its ability to explicitly incorporate EAF control objectives or cost and operational constraints defined in Chapter 4, thereby ensuring safe and optimal furnace performance. Moreover, by leveraging the detailed electrical EAF model developed in Chapter 3, the controller captures the complex interactions between components and across phases. The measurement or estimation of the parameters required for the models, summarized in Table 3.2–3.3, are provided in real-time with the feedback measurement of $\boldsymbol{p}^s$ and $|\boldsymbol{i}^e|$.

As is known, MPC allows handling discrete tap changer variations. This coordinated control scheme yields MIP problems, as shown in Section 6.1.2. As a result, the framework considerably increases the computational complexity due to the need to solve these NP-hard problems online at each control step. This necessitates the development of efficient algorithms in Section 6.1.3 to ensure real-time feasibility.

6.1.2 Mixed-integer programming formulation

Given the system models from Section 3.3 and the operational requirements from Section 4.1, we formulate a mixed-integer power and current predictive control problem at each sampling instant k:

$$\mathbf{u}^*(\cdot|k) = \arg\min_{\mathbf{u}(\cdot|k)} \sum_{s=0}^{N_p-1} \underbrace{\overbrace{J_{PI}(s+1|k)}^{(4.3)} + \overbrace{J_{\tau}(s+1|k)}^{(4.4)}}_{L_{PI\tau}\left(\boldsymbol{p}^s(s+1|k),\, |\boldsymbol{i}^e(s|k)|,\, \boldsymbol{\delta\tau}(s|k)\right)}, \tag{6.1a}$$

s.t. $\forall s \in [0,\, N_p - 1]$:

$$\boldsymbol{\tau}(0|k), \boldsymbol{h}(0|k), \boldsymbol{r}(0|k), \boldsymbol{x}(0|k) = \boldsymbol{\tau_0}, \boldsymbol{h_0}, \boldsymbol{r_0}, \boldsymbol{x_0}, \tag{6.1b}$$

Linear dynamics (3.11)–(3.14), (6.1c)

Nonlinear outputs (3.57), (6.1d)

Tap position constraints (4.6) and (4.9), (6.1e)

Electrode holder position constraint (4.10), (6.1f)

Electrode-process impedance constraints (4.12)–(4.13), (6.1g)

Electrical output constraints (4.14)–(4.16), (6.1h)

Tap deviation and integer constraints (4.7)–(4.8), (6.1i)

Electrode displacement constraint (4.11). (6.1j)

The control problem (6.1) is formulated over a finite prediction horizon N_p with the optimization variables, defined as a sequence of control signals $\mathbf{u}(\cdot|k) = \Big[\mathbf{u}(0|k),\, \mathbf{u}(1|k),\, \ldots,\, \mathbf{u}(N_p-1|k)\Big] \in \mathbb{R}^{6\times N_p}$, where each column is a vector of both integer tap variation and continuous electrode displacement, i.e., $\mathbf{u}(s|k) \triangleq [\boldsymbol{\delta\tau}(s|k),\, \boldsymbol{\delta h}(s|k)]^\top \in \mathbb{R}^6$ for

$s \in [0,\, N_p - 1]$. The control action applied to the system is taken from solving (6.1) and extracting the first element of its optimal sequence, i.e., $\mathbf{u}^*(\cdot|k)$.

The objective function (6.1a) aims to minimize the cumulative cost $L_{PI\tau}(\cdot)$, which combines power and current regulation cost $J_{PI}(\cdot)$ defined in (4.3) and tap switching penalty $J_\tau(\cdot)$ described in (4.4), over N_p. The optimization is subject to the initial conditions of taps positions $\boldsymbol{\tau_0} \in \mathbb{Z}^3$, electrodes positions $\boldsymbol{h_0} \in \mathbb{R}^3$, resistances $\boldsymbol{r_0} \in \mathbb{R}^3$, reactances $\boldsymbol{x_0} \in \mathbb{R}^3$ and various constraints, including the system dynamics (6.1c), nonlinear output relation (6.1d) and all operational constraints (6.1e)–(6.1j), which are detailed in corresponding chapters.

The mixed-integer condition appearing in (6.1i) together with the nonlinear constraint (6.1d) transforms the optimization (6.1) into a non-convex MINLP problem, which is known for its significant computational complexity in real-time and high infeasibility over long prediction horizons, as discussed in Section 4.3.2.1, even when considering the state-of-the-art MINLP solver, e.g., `Bonmin`.

To address this challenge, one common approach is to linearize the nonlinear constraint (6.1d) around the operating points at each time step k. Thus, we replace the nonlinear output equation with its linearized form, as detailed in (3.58). Hence, the MINLP problem (6.1) is approximated by a mixed-integer quadratic programming (MIQP) problem:

$$\mathbf{u}^*(\cdot|k) = \arg\min_{\mathbf{u}(\cdot|k)} L_{PI\tau}(\cdot) \text{ in (6.1a)}, \tag{6.2a}$$

$$\text{s.t.} \quad \forall s \in [0,\, N_p - 1]:$$

$$\mathbf{x}(s+1|k) = \mathbf{A}\mathbf{x}(s|k) + \mathbf{B}(k)\mathbf{u}(s|k), \tag{6.2b}$$

$$\mathbf{F}\mathbf{x}(s+1|k) - \mathbf{q} \leq 0,\ \mathbf{x}(0|k) = \mathbf{x_0}, \tag{6.2c}$$

$$\mathbf{G}\mathbf{u}(s|k) - \mathbf{k} \leq 0, \tag{6.2d}$$

$$\boldsymbol{\delta\tau}(s|k) \in \mathbb{Z}^3. \tag{6.2e}$$

While, $\boldsymbol{u}(s|k) \in \mathbb{R}^6$ is similar to the input vector defined in (6.1), the state vector $\mathbf{x}(s|k) \triangleq [\boldsymbol{\tau},\, \boldsymbol{h},\, \boldsymbol{r},\, \boldsymbol{x},\, \mathbf{y}]^\top \in \mathbb{R}^{21}$ is additionally defined, representing tap and electrode positions, electrode-process resistances and reactances, electrical outputs from (3.57).

The cost function (6.2a) remains the same as in (6.1a). The constraint (6.2b) describes the linearized dynamics with $\mathbf{A} = \mathbf{I}_{21}$ is an identity matrix and $\mathbf{B}(k) \in \mathbb{R}^{21\times 6}$ is a time-varying matrix. The $\mathbf{B}(k)$ matrix is derived by combining the linear models from (6.1c) and the linearized output in (3.58). In particular, it can be expressed as:

$$\mathbf{B}(k) \triangleq \begin{bmatrix} \mathbf{0}_3 & \mathbf{I}_3 \\ \mathbf{0}_3 & \boldsymbol{\Gamma}^{\boldsymbol{x}}(k) \\ \mathbf{0}_3 & \boldsymbol{\Gamma}^{\boldsymbol{r}}(k) \\ \mathbf{J}^{\boldsymbol{\tau}}(k) & \mathbf{J}^{\boldsymbol{h}}(k) \end{bmatrix},$$

where, we have $\mathbf{I}_3$ and $\mathbf{0}_3$ are the identity and zero matrices, respectively. The Jacobian matrices $\boldsymbol{\Gamma}^{\boldsymbol{x}}(k)$, $\boldsymbol{\Gamma}^{\boldsymbol{r}}(k) \in \mathbb{R}^{3\times 3}$ taken from (3.13), (3.14) and $\mathbf{J}^{\boldsymbol{\tau}}(k)$, $\mathbf{J}^{\boldsymbol{h}}(k) \in \mathbb{R}^{9\times 3}$ defined in (3.58), are evaluated at each time step k.

The linear inequality constraints (6.2c) and (6.2d) provide compact representations of the operational constraints presented in (6.1e)–(6.1h) and (6.1i)–(6.1j), respectively. In particular, we have their corresponding coefficients explicitly specified as follows:

$$\mathbf{F} \triangleq \begin{bmatrix} \mathbf{I_{21}} \\ -\mathbf{I_{21}} \\ \mathbf{L} \quad \mathbf{0_{6\times 18}} \end{bmatrix}, \ \mathbf{L} \triangleq \begin{bmatrix} 1 & -1 & 0 \\ -1 & 1 & 0 \\ 0 & 1 & -1 \\ 0 & -1 & 1 \\ 1 & 0 & -1 \\ -1 & 0 & 1 \end{bmatrix}, \ \mathbf{q} \triangleq \begin{bmatrix} \mathbf{x_{ub}} \\ -\mathbf{x_{lb}} \\ \gamma \times \mathbf{I_{6\times 1}} \end{bmatrix},$$

$$\mathbf{G} \triangleq \begin{bmatrix} \mathbf{I_6} \\ -\mathbf{I_6} \end{bmatrix}, \quad \mathbf{k} \triangleq \begin{bmatrix} \mathbf{u_b} \\ \mathbf{u_b} \end{bmatrix}, \quad \mathbf{u_b} \triangleq \begin{bmatrix} \boldsymbol{\Delta\tau_{max}} & \boldsymbol{\Delta h_{max}} \end{bmatrix}^\top,$$

with $\mathbf{x_{ub}}$, $\mathbf{x_{lb}} \in \mathbb{R}^{21}$, denoting the upper and lower bounds of state vector $\mathbf{x}$, defined as:

$$\mathbf{x_{ub}} \triangleq \begin{bmatrix} \boldsymbol{\tau}_{\mathbf{ub}}, \boldsymbol{h}_{\mathbf{ub}}, \boldsymbol{r}_{\mathbf{ub}}, \boldsymbol{x}_{\mathbf{ub}}, \boldsymbol{p}^{\boldsymbol{s}}_{\mathbf{ub}}, \boldsymbol{I}^{\boldsymbol{s}}_{\mathbf{ub}}, \boldsymbol{I}^{\boldsymbol{e}}_{\mathbf{ub}} \end{bmatrix}^\top,$$
$$\mathbf{x_{lb}} \triangleq \begin{bmatrix} \boldsymbol{\tau}_{\mathbf{lb}}, \boldsymbol{h}_{\mathbf{lb}}, \boldsymbol{r}_{\mathbf{lb}}, \boldsymbol{x}_{\mathbf{lb}}, \boldsymbol{p}^{\boldsymbol{s}}_{\mathbf{lb}}, \boldsymbol{I}^{\boldsymbol{s}}_{\mathbf{lb}}, \boldsymbol{I}^{\boldsymbol{e}}_{\mathbf{lb}} \end{bmatrix}^\top.$$

These bounds together with the scalar γ in vector $\mathbf{q}$ and the actuator limits $\boldsymbol{\Delta\tau_{max}}$, $\boldsymbol{\Delta h_{max}}$ in input bound vector $\mathbf{u_b} \in \mathbb{R}^6$ are detailed in Section 4.1.4. The value of the

initial state vector $\mathbf{x_0} \in \mathbb{R}^{21}$ in (6.2c) is fully given by the measurement system. In addition to the initial values used in (6.1b), measurements of the electrical outputs $\mathbf{y_0} \in \mathbb{R}^{9}$ are also required due to the presence of the linearized output model (3.58). Lastly, the formulation remains the explicit integer constraint on tap variation in (6.2e).

As all the constraints are defined as linear functions and the cost function is originally quadratic, the reformulated problem (6.2) becomes a MIQP problem, which is more tractable and can be solved by well-established commercial MIQP solvers such as `Gurobi`, `Cplex`.

6.1.3 Bilevel strategy

Solving the MINLP problem (6.1) for the optimal solution is computationally intensive and impractical for real-time. Reformulating it as the MIQP problem (6.2) reduces complexity but remains challenging and may lead to infeasibility due to linearization errors.

To address this, we propose a novel BILEVEL optimization strategy, inspired by our previous MIOR strategy introduced in Section 5.2.3, to approximate the MINLP solution by decomposing it into QP subproblems and employing heuristic search techniques in a two-level framework.

This approach is designed to efficiently solve the original MINLP problem with a good balance between solution quality and computational efficiency, thus replacing traditional MIP solvers, i.e., `Gurobi`, `Cplex`, or `Bonmin`. The overall workflow of the proposed BILEVEL strategy, illustrated in Figure 6.2, will be detailed in the following subsections.

6.1.3.1 Subproblem formulations

In the BILEVEL framework, we consider two distinct optimization problems, one at each level. Particularly, we have the inner problem for the first-level, which is a relaxation of the MIQP in (6.2), whereas the outer problem in the second-level is a pure QP optimization problem, disregarding the tap variation. Particularly, we have:

- Inner optimization problem in first-level (QP-relaxation of MIQP problem):

$$\begin{bmatrix} \boldsymbol{\delta\breve{\tau}}(s|k) \\ \boldsymbol{\delta\breve{h}}(s|k) \end{bmatrix} = \arg\min_{\substack{\boldsymbol{\delta\tau}(\cdot|k) \\ \boldsymbol{\delta h}(\cdot|k)}} L_{PI\tau}(\cdot) \text{ in (6.1a)}, \tag{6.3a}$$

s.t. $\forall s \in [0,\, N_p - 1]$:

Linear dynamics (6.2b), (6.3b)

State and input constraints (6.2c), (6.2d), (6.3c)

The first subproblem is derived from the MIQP problem (6.2) by omitting the integer constraint in (6.2e), resulting in a QP relaxation. This relaxation allows tap variation variables $\boldsymbol{\delta\tau}(\cdot|k) \in \mathbb{R}^{3\times N_p}$ to take continuous values. Thus, the problem provides a lower

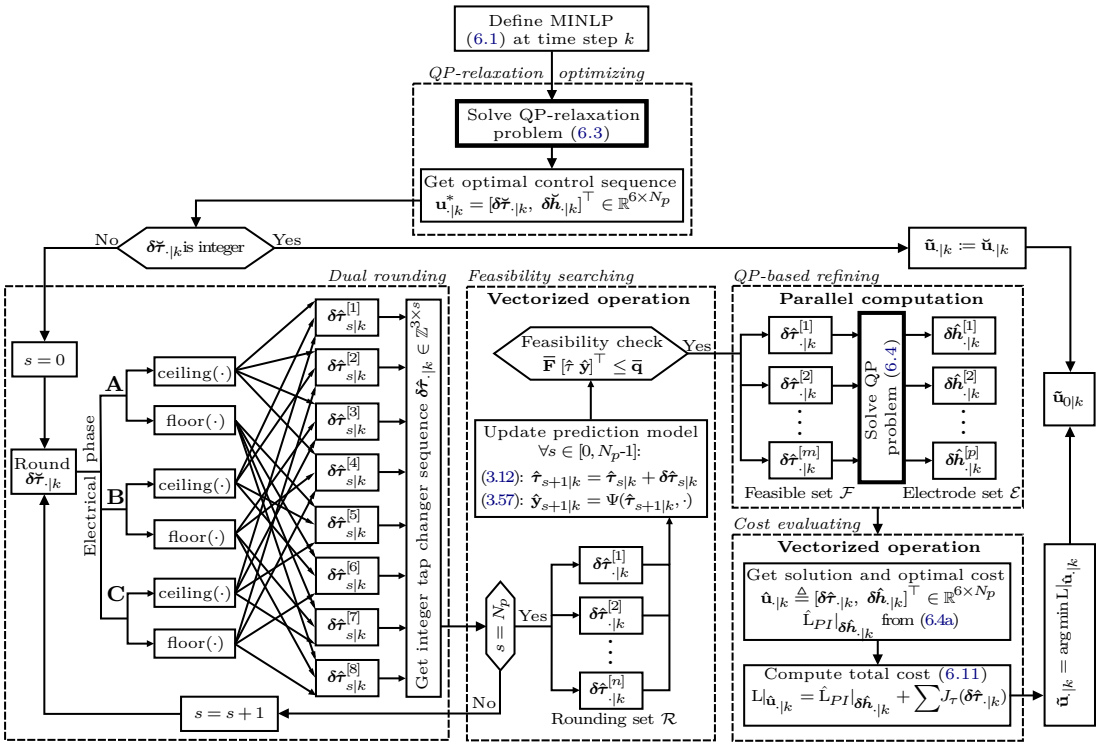

FIGURE 6.2: Flowchart of the proposed BILEVEL optimization strategy for real-time solution of the MINLP problem. The approach consists of an inner QP-relaxation problem and is followed by multiple outer QP problems to select the (sub)-optimal control input for the initial MINLP problem (6.1).

bound on the optimal objective value of the MIQP with the obtained solution denoted as $\breve{\mathbf{u}}(\cdot|k) \triangleq \left[\boldsymbol{\delta}\breve{\boldsymbol{\tau}}(\cdot|k);\ \boldsymbol{\delta}\breve{\boldsymbol{h}}(\cdot|k)\right] \in \mathbb{R}^{6\times N_p}$, serves as a guide for the outer problem.

- Outer optimization problem in second-level (QP problem given $\boldsymbol{\delta}\hat{\boldsymbol{\tau}}(\cdot|k)$):

$$\boldsymbol{\delta}\hat{\boldsymbol{h}}(\cdot|k) = \arg \underbrace{\min_{\boldsymbol{\delta h}(\cdot|k)} \sum_{s=0}^{N_p-1} J_{PI}(s+1|k)}_{\hat{\mathrm{L}}_{PI}}, \tag{6.4a}$$

s.t. $\forall s \in [0,\ N_p - 1]$:

$$\boldsymbol{h}(0|k), \boldsymbol{r}(0|k), \boldsymbol{x}(0|k), \mathbf{y}(0|k) = \boldsymbol{h_0}, \boldsymbol{r_0}, \boldsymbol{x_0}, \mathbf{y_0}, \tag{6.4b}$$

Linear dynamics (3.11), (3.13)–(3.14), (6.4c)

$$\mathbf{y}(s+1|k) = \Psi\Big(\boldsymbol{\tau}(s|k) + \boldsymbol{\delta}\hat{\boldsymbol{\tau}}(s|k), \boldsymbol{r}(s|k), \boldsymbol{x}(s|k)\Big) + \mathbf{J}^{\boldsymbol{h}}\boldsymbol{\delta h}(s|k), \tag{6.4d}$$

Operational constraints (4.10)–(4.16) (6.4e)

The second subproblem focuses on refining the sequence of electrode movements $\boldsymbol{\delta}\breve{\boldsymbol{h}}(\cdot|k) \in \mathbb{R}^{3\times N_p}$ based on the integer sequences of tap variation $\boldsymbol{\delta}\hat{\boldsymbol{\tau}}(\cdot|k) \in \mathbb{Z}^{3\times N_p}$. So, in this formulation, the tap switching is no longer considered as an optimization variable but a fixed parameter. Consequently, cost function (6.4a) does not include the switching penalty term $J_\tau(\cdot)$, as in (6.3a). The output constraint (6.4d) only depends on electrode movement with $\mathbf{J}^{\boldsymbol{h}}$ is the Jacobian matrix, shown in (3.58), and $\boldsymbol{\delta}\hat{\boldsymbol{\tau}}(\cdot|k)$ is used to update the nonlinear output (3.57). The problem remains subject to the same operational constraints as in (6.3), except those associated with tap changers. The resulting solution of this QP problem is denoted as $\boldsymbol{\delta}\hat{\boldsymbol{h}}(\cdot|k) \in \mathbb{R}^{3\times N_p}$.

6.1.3.2 Algorithm workflow

Given the sub-problems (6.3) and (6.4), we describe the detailed workflow of the BILEVEL optimization strategy, shown in Figure 6.2. This strategy is developed based on the MIOR algorithm Algorithm 5.1 and consists of two main levels:

First-Level : handles the integer variables in the control signals, i.e., the tap variations $\boldsymbol{\delta\tau}(\cdot|k)$ by generating a set of feasible integer candidate sequences $\boldsymbol{\delta}\hat{\boldsymbol{\tau}}(\cdot|k)$.

- *QP-relaxation finding:* Construct and solve the inner problem (6.3) at each time step k to obtain an optimal sequence of control input $\mathbf{u}^*(\cdot|k) \triangleq [\boldsymbol{\delta}\breve{\boldsymbol{\tau}}(\cdot|k), \boldsymbol{\delta}\breve{\boldsymbol{h}}(\cdot|k)]^\top \in \mathbb{R}^{6\times N_p}$. This step provides a continuous approximation of (6.2), yielding a promising region in the solution space and a lower bound on the optimal cost.
- *Dual rounding:* Apply ceiling $\lceil\cdot\rceil$ and floor $\lfloor\cdot\rfloor$ operations to each fractional component of the tap variation sequence $\boldsymbol{\delta}\breve{\boldsymbol{\tau}}(\cdot|k) \in \mathbb{R}^{3\times N_p}$. This generates a set of integer candidate sequences $\boldsymbol{\delta}\hat{\boldsymbol{\tau}}(\cdot|k) \in \mathbb{Z}^{3\times N_p}$, denoted as the *rounding set* $\mathcal{R}(k)$:

$$\mathcal{R}(k) \triangleq \left\{ \boldsymbol{\delta}\hat{\boldsymbol{\tau}}(\cdot|k) \in \mathbb{Z}^{3\times N_p} \;\middle|\; \forall s, j:\ \delta\hat{\tau}_j(s|k) \in \left\{ \lfloor \delta\breve{\tau}_j(s|k) \rfloor, \lceil \delta\breve{\tau}_j(s|k) \rceil \right\} \right\}, \tag{6.5}$$

  where $s \in [0,\, N_p - 1]$ is the time step along the prediction horizon and $j \in \{1, 2, 3\}$ denotes the phase. This step explores the neighborhood of the relaxed solution in the integer space, enabling a local search around the promising region.
- *Feasibility searching:* Evaluate each candidate sequence $\boldsymbol{\delta}\hat{\boldsymbol{\tau}}(\cdot|k)$ in the *rounding set* $\mathcal{R}(k)$ for operational feasibility. This involves predicting the system response by updating tap positions in (3.12) and calculating the corresponding electrical output using the nonlinear model (3.57). Candidates that satisfy all operational constraints in (4.6), (4.9), and (4.14)–(4.16) are selected for the *feasible set* $\mathcal{F}(k)$:

$$\mathcal{F}(k) \triangleq \left\{ \boldsymbol{\delta}\hat{\boldsymbol{\tau}}(\cdot|k) \in \mathcal{R}(k) \;\middle|\; \forall s \in [0, N_p - 1]:\ \overline{\mathbf{F}} \begin{bmatrix} \hat{\boldsymbol{\tau}}(s+1|k) \\ \hat{\mathbf{y}}(s+1|k) \end{bmatrix} \leq \overline{\mathbf{q}} \right\}, \tag{6.6}$$

  where $\hat{\boldsymbol{\tau}}(s+1|k) = \hat{\boldsymbol{\tau}}(s|k) + \boldsymbol{\delta}\hat{\boldsymbol{\tau}}(s|k)$, $\hat{\boldsymbol{\tau}}(0|k) = \boldsymbol{\tau_0}$ and $\hat{\mathbf{y}}(s+1|k) = \Psi(\hat{\boldsymbol{\tau}}(s+1|k), \boldsymbol{r_0}, \boldsymbol{x_0})$. The constraint matrices $\overline{\mathbf{F}}$ and $\overline{\mathbf{q}}$ are detailed in the following subsection. This step enhances the feasibility of the final solution by filtering out candidates that would lead to constraint violations.

Second-Level : refines the electrode displacement actions $\boldsymbol{\delta}\breve{\boldsymbol{h}}(\cdot|k)$ based on the feasible tap variation sequences $\boldsymbol{\delta}\hat{\boldsymbol{\tau}}(\cdot|k)$ determined in the first level.

- *QP-based refining:* For each candidate $\boldsymbol{\delta\hat{\tau}}(\cdot|k) \in \mathcal{F}(k)$, we construct and solve the outer QP problem (6.4) to determine optimal electrode displacements $\boldsymbol{\delta\hat{h}}(\cdot|k) \in \mathbb{R}^{3\times N_p}$, thus forming the *electrode set* $\mathcal{E}(k)$. In other words, this step re-optimizes the electrode movement sequences corresponding to fixed integer variables $\boldsymbol{\delta\hat{\tau}}(\cdot|k)$:

$$\mathcal{E}(k) \triangleq \left\{ \boldsymbol{\delta\hat{h}}(\cdot|k) \in \mathbb{R}^{3\times N_p} \;\middle|\; \forall \boldsymbol{\delta\hat{\tau}}(\cdot|k) \in \mathcal{F}(k),\ \boldsymbol{\delta\hat{h}}(\cdot|k) \text{ is solution to (6.4)} \right\}. \tag{6.7}$$

- *Cost evaluating:* For each pair of $\boldsymbol{\delta\hat{h}}(\cdot|k) \in \mathcal{E}(k)$ and its corresponding $\boldsymbol{\delta\hat{\tau}}(\cdot|k) \in \mathcal{F}(k)$, which forms a complete candidate solution $\hat{\mathbf{u}}(\cdot|k) \triangleq [\boldsymbol{\delta\hat{\tau}}(\cdot|k), \boldsymbol{\delta\hat{h}}(\cdot|k)]^\top$, we find the solution $\tilde{\mathbf{u}}(\cdot|k)$ that minimizes the cost function $L(\cdot)$, defined in (6.11). This can be interpreted through the following equation:

$$\tilde{\mathbf{u}}(\cdot \mid k) = \arg \min_{\substack{\boldsymbol{\delta\hat{\tau}}(\cdot|k)\in\mathcal{F},\\ \boldsymbol{\delta\hat{h}}(\cdot|k)\in\mathcal{E}}} L\Big(\hat{\mathbf{u}}(\cdot|k)\Big). \tag{6.8}$$

  As the candidates $\hat{\mathbf{u}}(\cdot|k)$ are known from the previous steps, $L(\cdot)$ can be evaluated directly without solving any optimization problems. Thus, the solution $\tilde{\mathbf{u}}(\cdot|k)$ can be found by simple algorithmic comparisons. As a consequence, this step is obviously inexpensive in terms of computation.

6.1.3.3 Heuristic strategies

An important factor that enhances the effectiveness of the approach is the seamless integration of heuristic strategies across both levels:

- Dual rounding strategy (6.6) explores the feasible integer region in the neighborhood of the continuous optimum $\boldsymbol{\delta\breve{\tau}}(\cdot|k)$ of the relaxation problem (6.3). For each fractional component of $\boldsymbol{\delta\breve{\tau}}(\cdot|k)$, both upward and downward rounding operations are simultaneously applied, where $\lceil\cdot\rceil$ rounds up to the nearest integer and $\lfloor\cdot\rfloor$ rounds down to the greatest integer less than or equal to the value.
- Hybrid model utilization across both levels balances prediction accuracy and computational efficiency. Particularly, the accurate nonlinear model $\Psi(\cdot)$ in (3.57)

is reserved for the feasibility searching (6.6), where the solution $\boldsymbol{\delta\hat{\tau}}(\cdot|k)$ is evaluated via its corresponding output $\hat{\boldsymbol{y}}(\cdot|k)$. Conversely, the computationally inexpensive linearized model (3.58) is employed within the QP formulations (6.3)–(6.4).

- Feasibility searching (6.6) uses predicted tap position $\hat{\boldsymbol{\tau}}(\cdot|k)$ and electrical outputs $\hat{\boldsymbol{y}}(\cdot|k)$ to early eliminate infeasible candidates by assessing $\overline{\mathbf{F}}[\hat{\boldsymbol{\tau}}\ \hat{\mathbf{y}}]^\top \leq \overline{\mathbf{q}}$, with:

$$\overline{\mathbf{F}} \triangleq \begin{bmatrix} \mathbf{I_{12}} \\ -\mathbf{I_{12}} \\ \mathbf{L} \end{bmatrix},\ \overline{\mathbf{q}} \triangleq \begin{bmatrix} [\boldsymbol{\tau}_{\mathbf{ub}}\ \mathbf{y_{ub}}]^\top \\ -[\boldsymbol{\tau}_{\mathbf{lb}}\ \mathbf{y_{lb}}]^\top \\ \gamma \cdot \mathbf{I_{6\times 1}} \end{bmatrix}, \tag{6.9}$$

$$\mathbf{y_{ub}} \triangleq \left[\boldsymbol{p}^{\boldsymbol{s}}_{\mathbf{ub}}, \boldsymbol{I}^{\boldsymbol{s}}_{\mathbf{ub}}, \boldsymbol{I}^{\boldsymbol{e}}_{\mathbf{ub}}\right]^\top, \quad \mathbf{y_{lb}} \triangleq \left[\boldsymbol{p}^{\boldsymbol{s}}_{\mathbf{lb}}, \boldsymbol{I}^{\boldsymbol{s}}_{\mathbf{lb}}, \boldsymbol{I}^{\boldsymbol{e}}_{\mathbf{lb}}\right]^\top, \tag{6.10}$$

are drawn from (4.6), (4.9) and (4.14)–(4.16). Because the transformer tap changes instantly via the electrical actuator, unlike the slower response of the electrode hydraulic system, sudden tap switching can cause large electrical variations before the electrode system reacts, potentially violating operational constraints. By pre-evaluating the feasibility of tap candidates, the strategy (6.6) ensures that only those leading to safe electrical states are passed to the second level.

- Cost evaluation function in the second level computes the new objective value along the horizon N_p for $\boldsymbol{\delta\hat{\tau}}(\cdot|k) \in \mathcal{F}$ and $\boldsymbol{\delta\hat{h}}(\cdot|k) \in \mathcal{E}$ using the following formulation:

$$L\Big(\hat{\mathbf{u}}(\cdot|k)\Big) = \hat{\mathrm{L}}_{PI}\Big|_{\boldsymbol{\delta\hat{h}}(\cdot|k)} + \sum_{s=0}^{N_p-1} J_\tau\Big(\boldsymbol{\delta\hat{\tau}}(s|k)\Big), \tag{6.11}$$

where the first term is already computed and taken from the QP problem (6.4), the second term is the penalty for the tap switching which does not appear in (6.4a). This heuristic evaluation acts as the original cost in (6.1a) and (6.2a), prioritizing solutions that achieved the best performance among the feasible ones.

6.1.3.4 Efficiency enhancements

In addition to the low complexity of the QP formulations, our approach allows the integration of different techniques, thereby enhancing computational efficiency. Especially:

- Candidate reduction: The dual rounding strategy (6.5) can generate up to 8^{N_p} candidates in the worst case scenario, which becomes computationally expensive as N_p increases. To manage this complexity, the number of candidates is significantly reduced by feasibility search (6.6), which discards any sequence that violates operational constraints. Additionally, rounding can be applied only to the first few steps of the horizon, providing a trade-off between solution quality and computational load.

- Vectorized operation: The feasibility searching (6.6) and final cost evaluation (6.8) involve repetitive calculations for each candidate sequence. Since these evaluations are independent, they can be implemented using vectorized operations. This approach processes all candidates in a single slot, significantly reducing the computational overhead of loop-based implementations.

- Parallel computation: The most computationally intensive part in this approach is the QP-based refining process (6.7), which requires solving multiple QP problems (6.4). As these problems are independent, simultaneous computation can be employed when the number of problems becomes significantly large. Thus, this parallelism can drastically reduce the overall computation time.

6.2 SIL simulation results

This section presents a comprehensive evaluation of the proposed control strategies applied for coordinated active power and current magnitude. In particular, we first detail the simulation scenarios and controller configurations that were conducted through the SIL simulations described in Section 4.2.2. Subsequently, we analyze the obtained results to evaluate our BILEVEL optimization approach developed in Section 6.1.3 and compare it against both conventional industrial controllers and other optimization-based methods.

6.2.1 Scenario setup

Similarly to previous validation, we introduce various simulation circumstances, which can be categorized into two main scenarios, as summarized in Table 6.1:

TABLE 6.1: Detail of implemented scenarios for power and current control.

Scen.	Approach	Reference Value	Ref. Characteristics	Run Time
1	RB-GS vs. BILEVEL	12×10^3 kW, 140 kA	Equal, Constant	24 hours
2	See Table 6.2	See Table 6.3	Unequal, Time-varying	28 hours

- Scenario 1 compares our proposed optimization-based approach against a conventional controller described in the previous chapter. The simulation runs for 24 hours with constant, equal setpoints for power, i.e., 12 MW per phase and current, i.e., 140 kA per phase. This setup is designed to showcase the comparison with implemented industrial controllers under balanced conditions.
- Scenario 2 provides a comparative analysis between our BILEVEL strategy and other formulation approaches solved by the state-of-the-art solvers. The simulation spans 28 hours with time-varying, unequal setpoints for power and current, as detailed in Table 6.3. This challenging scenario is designed to test the adaptability, robustness and computational efficiency of each approach under unbalanced conditions.

Regarding the conventional controller, we consider the combination of the simple GS and RB controller mentioned in Section 5.2.4 and Section 5.1.3, respectively.

$$\mathbf{u}(k) = \begin{bmatrix} \boldsymbol{\delta\tau}(k) \\ \boldsymbol{\delta h}(k) \end{bmatrix} = \begin{Bmatrix} \text{RB controller in (5.9)} \\ \text{GS controller in (5.3)} \end{Bmatrix}. \tag{6.12}$$

While the RB controls the total power using rule-based logic to adjust the three tap changers at the same positions, GS manages the electrode heights in three phases to stabilize current magnitude tracking errors by proportional gains. This combination reflects the real existing industrial control system for a SAF taken from the control scheme in Figure 2.14b. The control system is decoupled between the two variables, i.e., power and current, and across the three phases.

For scenario 2, we evaluate and compare multiple optimization-based approaches, excluding the RB-GS controller. Similarly to the power control validation in Section 5.2.4, we implement three other methods as benchmarks for our proposed BILEVEL strategy. All of them are summarized in Table 6.2 and described as follows:

TABLE 6.2: A summary of the implemented optimization-based control approaches.

No.	Approach	Problem	Solver	Strategy
i	MINLP	(6.1)	`Bonmin`	Solves the original MINLP problem directly using a MINLP solver interface.
ii	MIQP	(6.2)	`Gurobi 12.0.3`	Solves the MIQP formulation directly using a MIQP solver interface.
iii	SR	(6.3)	`qpOASES`	First solves the QP-relaxation, then applies a nearest-integer rounding strategy.
iv	BILEVEL	(6.3) & (6.4)	`qpOASES`	Applies the BILEVEL strategy detailed in Section 6.1.3.

i) MINLP directly solves the original non-convex problem (6.1) using `Bonmin`, a state-of-the-art MINLP solver. This solver is often computationally intensive for real-time but can serve as a benchmark because of its robustness.

ii) MIQP solves the MIQP problem (6.2) using the `Gurobi 12.0.3`, a modern commercial MIP solver. As mentioned, this solver is claimed to be the fastest solver for MIP problems at the moment.

iii) SR solves the QP-relaxation problem (6.3) and rounds the continuous tap variation variables to the nearest integers. This relax-and-round strategy is often implicitly used in practice due to its simplicity and low computational cost.

iv) BILEVEL represents our proposed bilevel optimization strategy presented in Section 6.1.3. This approach decomposes the original MIP problem into two-level problems and searches for the sub-optimal solution by heuristic strategies.

TABLE 6.3: Numerical values of control reference over four periods.

Period	**Power**(kW)			**Current**(kA)		
	$P_a^{s,\mathrm{ref}}$	$P_b^{s,\mathrm{ref}}$	$P_c^{s,\mathrm{ref}}$	$I_1^{e,\mathrm{ref}}$	$I_2^{e,\mathrm{ref}}$	$I_3^{e,\mathrm{ref}}$
1	10	10	10	132	134	136
2	8	10	10	132	132	132
3	10	8	8	138	130	134
4	12	12	12	140	140	140

Table 6.3 summarizes the time-varying references for power and current tracking in scenario 2. The references are updated every 8 hours to evaluate the adaptability of the

control strategies. We start with balanced power at 10 MW per phase and unbalanced current. In the second stage, the current is balanced to 132 kA per phase, while the power becomes unbalanced. In the third stage, both power and current are unbalanced across the three phases. Finally, in the last stage, power and current are increased to 12 MW and 145 kA, respectively.

TABLE 6.4: Numerical values of control parameters.

Parameter	Value	Unit	Parameter	Value	Unit
Time			**Constraint**		
T_s	500	ms	γ	1	step
N_p	1	–	$[\boldsymbol{\tau}_{\mathbf{lb}}, \boldsymbol{\tau}_{\mathbf{ub}}]$	$[1, 33]\,\mathbf{I}_{3\times1}$	step
Objective			$[\boldsymbol{h}_{\mathbf{lb}}, \boldsymbol{h}_{\mathbf{ub}}]$	$[5, 105]\,\mathbf{I}_{3\times1}$	cm
			$[\boldsymbol{r}_{\mathbf{lb}}, \boldsymbol{r}_{\mathbf{ub}}]$	$[0.2, 2\times10^3]\,\mathbf{I}_{3\times1}$	mΩ
$\boldsymbol{\epsilon}^{\boldsymbol{p}}$	$500\mathbf{I}_{\mathbf{3\times1}}$	kW	$[\boldsymbol{x}_{\mathbf{lb}}, \boldsymbol{x}_{\mathbf{ub}}]$	$[0.2, 2\times10^3]\,\mathbf{I}_{3\times1}$	mΩ
$\boldsymbol{\epsilon}^{\boldsymbol{i}}$	$0.5\mathbf{I}_{\mathbf{3\times1}}$	kA	$[\boldsymbol{p}^{\boldsymbol{s}}_{\mathbf{lb}}, \boldsymbol{p}^{\boldsymbol{s}}_{\mathbf{ub}}]$	$[1, 25\times10^3]\,\mathbf{I}_{3\times1}$	kW
$\left[\boldsymbol{p}^{\boldsymbol{s},\mathrm{ref}}, \boldsymbol{I}^{\boldsymbol{e},\mathrm{ref}}\right]$	Defined in Table 6.1	–	$[\boldsymbol{I}^{\boldsymbol{s}}_{\mathbf{lb}}, \boldsymbol{I}^{\boldsymbol{s}}_{\mathbf{ub}}]$	$[10, 84.2]\,\mathbf{I}_{3\times1}$	kA
$[\mathbf{Q}^{\mathbf{p}}, \mathbf{Q}^{\mathbf{i}}]$	$[1, 10^7]\,\mathbf{I}_{\mathbf{3\times1}}$	–	$[\boldsymbol{I}^{\boldsymbol{e}}_{\mathbf{lb}}, \boldsymbol{I}^{\boldsymbol{e}}_{\mathbf{ub}}]$	$[17, 145]\mathbf{I}_{\mathbf{3\times1}}$	kA
$[\lambda_{\max}, \mu, \nu]$	$[10^{11}, 1, 2]$	–	$\boldsymbol{\Delta\tau}_{\mathbf{max}}$	$\mathbf{I}_{\mathbf{3\times1}}$	step
$\boldsymbol{\kappa}$	$[\mathbf{I}_{\mathbf{3\times1}}, \boldsymbol{\epsilon}^{\boldsymbol{p}}/\boldsymbol{\epsilon}^{\boldsymbol{i}}]^\top$	–	$\boldsymbol{\Delta h}_{\mathbf{max}}$	$5\mathbf{I}_{\mathbf{3\times1}}$	cm

Table 6.4 details the numerical values of optimization-based parameters that will be consistently used throughout the simulations. These parameters contain the control sampling time T_s, prediction horizon N_p, tolerances for power and current ($\epsilon^{\mathbf{p}}$, $\epsilon^{\mathbf{i}}$), their respective references ($\boldsymbol{p}^{\boldsymbol{s},\mathrm{ref}}$, $\boldsymbol{I}^{\boldsymbol{e},\mathrm{ref}}$) and the associated weights ($\mathbf{Q}^{\mathbf{p}}$, $\mathbf{Q}^{\mathbf{i}}$). Additionally, tap penalty parameters ($\lambda_{\max}$, μ, ν, $\boldsymbol{\kappa}$) and all constraint-related variables are also included. Notably, the prediction horizon is kept very short, $N_p = 1$, due to the limited validity of linear approximation models (3.13) and (3.14) over longer prediction horizons.

6.2.2 Performance analysis

Herein, we present a detailed analysis of the SIL simulation results for the two scenarios defined in Section 6.2.1. We evaluate the results using metrics established in Section 4.2.1.

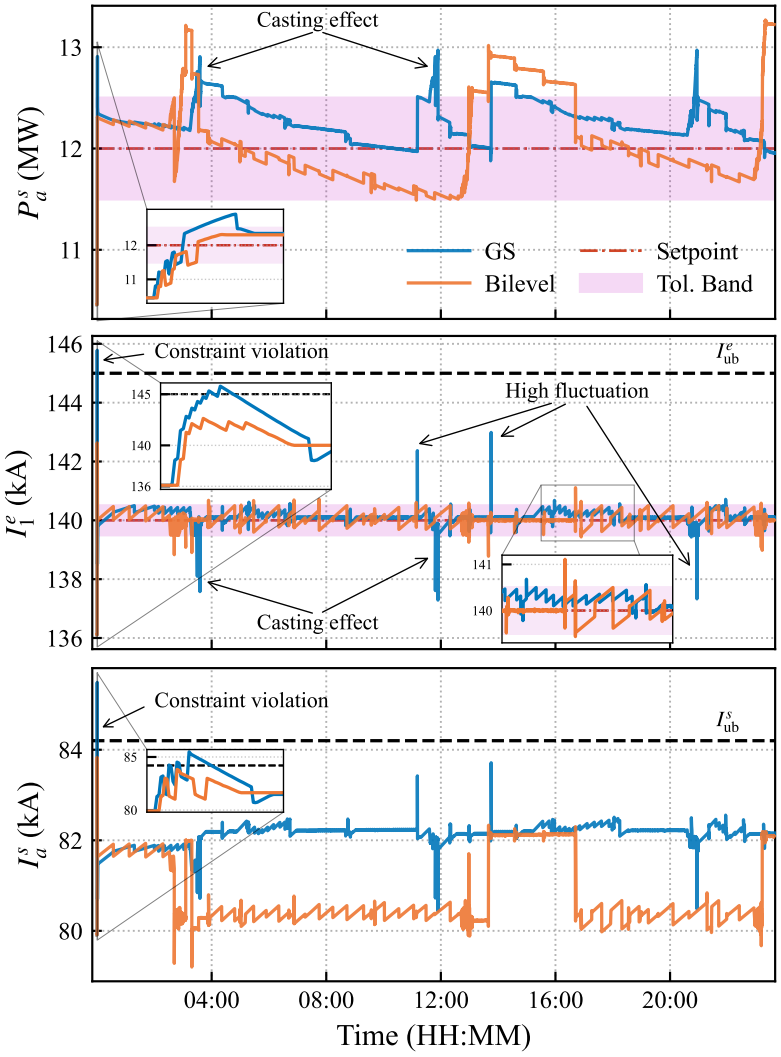

FIGURE 6.3: Performance comparison in phase 1: transformer power (top), electrode current (middle), and transformer current (bottom) under conventional GS control (blue) and the proposed BILEVEL approach (red) over 24 hours (Scenario 1).

6.2.2.1 Scenario 1: Conventional versus advanced control

In this scenario, we compare performance between our proposed BILEVEL approach and the RB-GS controller through the output evolution of electrical phase one, illustrated in Figure 6.3, and the statistical comparison of all three phases, including the number of tap switches, provided in Table 6.5.

Figure 6.3 illustrates that, in both approaches, power and current generally track their references. However, the gain-scheduling controller exhibits some critical issues during the simulation. In particular, it shows a significant overshoot at the start, leading to some constraint violations in both electrode and transformer currents, i.e., $|i_1^e| > I_{\text{ub}}^e = 145\,\text{kA}$ and $|i_a^s| > I_{\text{ub}}^s = 84.2\,\text{kA}$. This shows the drawbacks of the classical approach in ensuring furnace safety conditions. As a result, the EAF system is usually operated at lower power and current levels to ensure safety, e.g., powers are below 10 kW and currents are below 135 kA per phase. The system is also equipped with a separate safety mechanism that triggers and powers off the furnace in the event of violations.

Moreover, the conventional controller shows more frequent deviations and larger fluctuations in the electrode current control, e.g., $|i_1^e|$ suddenly increases from 140 kA to 143 kA. This is a result of the coupling between tap and electrode movements in the electrical system, as these control actions are not coordinated in the conventional approach. In contrast, our BILEVEL approach maintains more consistent tracking performance, with some increase in power due to the casting operation. However, no constraint violations or sudden current overshoots are observed across all three phases.

TABLE 6.5: Statistical results in three phases over 24 hours (Scenario 1).

PHASE	**Power** (%)				**Current** (%)		**Tap Switch**
	RPD$_j$	**RPD**$_\text{M}$	**OPT**$_j$	**OPT**$_\text{M}$	**RCD**	**OCT**	
RB-GS							
Phase 1	2.75	**2.15**	14.69	**0.04**	0.17	0.31	14
Phase 2	3.96		41.69		0.17	0.34	14
Phase 3	3.29		22.8		0.16	0.35	14
BILEVEL							
Phase 1	3.54	**2.00**	19.67	**4.65**	0.16	0.2	10
Phase 2	2.62		8.51		0.16	0.19	6
Phase 3	1.97		5.84		0.15	0.23	6

Lower value represents better performance.

Because the RB-GS approach controls the total power across three phases, whereas the BILEVEL approach handles all three powers concurrently, we introduce, in Table 6.5, power indicators RPD and OPT computed for each phase and for total power tracking to ensure a fair comparison. While total power control is well achieved in the RB-GS approach with 2.15% RPD and very low OPT of 0.04%, individual-phase power tracking

cannot be guaranteed, especially in phase 2, where OPT exceeds 40%. This happens even when currents and tap positions are balanced, due to consistent impedance unbalance caused by the furnace loads. This indicates that the power distribution among the three phases is poorly managed, thereby affecting heating and consumption in the system. In contrast, our BILEVEL approach yields better overall phase RPD and OPT values. Although tracking performance in phase 1 is less effective, with 3.54% RPD and 19.67% OPT, results in the other phases are significantly better, with both RPD and OPT below 3% and 10%, respectively. Regarding current control, RCD and OCT show better tracking performance under the BILEVEL approach, with consistently smaller values across all phases. Moreover, tap operations in the BILEVEL approach are nearly halved compared to the conventional method.

These results indicate that our approach achieves a better performance in stabilizing transformer powers and electrode currents across three phases while reducing unnecessary tap operations. More importantly, it remains stable and robust under varying conditions in the molten bath, e.g., casting or slipping operation, while ensuring operational safety. Additionally, unlike the conventional method, our approach is an optimization-based method that requires online computation to determine the optimal tap positions and electrode heights. Even so, the BILEVEL approach imposes only a small computational burden, averaging 14 ms, significantly less than the control sampling time of 500 ms. The computational analysis of the approach will be further investigated in the second scenario.

6.2.2.2 Scenario 2: BILEVEL analysis

In this scenario, we aim to evaluate our proposed BILEVEL control approach on longer, more complex references. Before comparing its performance with the other optimization-based approaches, we first present and analyze its standalone results across all three phases. Specifically, Fig. 6.4 illustrates the system evolution and control signals under the BILEVEL approach throughout the three phases. The corresponding statistical indicators are then specified in Table 6.6.

Fig. 6.4a shows the output tracking performance of the BILEVEL approach under time-varying and unbalanced electrical conditions in three phases over 28 hours. We observe that the transformer's active power and the electrode currents generally follow their

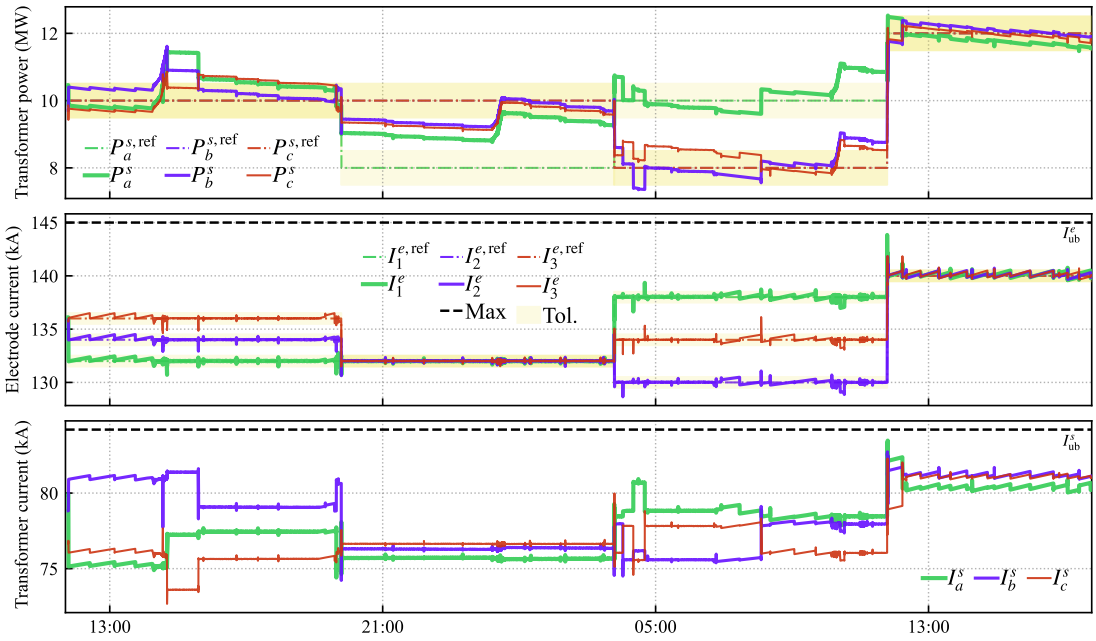

(A) Electrical outputs of the BILEVEL approach across three phases: transformer active power (top), electrode current (middle), and transformer current (bottom).

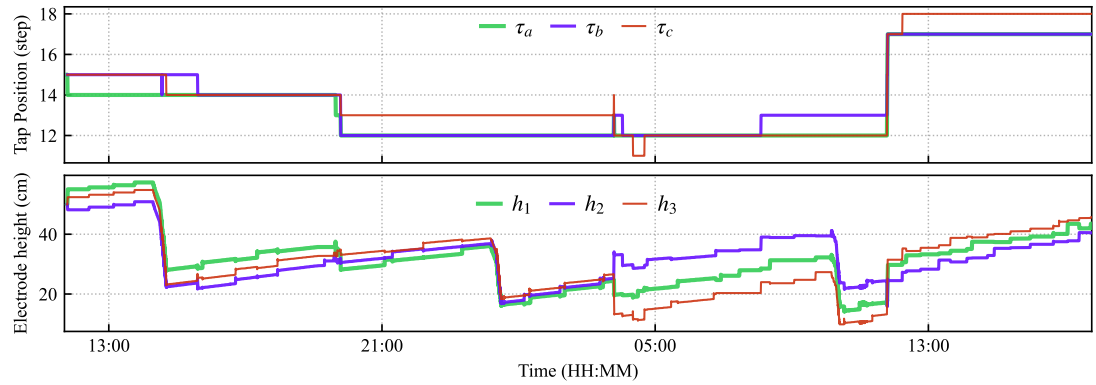

(B) Control actions of the BILEVEL approach sent to the PLC across three phases: transformer tap positions (top) and electrode positions (bottom).

FIGURE 6.4: Performance of the BILEVEL approach under time-varying, unbalanced setpoints (Scenario 2). The controller effectively tracks references while respecting all operational constraints, including tap balancing.

references across all phases. However, Table 6.6 shows that current tracking demonstrates much better performance with mean values of RCD and OCT being less than 1%, while these values in power tracking, RPD and OPT, are 5.54% and 36.11%, respectively. This is because power cannot track the reference perfectly, especially in the second stage of the reference. This is reasonably expected, as we have restricted the number of tap

switches to mitigate the hunting problem and have maintained balanced tap positions via constraint (4.9). Strict compliance is satisfied, as shown in Fig. 6.4b, where the difference in tap positions between any two phases never exceeds two steps. Furthermore, Table 6.6 shows that the number of tap switches in the three phases is relatively balanced, with 13, 12, and 10 operations, respectively. Noticeably, the electrode currents are effectively stabilized around the reference values, with smooth transitions in the electrode heights shown in Fig. 6.4b.

TABLE 6.6: Statistical results of BILEVEL approach in three phases (Scenario 2).

Phase	**Power** (%)		**Current** (%)		**Tap Switch**	**CPU** (ms)
	RPD	OPT	RCD	OCT		
Phase 1	7.55	42.08	0.13	0.62	13	
Phase 2	4.27	26.27	0.13	0.59	12	13.91
Phase 3	4.80	39.96	0.13	0.60	10	
Mean	**5.54**	**36.11**	**0.13**	**0.60**	**11.67**	

At the beginning of the simulation, we set balanced power and unbalanced current references. While the current is well tracked, the power shows some deviations during casting. However, it gradually returns to its reference value at 10 MW as tap switches are allowed. In the second stage, transformer powers are intentionally unbalanced with 8 MW in phase 1 and 10 MW in the other phases, whereas electrode currents are kept balanced at 132 kA. As discussed, the transformer powers cannot follow their references properly and fluctuate between 8 MW and 10 MW, whereas the current is still tracked perfectly. The purpose of introducing this power imbalance is also to test the BILEVEL approach's ability to handle system constraints, especially in tap changer coordination.

In the third stage, both transformer powers and electrode current setpoints are unbalanced, allowing greater flexibility in control actions. As a result, power tracking improves alongside the current tracking. In particular, we observe that power in phase 1 converges to 10 MW, while the other phases reach 12 MW. During the last stage, transformer powers and electrode currents are all increased to 12 MW and 140 kA, respectively, which is a significant increase compared to the previous stages. The BILEVEL control approach still allows effective tracking, with minor overshoot in currents during the transition as the tap rises considerably. However, the currents in both electrodes and transformers always remain within the safety limits, i.e., 145 kA and 84.2 kA.

6.2.2.3 Scenario 2: Optimization-based comparison

In the following analysis, we present in Fig. 6.6 the system behaviors in phase one of the three-phase rotation between the BILEVEL approach and other optimization-based approaches. Moreover, we have Figs. 6.5-6.8 visually demonstrate the performance metrics, offering a more intuitive comparison. It includes the tracking performance and the number of tap switching operations, averaged across the three phases, along with the computation time, analyzed throughout the simulation.

In particular, Fig. 6.6a shows the behavior of transformer power, electrode current and transformer current for each approach in 28 hours. The results indicate that, besides the BILEVEL approach, the MINLP approach also demonstrates good tracking performance for both power and current. In contrast, the MIQP approach, implemented using `Gurobi` solver, fails to track the power reference for most of the simulation period. The SR approach suffers from considerable fluctuations in current tracking due to the rounding errors in the integer decision variables. More critically, as expected, it also fails to guarantee the constraint satisfaction due to the rounding. Remarkably, the transformer current temporarily exceeds its upper limit, i.e., $|i_a^s| > I_{\text{ub}}^s = 84.2\,\text{kA}$, when the power reference suddenly rises to 12 MW. The control actions, illustrated by the evolution of tap position and electrode height in Fig. 6.6b, exhibit different behaviors depending on the control strategy implemented.

In the following, we compare the optimization-based approaches through the performance indicator values. Fig. 6.5a evaluates the reference deviation of power (RPD) and current (RCD). Among the four approaches, MINLP and BILEVEL approaches yield the lowest power deviation with 5.50% and 5.54%, respectively. In contrast, MIQP shows the highest variation with 15.86%, followed by SR with 9.17%. For current control, MINLP, MIQP and BILEVEL perform very well with the current deviation below 0.2%. SR, however, shows a deviation more than twice that, reaching 0.51%. Fig. 6.5b presents the percentage of time the system operates outside the power tolerance (OPT) and current tolerance (OCT). In terms of power tracking, MINLP, SR, and BILEVEL approaches perform similarly, with OPT values around 33-36%. On the other hand, MIQP spends a significantly higher proportion of time outside the tolerance, which is 75.78%. For

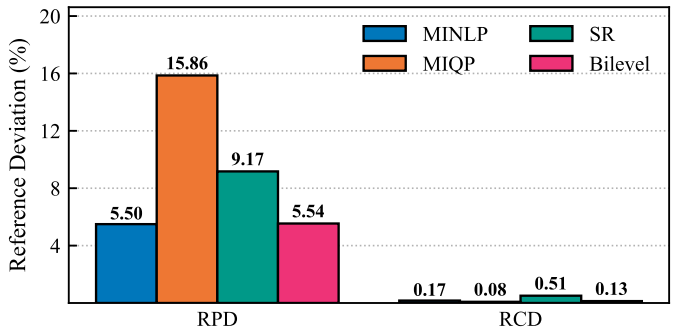

(A) Mean reference deviation for power (RPD) and current (RCD).

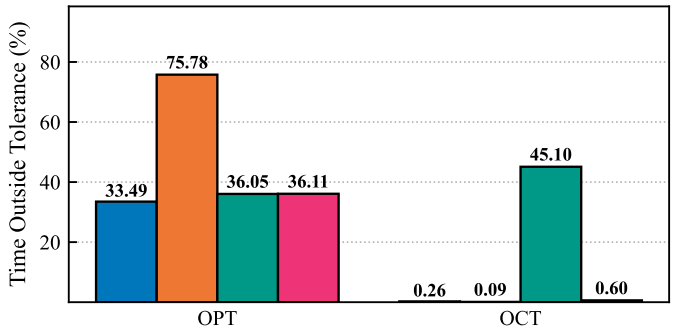

(B) Mean time outside tolerance for power (OPT) and current (OCT).

FIGURE 6.5: Tracking performance metrics for the four optimization-based approaches, averaged over three phases.

current tracking, MINLP, MIQP, and BILEVEL approaches have no OCT values above 0.6%, whereas SR shows a much higher value of 45.1%.

The number of switching operations illustrated in Fig. 6.7 is also an important factor for assessing the performance of different approaches. According to the best power tracking performance, the MINLP approach requires a relatively high number of tap changes, up to 47 switches in total, with a noticeable imbalance of 9 steps between phases. In contrast, MIQP exhibits the fewest switches, with only 20 operations, showing a more conservative behavior that compromises power tracking performance. The SR approach allows the highest switching operations at 50, primarily because of the nearest-integer rounding mechanism, which aggressively adjusts the taps. Meanwhile, the BILEVEL approach offers a balanced compromise, with 35 switches evenly distributed across phases.

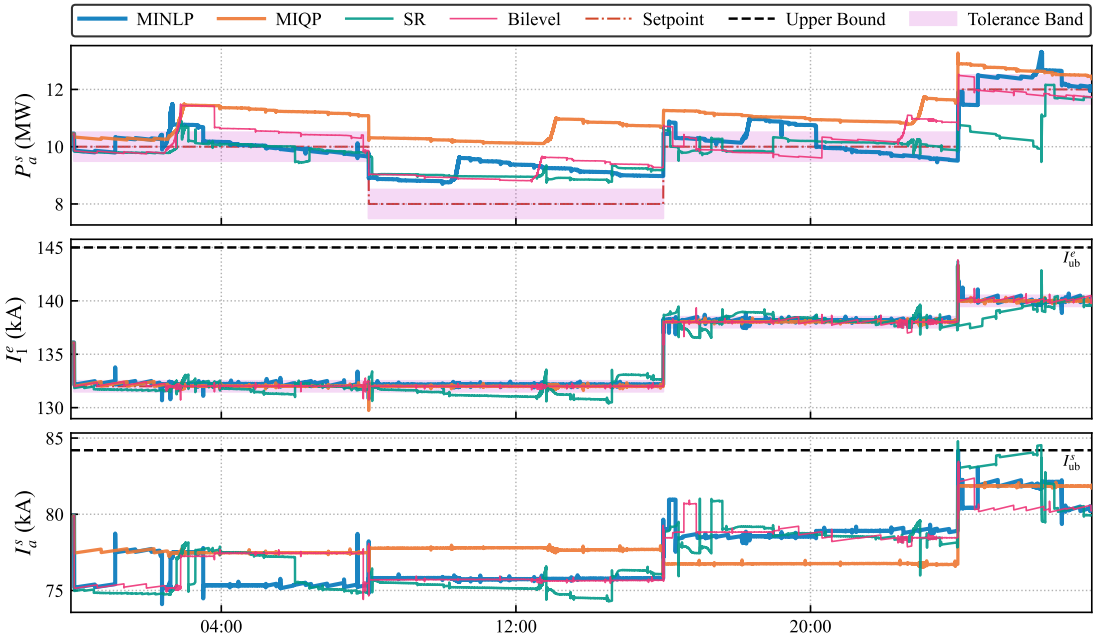

(A) Electrical outputs across different control strategies in phase 1: transformer power (top), electrode current (middle) and transformer current (bottom).

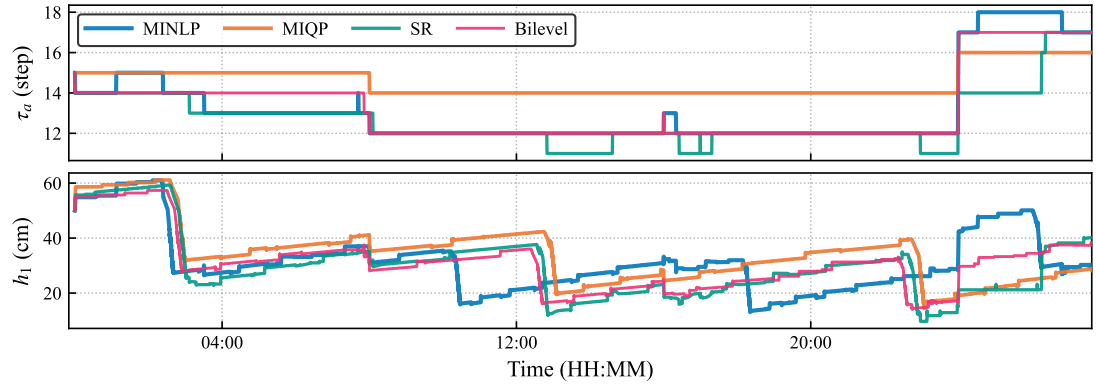

(B) Control actions sent to the PLC by different control strategies in phase 1: transformer tap positions (top) and electrode positions (bottom).

FIGURE 6.6: Performance comparison across four different optimization-based control strategies in phase 1: critical electrical output behaviors and corresponding control actions over 28 hours with time-varying unbalanced references (Scenario 2).

In addition to control performance, computational efficiency is a critical factor for real-time implementation in EAF when using an optimization-based approach. As a result, we analyze the computation time of four approaches over the simulation period deeply using a distribution plot, as shown in Fig. 6.8. This provides a comprehensive view of

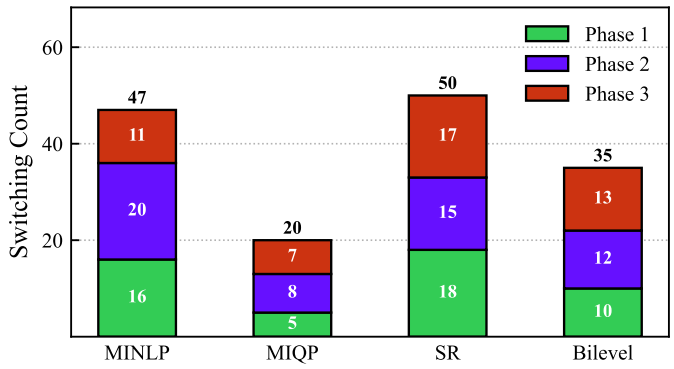

FIGURE 6.7: Total tap switching operations for each approach. The BILEVEL strategy finds a good compromise between performance and actuator usage.

the time required for each approach, including min, max, median, and mean values, thus offering deeper insights into their practical feasibility for real-time implementation.

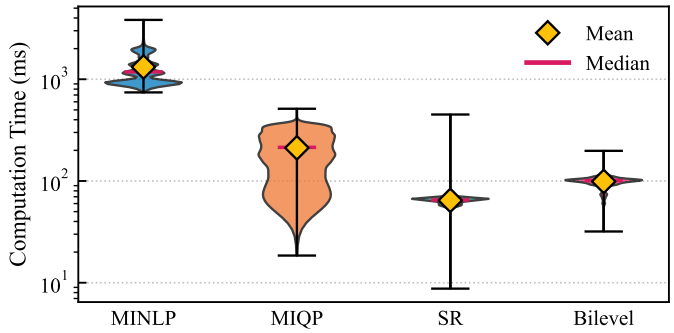

FIGURE 6.8: Distribution of computation time per control step. The BILEVEL approach is significantly faster than MINLP and MIQP, making it suitable for real-time implementation.

Fig 6.8 highlights the most important advantage of our proposed BILEVEL approach, which is the computational performance. The MINLP, while guaranteeing optimality, is computationally intensive, with a mean CPU time of 284 ms and a maximum of 648.5 ms, which exceeds the sampling time of 500 ms. Note that the best commercial MIP solver integrated with MIQP formulation significantly reduces the average computation time to 32.35 ms and the maximum time to 77.97 ms. However, MIQP does not deliver reasonable solutions for the original MINLP problem as illustrated in Fig. 6.5. The SR approach is the fastest, with an average time of 1.92 ms, but, as previously discussed, its speed comes at the cost of constraint violations, making it an unreliable solution. In contrast, our proposed BILEVEL approach achieves a mean CPU time of 13.91 ms, which is more

than 20 times lower than that of the MINLP approach and 2 times lower than that of the MIQP approach. Furthermore, the maximum value of 90.19 ms is 5 times below the sampling time.

6.2.3 Discussion

The two simulation scenarios presented above validate our proposed coordinated power and current control strategies using the MPC framework in Figure 6.1. They show the effectiveness of our BILEVEL heuristic algorithm, an extension of the MIOR concept presented in Section 5.2.3, for solving mixed-integer control problems.

The conventional RB-GS controller, which mimics industrial practice, was compared with our BILEVEL approach in scenario 1. However, it exhibited significant drawbacks, including violations of constraints on both electrode and transformer currents. This confirms the need for larger safety margins in practical operations, thereby reducing overall production efficiency.

The MI-MPC formulations, solved by the exact methods in scenario 2, effectively manage system interactions and constraints. Particularly, the MINLP approach, solved with `Bonmin`, delivered the most efficient tracking performance for both power and current. However, its computational cost is high, occasionally exceeding the sampling time. The MIQP formulation, solved by `Gurobi`, significantly reduces computation time but at the cost of poor power tracking performance, requiring insufficient tap switches. Conversely to the only-power control problem in the previous chapter, where we saw a large number of tap switches. This shows an inconsistency in the approach, which may stem from the MIQP formulation or the solver.

Regarding the relax-and-round solving technique using the SR strategy, while it can significantly reduce the optimizer's computational effort, it degrades tracking performance. Its simple rounding mechanism imposes greater limitations on tracking performance when the optimization problem involves continuous variables. Difference from the purely integer problem in power control, rounding in this MIP problem results in larger deviations from the optimal values. More importantly, it fails to provide feasible solutions to the original MIP problem, leading to critical constraint violations. Consequently, despite

its simplicity and low computational expenses, the SR approach cannot be considered a reliable solution for SAF control.

In contrast, our proposed BILEVEL heuristic provides a high-quality solution with competitive performance compared to the other implemented methods, i.e., lower RPD and RCD values and fewer tap switching operations. It also stands out for its high computational efficiency, with the maximum computation being at least five times shorter than the sampling interval. This is achieved by decomposing the MINLP into a sequence of simpler QP problems and incorporating heuristics to guide the search for sub-optimal solutions.

Similarly to the previous validations, our proposed BILEVEL approach was tested over a prediction horizon of only one step. Extending the prediction horizon would require more accurate approximations of the system dynamics. Then, the performance of the BILEVEL approach under longer horizons would be more interesting to investigate in future works.

6.3 Concluding remarks

In this chapter, we introduced a coordinated power and current control framework for the SiMn SAF simulator, which is summarized in Figure 6.1. The control problem was formulated as the MINLP problem (6.1) to handle both continuous electrode displacement and discrete tap changer switches. Its switching cost function is penalized by an adaptive weight-tuning algorithm developed in Algorithm 4.1 to reduce the number of tap operations effectively.

To overcome the computational burden of MINLP, we developed a novel BILEVEL optimization strategy, as illustrated in Figure 6.2, which approximates the optimal solution through a two-level hierarchical structure. In particular, it combines a QP-relaxation problem (6.3) with a QP-based refinement problem (6.4) and heuristic procedures, providing a computationally efficient alternative to traditional MIP solvers.

Our SIL simulation results in Section 6.2 confirmed the effectiveness of the BILEVEL strategy against not only a conventional RB-GS controller but also state-of-the-art MIP

solvers. The BILEVEL method delivers a high-quality solution with robust tracking of both power and current references, a reduced number of tap switching operations and strict adherence to operational constraints. Most critically, its low computational effort for the MINLP problem makes it a promising solution for real-time SAF control.

Chapter 7

Conclusions and future developments

7.1 Conclusions

This manuscript has addressed the complex challenge of designing an advanced, real-time optimal control system for a three-phase, high-intensity SiMn SAF. While electrical control of SAFs has been studied for decades, existing industrial furnaces still rely heavily on manual control or simple rule-based controllers that often neglect the intricate interdependencies and nonlinearity in the furnace dynamics. As a result, the furnace is often operated suboptimally, leading to inefficiency. To address this issue, our work aims to improve the current SAF control system by proposing a systematic, model-based scheme that leverages detailed furnace modeling and advanced optimization techniques. To this end, we have developed a comprehensive framework, from electrical modeling to the control formulation and implementation of various control strategies. The outcomes are validated through the SIL simulation environment that imitates the actual industrial SAF. With the development of standalone software for the SIL simulator, the validation comes as a real-time simulation, not just by applying the controller to a simplified model in an offline manner.

7.1.1 Comprehensive electrical modeling and analysis

An indispensable ingredient of this thesis is the development of a detailed, physics-based electrical model for the SiMn SAF, as presented in Chapter 3, which served as the cornerstone for the design of the advanced control strategies. Inspired by fundamental electrical law, we constructed a full three-phase model that captures the furnace's behavior from the primary side of the transformers to the molten bath. Unlike simplified models that often neglect the primary side or assume balanced conditions, our model explicitly accounts for the influence of discrete tap positions and the inherent interconnection and nonlinearity of the system. The dynamical models, which capture tap switching and electrode movement, are driven from real-time data using regression methods.

Through simulation and visualization, we intuitively demonstrated how the discrete tap positions and continuous electrode heights influence key electrical variables such as transformer powers and electrode currents. This analysis revealed the intricate electrical behaviors of the furnace. It also interprets the complex interdependencies among phases, which are often overlooked by traditional decentralized control schemes.

7.1.2 Advanced control design and real-time optimization

Regarding the main contribution of this thesis, we developed advanced model-based control strategies for the SiMn SAF, leveraging the detailed electrical model. Beforehand, we introduced the existing control methods and their limitations in Chapter 2, setting the stage for our proposed approaches. Right after the model formulation in Chapter 3, we thoroughly analyzed the control requirements and challenges specific to the SiMn SAF in Chapter 4, thereby confirming the need to adopt MPC as the core control framework. In particular, different control strategies can be formulated to effectively manage the complexity of the system, i.e., multi-variables, phase interactions, and the hybrid nature of control actions. Furthermore, we provided a detailed review of the existing numerical tools suitable for addressing our control problems. Based on the analysis, we selected open-source CasADi as the primary optimization framework due to its flexibility, computational efficiency and seamless integration with multiple high-performance solvers.

With the necessary ingredients in place, we proceeded to design various control strategies throughout Chapter 5 to Chapter 6. Initially, we designed multi-variable current control strategies that allow effective control of three current magnitudes while accounting for system interactions and the furnace's operational constraints. In addition, we formulated integer-based control problems with adaptive weight-tuning cost to regulate transformer active power via integer tap positions while minimizing switching. Chapter 6 combines two previous control schemes into a coordinated power and current framework. This novel approach, which has not been explored before, allows us to account for the interactions not only among the phases but also between the two actuators.

The integration of discrete tap variables, however, transforms the control problem into an MIP. MIPs are known to be NP-hard and challenging to solve in real time, even with the most advanced solvers. As a result, we developed novel algorithms tailored to our control problem using a heuristic rounding strategy. In particular, in Chapter 5, we introduced a simple yet effective model-informed optimal rounding (MIOR) strategy to tackle the purely integer power control problem. Whereas in Chapter 6 we built on this idea, developing a bilevel optimization strategy to address the computational burden of the coordinated MIP problem. This innovation makes the coordinated control strategy computationally inexpensive, enabling a promising path toward real-time implementation.

7.1.3 SIL validation in a more realistic environment

The performance of the proposed control strategies was rigorously validated through simulations in a SIL environment, as described in Chapter 4. This SIL simulator has been built as a standalone software with complex electrical models and integrated with several operational events appearing in real industrial furnaces. This helps us evaluate the controllers under more realistic conditions before putting them in an actual furnace.

The simulation results demonstrated the enhancement of the proposed coordinated control approach in the SiMn SAF. Compared to conventional decentralized control methods, our strategy enables flexible and optimal coordination across phases while mitigating tap hunting problem with fewer switches. When benchmarked against state-of-the-art MINLP and MIQP solvers over a short prediction horizon, our bilevel algorithm is more computationally efficient and achieves even better tracking performance.

In summary, the preliminary simulation results provide evidence of an efficient, implementable solution for the real-time control of SiMn SAF. Nevertheless, the validation lacks experimental verification in an actual industrial furnace, which is currently ongoing work. Along with this, there are rooms for improvement in many aspects of the modeling or control, which we outline in the next section. To conclude, we believe our work brings valuable insights and opens up future directions for both academic research and industrial applications in electric arc furnace control.

7.2 Future developments

At the beginning of the manuscript, we reviewed the existing literature and identified several open challenges in controlling EAF. Along with the manuscript, we showed our contributions, ranging from comprehensive electrical modeling to advanced control strategies, to address some of these issues in SiMn SAFs. However, given the scope of the thesis and the limited time for the investigation, we acknowledge that there are certainly areas for improvement and limitations to be addressed. As a result, we outline promising directions for advancing our work in the future at the end of the manuscript.

7.2.1 Model enhancement

While the steady-state electrical is well-established in this thesis, the dynamic models still need further improvement to capture the impact of control actuators on electrical variables more accurately.

7.2.1.1 Electrode-process impedance modeling

As discussed in Section 3.3.1.2, the relationship between electrode-process impedance and electrode displacement becomes highly nonlinear and unpredictable under varying operating conditions. During such periods, the linear model may fail to accurately capture impedance dynamics. Future work could investigate the use of data-driven modeling frameworks, such as those proposed by Biswas et al. [2024], to approximate these complex relationships using historical operational data. Integrating data-driven models with

the existing physics-based framework could significantly improve model accuracy across diverse operating conditions.

7.2.1.2 Effect of electrode movement on transmission line modeling

The current transmission line model assumes constant line parameters regardless of electrode position. However, in practice, electrode movement can alter the effective length and configuration of the transmission lines, thereby influencing their electrical characteristics. Future research should focus on developing dynamic transmission line models that explicitly account for electrode movements, as suggested by Khoshkhoo et al. [2011a]. Although the effect may be minor, incorporating this aspect could enhance the overall fidelity of the electrical model, particularly during significant electrode adjustments.

7.2.2 Alternative control strategies

In addition to the proposed control strategies, several alternatives can be explored. Moreover, the supervisory MPC control layer for optimizing the energy consumption and production costs is also of great interest.

7.2.2.1 Phase-magnitude control

From the current control viewpoint, regulating the magnitudes of the three electrode currents is the most common approach, but it may not be unique. Instead of focusing only on the magnitude control as we design the problem in Section 5.1, one question is whether it is also interesting to manage the phase relationships among the three currents.

To answer this, we come up with a novel control approach, illustrated in Figure 7.1, that stabilizes the current magnitude of one designated electrode $|i_j^e|$ around $I_j^{e,\text{ref}}$ while simultaneously regulating the phase shifts of the other currents relative to this one. Specifically, it enforces $\angle i_j^e - \angle i_{j-1}^e$ and $\angle i_{j+1}^e - \angle i_j^e$ to the desired values $\Delta\phi_{\pm}^{\text{ref}}$. This approach can be particularly useful in scenarios where maintaining a specific phase shift between the electrode currents can guarantee a balance in current magnitudes.

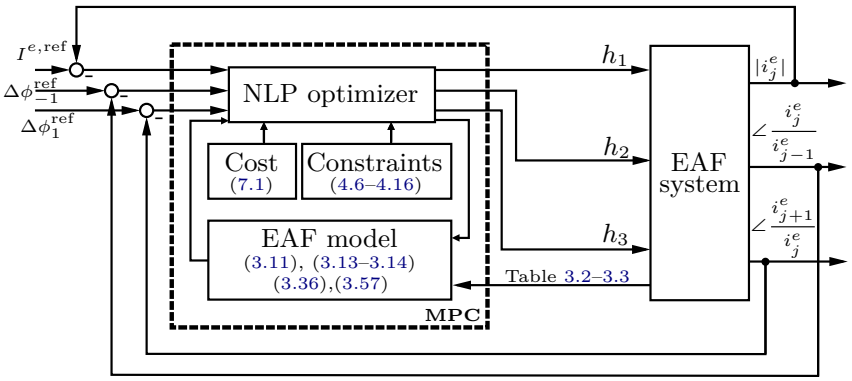

FIGURE 7.1: Phase-magnitude predictive control scheme.

To this end, we formulate a control objective that minimizes two main terms: i) the deviation of current magnitude in a designated phase from its predefined target and ii) the phase shift error between the other two electrode currents with the designated one:

$$J_{I,j}(k) = \underbrace{Q^{I,\text{mag}}\Big[|i_j^e(k)| - I^{e,\text{ref}}(k)\Big]^2}_{\text{i) Magnitude deviation}} + \underbrace{\sum_{n=0}^{1} Q_{2n-1}^{I,\text{pha}}\Big[\angle\frac{i_{j+n}^e(k)}{i_{j+n-1}^e(k)} - \Delta\phi_{2n-1}^{\text{ref}}\Big]^2}_{\text{ii) Phase shift}}, \tag{7.1}$$

where $j \in \{1,2,3\}$ is the index of the chosen designated phase. The summation term iterates for $n \in \{0,1\}$, calculating the phase shifts between adjacent phases in a rotational manner. For instance, if phase $j = 3$ is selected as the reference, the sum includes the phase shift between phase 3 and phase 2 ($\angle\{i_3^e/i_2^e\}$) and the phase shift between phase 1 and phase 3 ($\angle\{i_1^e/i_3^e\}$). $I^{e,\text{ref}} \in \mathbb{R}$ is the reference current magnitude for the designated phase j, whereas $\Delta\phi_{-1}^{\text{ref}}$ and $\Delta\phi_{1}^{\text{ref}}$ represent the desired phase shifts, such as $\pm 120°$ for a balanced three-phase system. The weighting coefficients $Q^{I,\text{mag}}$ and $Q_{\pm 1}^{I,\text{pha}} \in \mathbb{R}$ define the relative importance of the magnitude and phase shift terms in the cost function.

It is worth noting that, due to the computation of current phase angles, the cost (7.1) becomes a non-convex function, requiring the complex current models in (3.36). As a result, we consider the following NMPC formulation for this control problem.

- NLP problem for phase-magnitude control (NMPC):

$$\delta\mathbf{h}^*(\cdot|k) = \arg\min_{\delta\mathbf{h}(\cdot|k)} \sum_{s=0}^{N_p-1} \overbrace{J_{I,j}(s+1|k)}^{(7.1)}, \tag{7.2a}$$

$$\text{s.t.} \quad \forall s \in [0,\, N_p - 1]:$$

$$(5.1b) - (5.1h), \tag{7.2b}$$

$$\text{Electrode instantaneous current } (3.36), \tag{7.2c}$$

In optimization problem (7.2), we look for the optimal sequence of electrode displacements $\delta\mathbf{h}(\cdot|k)$ that minimizes the combined magnitude and phase-shift cost $J_{I,j}(\cdot)$ over N_p. The optimization is subject to the same set of constraints as the magnitude control problem (5.1). In addition, the instantaneous electrode current model (3.36) is explicitly included in constraint (7.2c) to compute the phase angles required for the cost.

TABLE 7.1: Detailed implementation scenarios for phase-magnitude current control.

Scenario	**Approach**	**Designated phase j**	**Current**	**Phase shift**		**Run Time**
			$I_j^{e,\text{ref}}$ (kA)	$\Delta\phi_{-1}$ (°)	$\Delta\phi_1$ (°)	
1	NMPC (7.2)	1	140	120	120	24 hours
2	NMPC (7.2)	2	130	125	115	24 hours

For preliminary validation, we implemented two scenarios with different setpoints as indicated in Table 7.1. In particular, the designated phase j in scenario one is chosen as the first phase with a magnitude setpoint of 140 kA, while in scenario two, it is set to the second phase with 130 kA. Correspondingly, the phases are designed to have an equal shift of 120° among phases in scenario one. Whereas, the desired phase shifts are unbalanced in scenario two, with the second phase (designated phase) leading the first by 125°, and lagging the third by 115°.

The simulation results cannot be compared with those of classical control methods because the control problem involves complex objectives, and decoupling phase and magnitude control in the conventional technique is not straightforward. As a consequence, this highlights the advantage of the MPC framework, which is well-suited for handling such complex control objectives.

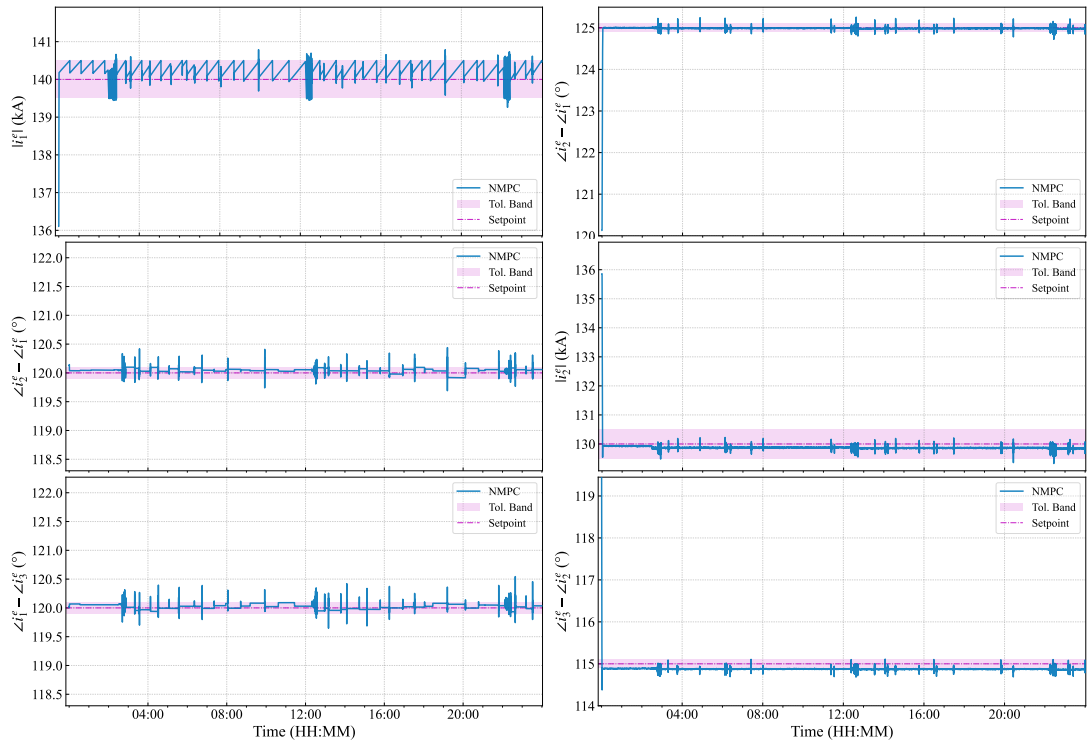

(A) Scenario 1: phase 1 is the reference. (B) Scenario 2: phase 2 is the reference.

FIGURE 7.2: Performances of current magnitude and phase shift regulation under NMPC-based controller over a 24-hour simulation.

From Figure 7.2, we observe that the NMPC controller effectively tracks both the current magnitude target for the designated phase and the phase-shift references. Although scenario 4 presents more significant challenging unbalanced conditions, NMPC can still stabilize the designated magnitude and one phase shift while keeping the other phase shift within minor deviations, i.e., 0.1° from the tolerance band.

7.2.2.2 Resistance control

As mentioned in Section 2.1.3.2, resistance control is an alternative approach with current control to regulate the electrode tip positions under power control. In classical control methods, resistance is often preferred over current control due to its linear relationship with electrode positions, which avoid the interaction effects. However, in our model-based framework, as we can directly incorporate the electrical model, this advantage is no longer significant. Moreover, while considering resistance in the control objective, we still need to

take into account the electrical model of interest variables, e.g., currents to guarantee the operational constraints. As a result, the complexity of resistance optimization problem should be similar to that of current control.

However, it is worth exploring resistance control in comparison with current control to have more insights into the overall control performance. Therefore, we propose a standard NMPC formulation to maintain the electrode-process resistances at their desired values $\boldsymbol{r}^{\text{ref}}$ by adjusting the electrode displacements $\boldsymbol{\delta h}$. Specifically, we have:

- NMPC problem for resistance control:

$$\delta \mathbf{h}^*(\cdot|k) = \arg\min_{\delta \mathbf{h}(\cdot|k)} \sum_{s=0}^{N_p-1} \left\| \boldsymbol{r}(k) - \boldsymbol{r}^{\text{ref}}(k) \right\|^2_{\mathbf{Q}^{\boldsymbol{R}}}, \tag{7.3a}$$

$$\text{s.t.} \quad \forall s \in [0,\, N_p - 1] : (5.1\text{b}) - (5.1\text{h}) \tag{7.3b}$$

Where the quadratic resistance deviation cost is penalized by the weighting matrix $\mathbf{Q}^R \in \mathbb{R}^{3\times 3}$:

$$\mathbf{Q}^{\boldsymbol{R}} = \begin{bmatrix} Q_1^R & 0 & 0 \\ 0 & Q_2^R & 0 \\ 0 & 0 & Q_3^R \end{bmatrix}.$$

The constraints are exactly the same as those in the current control problem (5.1).

7.2.3 Multi-level control frameworks

7.2.3.1 Decentralized MPC framework

While this thesis primarily focuses on centralized MPC strategies that jointly optimize all control actions, an alternative approach worth exploring, mentioned in Section 2.3.2 is a decentralized MPC framework.

As illustrated in Figure 2.15a, a decentralized strategy could involve two MPC controllers operating in parallel on different time scales. An MI-MPC could regulate transformer power via discrete tap variations on a slower time scale, while a classical MPC manages electrode displacements for current control on a faster time scale.

7.2.3.2 Supervisory MPC

Building upon the control strategies developed in this thesis, a higher-level supervisory MPC layer could be introduced to optimize overall energy consumption and production costs in SAF operations. Such hierarchical control structures have been explored in the literature, demonstrating their potential to improve economic performance while maintaining process stability [Liu et al., 2022, Ren et al., 2025].

The supervisory controller would operate on a longer time scale, providing setpoint for low-level controllers based on operational modes, forecasts of electricity prices, raw material costs and production demands [Carlsson et al., 2019, Manojlović et al., 2022]. By coordinating with lower-level MPC controllers, this layer ensures that the furnace operates not only safely and efficiently but also economically.

7.2.4 Open-loop implementation

While we have validated our proposed control strategies in a SIL environment, the next important stage is experimental validation through real plant implementation. This transition should be done with prudence to ensure safety and reliability, especially in an industrial setting. Therefore, we propose to begin this with a step-by-step deployment process. The initial phase of this deployment consists of an open-loop implementation, in which the controllers generate control actions based on real-time measurements without directly influencing furnace operation.

To achieve this, we first establish a reliable real-time data acquisition system capable of synchronizing and collecting measurements from the furnace. This system also performs efficient computation of the variables required by the prediction models, ensuring accurate inputs for the controllers.

Next, we deploy the developed MPC framework on a dedicated computer that receives real-time data from the measurement system. This setup requires establishing a robust communication link between the data acquisition system and the MPC computer to facilitate seamless data transfer.

Once the controllers integrated with the data acquisition system, we conduct real-time open-loop testing, where the controllers compute optimal control actions using real-time data but do not apply these actions to the furnace. Instead, the computed actions are logged and analyzed offline.

After, we evaluate the performance by comparing these logged actions with the actual furnace behavior to assess the potential benefits of the proposed strategies. The insights gained from this analysis allow us to identify any problems and refine the algorithms for closed-loop implementation.

This open-loop phase represents a critical step toward full closed-loop control. It allows us to validate the controllers under real operating conditions while minimizing risks to furnace operation, thereby ensuring a safe and effective transition to advanced control.

Appendices

Appendix A

Appendix

A.1 Electrical steady-state model analysis in Section 3.3

We provide here an alternative transformation to arrive at the secondary current $\boldsymbol{i^s}$ and electrode current $\boldsymbol{i^e}$ models in function of circuit parameters. To this end, we first choose to express the electrode currents i_1^e, i_2^e and i_3^e in terms of the secondary currents i_1^s, i_2^s and i_3^s by substituting (3.23)–(3.25) into (3.20)–(3.22):

$$\left[Z_1\left(i_a^s - i_c^s\right) - Z_2\left(i_b^s - i_a^s\right)\right] + Z_a^s\, i_a^s = \frac{u_{12}^p}{m_a}, \tag{A.1}$$

$$\left[Z_2\left(i_b^s - i_a^s\right) - Z_3\left(i_c^s - i_b^s\right)\right] + Z_b^s\, i_b^s = \frac{u_{23}^p}{m_b}, \tag{A.2}$$

$$\left[Z_3\left(i_c^s - i_b^s\right) - Z_1\left(i_a^s - i_c^s\right)\right] + Z_c^s\, i_c^s = \frac{u_{31}^p}{m_c}. \tag{A.3}$$

Then, we rearrange (A.1)–(A.3) by isolating all secondary current terms on the left-hand side and grouping their coefficients. This yields a symmetric linear system, allowing the

secondary current vector $\boldsymbol{i^s} = [i_a^s,\ i_b^s,\ i_c^s]^\top \in \mathbb{C}^3$ to be compactly written as:

$$\underbrace{\begin{bmatrix} Z_1 + Z_2 + Z_a^s & -Z_2 & -Z_1 \\ -Z_2 & Z_2 + Z_3 + Z_b^s & -Z_3 \\ -Z_1 & -Z_3 & Z_1 + Z_3 + Z_c^s \end{bmatrix}}_{\mathbf{A_s}} \underbrace{\begin{bmatrix} i_a^s \\ i_b^s \\ i_c^s \end{bmatrix}}_{\boldsymbol{i^s}} = \underbrace{\begin{bmatrix} \frac{u_{12}^p}{m_a} \\ \frac{u_{23}^p}{m_b} \\ \frac{u_{31}^p}{m_c} \end{bmatrix}}_{\mathbf{b_s}} \tag{A.4}$$

or

$$\boxed{\boldsymbol{i^s} \ = \ \mathbf{A_s}^{-1}\mathbf{b_s}}. \tag{A.5}$$

Finally, by substituting the solution of the secondary current system (A.5) into the node relations (3.23)–(3.25), we can express in an explicit form the electrode current vector $\boldsymbol{i^e} = [i_1^e,\ i_2^e,\ i_3^e]^\top \in \mathbb{C}^3$ by the following matrix transformation:

$$\boxed{\boldsymbol{i^e} \ = \ \mathbf{M_s}\mathbf{A_s}^{-1}\mathbf{b_s}}. \tag{A.6}$$

Whereas, $\mathbf{M}$ is the coefficient matrix of the node relations (3.23)–(3.25) that maps secondary currents to electrode currents as an affine function $\boldsymbol{i^e} = \mathbf{M_s}\,\boldsymbol{i^s}$, with:

$$\mathbf{M_s} \ = \ \begin{bmatrix} 1 & -1 & 0 \\ 0 & 1 & -1 \\ -1 & 0 & 1 \end{bmatrix}, \tag{A.7}$$

and $\mathbf{A_s}^{-1}$ is the inverse of the coefficient matrix $\mathbf{A_s}$ in (A.5). □

A.2 Classical mixed-integer linear programming algorithms

This appendix provides a more detailed explanation of the branch-and-bound and cutting plane algorithms for solving MILP problems.

A.2.1 Branch-and-bound algorithm

Considering the minimization MILP (4.35), branch-and-bound first solves the LP relaxation problem of the original MIP, i.e., ignoring the integer constraints (4.35c). Suppose the obtained solution is fractional, i.e., $\mathbf{x}_j^* \in \mathbb{R}$, the algorithm proceeds by branching on this variable. This creates two subproblems (nodes) with added constraints that force the variable toward the integer value, i.e., one branch with $\mathbf{x}_j \leq \lfloor \mathbf{x}_j^* \rfloor$, the other with $\mathbf{x}_j \geq \lceil \mathbf{x}_j^* \rceil$. The relaxations of these MILP subproblems are then solved recursively. By taking the minimum of the optimal objective values from the existing nodes, we obtain a *lower bound* (J_{lb}) on the optimal solution. The first node yields a feasible integer solution, which is considered as an *incumbent*, i.e., the node has the best feasible solution so far, with the cost value serving as an *upper bound* (J_{ub}) on the optimal solution. Any node whose solution is infeasible or whose cost value is worse than the current *upper bound* is called *fathomed* and will be pruned from the search. In contrast, nodes with a cost value lower than the current *upper bound* are recorded as a new *incumbent*, and the *upper bound* is updated accordingly. This process continues until all nodes are either explored or the gap between *upper bound* and *lower bound* becomes zero, i.e., $J_{\text{ub}} = J_{\text{lb}}$, ensuring that the optimal integer solution is found.

A.2.2 Cutting plane method

In particular, similar to branch-and-bound, the algorithm starts by solving the LP relaxation of the original MILP problem. If the solution is integer, i.e., $\mathbf{x}_j^* \in \mathbb{Z}$, it is optimal. If not, a valid inequality constraint is generated such that it separates the current fractional solution $\mathbf{x}_j^* \in \mathbb{R}$ from the *convex hull* of mixed integer solutions, i.e., constraint (4.35b). This means that the cut generated, e.g., by the inequality $\alpha^T \mathbf{x}_j \leq \alpha_0$ is constructed so that it is satisfied by all feasible integer solutions of (4.35) but violated by the current fractional variables, i.e., $\alpha^T \mathbf{x}_j^* > \alpha_0$. This cut is then added to the problem and the process iteratively repeats until an integer solution is found or no further valid cut can be generated. The key challenge is how to identify the valid inequality, i.e., determining α^T, α_0. In addition to Gomory cuts, various cutting-plane strategies have been studied to accelerate convergence [Jünger et al., 1995].

For comparison, branch-and-bound consecutively partitions the original problem into a tree of subproblems, while cutting-plane iteratively refines the feasible region of a single problem. As a result, branch-and-bound could be more computationally intensive in large problems due to the exponential growth of nodes, but it guarantees the optimality conditions. Cutting-plane methods can be more efficient for certain problem structures, but generally require a lot of iterations to converge and can be numerically instability due to large LPs presented by added cuts. Consequently, there are significant variants which integrate both methods in a branch-and-cut framework, thus allowing to tighten relaxations early and reduce the search size of the tree in branching [Padberg and Rinaldi, 1991, Mitchell, 2002].

Bibliography

Mahmoud Makki Abadi, Hongyan Tang, and Mohammad Mehdi Rashidi. A review of simulation and numerical modeling of electric arc furnace (eaf) and its processes. *Heliyon*, 2024.

A.B.Stewart. The measurement of electrical variable in a submerged-arc furnace. 1981.

A. Akdag, I. Cadirci, E. Nalcaci, M. Ermis, and S. Tadakuma. Effects of main transformer replacement on the performance of an electric arc furnace system. *IEEE Transactions on Industry Applications*, 36(2):649–658, 2000.

Mazen Alamir. Derivation of certification-based admissibility dashboard of nmpc implementation settings: Framework and associated python package. *IEEE Transactions on Control Systems Technology*, 2024.

Alessandro Alessio, Alberto Bemporad, Mircea Lazar, and WP Maurice H Heemels. Convex polyhedral invariant sets for closed-loop linear mpc systems. In *Proceedings of the 45th IEEE Conference on Decision and Control*, pages 4532–4537. IEEE, 2006.

Joel Andersson, Johan Åkesson, and Moritz Diehl. Dynamic optimization with casadi. In *2012 IEEE 51st IEEE Conference on Decision and Control (CDC)*, pages 681–686. IEEE, 2012.

Joel AE Andersson and James B Rawlings. Sensitivity analysis for nonlinear programming in casadi. *IFAC-PapersOnLine*, 51(20):331–336, 2018.

Joel AE Andersson, Joris Gillis, Greg Horn, James B Rawlings, and Moritz Diehl. Casadi: a software framework for nonlinear optimization and optimal control. *Mathematical Programming Computation*, 11:1–36, 2019.

FV Andreae. Design and control of ferroalloy furnaces. *Electrical Engineering*, 69(6): 531–531, 1950.

Daniel Arnström, Alberto Bemporad, and Daniel Axehill. A dual active-set solver for embedded quadratic programming using recursive ldl$^\top$ updates. *IEEE Transactions on Automatic Control*, 67(8):4362–4369, 2022.

Nuzhet Atay and Burchan Bayazit. Mixed-integer linear programming solution to multi-robot task allocation problem. 2006.

Radu Balan, Olimpiu Hancu, and Eugen Lupu. Modeling and adaptive control of an electric arc furnace. *IFAC Proceedings Volumes*, 40(8):163–168, 2007.

Antoine Bambade, Sarah El-Kazdadi, Adrien Taylor, and Justin Carpentier. Prox-qp: Yet another quadratic programming solver for robotics and beyond. In *RSS 2022-Robotics: Science and Systems*, 2022.

Alex Barclay, Philip E Gill, and J Ben Rosen. Sqp methods and their application to numerical optimal control. In *Variational Calculus, Optimal Control and Applications: International Conference in Honour of L. Bittner and R. Klötzler, Trassenheide, Germany, September 23–27, 1996*, pages 207–222. Springer, 1998.

I.J. Barker. An electrode controller for submerged arc furnaces. *IFAC Proceedings Volumes*, 13(7):611–621, 1980. ISSN 1474-6670. Proceedings of the 3rd IFAC Symposium on Automation in Mining, Mineral, and Metal Processing.

IJ Barker and AB Stewart. Inductive reactance and the operation of large submerged-arc furnaces. *Journal of the Southern African Institute of Mining and Metallurgy (JSAIMM)*, 80(3):123–128, 1980.

Timothy J Barth, Michael Griebel, David E Keyes, Risto M Nieminen, Dirk Roose, and Tamar Schlick. *Lecture notes in computational science and engineering*, volume 49. Springer, 2005.

JG Bekker, IK Craig, and PC Pistorius. Model predictive control of an eaf off-gas process. *IFAC Proceedings Volumes*, 32(2):7050–7055, 1999.

Timo Berthold. Rens: the optimal rounding. *Mathematical Programming Computation*, 6:33–54, 2014.

Timo Berthold. *Heuristic algorithms in global MINLP solvers*. Verlag Dr. Hut, 2015.

Dimitri P Bertsekas. *Constrained optimization and Lagrange multiplier methods*. Academic press, 2014.

Lorenz T Biegler and Victor M Zavala. Large-scale nonlinear programming using ipopt: An integrating framework for enterprise-wide dynamic optimization. *Computers & Chemical Engineering*, 33(3):575–582, 2009.

BigMint. Share of eaf route in global steel production likely to rise to 40% in 2030, 2024. URL https://www.bigmint.co/insights/detail/share-of-eaf-route-in-global-steel-production-likely-to-rise-to-40-in-2030-bigmint-an Available online. Accessed: 2025-07-03.

SA Billings and H Nicholson. Modelling a three-phase electric arc furnace: a comparative study of control strategies. *Applied Mathematical Modelling*, 1(7):355–361, 1977.

Stephen A Billings, Francis M Boland, and H Nicholson. Electric arc furnace modelling and control. *Automatica*, 15(2):137–148, 1979.

Erica Bishop, Ruth Enriquez, Amrit Sandhu, and Michael Zargari. Evaluating carbon emissions from electric arc furnace steel plants in the united states, 2023.

Sinchan Biswas, Vetle Kjær Risinggård, Manuel Sparta, and Damiano Varagnolo. Data-driven modelling of electrode resistance in submerged arc furnaces. In *2024 IEEE 19th Conference on Industrial Electronics and Applications (ICIEA)*, pages 1–7. IEEE, 2024.

Christian Bliek1ú, Pierre Bonami, and Andrea Lodi. Solving mixed-integer quadratic programming problems with ibm-cplex: a progress report. In *Proceedings of the twenty-sixth RAMP symposium*, pages 16–17, 2014.

O Bockman. Arrangement for measuring the crater voltages in a three-phase electric furnace with electrodes arranged in a delta, September 4 1973. US Patent 3,757,021.

Pierre Bonami, Lorenz T Biegler, Andrew R Conn, Gérard Cornuéjols, Ignacio E Grossmann, Carl D Laird, Jon Lee, Andrea Lodi, François Margot, Nicolas Sawaya, et al. An algorithmic framework for convex mixed integer nonlinear programs. *Discrete optimization*, 5(2):186–204, 2008.

Pierre Bonami, Gérard Cornuéjols, Andrea Lodi, and François Margot. A feasibility pump for mixed integer nonlinear programs. *Mathematical Programming*, 119(2):331–352, 2009.

B. Boulet, G. Lalli, and M. Ajersch. Modeling and control of an electric arc furnace. In *Proceedings of the 2003 American Control Conference.*, volume 4, pages 3060–3064, 2003.

Benoit Boulet, Vit Vaculik, and Geoff Wong. Control of non-ferrous electric arc furnaces. *IEEE Canadian review*, pages 1–13, 1997.

Stephen Boyd, Stephen P Boyd, and Lieven Vandenberghe. *Convex optimization*. Cambridge university press, 2004.

Stephen Boyd, Neal Parikh, Eric Chu, Borja Peleato, Jonathan Eckstein, et al. Distributed optimization and statistical learning via the alternating direction method of multipliers. *Foundations and Trends® in Machine learning*, 3(1):1–122, 2011.

Anthony Brook, David Kendrick, and Alexander Meeraus. Gams, a user's guide. *ACM Signum Newsletter*, 23(3-4):10–11, 1988.

Geoffrey Brooks. Developments in electric arc furnace steelmaking. 2001.

Christof Büskens and Dennis Wassel. The esa nlp solver worhp. In *Modeling and optimization in space engineering*, pages 85–110. Springer, 2012.

Richard H Byrd, Jorge Nocedal, and Richard A Waltz. Knitro: An integrated package for nonlinear optimization. In *Large-scale nonlinear optimization*, pages 35–59. Springer, 2006.

Yankai Cao, Arpan Seth, and Carl D Laird. An augmented lagrangian interior-point approach for large-scale nlp problems on graphics processing units. *Computers & Chemical Engineering*, 85:76–83, 2016.

Leo S Carlsson, Peter B Samuelsson, and Pär G Jönsson. Predicting the electrical energy consumption of electric arc furnaces using statistical modeling. *Metals*, 9(9):959, 2019.

Tian-you Chai, Zhi-wei Wu, and Hong Wang. A cps based optimal operational control system for fused magnesium furnace. *IFAC-PapersOnLine*, 50(1):14992–14999, 2017.

Amit Chatterjee and Banshidhar Pandey. *Metallics for steelmaking: production and use*. Allied Publishers, 2001.

Hong Chen and Frank Allgöwer. A quasi-infinite horizon nonlinear model predictive control scheme with guaranteed stability. *Automatica*, 34(10):1205–1217, 1998.

Charles R Cutler. Method for removal of pid dynamics from mpc models, August 28 2007. US Patent 7,263,473.

Luis G Wesz da Silva, Rodrigo A Fernandes Pereira, Juan Rivier Abbad, and Jose R Sanches Mantovani. Optimised placement of control and protective devices in electric distribution systems through reactive tabu search algorithm. *Electric Power Systems Research*, 78(3):372–381, 2008.

George B Dantzig, Alex Orden, Philip Wolfe, et al. The generalized simplex method for minimizing a linear form under linear inequality restraints. *Pacific Journal of Mathematics*, 5(2):183–195, 1955.

Alberto De Marchi. On a primal-dual newton proximal method for convex quadratic programs. *Computational Optimization and Applications*, 81(2):369–395, 2022.

A. De Waal, U. Barker, M.S. Rennie, J. Klopper, and B.S. Groeneveld. Electrical factors affecting the economic optimization of submerged-arc furnaces. In *INFACON 6. Proceedings of the 6th International Ferroalloys Congress*, volume I, pages 247–252, Cape Town, South Africa, 1992.

Minh Tuan Dinh, Ionela Prodan, Olivier Lesage, and Eduardo Mendes. Mixed-integer predictive control for a three-phase electric arc furnace producing silico manganese. In *2024 European Control Conference*, 2024.

Minh Tuan Dinh, Ionela Prodan, Olivier Lesage, and Eduardo Mendes. Efficient switching in mixed-integer predictive control for a three-phase electric arc furnace. In *2025 American Control Conference*, 2025a.

Minh Tuan Dinh, Ionela Prodan, Olivier Lesage, and Eduardo Mendes. Computationally efficient mixed-integer predictive control for a three-phase electric arc furnace. *Control Engineering Practice*, 2025b. Under review.

Yachao Dong, Jose M Pinto, Arul Sundaramoorthy, and Christos T Maravelias. Mip model for inventory routing in industrial gases supply chain. *Industrial & Engineering Chemistry Research*, 53(44):17214–17225, 2014.

Iain Dunning, Joey Huchette, and Miles Lubin. Jump: A modeling language for mathematical optimization. *SIAM review*, 59(2):295–320, 2017.

Marco A Duran and Ignacio E Grossmann. An outer-approximation algorithm for a class of mixed-integer nonlinear programs. *Mathematical programming*, 36:307–339, 1986.

Thomas Echterhof. Review on the use of alternative carbon sources in eaf steelmaking. *Metals*, 11(2):222, 2021.

AS El-Bakry, Richard A Tapia, T Tsuchiya, and Yin Zhang. On the formulation and theory of the newton interior-point method for nonlinear programming. *Journal of Optimization theory and Applications*, 89(3):507–541, 1996.

M. Enrico, B. Aurelio, and K. Bernd. Green steel by eaf route: a sustainable value chain in the eu circular economy scenario. In *Green Steel by EAF Workshop Report*, 2019.

Eramet. Silicomanganese simn. Internal report, 2013.

Abolgasem Esmaeily and Felix Loge. Portfolio optimization problems with cardinality constraints, 2023.

Eurofer. European steel in figures 2024, 2024.

Timm Faulwasser and Gabriele Pannocchia. Toward a unifying framework blending real-time optimization and economic model predictive control. *Industrial & Engineering Chemistry Research*, 58(30):13583–13598, 2019.

V Feliu-Batlle and R Rivas-Perez. Robust fractional-order controller for an eaf electrode position system. *Control Engineering Practice*, 56:159–173, 2016.

V Feliu-Batlle, R Rivas-Perez, FJ Castillo-Garcia, and CA Rodriguez-Martinez. A robust fractional order controller for an eaf electrode position system. *IFAC Proceedings Volumes*, 47(3):10670–10675, 2014.

Hans Joachim Ferreau, Christian Kirches, Andreas Potschka, Hans Georg Bock, and Moritz Diehl. qpoases: A parametric active-set algorithm for quadratic programming. *Mathematical Programming Computation*, 6:327–363, 2014.

Matteo Fischetti and Andrea Lodi. Local branching. *Mathematical programming*, 98: 23–47, 2003.

JA Fleming. The applications of electric heating. lecture ii. *Journal of the Royal Society of Arts*, 59(3060):857–865, 1911.

G Folmo, C Perdon, T Hitter, R Ishak, F Wasser, and D Haaland. Furnace management in eramet manganese during the 2009 crisis. *INFACON XII, Helsinki, Finland*, pages 521–530, 2010.

Anders Forsgren, Philip E Gill, and Margaret H Wright. Interior methods for nonlinear optimization. *SIAM review*, 44(4):525–597, 2002.

Michel Fortin and Roland Glowinski. *Augmented Lagrangian methods: applications to the numerical solution of boundary-value problems*, volume 15. Elsevier, 2000.

Robert Fourer, David M Gay, and Brian W Kernighan. Ampl: A mathematical programming language. *Management Science*, 36(5):519–554, 1990.

GAMS. Extrinsic functions: Automatic differentiation. https://www.gams.com/50/docs/UG_ExtrinsicFunctions.html#UG_ExtrinsicFunctions_AutomaticDifferentiation, 2025. Accessed: 2025-09-30.

Vladimir B Gantovnik, Zafer Gurdal, Layne T Watson, and Christine M Anderson-Cook. Genetic algorithm for mixed integer nonlinear programming problems using separate constraint approximations. *AIAA journal*, 43(8):1844–1849, 2005.

Carlos E Garcia, David M Prett, and Manfred Morari. Model predictive control: Theory and practice—a survey. *Automatica*, 25(3):335–348, 1989.

David M Gay. Automatic differentiation of nonlinear ampl models. *Automatic Differentiation of Algorithms: Theory, Implementation, and Application*, pages 61–73, 1991.

Arthur M Geoffrion. Generalized benders decomposition. *Journal of optimization theory and applications*, 10:237–260, 1972.

E Michael Gertz and Stephen J Wright. Object-oriented software for quadratic programming. *ACM Transactions on Mathematical Software (TOMS)*, 29(1):58–81, 2003.

Bogdan Gheorghe, Florin Stoican, and Ionela Prodan. On the complexity of computing the maximal positive invariant set. In *2024 European Control Conference (ECC)*, pages 2697–2703. IEEE, 2024.

Loredana Ghiormez and Manuela Panoiu. Current control of a 3-phase electric arc furnace using fuzzy. 2015.

Philip E Gill, Walter Murray, and Michael A Saunders. Snopt: An sqp algorithm for large-scale constrained optimization. *SIAM review*, 47(1):99–131, 2005.

Philip E Gill, Michael A Saunders, and Elizabeth Wong. On the performance of sqp methods for nonlinear optimization. *Modeling and optimization: theory and applications*, pages 95–123, 2015.

Joris Gillis. Lookup tables in optimization with casadi and optispline. In *Benelux Meeting on Systems and Control, Date: 2018/03/27-2018/03/29, Location: Soesterberg, Netherlands*, 2018.

Ralph E Gomory. Outline of an algorithm for integer solutions to linear programs and an algorithm for the mixed integer problem. 1957.

A Gosiewski and A Wierzbicki. Dynamic optimization of a steel-making process in electric arc furnace. *Automatica*, 6(6):767–778, 1970.

Paul J Goulart and Yuwen Chen. Clarabel: An interior-point solver for conic programs with quadratic objectives. *arXiv preprint arXiv:2405.12762*, 2024.

Alasdair Graham. Making net-zero steel possible, 2025. URL https://worldsteel.org/wp-content/uploads/2b.-Pathway-to-Paris-Mission-Possible-Partnership-net-zero-steel-sector-transition-strate pdf. Available online. Accessed: 2025-07-03.

Alexandra Grancharova, Ivana Valkova, Nadja Hvala, and Juš Kocijan. Distributed predictive control based on gaussian process models. *Automatica*, 149:110807, 2023.

Andreas Griewank and Andrea Walther. *Evaluating derivatives: principles and techniques of algorithmic differentiation*. SIAM, 2008.

Astrid Grigsby-Schulte, Henna Khadeeja, Caitlin Swalec, Rolando Almada, Ziwei Zhang, and Jessie Zhi. Pedal to the metal 2025: Evaluating progress toward 2030 iron and steel decarbonization goals, May 2025. Accessed August 12, 2025.

Ignacio E Grossmann. Review of nonlinear mixed-integer and disjunctive programming techniques. *Optimization and engineering*, 3:227–252, 2002.

Ignacio E Grossmann and Juan P Ruiz. Generalized disjunctive programming: A framework for formulation and alternative algorithms for minlp optimization. In *Mixed Integer Nonlinear Programming*, pages 93–115. Springer, 2011.

Juan Guerra-Serrano, Angel Sánchez-Roca, Guillermo González-Yero, Mario C Sánchez-Orozco, Mercedes Pérez de la Parte, Emilio Jiménez Macías, and Julio Blanco-Fernández. New arc stability index for industrial ac three-phase electric arc furnaces based on acoustic signals. *Sensors*, 20(23):6840, 2020.

LLC Gurobi Optimization. Gurobi optimizer reference manual. 2023.

William W Hager and Hongchao Zhang. A survey of nonlinear conjugate gradient methods. *Pacific journal of Optimization*, 2(1):35–58, 2006.

M Hariharan and MP Gunasekar. Recent trends in electric arc furnace practice. *Transactions of the Indian Institute of Metals*, 51(05):363–367, 1998.

William E Hart, Jean-Paul Watson, and David L Woodruff. Pyomo: modeling and solving mathematical programs in python. *Mathematical Programming Computation*, 3(3):219–260, 2011.

Anna Soffia Hauksdóttir, Arnar Gestsson, and Ari Vésteinsson. Current control of a three-phase submerged arc ferrosilicon furnace. *Control Engineering Practice*, 10(4): 457–463, 2002.

Magnus R Hestenes. Multiplier and gradient methods. *Journal of optimization theory and applications*, 4(5):303–320, 1969.

Dusan Horvath, Riccardo Bacci Di Capaci, Maximilian Stremy, and Gabriele Pannocchia. Integrated testing of model predictive control on industrial plc. In *2025 Cybernetics & Informatics (K&I)*, pages 1–6. IEEE, 2025.

Daniel Ioan, Ionela Prodan, Sorin Olaru, Florin Stoican, and Silviu-Iulian Niculescu. Mixed-integer programming in motion planning. *Annual Reviews in Control*, 51:65–87, 2021.

Dennis Janka. *Sequential quadratic programming with indefinite Hessian approximations for nonlinear optimum experimental design for parameter estimation in differential–algebraic equations*. PhD thesis, 2015.

Sudi Jawahery, Ville-Valtteri Visuri, Stein O Wasbø, Andreas Hammervold, Niko Hyttinen, and Martin Schlautmann. Thermophysical model for online optimization and control of the electric arc furnace. *Metals*, 11(10):1587, 2021.

RT Jones and TR Curr. Pyrometallurgy at mintek. *Southern African Pyrometallurgy*, pages 127–150, 2006.

JuMP. Automatic differentiation of user-defined operators. https://jump.dev/JuMP.jl/stable/tutorials/nonlinear/operator_ad/, 2024. Accessed: 2025-09-30.

Michael Jünger, Gerhard Reinelt, and Stefan Thienel. Practical problem solving with cutting plane algorithms in combinatorial optimization. *DIMACS series in discrete mathematics and theoretical computer science*, 20(1995):111–152, 1995.

Michael Jünger, Thomas M Liebling, Denis Naddef, George L Nemhauser, William R Pulleyblank, Gerhard Reinelt, Giovanni Rinaldi, and Laurence A Wolsey. *50 Years of integer programming 1958-2008: From the early years to the state-of-the-art*. Springer Science & Business Media, 2009.

Miroslaw Karbowniczek. *Electric Arc Furnace Steelmaking*. CRC Press, 2021.

Hassan K Khalil. Lyapunov stability. *Control systems, robotics and automation*, 12:115, 2009.

H Khoshkhoo, Seyed Hossein Hesamedin Sadeghi, Rouzbeh Moini, and Heidar Ali Talebi. An efficient power control scheme for electric arc furnaces using online estimation of flexible cable inductance. *Computers & Mathematics with Applications*, 62(12): 4391–4401, 2011a.

Hamid Khoshkhoo, Seyed Sadeghi, Rouzbeh Moini, and H.A. Talebi. An efficient power control scheme for electric arc furnaces using online estimation of flexible cable inductance. *Computers & Mathematics with Applications*, 62:4391–4401, 12 2011b.

Marcus Kirschen, Victor Risonarta, and Herbert Pfeifer. Energy efficiency and the influence of gas burners to the energy related carbon dioxide emissions of electric arc furnaces in steel industry. *Energy*, 34(9):1065–1072, 2009.

Bernd Kleimt, Waldemar Krieger, Diana Mier Vasallo, Asier Arteaga Ayarza, and Inigo Unamuno Iriondo. Model-based decision support system for electric arc furnace (eaf) online monitoring and control. *Metals*, 13(8):1332, 2023.

Štefan Kozák. From pid to mpc: Control engineering methods development and applications. In *2016 cybernetics & informatics (K&I)*, pages 1–7. IEEE, 2016.

Jan Kronqvist, David E Bernal, Andreas Lundell, and Ignacio E Grossmann. A review and comparison of solvers for convex minlp. *Optimization and Engineering*, 20:397–455, 2019.

Jouni Lampinen and Ivan Zelinka. Mixed integer-discrete-continuous optimization by differential evolution. In *Proceedings of the 5th international conference on soft computing*, volume 71, page 76. Citeseer, 1999.

AH Land and AG Doig. An automatic method of solving discrete programming problems. *Econometrica*, 28(3):497–520, 1960.

W. Krieger Leopold Gmelin, H. Trenkler. *Gmelin handbook of inorganic chemistry: practice of steelmaking 2*, volume 8a of *Sustainable energy strategies*. Springer Berlin Heidelberg, 1984. ISBN 9783540935148. URL https://books.google.fr/books/about/Practice_of_Steelmaking_II.html?id=C5gVyAEACAAJ&redir_esc=y.

Hao Liu, Zhengqiang Miao, Nan Wang, and Yuwei Yang. A two-layer optimization of design and operational management of a hybrid combined heat and power system. *Frontiers in Energy Research*, 10:959774, 2022.

Pei Liu, Alan Whitaker, Efstratios N Pistikopoulos, and Zheng Li. A mixed-integer programming approach to strategic planning of chemical centres: A case study in the uk. *Computers & chemical engineering*, 35(8):1359–1373, 2011.

Johan Lofberg. Yalmip: A toolbox for modeling and optimization in matlab. In *2004 IEEE international conference on robotics and automation (IEEE Cat. No. 04CH37508)*, pages 284–289. IEEE, 2004.

Ellen K Luckins, James M Oliver, Colin P Please, Benjamin M Sloman, Aasgeir M Valderhaug, and Robert A Van Gorder. Modelling alternating current effects in a submerged arc furnace. 87(3):492–520, 2022. ISSN 0272-4960, 1464-3634.

Yassir Maataoui, Hamid Chekenbah, Omar Boutfarjoute, Vicenç Puig, and Rafik Lasri. A coordinated voltage regulation algorithm of a power distribution grid with multiple photovoltaic distributed generators based on active power curtailment and on-line tap changer. *Energies*, 16(14):5279, 2023.

Jorge Madias. *Electric Furnace Steelmaking*, volume 3, pages 271–300. 12 2014. ISBN 9780080969886. doi: 10.1016/B978-0-08-096988-6.00013-4.

Giulio M Mancuso, Enrico Bini, and Gabriele Pannocchia. Optimal priority assignment to control tasks. *ACM Transactions on Embedded Computing Systems (TECS)*, 13(5s): 1–17, 2014.

Vaso Manojlović, Željko Kamberović, Marija Korać, and Milan Dotlić. Machine learning analysis of electric arc furnace process for the evaluation of energy efficiency parameters. *Applied Energy*, 307:118209, 2022.

David Q Mayne, James B Rawlings, Christopher V Rao, and Pierre OM Scokaert. Constrained model predictive control: Stability and optimality. *Automatica*, 36(6): 789–814, 2000.

Juan C Meza. Steepest descent. *Wiley Interdisciplinary Reviews: Computational Statistics*, 2(6):719–722, 2010.

John E Mitchell. Branch-and-cut algorithms for combinatorial optimization problems. *Handbook of applied optimization*, 1(1):65–77, 2002.

Mahmood Moghadasian and Emad Alenasser. Modelling and artificial intelligence-based control of electrode system for an electric arc furnace. *Journal of Electromagnetic Analysis and Applications*, 2011.

Manfred Morari and N Lawrence Ricker. Model predictive control toolbox. *The Mathworks Inc*, 1994.

Matthias A Müller and Karl Worthmann. Quadratic costs do not always work in mpc. *Automatica*, 82:269–277, 2017.

Richard M Murray et al. Optimization-based control. *California Institute of Technology, CA*, pages 111–128, 2009.

Joonhyun Nam, Marie-Aline Van Ende, and In-Ho Jung. Ferromanganese production in a submerged arc furnace: Thermodynamic and energy balance analysis. *JOM: the journal of the Minerals, Metals & Materials Society*, 74, 2022.

Giacomo Nannicini and Pietro Belotti. Rounding-based heuristics for nonconvex minlps. *Mathematical Programming Computation*, 4:1–31, 2012.

M. D. Nguyen, Minh Tuan Dinh, Ionela Prodan, Olivier Lesage, and Eduardo Mendes. From conventional to optimization-based control for electric arc furnaces, 2025. Under preparation.

Ngoc Thinh Nguyen, Ionela Prodan, and Laurent Lefèvre. Stability guarantees for translational thrust-propelled vehicles dynamics through nmpc designs. *IEEE Transactions on Control Systems Technology*, 29(1):207–219, 2020.

Bethany Nicholson, John D Siirola, Jean-Paul Watson, Victor M Zavala, and Lorenz T Biegler. pyomo. dae: A modeling and automatic discretization framework for optimization with differential and algebraic equations. *Mathematical Programming Computation*, 10(2):187–223, 2018.

H Nicholson and R Roebuck. Simulation and control of electrode position controllers for electric arc furnaces. *Automatica*, 8(6):683–693, 1972.

H. Nicholson and R. Roebuck. Online optimal control of arc impedance for an electric-arc-furnace model. 120(3):365, 1973. ISSN 00203270.

Jorge Nocedal and Stephen J Wright. *Numerical optimization*. Springer, 2006.

T Norgate, S Jahanshahi, and WJ Rankin. Alternative routes to stainless steel–a life cycle approach. In *Tenth international ferroalloys congress*, pages 1–4, 2004.

Audu Umar Omesa, Sulaiman Mohammed Ibrahim, Rabiu Bashir Yunus, Issam AR Moghrabi, Muhammad Y Waziri, and Aceng Sambas. A brief survey of line search methods for optimization problems. *Results in Control and Optimization*, 19:100550, 2025.

Daniel Jacobus Oosthuizen, IK Craig, and PC Pistorius. Economic evaluation and design of an electric arc furnace controller based on economic objectives. *Control engineering practice*, 12(3):253–265, 2004.

Florian Opitz and Peter Treffinger. Physics-based modeling of electric operation, heat transfer, and scrap melting in an ac electric arc furnace. *Metallurgical and Materials Transactions B*, 47:1489–1503, 2016.

Christopher A Orrico, Matthijs van Berkel, Thomas OSJ Bosman, WPMH Heemels, and Dinesh Krishnamoorthy. Mixed-integer mpc strategies for fueling and density control in fusion tokamaks. *IEEE Control Systems Letters*, 7:1897–1902, 2023.

Andrés F Osorio and HH Toro. An mip model to optimize a colombian cash supply chain. *International Transactions in Operational Research*, 19(5):659–673, 2012.

Manfred Padberg and Giovanni Rinaldi. A branch-and-cut algorithm for the resolution of large-scale symmetric traveling salesman problems. *SIAM review*, 33(1):60–100, 1991.

Guan Ping, Li Ji-chao, and Liu Xiao-he. Direct adaptive fuzzy sliding mode control of arc furnace electrode regulator system. In *2009 Chinese Control and Decision Conference*, pages 2776–2781, 2009.

Ionela Prodan and Enrico Zio. A model predictive control framework for reliable microgrid energy management. *International Journal of Electrical Power & Energy Systems*, 61: 399–409, 2014.

Ionela Prodan, Florin Stoican, Sorin Olaru, Cristina Stoica, and S-I Niculescu. Mixed-integer programming techniques in distributed mpc problems. In *Distributed Model Predictive Control Made Easy*, pages 275–291. Springer, 2013.

Ionela Prodan, Florin Stoican, Sorin Olaru, and Silviu-Iulian Niculescu. *Mixed-integer representations in control design: Mathematical foundations and applications*. Springer, 2015.

AI Propoi. Use of linear programming methods for synthesizing sampled-data automatic systems. *Automn. Remote Control*, 24(7):837–844, 1963.

S Joe Qin and Thomas A Badgwell. A survey of industrial model predictive control technology. *Control engineering practice*, 11(7):733–764, 2003.

Ignacio Quesada and Ignacio E Grossmann. An lp/nlp based branch and bound algorithm for convex minlp optimization problems. *Computers & chemical engineering*, 16(10-11): 937–947, 1992.

Rien Quirynen and Stefano Di Cairano. Sequential quadratic programming algorithm for real-time mixed-integer nonlinear mpc. In *2021 60th IEEE Conference on Decision and Control (CDC)*, pages 993–999. IEEE, 2021.

Rien Quirynen and Stefano Di Cairano. Tailored presolve techniques in branch-and-bound method for fast mixed-integer optimal control applications. *Optimal Control Applications and Methods*, 44(6):3139–3167, 2023.

Rien Quirynen, Sleiman Safaoui, and Stefano Di Cairano. Real-time mixed-integer quadratic programming for vehicle decision-making and motion planning. *IEEE Transactions on Control Systems Technology*, 2024.

Gautham Ram, Venugopal Prasanth, Pavol Bauer, and Eva-Maria Bärthlein. Comparative analysis of on-load tap changing (oltc) transformer topologies. In *2014 16th International Power Electronics and Motion Control Conference and Exposition*, pages 918–923. IEEE, 2014.

Mudassir M Rashid, Prashant Mhaskar, and Christopher LE Swartz. Multi-rate modeling and economic model predictive control of the electric arc furnace. *Journal of Process Control*, 40:50–61, 2016.

James Blake Rawlings, David Q Mayne, and Moritz Diehl. *Model predictive control: theory, computation, and design*, volume 2. Nob Hill Publishing Madison, WI, 2017.

Marcus Reble and Frank Allgöwer. Unconstrained model predictive control and suboptimality estimates for nonlinear continuous-time systems. *Automatica*, 48(8):1812–1817, 2012.

MA Redfern and WRC Handley. Duty based maintenance for on-load transformer tap changers. In *2001 Power Engineering Society Summer Meeting.*, volume 3, pages 1824–1829. IEEE, 2001.

Kexin Ren, Yibo Wang, Shunjiang Wang, Chuang Liu, and Xudong Zhao. Hierarchical optimization strategy considering regulation of electric-fused magnesium high-energy-consuming load and deep peak regulation of thermal power. *Energies*, 18(20):5361, 2025.

QG Reynolds. The dual-electrode dc arc furnace-modelling brush arc conditions. *Journal of the Southern African Institute of Mining and Metallurgy*, 112(7):605–611, 2012.

QG Reynolds and RT Jones. Twin-electrode dc smelting furnaces—theory and photographic testwork. *Minerals Engineering*, 19(3):325–333, 2006.

Jacques Richalet and Donal O'Donovan. *Predictive functional control: principles and industrial applications*. Springer, 2009.

R Tyrrell Rockafellar. Monotone operators and the proximal point algorithm. *SIAM journal on control and optimization*, 14(5):877–898, 1976.

R.P.Paiva. Modelling and control of an electric arc furnace, 1996.

Yadollah Saboohi, Amirhossein Fathi, Igor Škrjanc, and Vito Logar. Optimization of the electric arc furnace process. *IEEE Transactions on Industrial Electronics*, 66(10): 8030–8039, 2018.

Nikolaos V Sahinidis. Baron: A general purpose global optimization software package. *Journal of global optimization*, 8:201–205, 1996.

Sergio E Samada, Vicenç Puig, Fatiha Nejjari, and Ramon Sarrate. Safe planning using mixed-integer programming for autonomous vehicles coordination. *Robotics and Autonomous Systems*, page 105078, 2025.

Max Schwenzer, Muzaffer Ay, Thomas Bergs, and Dirk Abel. Review on model predictive control: An engineering perspective. *The International Journal of Advanced Manufacturing Technology*, 117(5):1327–1349, 2021.

Yu. A. Shurygin. Symmetry of arc furnace operation. 47(11):732–736, 2017. ISSN 1935-0988.

Smriti Shyamal and Christopher L.E. Swartz. Real-time energy management for electric arc furnace operation. *Journal of Process Control*, 74:50–62, 2019. ISSN 0959-1524.

CA Smith, MA Redfern, and S Potts. Improvement in the performance of on-load tap changer transformers operating in series. In *2003 IEEE Power Engineering Society General Meeting*, volume 3, pages 1905–1905. IEEE, 2003.

Manuel Sparta, Vetle Kjær Risinggård, and Ulrik Thisted. Bockman method for measuring furnace core voltages: a modelling review. *Available at SSRN 4942623*, 2024.

Bartolomeo Stellato, Goran Banjac, Paul Goulart, Alberto Bemporad, and Stephen Boyd. Osqp: An operator splitting solver for quadratic programs. *Mathematical Programming Computation*, 12(4):637–672, 2020.

AB Stewart. The measurement of electrical variables in a submerged-arc furnace. *National Institute for Metallurgy*, page 55, 1981.

Alistair Bruce Stewart. An analysis of the electrical circuit of submerged-arc furnaces. 1980.

Florin Stoican, Ionela Prodan, and Dan Popescu. Flat trajectory generation for waypoints relaxations and obstacle avoidance. In *2015 23rd Mediterranean Conference on Control and Automation (MED)*, pages 695–700. IEEE, 2015.

Florin Stoican, Theodor-Gabriel Nicu, and Ionela Prodan. A mixed-integer mpc with polyhedral potential field cost for obstacle avoidance. In *2022 American Control Conference (ACC)*, pages 2039–2044. IEEE, 2022.

Nilesh Suriyarachchi, Rien Quirynen, John S Baras, and Stefano Di_Cairano. Optimization-based coordination and control of traffic lights and mixed traffic in multi-intersection environments. In *Proceedings of the American Control Conference*. IEEE, 2023.

Simon Tomažič, Goran Andonovski, Igor Škrjanc, and Vito Logar. Data-driven modelling and optimization of energy consumption in eaf. *Metals*, 12(5):816, 2022.

Yuri N Toulouevski and Ilyaz Y Zinurov. Innovation in electric arc furnaces. *Holland Landing, Canada*, 2, 2010.

Yuri N. Toulouevski and Ilyaz Y. Zinurov. Modern steelmaking in electric arc furnaces: History and development. In *Innovation in Electric Arc Furnaces: Scientific Basis for Selection*, pages 1–24. Springer Berlin Heidelberg, 2013. ISBN 978-3-642-36273-6.

Marco Vaccari, Riccardo Bacci di Capaci, Elisabetta Brunazzi, Leonardo Tognotti, Paolo Pierno, Roberto Vagheggi, and Gabriele Pannocchia. Optimally managing chemical plant operations: An example oriented by industry 4.0 paradigms. *Industrial & Engineering Chemistry Research*, 60(21):7853–7867, 2021.

Aasgeir Mikael Valderhaug. *Modelling and Control of Submerged-Arc Ferrosilicon Furnaces*. PhD thesis, Department of Engineering Cybernetics, The Norwegian Institute of Technology, Norway, 1992.

Jan van Leuween. Handbook of theoretical computer science, algorithms and complexity, 1990.

Robert J Vanderbei and David F Shanno. An interior-point algorithm for nonconvex nonlinear programming. *Computational Optimization and Applications*, 13(1):231–252, 1999.

Lander Vanroye, Ajay Sathya, Joris De Schutter, and Wilm Decré. Fatrop: A fast constrained optimal control problem solver for robot trajectory optimization and control. In *2023 IEEE/RSJ International Conference on Intelligent Robots and Systems (IROS)*, pages 10036–10043. IEEE, 2023.

Sara Velez and Christos T Maravelias. Mixed-integer programming model and tightening methods for scheduling in general chemical production environments. *Industrial & Engineering Chemistry Research*, 52(9):3407–3423, 2013.

Robin Verschueren, Gianluca Frison, Dimitris Kouzoupis, Jonathan Frey, Niels van Duijkeren, Andrea Zanelli, Branimir Novoselnik, Thivaharan Albin, Rien Quirynen, and Moritz Diehl. acados—a modular open-source framework for fast embedded optimal control. *Mathematical Programming Computation*, 14(1):147–183, 2022.

Stefan Vigerske and Ambros Gleixner. Scip: Global optimization of mixed-integer nonlinear programs in a branch-and-cut framework. *Optimization Methods and Software*, 33(3):563–593, 2018.

Sanjana Vijayshankar, Zachary Tully, Mariya Koleva, Evan Reznicek, Kathryn Johnson, and Jennifer King. Optimizing electrolyzers: Simultaneous degradation minimization and hydrogen flow maximization with mixed-integer programming. In *2025 American Control Conference (ACC)*, pages 4762–4769. IEEE, 2025.

Pauli Virtanen, Ralf Gommers, Travis E. Oliphant, Matt Haberland, Tyler Reddy, David Cournapeau, Evgeni Burovski, Pearu Peterson, Warren Weckesser, Jonathan Bright, Stéfan J. van der Walt, Matthew Brett, Joshua Wilson, K. Jarrod Millman, Nikolay Mayorov, Andrew R. J. Nelson, Eric Jones, Robert Kern, Eric Larson, C J Carey, İlhan Polat, Yu Feng, Eric W. Moore, Jake VanderPlas, Denis Laxalde, Josef Perktold, Robert Cimrman, Ian Henriksen, E. A. Quintero, Charles R. Harris, Anne M. Archibald, Antônio H. Ribeiro, Fabian Pedregosa, Paul van Mulbregt, and SciPy 1.0 Contributors. SciPy 1.0: Fundamental Algorithms for Scientific Computing in Python. *Nature Methods*, 17:261–272, 2020. doi: 10.1038/s41592-019-0686-2.

Andreas Wächter and Lorenz T Biegler. On the implementation of an interior-point filter line-search algorithm for large-scale nonlinear programming. *Mathematical programming*, 106:25–57, 2006.

Ye Wang, Vicenç Puig, and Gabriela Cembrano. Non-linear economic model predictive control of water distribution networks. *Journal of Process Control*, 56:23–34, 2017.

Zheming Wang, Raphaël M Jungers, and Chong-Jin Ong. Computing invariant sets of discrete-time nonlinear systems via state immersion. *IFAC-PapersOnLine*, 53(2): 5505–5510, 2020.

Stein O Wasbø. Ferromanganese furnace modelling using object-oriented principles. 1996.

Tapio Westerlund and Frank Pettersson. An extended cutting plane method for solving convex minlp problems. *Computers & chemical engineering*, 19:131–136, 1995.

Jesse Franklin White, Luis Miguel López Renau, and Björn Glaser. A review of biocarbon substitutes in electrodes and refractories for the metallurgical industries. *Journal of Sustainable Metallurgy*, 10(3):1051–1069, 2024.

Soderberg Carl Wilhelm. Electrode for electric furnaces and process for manufacturing the same, January 2 1923. US Patent 1,440,724.

Philip Wolfe. The simplex method for quadratic programming. *Econometrica: Journal of the Econometric Society*, pages 382–398, 1959.

Worldsteel. World steel in figures 2025, 2025.

Karl Worthmann, Marcus Reble, Lars Grune, and Frank Allgower. The role of sampling for stability and performance in unconstrained nonlinear model predictive control. *SIAM Journal on Control and Optimization*, 52(1):581–605, 2014.

Stephen J Wright. *Primal-dual interior-point methods*. SIAM, 1997.

Luo Yiqing, Yuan Xigang, and Liu Yongjian. An improved pso algorithm for solving non-convex nlp/minlp problems with equality constraints. *Computers & chemical engineering*, 31(3):153–162, 2007.

Ya-xiang Yuan. Recent advances in trust region algorithms. *Mathematical Programming*, 151(1):249–281, 2015.